



UNIVERSIDAD DE CHILE

FACULTAD DE CIENCIAS FÍSICAS Y MATEMÁTICAS

DEPARTAMENTO DE GEOLOGÍA

CONDICIONES PREERUPTIVAS DE LOS BASALTOS DEL RÍO MURTA, ANDES
PATAGÓNICOS, CHILE: UNA APROXIMACIÓN DESDE LA GEOQUÍMICA Y
PETROLOGÍA

TESIS PARA OPTAR AL GRADO DE MAGÍSTER EN CIENCIAS, MENCIÓN
GEOLOGÍA

MEMORIA PARA OPTAR AL TÍTULO DE GEÓLOGA

JAVIERA CONSTANZA VÉLIZ VERA

PROFESOR GUÍA:

DIEGO MORATA CÉSPEDES

PROFESOR CO-GUÍA:

ÁLVARO AMIGO RAMOS

MIEMBROS DE LA COMISIÓN:

PATRICIA LARREA MÁRQUEZ

MIGUEL ÁNGEL PARADA REYES

Este trabajo ha sido financiado por el Centro de Excelencia en Geotermia de los Andes
(CEGA), proyecto FONDAP-ANID 15090013/15200001/ACE210005

SANTIAGO DE CHILE

2023

RESUMEN

TESIS PARA OPTAR AL: Grado de Magíster en Ciencias, mención Geología

MEMORIA PARA OPTAR AL: Título de Geóloga

POR: Javiera Constanza Véliz Vera

FECHA: 2023

PROFESOR GUÍA: Diego Morata Céspedes

CONDICIONES PRERUPTIVAS DE LOS BASALTOS DEL RÍO MURTA, ANDES PATAGÓNICOS, CHILE: UNA APROXIMACIÓN DESDE LA GEOQUÍMICA Y PETROLOGÍA

Hace aproximadamente 15-14 Ma. en el continente sudamericano se desarrolló un punto triple donde colisionan tres placas tectónicas. Esta configuración evolucionó en la generación de una apertura o ventana que permitiría el ascenso de fluidos directo del manto. Se han atribuido a este proceso el desarrollo de grandes mesetas en el sector chileno y argentino. En el sector de Bahía Murta, también se han descrito lavas que tendrían relación con esta ventana, las cuales se han tomado como objeto de este estudio para ampliar la información sobre ellas y comprobar su origen.

La presente investigación estudia en detalle la mineralogía de las rocas recolectadas en terreno a nivel macroscópico y microscópico, además de sus texturas y química a través de metodologías semi-cuantitativas. Todos estos resultados se integraron en una serie de modelaciones y gráficas que han permitido la interpretación del posible origen de estos basaltos en superficie.

Con respecto a la química de roca total, las muestras corresponden a basaltos de olivino y una traquita, con patrones de elementos trazas que revelan la participación cortical en la evolución de estas lavas. En cuanto a los isótopos, las rocas examinadas muestran un patrón descendente por el arreglo mantélico, específicamente, entre el PREMA (*prevalent mantle*) y HIMU, donde la traquita es la muestra más diferenciada ubicándose cerca de la BSE (*Bulk Silicate Earth*). Los datos geoquímicos de la mineralogía presente dieron indicios tempranamente de diferencias en la composición de la masa fundamental en algunas rocas. En particular, en los minerales máficos como el olivino, se midió un contenido de forsterita (%Fo) bastante amplio como para pertenecer a una misma fase de crecimiento. Para esto, se realizaron test de equilibrio que permitieron confirmar la existencia de cristales fuera del equilibrio y, por lo tanto, heredados en el actual sistema. Lo anterior, también fue comprobado por evidencias de texturas de flujo en las secciones transparentes analizadas, reflejadas en diferencias de coloración en la masa fundamental y en el porcentaje de cristales. En cuanto a la proveniencia de estos basaltos, se infiere que, si bien no podemos negar la presencia de una ventana astenosférica bajo el continente en estas latitudes, estos no derivan directamente de la fusión del manto, sino que es posible reconstruirlos a través de procesos de cristalización fraccionada, leve contaminación y asimilación cortical más evidente hacia el norte de la zona de estudio, donde se encuentra el borde superior de la ventana; y además, por procesos de mezcla que han sido capaz de preservar cristales en desequilibrio con el sistema.

Este estudio refleja la complejidad en la evolución de las rocas en esta zona, que se encuentra bajo la influencia de una apertura astenosférica, pero también en una zona mixta donde se tiene aporte de fluidos del slab.

Para María Ignacia, Gaspar y Bruno, mi motivación

AGRADECIMIENTOS

Quiero partir agradeciendo a mi profesor guía, Diego, por la confianza depositada en mí en todo este tiempo. Por haberme acogido luego de los difíciles momentos que sucedieron al principio de este proyecto que lo hicieron peligrar. Gracias por acogerme con el alero del CEGA y por las conversaciones y palabras compartidas en cada una de nuestras reuniones.

A mi querido Álvaro, por creer en mí sin conocerme de maneras que ni yo hago, por regalarme la oportunidad de unirme siempre cuando puede a él y a su grupo de trabajo, de adentrarme en el servicio público y de darme tantas oportunidades para explorar en el área de la Volcanología, que son bastante escasas. Te agradezco profundamente cada café compartido, almuerzo y largas y tendidas conversaciones. Y por cumplirme el sueño de, por fin, ir a un Cities, y juntos. Tú sabes lo importante para mí que era participar de uno.

A Patri, porque a partir de tu llegada mi tesis comenzó a dar vuelco importante, tener tus ojos y tu conocimiento fue un verdadero placer y honor. Gracias por compartir y contagiar tu pasión por lo que haces y por toda la ayuda brindada en el tiempo que trabajamos juntas. Eres totalmente admirable y me encantó poder trabajar contigo.

Al profesor Miguel Ángel, por aceptar participar a último momento de este proyecto. Me siento muy privilegiada de haber podido tener clases con usted, que fue uno de los primeros que comenzó a instaurar el bichito de la Petrología y del mundo microscópico en mi camino como estudiante.

A mis padres, hermanos, sobrinos y familia en general. Por darme la posibilidad de estudiar en la universidad que quería, por el apoyo constante y por darme la posibilidad de explorar libremente mis gustos. Espero algún día poder retribuirles todo lo que me entregan día a día.

A mis amigos de Plan común, los que están y los que se perdieron. Cada uno impactó de una manera significativa el curso de mi vida. Mis queridos Gio y Agu, por ser incondicionales y por estar siempre cuando los necesito.

A mis queridos amigos, los Geochipamoglis: Gabby, Cami, Tomi y Vicho, por cada risa compartida, por todo el apañe, por las pijamadas, por las conversaciones a corazón abierto, por los abrazos y por apoyarnos y sentirnos orgullosos siempre del otro. Por haber hecho de mi paso por Geología unos de mis mejores años.

A todos y cada uno de los chicos y chicas con lo que compartí mis años de Geología, por las risas en terreno, por ser tan unidos y por generar un ambiente grato de compartir.

Al gran descubrimiento que fueron los Panitas, Ratonitas, Luchos, Amiguitas de posgrado. Me siento muy afortunada de haberlos conocido y sorprendida del apañe que se generó en tan poco tiempo, espero nos sigamos encontrando. Gracias Diego, Vale, Cami, Lore, Alejo, Luchini, Amandis, Bele, Gabs, Lolo, Ali y a todos los de la salita.

A mis estudiantes, por darme la posibilidad de enseñar, de mejorar mis habilidades comunicativas con ellos, por confiar en mí y por desarrollar mi gusto por la docencia.

A la Rosita, tía Mariela, Blanquis, por aguantarme cada vez que las iba a molestar. Son parte importante del departamento.

A Pituso y Franco por su apañe en terreno, por inundarme de sus conocimientos y por la guía en todos los días que compartimos en nuestro bello sur.

A Roberto por soportarme cada vez que lo iba a molestar para pedirle una paleteada, por prestarme materiales en plena pandemia para poder avanzar remotamente.

A cada una de las personas que se ha cruzado en mi camino y que, finalmente, ha aportado en construir la mujer que soy hoy. Agradecida de cada tropiezo y enseñanza, porque son lo que me han llevado hasta acá.

Eternamente agradecida.

TABLA DE CONTENIDO

1. INTRODUCCIÓN	1
1.1. Estructura de la tesis	1
1.2. Presentación del problema	1
1.3. Objetivos	8
1.3.1. General.....	8
1.3.2. Específicos.....	8
1.4. Hipótesis de trabajo	8
1.5. Área de estudio y rutas de acceso	9
1.6. Resúmenes en congresos	10
2. PRE-ERUPTIVE CONDITIONS OF THE MURTA RIVER BASALTS, PATAGONIAN ANDES, CHILE: AN APPROACH THROUGH GEOCHEMISTRY AND PETROLOGY	11
2.1. ABSTRACT.....	11
2.2. INTRODUCTION	12
2.3. GEOLOGICAL BACKGROUND	14
2.4. SAMPLES AND METHODS	17
2.5. RESULTS	19
2.5.1. Deposits characterization.....	19
2.5.2. Petrography and mineral chemistry	20
2.5.3. Mixing evidence	2
2.5.4. Major elements	4
2.5.5. Minor and trace-element features	5
2.5.6. Sr and Nd isotopic data.....	5
2.6. DISCUSSION	6
2.6.1. Origin of the Murta basalts.....	6
2.6.2. Fractional crystallization	8
2.6.3. Crustal contamination.....	10
2.6.4. Origin of the crystals	11
2.6.5. Origin of trachyte mineralogy	12
2.6.6. Mixing	13
2.6.7. Geodynamic implications	16

2.6.8. Magmatic evolution.....	17
2.7. CONCLUDING REMARKS.....	18
2.8. ACKNOWLEDGEMENTS.....	20
2.9. REFERENCES	21
2.10. FIGURES	28
2.11. TABLES.....	53
3. DISCUSIONES.....	56
3.1. Origen basaltos y traquita	56
3.2. Fisura río Ibáñez-Chiflón.....	57
3.3. Importancia turística y peligro asociado	59
4. CONCLUSIONES	60
BIBLIOGRAFÍA	62
ANNEXES.....	66
Annex A.....	66
A.1 Trabajo de terreno.....	66
Annex B.....	67
B.1 Descripción de cortes transparentes.....	67
Annex C.....	96
C.1 Datos análisis SEM lavas.....	96
C.2 Datos análisis SEM intrusivos	156
Annex D.....	162
D.1 Termo-oxibarometría en muestra evolucionada	162

ÍNDICE DE FIGURAS

Fig. 1. Esquema genérico de un slab window entre dos placas oceánicas subducentes (modificado de Thorkelson, 1996).	2
Fig. 2. Slab windows en borde Pacífico. Extraído de Thorkelson et al. (2011).	3
Fig. 3. Desarrollo de la ventana astenosférica bajo el continente proyectado a partir de la proyección en superficie de la Dorsal de Chile y las anomalías magnéticas de la Fig. 4 (Murdie y Russo, 1999 modificado por Russo et al., 2010).	6
Fig. 4. Mapa de anomalías en la velocidad de la onda P a 100 km (izquierda) y 200 km (derecha). Las velocidades altas se presentan en azul, las bajas en rojo y donde la resolución es baja se muestra de color negro. Las estructuras relacionadas a la Dorsal de Chile proyectadas en profundidad se encuentran en líneas grises. Las estaciones utilizadas están en cuadrados blancos y los triángulos rojos muestran la ubicación del volcanismo de arco activo. Extraído de Russo et al. (2010).	6
Fig. 5. Basaltos de Murta mapeados en Geología del Área Bahía Murta-Cerro Sin Nombre por Quiroz y Belmar (2010). Además, puntos de control existentes y muestras tomadas por Guivel et al. (2006) y Gutiérrez et al. (2005) en campañas anteriores (1:120.000).	9
Fig. 6. Volcanic and nonvolcanic segments (Pampean flat-slab segment and Patagonian volcanic gap) along the Andes. Red triangles represent the Holocene and Pleistocene volcanoes available in the Smithsonian Global Volcanism Program. CVZ = Central Volcanic Zone, SVZ = Southern Volcanic Zone and AVZ = Austral Volcanic Zone.	28
Fig. 7. Kinematic evolution of the Patagonia and Antarctic slab windows from 20 Ma to present. Rectangle in (F) indicates location of Fig. 8. AVZ = Austral Volcanic Zone; MF = Magallanes–Fagnano Fault; P = Phoenix; SF = Shackleton Fault; SVZ = Southern Volcanic Zone. All references used for the figure are detailed in Fig. 3 in Breitsprecher & Thorkelson (2009). Modified from Breitsprecher & Thorkelson (2009).	29
Fig. 8. Evolution of the Patagonia slab window through time. The colored points indicate the CTJ position from 12 Ma to present. The red star represents the Murta basalts location. MF = Magallanes–Fagnano Fault. All references used for the figure are detailed in Fig. 5 in Breitsprecher & Thorkelson (2009). Modified from Georgieva et al. (2019) after Breitsprecher & Thorkelson (2009).	30
Fig. 9. Location of the Murta basalts in a red square. Red stars highlight some sites of interest near the Murta basalts, such as Hudson Volcano to the north and General Carrera Lake to the south.	31
Fig. 10. Geological map of the study area. Modified from Quiroz & Belmar (2010). Murta basalts in pink.	32
Fig. 11. Regional-scale geometry of the Liquiñe-Ofqui fault zone. Dots = Quaternary volcanoes, the size of the dot is roughly proportional to the volume of lava erupted; filled triangles = Nazca-South America-Antarctica triple junction. Red square = study area. Modified from Cembrano et al. (1996).	32
Fig. 12. Geological context of the study area. (a) Plate tectonic frame of the subduction of the South Chile Ridge (SCR), its transform faults zones (FZ), and active segments (SCR1 to SCR 4) with collision ages. (b) Geology of the region around the Lago General Carrera-	

Buenos Aires showing the location of Murta basalts, Meseta de Chile Chico, and Lago Buenos Aires in frames. Modified from Lagabrielle et al. (2007).	33
Fig. 13. (A) First field trip with the sampling and control points. (B), (C) and (D) Zoom to the northern (Ibáñez-Chiflón rivers), central (Cajón River) and southern (Murta River) parts of the study area.....	34
Fig. 14.(A) Second field trip with the sampling and control points. (B) Zoom to the northern (Ibáñez-Chiflón rivers) part of the study area.	35
Fig. 15. (A) Samples with major, trace and isotope analysis. (B) Zoom to the northern (Ibáñez-Chiflón rivers) part of the study area.	36
Fig. 16. Images of the deposits found in the Cajón and Murta rivers. (A) Basalts with prismatic jointing located in the Cajón River. (B) Pillow lavas found in deposits near the Murta River. (C) Lighter-colored lavas with prismatic jointing, very thick with a fall deposit at the top. (D) Sample of lava near the Murta River with centimetric plagioclase macrocrysts.	36
Fig. 17. Deposits mapped at the intersection of the Ibáñez and Chiflón rivers. (A) Columnar basalts in Chiflón River. (B) Massive and highly vesiculated lavas. (C) Xenoliths within columnar basalts described in A.	37
Fig. 18. Summary of Murta basalts mineral composition illustrating the compositional evolution of macrocrysts, microphenocrysts, and groundmass crystals. As shown in the legend, dark filled symbol corresponds to center macrocrysts/phenocrysts (FCC), white symbols correspond to border macrocrysts/phenocrysts (FCB), tiny dark-filled symbol corresponds to microphenocrysts (MFC), and light-filled symbol corresponds to groundmass crystals (GM). (A) Feldspar (An-Ab-Or), (B) pyroxene (En-Wo-Fs), and (C) olivine (Fo).	37
Fig. 19. Main textures observed in the plagioclase macrocrysts and microcrysts in the thin sections. (A) JV031219-1 showing sieve texture. (B) JV021219-1 showing pilotaxitic texture with oriented plagioclase. (C) JV031219-3 showing patchy texture. (D) JV230220-2 showing poikilitic texture. (E) JV021219-1 showing diffuse zoning.....	38
Fig. 20. Main photographs of the olivine macrocrysts observed in the thin sections. (A) JV230220-2 showing olivine with skeletal form. (B) JV031219-2A showing alteration of olivine on edge by iddingsite. (C) JV031219-2A showing glomeroporphyritic texture where olivine macrocrysts are clustered. (D) JV250220-1 showing olivine with resorption.	38
Fig. 21. Main textures observed in the pyroxene microphenocrysts in the thin sections. (A) JV051219-1 image of PPL showing a radial shape of pyroxene. (B) JV051219-1 XPL image of (A). (C) JV031219-3 showing subophitic texture of pyroxene partially enclosing smaller plagioclase.	39
Fig. 22. Thin sections of samples (A) JV021219-1 (XPL), (B) JV031219-2A (XPL), (C) JV031219-4 (PPL), (D) JV051219-8 (XPL) and (E) JV240220-2 (XPL). Yellow lines highlight some examples of areas that are different from the rest of the groundmass. Letter A represents the light zones and B the dark zones.	39
Fig. 23. Total alkali–silica classification diagram based on Le Bas et al. (1986) for the Murta Basalts recalculated to 100 wt. %, anhydrous basis. The dotted line represents the boundary between the alkaline and sub-alkaline series (Irvine and Baragar, 1971).	40

Fig. 24. Major element bivariate diagrams against magnesium number (Mg#) for basalts and trachyte.	40
Fig. 25. Zoom to major element bivariate diagrams against magnesium number (Mg#) for basalts.	41
Fig. 26. Primitive mantle normalized (Sun & McDonough, 1989) spider diagram. (A) All samples plotted. (B), (C), (D) and (E) correspond to the different subgroups defined in chapter 2.5.5.	42
Fig. 27. Chondrite normalized (Sun & McDonough, 1989) REE diagram.	43
Fig. 28. Plot of $^{87}\text{Sr}/^{86}\text{Sr}$ against $^{143}\text{Nd}/^{144}\text{Nd}$ for (A) the studied lavas (symbol size bigger than the error bars), some SVZ and AVZ volcanoes, and Neogene Patagonian plateau lavas for comparison. Llaima data extracted from Hickey et al. (1986) and Hickey et al. (2016), Villarrica from Hickey et al. (1986), Lonquimay from Hickey et al. (2016), Hudson from Lopez-Escobar et al. (1993), Maca and Cay from Lopez-Escobar et al. (1993) and D’Orazio et al. (2003), Mentolat from Lopez-Escobar et al. (1993), Murta from Guivel et al. (2006) and Demant et al. (1998), Meseta Chile Chico (MCC) from Guivel et al. (2006) and Espinoza et al. (2005), Meseta Lago Buenos Aires (MLBA) from Guivel et al. (2006) and Muerte, Belgrano, Central and NE from Gorryng & Kay (2001). These include the depleted mantle (DM), bulk silicate Earth (BSE), enriched mantle (EM1), high- μ (U/Pb) (HIMU), and the ‘prevalent mantle’ (PREMA) fields. (B) Zoom to more primitive samples with error bars.	44
Fig. 29. The petrogenetic model based on Ni vs Y. Batch melting models are in green. The modal melting model is in a solid line and the non-modal melting model is in a dotted line. The E-MORB mantle’s starting composition were taken from Mertz et al. (2001) and the K_D from Gorryng & Kay (2001) and are available in Table 4. Source mineral mode: 58% ol, 30% opx, 10% cpx, and 2% sp. Melt mineral mode: 10% ol, 20% opx, 65% cpx, and 5% sp. Two other curves in blue represent olivine fractionation trends with points marking increments of 5% olivine fractionation.	45
Fig. 30. The petrogenetic model using batch melting models and fractional crystallization on a Chondrite normalized (Sun & McDonough, 1989) REE diagram. (A) Modal melting model and (B) Non-modal melting model. The E-MORB mantle’s starting composition were taken from Mertz et al. (2001) and the K_D from Gorryng & Kay (2001) and are available in Table 4. Source mineral mode: 58% ol, 30% opx, 10% cpx, and 2% sp. Melt mineral mode: 10% ol, 20% opx, 65% cpx, and 5% sp. The gray lines represent olivine fractionation trends with increments of 10% olivine fractionation. The green lines represent the partial melting percentage for each model used as a starting point for the fractionation models.	45
Fig. 31. Simplified scheme with the location of the analyzed samples grouped according to geochemical behavior and approximate ages. Subgroups 3 and 4 ages are from Guivel et al. (2006) and subgroups 1, 2 and trachyte are from Quiroz & Belmar (2010). According to temporality, t1 represents the oldest rocks and t5 the younger ones.	46
Fig. 32. N-MORB normalized (Sun & McDonough, 1989) fractional crystallization models using JV031219-3 as parental magma fractionating olivine, clinopyroxene, plagioclase, and spinel (50:29:20:1). Gray lines represent the proportion of liquid remaining with 10% increments. The K_d ’s are available in Table 5.	46
Fig. 33. N-MORB normalized (Sun & McDonough, 1989) fractional crystallization models using JV051219-3 as parental magma fractionating olivine, clinopyroxene, plagioclase, and	

spinel (50:29:20:1). Gray lines represent the proportion of liquid remaining with 10% increments. The K_d 's are available in Table 5.	47
Fig. 34. N-MORB normalized (Sun & McDonough, 1989) fractional crystallization models using JV031219-1 as parental magma fractionating olivine, clinopyroxene, plagioclase, and spinel (50:29:20:1). Gray lines represent the proportion of liquid remaining with 10% increments. The K_d 's are available in Table 5.	47
Fig. 35. Th–Nb proxy for crustal input based on Pearce (2008). Oceanic basalts (intraplate islands, plume-distal ocean ridges, and oceanic plateau) predominantly plot within the MORB–OIB array (shaded) while volcanic arc basalts plot above the array.	48
Fig. 36. AFC model between $^{87}\text{Sr}/^{86}\text{Sr}$ vs Th. Lines from left to right are $r=0.5$ and $r=0.8$, respectively. r is the assimilation rate (the mass assimilated/mass crystallized). The $^{87}\text{Sr}/^{86}\text{Sr}$ composition of the assimilated wall rock was taken from Pankhurst et al. (1999) and the average from three samples was used and Th=10 ppm. The partition coefficients are available in Table 5. Every point represents F with increments of 0.05.	48
Fig. 37. N-MORB normalized (Sun & McDonough, 1989) AFC model for trace elements. $r=0.5$. The composition of the assimilated wall rock used was the sample JV240220-2x. The partition coefficients are available in Table 5. Every gray line represents F with increments of 10%. In green line $F=60\%$	49
Fig. 38. Rhodes' diagram for testing (A) olivine/whole-rock equilibrium using $K_D(\text{Fe-Mg})^{\text{ol-liq}} 0.30\pm 0.03$, (B) clinopyroxene/whole-rock equilibrium using $K_D(\text{Fe-Mg})^{\text{ol-liq}} 0.28\pm 0.08$ and (C) orthopyroxene/whole-rock equilibrium using $K_D(\text{Fe-Mg})^{\text{ol-liq}} 0.29\pm 0.06$. As shown in the legend, dark filled symbol corresponds to center macrocrysts/phenocrysts (FCC), white symbols correspond to border macrocrysts/phenocrysts (FCB), tiny dark-filled symbol corresponds to microphenocrysts (MFC), and light-filled symbol corresponds to groundmass crystals (GM). Black borders represent the darker zones in thin sections equivalent to zone B in Fig. 22.	49
Fig. 39. Sample JV021219-1 (Cross-polarized light, XPL) with some SEM images and olivine compositions in the groundmass. A and B correspond to the light zone and C and D to the dark zone.	50
Fig. 40. Sample 031219-4 (Plane-polarized light, PPL) with some SEM images and pyroxene macrocrysts compositions. A, B and C correspond to the light zone and D and E to the dark zone.	51
Fig. 41. Sample JV051219-1 (Cross-polarized light, XPL) with some SEM images and olivine, plagioclase, and pyroxene compositions. A-D macrocrysts and E-F microcrysts. .	52
Fig. 42. Mapa topográfico con las principales estructuras descritas en el texto. Basaltos de Murta en polígonos rosados y fisura descrita en este estudio en línea punteada roja. Falla Exploradores de Georgieva et al. (2016) y Falla Bosque Muerto de Persico (2021). LOFZ de Cembrano y Lara (2009) y los autores citados en él. Algunas localidades importantes se marcan con estrellas rojas y el volcán Hudson con triángulo rojo. LOFZ: Zona de falla Liquiñe-Ofqui.	58
Fig. 43. Principales texturas observadas. (A) NX cúmulo de plagioclasas con olivinos, (B) NP vesícula, (C) NX plagioclasea con zonación difusa y (D) NX plagioclasas orientadas en masa fundamental.	68

Fig. 44. Principales texturas observadas. (A) NX cúmulo de plagioclasas con olivinos, (B) NX abundancia de inclusiones en plagioclasa, (C) NP vesícula con crecimiento cristalino en sus paredes y (D) NX plagioclasa con zonación.	70
Fig. 45. Principales texturas observadas. (A) NX cúmulo de plagioclasas con olivinos, (B) NX plagioclasas encerradas parcialmente por piroxenos, (C) NX vesículas y (D) NX plagioclasa con inclusiones.	72
Fig. 46. Principales texturas observadas. (A) NX cúmulo de plagioclasas con olivinos, (B) NX plagioclasa con variación composicional e inclusiones, (C) NX leve orientación de plagioclasas en masa fundamental y (D) NX plagioclasas encerradas parcial o totalmente por piroxenos.	74
Fig. 47. Principales texturas observadas. (A) NP vesículas con crecimiento secundario, (B) NP inclusiones y oquedades en plagioclasas, (C) NX cúmulo de piroxenos microcristalino y (D) NX fenocristales de piroxenos observados.	75
Fig. 48. Principales texturas observadas. (A) NX cúmulo de plagioclasas con olivinos, (B) NX abundancia de inclusiones y oquedades en plagioclasa, (C) NP vesícula con crecimiento de piroxenos aciculares en borde y (D) NX plagioclasa con zonación.	77
Fig. 49. Principales texturas observadas. (A) NP pequeñas vesículas, (B) NX abundancia de inclusiones cristalinas en plagioclasa, (C) NX inclusiones vítreas en borde plagioclasa y (D) NX plagioclasa con zonación.	79
Fig. 50. Principales texturas observadas. (A) NX cúmulo de plagioclasas con olivinos, (B) NX abundancia de inclusiones en plagioclasa, (C) NP vesícula con óxidos en sus paredes y (D) NX plagioclasa con zonación.	81
Fig. 51. Principales texturas observadas. (A) NX cúmulo de plagioclasas con olivinos, (B) NX abundancia de inclusiones en plagioclasa y variación composicional, (C) NX vesícula y (D) NX plagioclasa con zonación.	83
Fig. 52. Principales texturas observadas. (A) NX cúmulo de plagioclasas con olivinos, (B) NX masa fundamental intergranular y plagioclasa con variación composicional, (C) NX plagioclasa con abundantes inclusiones y oquedades y (D) NX plagioclasa con zonación.	85
Fig. 53. Principales texturas observadas. (A) NX cúmulo de plagioclasas con olivinos, (B) NX plagioclasa con inclusiones cristalinas, (C) NX abundancia de inclusiones en plagioclasa y (D) NP vesícula con crecimiento cristalino en borde y óxidos.	87
Fig. 54. Principales texturas observadas. (A) NX cúmulo de plagioclasas con olivinos, (B) NX plagioclasa con oquedades y variación composicional, (C) NX abundancia de inclusiones en plagioclasa y (D) NP vesículas.	89
Fig. 55. Principales texturas observadas. (A) NP borde entre lava y xenolito granítico, (B) NX cristales de cuarzo granular y feldespato potásico, (C) LR óxidos en xenolito granítico y (D) NX lamelas de exsolución en feldespato potásico.	90
Fig. 56. Principales texturas observadas. (A) NP clorita mineralogía secundaria, (B) NX epidota mineralogía secundaria, (C) LR óxidos y (D) NX lamelas de exsolución en feldespato potásico.	92
Fig. 57. Principales texturas observadas. (A) NX cúmulo de plagioclasas con olivinos, (B) NX abundancia de inclusiones en plagioclasa, (C) NP vesícula con óxidos en sus paredes y (D) NX plagioclasa con zonación.	94

Fig. 58. Principales texturas observadas. (A) NP contacto entre lava y xenolito granítico, (B) NX textura de los feldespatos potásicos, (C) NX textura micrográfica en feldespato y (D) NX crecimiento vermicular entre cristales de cuarzo y feldespatos.	95
Fig. 59. Imagen a polarizadores cruzados de la muestra JV021219-1.	97
Fig. 60. Imagen a polarizadores cruzados de la muestra JV031219-2A.	98
Fig. 61. Imagen a polarizadores cruzados de la muestra JV031219-4.	99
Fig. 62. Imagen a polarizadores cruzados de la muestra JV051219-1.	100
Fig. 63. Imagen a polarizadores cruzados de la muestra JV051219-8.	101
Fig. 64. Imagen a polarizadores cruzados de la muestra JV230220-2.	102
Fig. 65. Imagen a polarizadores cruzados de la muestra JV240220-2.	103
Fig. 66. Imagen a polarizadores cruzados de la muestra JV250220-1.	104
Fig. 67. Imagen a polarizadores cruzados de la muestra JV250220-6.	105
Fig. 68. Imagen a polarizadores cruzados de la muestra JV240220-2xeno.	157
Fig. 69. Imagen a polarizadores cruzados de la muestra JV240220-3xeno.	158
Fig. 70. Imagen a polarizadores cruzados de la muestra JV250220-6xeno.	159
Fig. 71. Pares de magnetita-ilmenita encontrados en la muestra JV031219-4. (A) crx21, (B) crx27 y (C) crx29. Las imágenes fueron tomadas por un microscopio electrónico de barrido (SEM).	162
Fig. 72. Aplicación del test de intercambio Mg/Mn (Bacon y Hirschmann, 1988) para los pares seleccionados de magnetita-ilmenita para la muestra JV031219-4. Solo 4 pares pasaron el test. La línea gruesa del medio y las otras dos delgadas corresponden a la regresión lineal promedio y al error involucrado ($\pm 2\sigma$), respectivamente.	163
Fig. 73. Composición de los óxidos Fe–Ti en un diagrama de FeO–Fe ₂ O ₃ –TiO ₂ . Las líneas punteadas corresponden a las soluciones sólidas ilmenita-hematita y magnetita–ulvospinela.	165

ÍNDICE DE TABLAS

Table 1. Major and trace element data for Murta basalts.	53
Table 2. Normative elements according to CIPW (Cross, Iddings, Pirrson y Washington).53	
Table 3. Sr and Nd isotopic data for Murta basalts.	54
Table 4. Partition coefficients used in the batch melting and fractionation model extracted from Gorrington & Kay (2001). E-MORB source is from Mertz et al. (2001). The source mineral mode (d_i) and the phase proportions entering the melt (p_i) are those used in Guivel et al. (2006) for spinel lherzolite.	54
Table 5. Partition coefficients used in the fractionation and crustal assimilation models. The sources from which the data were extracted are shown on the right, representing the background color of each box. The elements are divided into two groups: elements used for spider diagrams and rare earth elements. X_i is the modal proportion in which the phases are fractionated.	55
Table 6. Detalles de las paradas realizadas durante la primera campaña de terreno a Bahía Murta.	66
Table 7. Detalles de las paradas realizadas durante la primera campaña de terreno a Río Ibáñez-Chiflón.	66
Table 8. Composición química de los tres pares magnetita-ilmenita encontrados en la muestra JV031219-4. En paréntesis se muestra el número de la medición en SEM. Para el número de los cristales ver Fig. 71.	163
Table 9. Temperatura y fO_2 calculada para la composición de los pares coexistentes de magnetita e ilmenita usando los geotermómetros de Powell y Powell (1977), Spencer y Lindsley (1981) y Andersen y Lindsley (1985). A la izquierda se encuentran los diferentes métodos usados para calcular la fracción molar de hematita, ilmenita, magnetita y ulvoespinela (X_{hem} , X_{ilm} , X_{mag} y X_{ulv}). M: magnetita, I: ilmenita.....	164

1. INTRODUCCIÓN

1.1. Estructura de la tesis

El presente documento consta de un *primer capítulo* introductorio en español para conocer el contexto de la investigación y enmarcar la zona de estudio, así como definir los objetivos generales y específicos. El *segundo capítulo* presenta estudios petrográficos y geoquímicos de los basaltos de Murta y se titula “Pre-eruptive conditions of the Murta River basalts, Patagonian Andes, Chile: An approach through geochemistry and petrology”, el que corresponde a un manuscrito en inglés con intenciones de someter a una revista de interés. En el *tercer y cuarto capítulo*, en español, se dan cuenta de las principales discusiones y conclusiones generales de la investigación.

Finalmente, se adjunta material anexo con datos relevantes recopilados en este estudio. Cabe destacar que los títulos de los anexos han sido escritos en inglés para su referenciación en el segundo capítulo. El Anexo/Annex A entrega tablas detalladas del trabajo en terreno, coordenadas, muestras tomadas, fotografías, etc. El Anexo/Annex B consta del detallado análisis petrográfico realizado en cada una de las muestras tomadas en terreno. El Anexo/Annex C corresponde a las tablas de datos químicos obtenidos con el uso del SEM para las diferentes fases presentes. El Anexo/Annex D corresponde a un análisis geotermobarométrico en óxidos realizado para la traquita.

1.2. Presentación del problema

El poder determinar las condiciones pre-eruptivas de flujos basálticos nos permite entender los mecanismos asociados a los procesos de fusión parcial a partir de un manto, así como cuantificar las variables intensivas y extensivas asociadas a la petrogénesis de los mismos. Los Basaltos de Murta son, sin lugar a duda, una singularidad en la geología de los Andes Patagónicos. De hecho, el área de estudio se ubica en una zona interesante y excepcional geológicamente hablando. Esto, debido a la subducción de la Dorsal de Chile, desde hace 15 Ma., bajo la Placa Sudamericana, lo que generaría una ventana astenosférica bajo el continente. El actual punto triple, es decir, el punto en el cual convergen las placas Sudamericana, Nazca y Antártica, y que coincide además con el punto donde subduce la

dorsal actualmente, se ubica en la Península de Taitao, directamente al oeste de la zona estudio.

Estos basaltos serían el reflejo de un importante cambio en la geodinámica global del continente, y compartirían la génesis de grandes mesetas ubicadas en la Patagonia. Podrían ser la respuesta a procesos magmáticos posteriores, debido a la continua evolución y movimiento de esta ventana hacia el norte, donde estos basaltos serían solo marcas o cicatrices del paso de esta apertura bajo el continente.

El impacto asociado a este estudio, entonces, está ligado a las ventanas atmosféricas o *slab windows* que se forman por la subducción de una dorsal activa, que mientras subduce produciría un espacio, o ventana, que permite el ascenso de la astenósfera bajo la placa (Fig. 1). Este escenario se conoce en pocas partes del mundo; entre ellas California, British Columbia, Península Antártica (extinto en la actualidad), América Central y en la Patagonia chilena (Fig. 2), donde se enmarca este proyecto. Los basaltos generados en estas zonas permiten aportar una información relevante y única respecto a los procesos de fusión parcial que ocurren en estos contextos geológicos tan singulares.

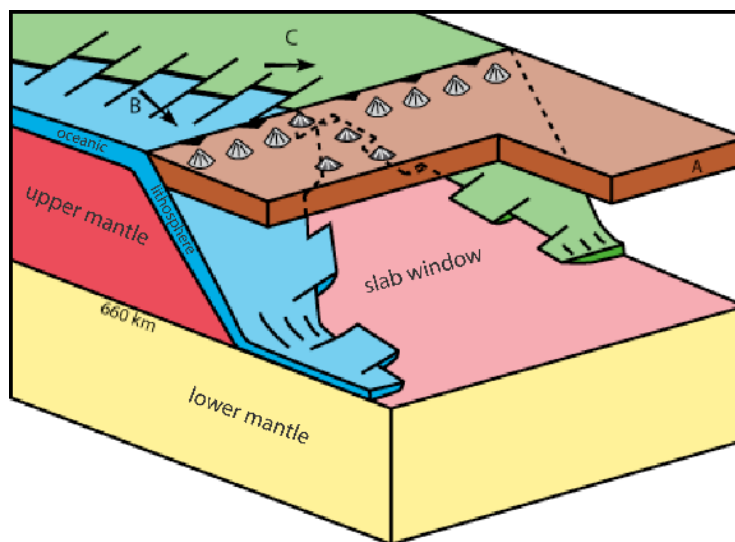


Fig. 1. Esquema genérico de un slab window entre dos placas oceánicas subducentes (modificado de Thorkelson, 1996).

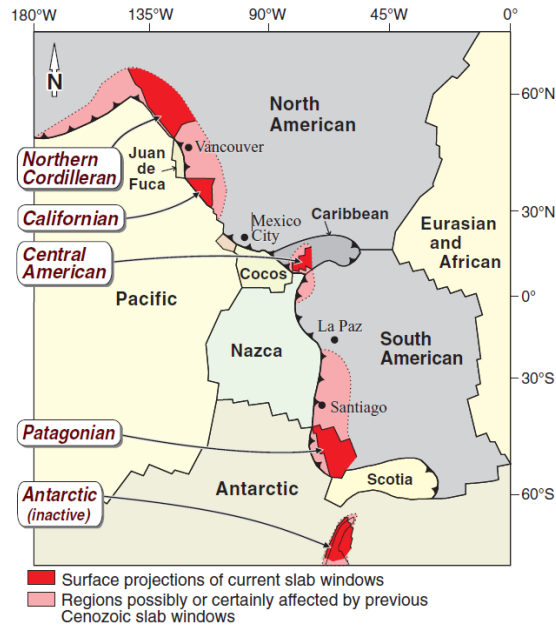


Fig. 2. Slab windows en borde Pacífico. Extraído de Thorkelson et al. (2011).

A diferencia de una zona de subducción normal, durante la subducción de una dorsal el estado térmico bajo el continente se ve perturbado. Al ser la litósfera oceánica delgada y cálida, su subducción producirá cambios en la estructura interna y dinámica del manto (Scalabrino, 2009).

El concepto de ventana astenosférica fue introducido por primera vez por Dickinson y Snyder (1979) en la costa de California, donde la apertura es desarrollada por la subducción de la falla transformante de San Andrés. Según los autores, posterior a la interacción dorsal/fosa se generaría una zona desprovista de litósfera oceánica sumergida. Y, además, se planteó la hipótesis de la presencia de flujos astenosféricos calientes bajo la placa norteamericana. Por lo tanto, la subducción de una dorsal activa puede considerarse como la sustitución de una subducción “fría” por otra “caliente”, generando una inversión completa del régimen térmico de la zona (Fig. 1).

La geometría esperada de los *slab windows*, dependiendo del ángulo en el cual subduce un *ridge*, fue descrita en detalle por Thorkelson (1996), quien supone que posterior al choque con el continente la subducción de las placas oceánicas continuaría y cesaría la acreción magmática a lo largo del eje del *ridge* formando el espacio entre ambas placas. Así, la forma de la ventana generada dependerá de tres factores (Dickinson y Snyder, 1979; Thorkelson y

Taylor, 1989): la tasa/velocidad de convergencia, la configuración de la dorsal subducida y el ángulo de subducción de las placas. El caso chileno, corresponde a la subducción de una dorsal a 15° (Bangs et al., 1992) con una migración del punto triple hacia el norte debido a su movimiento oblicuo relativo al margen sudamericano (Thomson et al., 2001).

La formación de *slab windows* estaría asociado espacial y temporalmente con volcanismo alcalino máfico, junto con un cese en la subducción a lo largo de márgenes activos, haciéndolo geoquímicamente indistinguible de algunos basaltos de islas oceánicas (Hole et al., 1991). Aunque no existe una relación temporal precisa entre ambos fenómenos se ha encontrado que, en la Península Antártica, luego del cese de la subducción precedida por una serie de colisiones de *ridge* de sur a norte del continente, una serie de basaltos alcalinos erupcionaron. El manto se fundiría como respuesta de la descompresión producida por el ascenso del manto a través de la ventana astenosférica generada por la subducción de un *ridge* (Hole et al., 1991). En términos generales la subducción de un *ridge* produce que entre las placas oceánicas divergentes se genere una anomalía termal, física y química en el manto astenosférico circundante, causando así un magmatismo anómalo involucrando, particularmente, volcanismo de antearco hasta trasarco, magmas alcalinos o toleíticos, tectonismo extensional y alzamiento. Además, por la reducción de la hidratación (típico de rocas calcoalcalinas) debido a la apertura del *slab*, el volcanismo de arco disminuiría o simplemente cesaría (Thorkelson, 1996).

Otro ejemplo de este evento ocurre, y como se mencionó anteriormente, en Norteamérica. Éste se caracteriza por la formación de dos *slab windows*: el Californiano (*Californian slab*) y el de la Cordillera del Norte en Canadá (*Northern Cordilleran slab*). En particular, en este último Thorkelson et al. (2011) realizaron análisis geoquímicos que entregaron interesantes resultados. El volcanismo de arco se encuentra interrumpido por un volcanismo de composiciones de intraplaca derivado de un manto anhidro, el cual concuerda espacialmente con la apertura del *slab*. Esta apertura permitiría el ascenso del manto anhidro que habría desplazado al manto hidratado de la cuña.

Continuando con el caso chileno y en cuanto a la validación de este fenómeno en Patagonia, existe evidencia geofísica que respalda la existencia del *slab window* bajo el continente (Fig. 3). Russo et al. (2010), han realizado un estudio que permite determinar la estructura interna

del manto superior con base en las anomalías de los tiempos de viaje de las ondas P. Una evidencia de primer orden es que en la zona del *slab* la onda P viaja a muy bajas velocidades, lo que podría representar una zona relativamente caliente. En la Fig. 4 se puede observar que la subducción de la placa de Nazca se refleja en una tendencia NNE de una anomalía de alta velocidad de las ondas P, mientras que en color rojo se encuentra la zona del *slab* a bajas velocidades, zona que se va ampliando en profundidad y moviendo levemente hacia el este. Lo anterior, se justifica debido a la creciente separación y aumento del espacio, con la profundidad, entre las placas de Nazca y Antártica.

Con lo anterior, se comprueba la existencia del *slab* entre las placas subducentes. Pero la pregunta de si el manto superior fluye o no bajo la litósfera subducente fue desarrollada por Murdie y Russo (1999) y Russo et al. (2010), quienes trabajaron con la división de las ondas de cizalla (*shear wave*) y sus tiempos de retardo al pasar por un medio anisótropo. Si bien los resultados de este trabajo se consideran preliminares, se encontró consistencia entre ellos, revelando anisotropías dentro del manto en la región del punto triple. La medida de la separación de las ondas de cizalla se ha usado para inferir el flujo del manto superior. Según Russo et al. (2010), al norte del punto donde subduce el *ridge*, la polarización de las ondas ocurre en dirección NW-SE (paralelo a la fosa), mientras que sobre la ventana ENE-WSW y, finalmente, al sur del *ridge* NE-SW. Esta inversión en la polarización de las ondas se ha interpretado como que el gap existente entre las placas permitiría el flujo del manto astenosférico entre ellas.

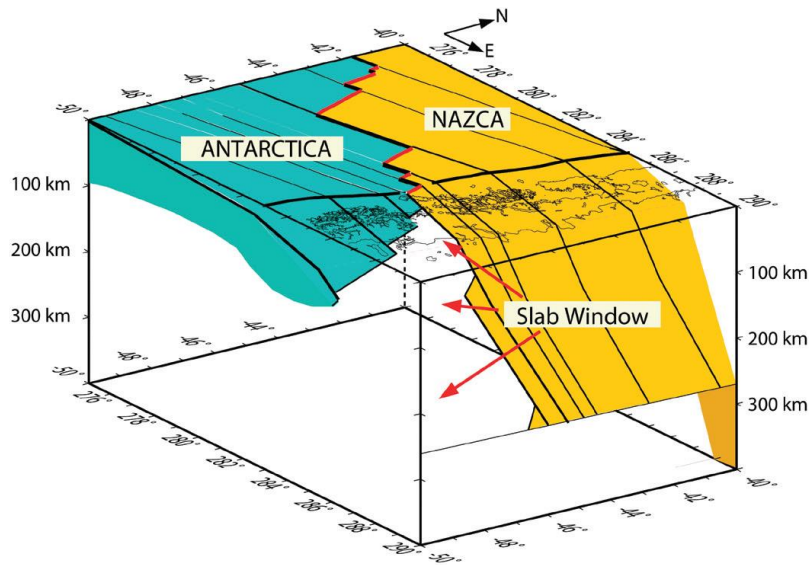


Fig. 3. Desarrollo de la ventana astenosférica bajo el continente proyectado a partir de la proyección en superficie de la Dorsal de Chile y las anomalías magnéticas de la Fig. 4 (Murdie y Russo, 1999 modificado por Russo et al., 2010).

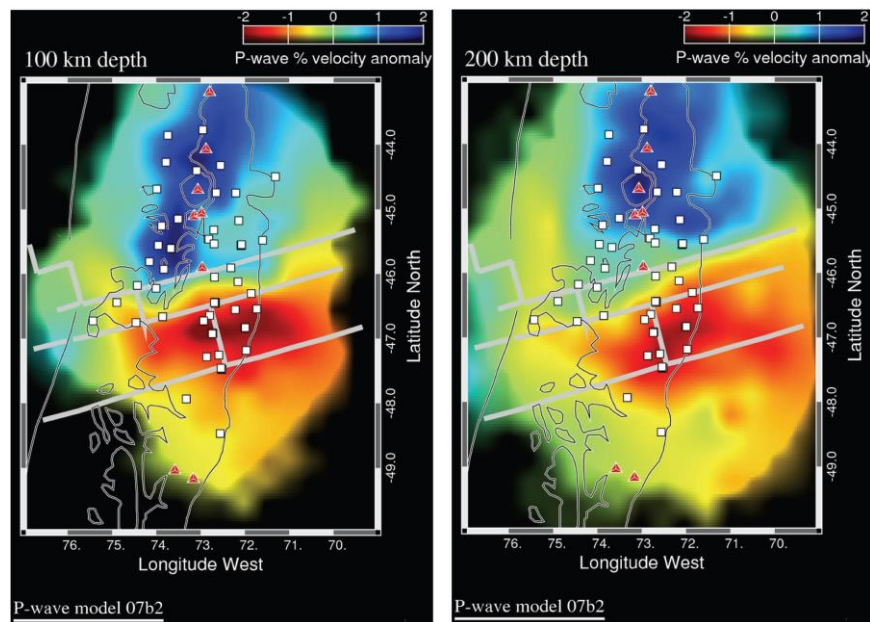


Fig. 4. Mapa de anomalías en la velocidad de la onda P a 100 km (izquierda) y 200 km (derecha). Las velocidades altas se presentan en azul, las bajas en rojo y donde la resolución es baja se muestra de color negro. Las estructuras relacionadas a la Dorsal de Chile proyectadas en profundidad se encuentran en líneas grises. Las estaciones utilizadas están en cuadrados blancos y los triángulos rojos muestran la ubicación del volcanismo de arco activo. Extraído de Russo et al. (2010).

En específico algunos de los basaltos generados en el contexto chileno de trasarco sobre el *slab*, que están ampliamente estudiados a nivel mundial, se mencionarán en los próximos capítulos. Pero en particular, se ha visto que uno de los efectos magmáticos incluye el desarrollo de basaltos geoquímicamente inusuales tipo MORB en la parte más cercana al

trench (Thorkelson y Breitsprecher, 2005) y la presencia de basaltos de *plateau* con afinidad OIB más al interior del *trench* (Hole et al., 1991; Gorrington et al., 1997).

En particular, los Basaltos de Murta fueron definidos por Demant et al. (1994, 1998) y Guivel et al. (2006). El interés que despertó en los primeros autores para estudiarlos era su signatura geoquímica. Además, su morfología de *pillow* lavas y de columnas fracturadas prismáticamente indica que este volcanismo se desarrolló bajo una espesa capa de hielo. En aspectos geoquímicos, estos autores concluyeron que corresponden a basaltos transicionales, es decir, que se encuentran en el límite entre el campo alcalino y subalcalino del diagrama TAS, sin una tendencia o afinidad clara. Son ligeramente diferenciados con un contenido de sílice de ~48%, 7% de MgO, Mg# entre 60-65 y Ni < 80 ppm.

Con respecto a elementos traza, la concentración de elementos compatibles es baja y cercana a magmas basálticos primitivos, mientras que presenta un leve enriquecimiento en elementos incompatibles LILE y LREE. Además, de presentar un leve empobrecimiento de Nb. Estas características indicarían una afinidad geoquímica relacionada a un componente de subducción. Por lo tanto, estos basaltos derivarían de la fusión del manto astenosférico con un débil componente de subducción, además de contaminación cortical posiblemente por el Batolito Patagónico por el cual ascendió. Esto último, en base a datos isotópicos de Sr y Nd. Si bien el origen de estos basaltos está constreñido en base a análisis de roca total, lo que se pretende con este estudio es realizar un análisis acabado de la petrología de las rocas analizadas y geoquímica para complementar la información existente; y así, entender la evolución de estos basaltos hasta la superficie.

A través de la química mineral y petrografía intentaremos conocer las condiciones pre-eruptivas de estos basaltos, su fuente y cómo estos interactúan con el entorno para llegar a ser lo que son hoy. La presente investigación trata de responder a las siguientes preguntas científicas: ¿Cuál es el nivel de interacción entre el magma parental y la corteza? ¿Cuáles fueron las etapas de ascenso del magma? ¿Cuánto tiempo permanecieron almacenados estos magmas antes de ser expulsados a superficie? ¿Qué rol juega el desarrollo de *slab window* en el origen de estos basaltos?

1.3. Objetivos

1.3.1. General

Definir y cuantificar los mecanismos de génesis y evolución magmática de los Basaltos de Murta enmarcados en un contexto geológico regional dominado por la subducción de la Dorsal activa de Chile.

1.3.2. Específicos

- Determinar de manera precisa la naturaleza geoquímica de los Basaltos de Murta, a través de su composición de elementos mayores y trazas.
- Establecer las condiciones de fusión parcial, así como la naturaleza del manto a partir del cual se generaron estos basaltos.
- Identificar procesos a través del estudio petrográfico de las muestras con la determinación de texturas claves dentro de ellas.
- Caracterizar químicamente las fases minerales presentes y corroborar sus equilibrios con respecto al sistema.
- Establecer la temporalidad de los flujos basálticos en el sector del Río Murta, así como sus diferentes mecanismos eruptivos.
- Generar un modelo evolutivo que permita explicar la presencia de estos basaltos en superficie a partir de los datos obtenidos.

1.4. Hipótesis de trabajo

Los Basaltos de Murta se generaron por fusión del manto astenosférico como consecuencia de la subducción de la Dorsal activa de Chile. Durante su ascenso, sufrieron procesos de diferenciación y contaminación cortical, la que se pone de manifiesto mediante xenolitos dentro de los basaltos, por lo que a través de la geoquímica y petrología se definirán las condiciones mantélicas de génesis, grados de fusión, fraccionamiento e interacción con la corteza que caracterizan a estos basaltos.

1.5. Área de estudio y rutas de acceso

El área de estudio se ubica en la Región de Aysén del General Carlos Ibáñez del Campo, sur de Chile. El recuadro que encierra el área tiene como límites 4900000-4880000 S y 668000-689000 E aproximadamente, como muestra la Fig. 5.

Los depósitos de los Basaltos de Murta se disponen siguiendo los cursos de los ríos Murta, Cajón, Ibáñez y Chiflón. Se encuentran a 30 kilómetros al sureste del volcán Hudson, volcán con actividad histórica importante, donde su última erupción relevante tuvo lugar en 1991 con reactivación de su actividad en el año 2011.

Se puede acceder por tierra a gran parte del área de estudio desde Cerro Castillo, siguiendo la Ruta 7 o Carretera Austral hacia el oeste, que une gran parte del sur de Chile. El resto de los depósitos ubicados en la confluencia del río Ibáñez con Chiflón se acceden mediante caminos de tierra privados y a pie bordeando el río Ibáñez.

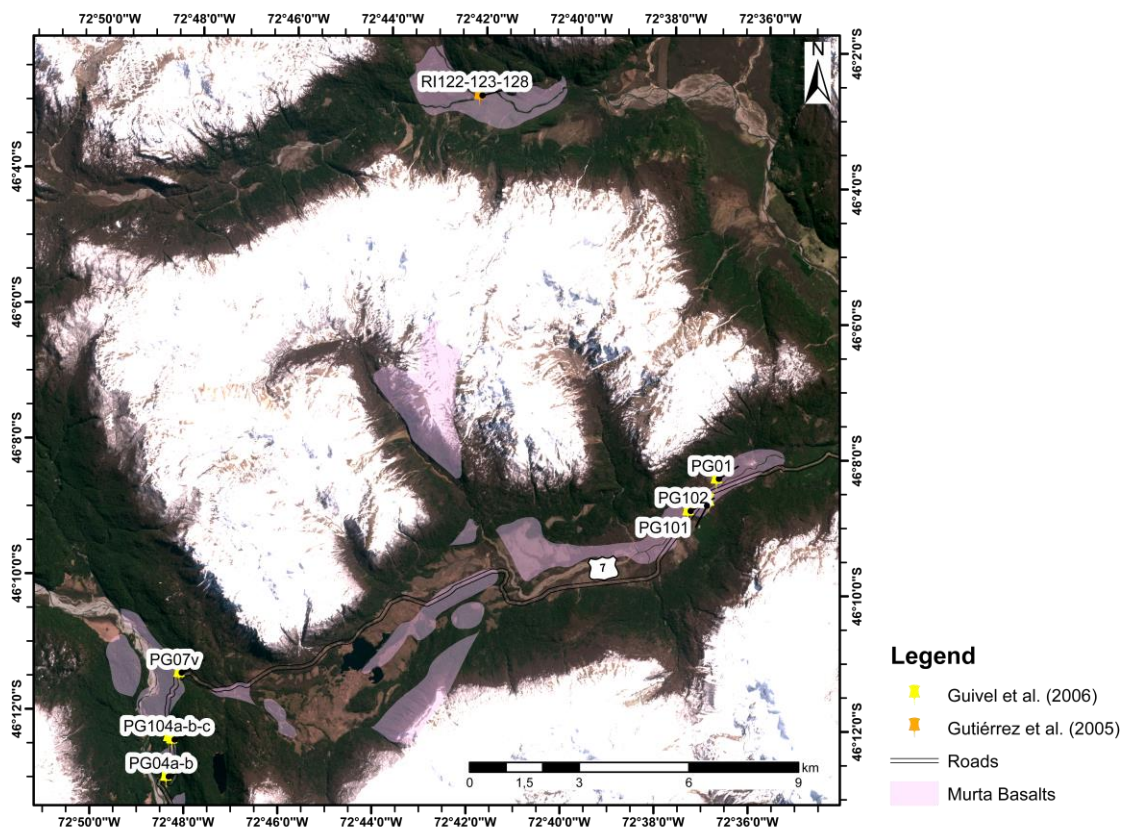


Fig. 5. Basaltos de Murta mapeados en Geología del Área Bahía Murta-Cerro Sin Nombre por Quiroz y Belmar (2010). Además, puntos de control existentes y muestras tomadas por Guivel et al. (2006) y Gutiérrez et al. (2005) en campañas anteriores (1:120.000).

1.6. Resúmenes en congresos

Véliz, J & Amigo, A. Volcanic hazards assessment and petrological insights of Murta basalts, Aysen region, Southern Chile. Cities on Volcanoes (COV) 11. June 12-17, 2022. Heraklion, Crete. Greece.

2. PRE-ERUPTIVE CONDITIONS OF THE MURTA RIVER BASALTS, PATAGONIAN ANDES, CHILE: AN APPROACH THROUGH GEOCHEMISTRY AND PETROLOGY

Javiera Véliz^{1,2*}, Diego Morata^{1,2}, Álvaro Amigo^{3,2}, Patricia Larrea^{1,2}, Miguel Ángel Parada^{1,2}, Petrus Le Roux⁴

¹*Department of Geology, Facultad de Ciencias Físicas y Matemáticas, Universidad de Chile, Plaza Ercilla 803, Santiago, Chile.*

²*Andean Geothermal Center of Excellence (CEGA), Facultad de Ciencias Físicas y Matemáticas, Universidad de Chile, Plaza Ercilla 803, Santiago, Chile.*

³*Chilean National Geology and Mining Service (SERNAGEOMIN), Santa María 0104, Santiago, Chile.*

⁴*Department of Geological Sciences, University of Cape Town, Rondebosch 7700, South Africa.*

*Corresponding author: jconstanzaveliz@gmail.com

Keywords: slab window, basalts, primitive mantle, petrogenesis, Patagonia, Chile

2.1. ABSTRACT

The Murta basalts are located in the Aysén region (Southern Chile), north of General Carrera Lake. Despite volcanism in Chile being mostly associated with Andean magmatism, the Murta River basalts are related to the subduction of the Chile spreading ridge underneath the South American plate (since 15 Ma), which generates asthenospheric windows under the continental crust. One of the few "triple junctions" on the planet is located just west of the zone at the Taitao Peninsula, which is where the Antarctic, Nazca, and South American plates converge.

In recent years, detailed geological field mapping has allowed us to identify some monogenetic vents in an area of ca. 400 km², suggesting that the Murta lava flows form a volcanic field, like those observed along the Southern Andes.

In this contribution, we present our results obtained by using petrography, SEM analyses, whole rock, and mineral chemical analysis to provide an estimation of the pre-eruptive

conditions of the magma, origin, and evolution of the Murta basalts. The evolution of these lavas is characterized by different intensities and mixing efficiencies identified both petrographically and chemically, as well as fractionation and assimilation episodes. The latter allows us to reconstruct all the samples and confirm the genetic relationship between them. Using two samples as parental magmas is possible to reconstruct all the samples with a 10-30% fractionation of olivine, clinopyroxene, plagioclase, and spinel. However, a more evolved trachyte coexisting with more primitive samples, and outcropping as a dome was generated by crustal assimilation and fractionation. The presence of granitic xenoliths in some basalts, confirms the upper crustal participation in the evolution of these lavas, but in a smaller proportion to the fractionated part.

Our results suggest that the Murta basalts were generated by rather complex processes and that primitive fluids do not ascend directly suffering differentiation processes that changed their chemistry to a more evolved one. Moreover, magma mixing and crustal contamination processes participate in the genesis of these basalts allowing the formation of even differentiated trachytic magmas.

2.2. INTRODUCTION

The modern Andes can be divided into volcanic and nonvolcanic segments (Fig. 6) that correlate with different tectonic arrangements and with the dip of the subduction zone (Kay et al., 1987). Active volcanism is restricted to zones where the angle of dip is approximately 30° (Kay et al., 1988). In the Chilean Andes, there are two important zones where volcanism is absent, the first one is related to the “flat-slab” region between 28°S and 33°S caused by the near sub-horizontal angle of subduction and asthenosphere thinning (Kay et al., 1988). The second one is the slab window region developed from 46°S and caused by ridge subduction. Our study area (Murta basalts) is located within this second arrangement.

The collision of the Chilean ridge formed by the interaction between the Nazca and Antarctic plates began at approximately 15-14 Ma at 55°S (Fig. 7) forming the triple point between the Nazca, Antarctic, and South American plates, based on plate reconstructions by Cande & Leslie (1986).

The general NW-SE trend of the Chile rise and its oblique NE movement relative to the N-S margin of the South American plate caused a northward migration of the CTJ (Chile Triple Junction) along the Peru-Chile trench (Thomson et al., 2001) due to the morphology of the ridge.

Plate reconstruction for the evolution of triple point is now better constrained by marine magnetic anomaly studies. These analyses show that the motion of the Nazca plate relative to the South American plate before ridge subduction was quite complex. Before 49 Ma, the convergence was probably quite slow. Between 49 and 42 Ma the convergence rate increased and changed its direction. Between 42 and 26 Ma the convergence rate decreased to 5.2 cm/yr. Around 26 Ma the convergence rate increased again to 11-15 cm/yr followed by a gradual decrease to 7.8 cm/yr at present (Somoza, 1998).

In particular, it has been shown that one of the magmatic effects generated by the presence of the slab window includes the development of geochemically unusual MORB-type basalts closer to the trench (Thorkelson & Breitsprecher, 2005), and the presence of plateau basalts with OIB affinity further into the trench (Hole et al., 1991; Gorrying et al., 1997).

The Patagonian back-arc domain is characterized by numerous Neogene basaltic plateaus (Mesetas), that can be explained as melts formed as upwelling, sub-slab asthenosphere which flowed around the trailing edge of the descending Nazca Plate and then interacted with subduction altered asthenospheric wedge and continental lithosphere, or by weaker upwelling of sub-slab asthenosphere through the open slab window (Gorrying et al., 1997).

The Murta basalts are found near the northern boundary of the slab window (Fig. 8), south of Hudson volcano which is the last arc volcano before it is interrupted. These basalts have been studied by Demant et al. (1994, 1998), Corgne et al. (2001), Gutiérrez et al. (2005), and Guivel et al. (2006). All agree that the occurrence of these basalts comes from the melting of the asthenospheric mantle with a weak subduction component in an environment where the Chilean ridge subducts under the South American plate generating the asthenospheric window.

The ages of these deposits, included in the geological map of the study area with their respective locations (Fig. 10), are from Guivel et al. (2006) and range between 0.27 ± 0.39

and 0.9 ± 0.08 Ma (K-Ar, whole rock) in the Cajón River. In Murta River the ages are approximately 0.85 ± 0.1 Ma (K-Ar, whole rock). At the confluence of the Ibáñez and Chiflón rivers the ages found are 0.070 ± 0.030 and 0.160 ± 0.060 Ma (Ar-Ar in groundmass, Quiroz & Belmar, 2010).

In this article, we examine the petrology (textures) and geochemical data from whole rock (major, trace element, and Sr and Nd isotopic data) and mineral (major elements) of these basalts to complement past research, including new samples found in the area. We will show partial melting models, assimilation, and fractional crystallization (AFC) models to recreate the samples and to know the level of interaction with the crust.

2.3. GEOLOGICAL BACKGROUND

The Murta basalts are located in Murta Valley in the Aysén region of Chile, specifically to the north of General Carrera Lake. The study area is distributed in the back arc of the Patagonian gap, south of the Hudson volcano, where volcanism is interrupted along The Andes (Fig. 9).

Using the geological map (Fig. 10) developed by Quiroz & Belmar (2010) the oldest rocks that outcrop in the Patagonian Andes of southern Chile are the Eastern Andean Metamorphic Complex (Devonian-Upper Carboniferous). These are located to the east of the Patagonian Batholith and are composed of quartz-muscovite schists and phyllites. Also, it is possible to find mafic schists and ultramafic rocks, mainly serpentinites.

In angular unconformity over the Metamorphic Complex is the Ibáñez Formation (Jurassic-Lower Cretaceous) composed of volcanic, mainly pyroclastic acid rock, dacitic-rhyolitic domes, and minor presence of andesitic and basaltic lavas.

A large part of the Cordillera is formed by the Patagonian Batholith (Lower Cretaceous to Miocene) that intrudes the Metamorphic Complex and Jurassic volcanic rocks. This batholith corresponds to calc-alkaline intrusive rocks.

The Murta basalts are unconformably disposed over the metamorphic basement, Ibáñez Formation or Patagonian Batholith. These basalts are composed of basaltic lavas possibly

from the asthenospheric mantle passing through the slab window generated from subducted segments of the South Chile Ridge under the South American continent since 6 Ma ago.

The modified geological map of the area, made by Quiroz & Belmar (2010) is shown in Fig. 10 to understand the arrangement and relationship between the different components mentioned above, and to identify the Murta basalts (Plb) and their distribution in the area.

The global geodynamics in the study area is divided into 2 main tectonic stages related to a change in the subduction regime. The first is a pre-ridge subduction stage, from 30 to 15 Ma, where the Nazca plate subducts under the South American plate, and a second ridge subduction stage involves the opening of slab windows (Scalabrino et al., 2009), which will be discussed later.

The most important structural feature in the south of Chile is the Liquiñe-Ofqui Fault Zone (LOFZ) which accommodated continental-scale deformation arising from the plate convergence to the north of the triple point. The fault zone consists of two NNE-trending right-stepping straight lineaments and at least four NE-trending, straight, *en échelon* lineaments resulting in an extensional geometry. Also, three NNW-trending curved lineaments concave to the southwest (Cembrano et al., 1996). This system extends from the Golfo de Penas (~47°S) northward for about 1000 km (Fig. 11).

The Patagonian Cordillera is topographically continuous. Nevertheless, between latitudes 45°S and 47°S, at the latitude of the CTJ, it shows an unusual region having the highest mountains (Fig. 12a) like Mt. San Valentin (4058 m a.s.l.) and Mt. San Lorenzo (3706 m a.s.l.); and a series of deep transverse incisions occupied by postglacial lakes, one of them corresponds to the Lago General Carrera–Buenos Aires (LGCBA) (Lagabrielle et al., 2004; Scalabrino et al., 2009) that according to bathymetry data from Murdie & Russo (1999) would be 585 meters maximum depth (385 below sea level).

At the triple point latitude, the orogenic front is marked by a topographic jump of several hundred meters, due to an easterly vergent thrust system. This compressive stage started at around 32 Ma, as shown by contractional syn-sedimentary deformation recorded by Eocene, Oligocene, and Miocene deposits (Lagabrielle et al., 2004; Scalabrino et al., 2009).

In addition to the main relief of the Cordillera, the region is characterized by the occurrence of several plateaus or mesetas (Fig. 12) like Meseta del Lago Buenos Aires, Meseta del Guenguel, Meseta Chile Chico, and others, and by a deep transverse valley occupied by the LGCBA. The mesetas are delineated by steep erosional scarps. This morphology, interbedded with fluvial deposits and glacial sediments, would indicate that they were deposited in a major drainage area and, therefore, a recent relief inversion in response to regional vertical movements. This inversion would have occurred during Miocene-Pliocene (Lagabrielle et al., 2004).

The General Carrera Lake would correspond to the northern limit of a fold-and-thrust belt developed up to Tierra del Fuego. Suárez & De la Cruz (2000) have recognized late Early Cretaceous contractional tectonic events in the region as well as in the Miocene and probably in the Paleocene-Eocene. Although it must be recognized that evidence of recent deformation is scarce due to the strong action of glaciers during the evolution of the landscape (Suárez & De la Cruz, 2000; Lagabrielle et al., 2004, 2007).

The tectonic evolution of the northern Patagonian fold-and-thrust belt is more complex than previously thought, with pre-Late Paleocene-Early Eocene and post-Barremian contractional tectonic phase identified south of General Carrera Lake and a late Early Cretaceous contractional tectonism identified in the area between General Carrera Lake and Fontana Lake (Suárez & De la Cruz, 2000).

After the contractional event mentioned above, during Pliocene, it is suggested a regional extensional or transtensional possibly associated with the Chilean ridge subduction at 6 and 3 Ma (Lagabrielle et al., 2007). The first-order consequence of ridge subduction is the opening of asthenospheric windows (Thorkelson, 1996) producing first doming and then a weakening of the crust triggering in turn localized collapse (Lagabrielle et al., 2007).

Another line of evidence that may indicate abrupt Pliocene morphological changes comes from the occurrence of 4.5 Ma basalts which accumulated within topographic lows, but now form remnants at different altitudes and separated from General Carrera Lake. In this way, it was possible to confirm that the disruption and the dissection of the surface which formed the summit of the Cordillera occurred along two main directions: parallel to the trend of the Cordillera leading to incisions of Ghio, Jeinimeni, and Zeballos rivers and leaving the Meseta

Lago Buenos Aires relict surface, and transverse to the Cordillera forming the Lago General Carrera-Buenos Aires depression. The first N-S disruption started around 5 Ma, while the second E-W disruption started after 4.5 Ma (Lagabrielle et al., 2007).

Particularly and according to the geological map from Quiroz & Belmar (2010), the study area is characterized by faults and lineaments NNE to NE and NS that affect the Jurassic rocks and part of the metamorphic basement. Meanwhile, in the Patagonian Batholith rock, the faults and lineaments are mostly NW.

The major structures of regional scale are associated with the traces of main valleys, such as the upper course of the Ibáñez and Murta rivers, with NW orientation, and the Portezuelo Cofré-Cajón River, with NE trace. Both valleys would have constituted favorable structures to the emplacement of basaltic magmas in the middle-upper Pleistocene with the consequent effusion of lavas known as Murta basalts, the subject of this study (Quiroz & Belmar, 2010).

2.4. SAMPLES AND METHODS

Samples has been collected during two fieldwork investigations (see Annex), with the logistical and transportation support of the Chilean National Geology and Mining Service (SERNAGEOMIN). The sampling points were based on the locations provided by Guivel et al. (2006) and Gutiérrez et al. (2005), who visited the area previously and characterized the Murta basalts. However, sampling was made also in new outcrops not mapped before, in the case of sample JV250220-1 located in Ibáñez River and the samples found in the intersection of Ibáñez and Chiflón rivers, north of the study area (Fig. 13 and Fig. 14).

Fifteen samples were selected (12 volcanic rocks and 3 granitic xenoliths, Fig. 15 and Table 1) for major and trace analysis, based on their position and petrography. Major analyses were conducted on powders by X-ray fluorescence (XRF), at the Activation Laboratories LTD. (Canada) and trace-element analyses were conducted on powders by Mass Spectrometer (ICP-MS), at the University of Cape Town, Rondebosch, South Africa.

To minimize the matrix effects of the samples, the heavy absorber fusion technique of Norrish & Hutton (1969) is used for major element (oxide) analysis. Before fusion, the loss on ignition (LOI), which includes H₂O⁺, CO₂, S, and other volatiles, can be determined from

the weight loss after roasting the sample at 1000°C for 2 hours. The fusion disk is made by mixing a 0.75 g equivalent of the roasted sample with 9.75 g of a combination of lithium metaborate and lithium tetraborate with lithium bromide as a releasing agent. Samples are fused in platinum crucibles using an automated crucible fluxer and automatically poured into platinum molds for casting. Samples are analyzed on a Panalytical Axios Advanced wavelength dispersive XRF. The intensities are then measured, and the concentrations are calculated against the standard G-16 provided by Dr. K. Norrish of CSIRO, Australia. Matrix corrections were done by using the oxide alpha-influence coefficients provided also by K. Norrish.

For ICP-MS 50 mg of sample powder was dissolved in a 4:1 HF/HNO³ acid mixture in sealed Savilex beakers on a hotplate for 48 hours, followed by evaporation to incipient dryness and two treatments of 2 mL concentrated HNO₃. The final dried product was then taken up in a 5% HNO³ solution containing 10 ppb Re, Rh, In and Bi, used as internal standards. Peak-hopping mode was used for data acquisition. Samples are analyzed on an iCAP RQ Thermo Fisher ICP-MS. Calibration curves were obtained using artificial multi-element standards, from which standard solutions were made.

Also, Sr and Nd isotopic data were measured for 5 samples (Fig. 15 and Table 3), the trachyte and four basalts, based on their MgO content, in an attempt to cover the full spectrum of MgO. All isotope analyses were performed on a Nu Instruments NuPlasma HR in the MC-ICP-MS facility, housed in the Department of Geological Sciences, University of Cape Town, Rondebosch, South Africa. All Sr isotope data were referenced to an ⁸⁷Sr/⁸⁶Sr normalizing value of 0.710255 using NIST SRM987 as a reference standard (Waight et al., 2002). Sr isotope data were corrected for Rb interference using the measured signal for ⁸⁵Rb and the natural ⁸⁵Rb/⁸⁷Rb ratio, whereas instrumental mass fractionation was treated with exponential law and an ⁸⁶Sr/⁸⁸Sr value of 0.1194. The Nd isotope values were normalized to a ¹⁴³Nd/¹⁴⁴Nd value of 0.512115 using JNdi-1 as a reference standard, after Tanaka et al. (2000). All Nd isotope data were corrected for Sm and Ce interference using the measured signals for ¹⁴⁷Sm and ¹⁴⁰Ce and natural Sm and Ce isotope abundances, whereas instrumental mass fractionation was treated with exponential law and a ¹⁴⁶Nd/¹⁴⁴Nd value of 0.7219. Methodology as in Harris et al. (2015).

Mineral analyses were obtained on polished sections from 9 samples using Scanning Electron Microscopy (SEM) a FEI model Quanta 250 with EDX detector at the Department of Geology at the University of Chile. Before analysis, samples were coated with carbon. Analytical conditions were 5-6 μm spot size, 20-25 kV, counting time of 60 s at a pressure of 10^{-4} Pa.

2.5. RESULTS

2.5.1. Deposits characterization

The Murta basalts are located along the Cajón and Murta rivers. These are characterized by a variation in the coloration of the deposits. They occur either as columnar jointed basaltic flows (Fig. 16 A and C) or as pillow lavas up to 40 cm in diameter (Fig. 16 B). The vesicularity varies from deposit to deposit, being more abundant in the Murta River samples. In terms of mineralogy, jumps out the presence of large crystals of plagioclase macrocrysts up to 2 cm in Murta River samples (Fig. 16 D), which are associated with olivine and pyroxene macrocrysts in order of abundance.

It is possible to recognize a new deposit that could be part of Murta basalts at Ibáñez River to the north of its intersection with the Cajón River. The appearance of these basalts is more altered than the previous ones and with abundant vesicles.

The deposits in the intersection of the Chiflón and Ibáñez rivers show prismatic jointing (Fig. 17 A) an also massive deposits with a lot of vesicles (Fig. 17 B). It is necessary to note that granitic xenoliths have been found in the samples with no apparent reaction borders with the host (Fig. 17 C).

Outside the purpose of this research has been discovered a fissure with 7 eruptive centers, approximately, aligned in a NW-SE direction parallel to the Ibáñez River. That volcanic relief (see Fig. 10) characterized by Quiroz & Belmar (2010) corresponds to 3 nested craters. Because of vegetation, sampling was not possible, but near the Chiflón River volcanic bombs that could be part of these eruptive centers have been found.

2.5.2. Petrography and mineral chemistry

The Murta basalts present different general textures like porphyritic, vesicular, and cumulate textures. These basalts are composed of plagioclase ($An_{84-9}Ab_{16-85}Or_{0-45}$), olivine (Fo_{63-94}), and clinopyroxene ($Wo_{34-50}En_{24-61}Fs_{5-26}$), with a minor amount of orthopyroxene ($Wo_{2-7}En_{43-85}Fs_{13-54}$) macrocrysts set in a groundmass of plagioclase ($An_{7-71}Ab_{28-84}Or_{0-32}$), olivine (Fo_{48-93}), pyroxene ($Wo_{4-51}En_{10-75}Fs_{7-57}$) and Ti-magnetite microcrysts. See Fig. 18 A, B, and C for plagioclase, pyroxene, and olivine macrocrysts and microcrysts compositions, respectively. See Annex B for complete petrographic descriptions and Annex C for detailed chemical compositions of crystals analyzed by SEM.

The plagioclase macrocrysts (Fig. 19) are tabular with a middle to high integrity, reaching in some cases centimetric sizes (>2 cm). It is possible to recognize sieve, diffuse zoning, patchy and poikilitic textures. On the other hand, they present pilotaxitic and intergranular textures in the groundmass.

The olivine macrocrysts (Fig. 20), that correspond to the predominant mafic mineral, are characterized by prismatic and granular shapes, occasionally showing skeletal forms and reabsorption textures. They reach sizes up to 5 mm and are often found forming clusters with plagioclase or other olivine macrocrysts. The vast majority of olivine macrocrysts present normal zoning (decrease of %Fo to the rim) except for sample JV051219-1 showing reverse zoning (from ~70 to 84 %Fo toward the rim).

The pyroxene macrocrysts and microphenocrysts (Fig. 21) are characterized by granular and acicular shapes, where the latter is mostly attributed to pillow lava samples. Together with olivine and plagioclase, they make up the groundmass of these basalts. Two samples display subophytic texture as the main one, where they partially surround plagioclase of smaller size. A large part of the samples presents only pyroxene as microphenocrysts or in the groundmass. Just four samples present pyroxene macrocryst (JV031219-4, JV240220-2, JV250220-1, and JV250220-6).

The xenoliths mineralogy is restricted to quartz, plagioclase, K-feldspar (more abundant), and Fe oxides. Also, in sample JV240220-3, some completely chloritized biotite and epidote

crystals can be recognized. The major textures recognized are phaneritic, perthitic, micrographic, and vermicular.

According to the QAP diagram by Streckeisen (1976, 1979), almost all the extrusive rocks were classified as olivine basalts, while the sample JV031219-4 could be a trachyte. The intrusive rocks were classified as alkali feldspar granites and granites.

2.5.3. Mixing evidence

One of the more remarkable characteristics of the Murta basalt is the petrographic evidence of mixing processes. This evidence highly the complexity of petrogenetic processes responsible for the genesis of these basalts. Five samples show evidence of variation in the groundmass characteristics. This variation is related to changes in color, vesicularity, and mineralogy. The samples are JV021219-1, JV031219-2A, JV031219-4, JV051219-8 and JV240220-2 detailed below.

a) JV021219-1

At least two zones are recognized, a light and a dark one which generates a subparallel banding (Fig. 22 A). The light zone has compositions of Fo₇₆₋₈₅core and Fo₇₃₋₇₉rim in olivine macrocrysts and An₆₀₋₆₆core and An₄₄₋₆₆rim in plagioclase macrocrysts. In the groundmass, olivine microcrysts have compositions of Fo₆₉₋₉₁, plagioclase of An₂₇₋₅₈, and clinopyroxene of En₂₆₋₅₃. The dark zone has compositions of Fo₇₅₋₈₁core and Fo₇₁₋₇₉rim in olivine macrocrysts and An₆₂₋₆₇core and An₄₈₋₅₈rim in plagioclase macrocrysts. In the groundmass, olivine microcrysts have compositions of Fo₆₈₋₇₆, plagioclase of An₄₆₋₆₂, and clinopyroxene of En₂₇₋₃₄.

b) JV031219-2A

In this sample at least two zones are recognized, a first one where the groundmass has more and bigger pyroxene microcrysts and a second one where pyroxene microcrysts in the groundmass are smaller (Fig. 22 B). Another difference between zones is the presence of fewer and bigger vesicles in the first zone than in the second one. The first zone has compositions of Fo₇₇₋₈₉core and Fo₆₃₋₈₂rim in olivine macrocrysts and An₅₈₋₆₃core and An₅₆₋₆₁rim in plagioclase macrocrysts. In the groundmass, olivine microcrysts have compositions of Fo₅₈₋₈₃, plagioclase of An₄₅₋₅₇, and clinopyroxene of En₃₉₋₄₃. The second

zone has compositions of Fo₈₁₋₉₂core and Fo₇₂₋₇₇rim in olivine macrocrysts and An₆₀₋₆₃core and An₅₆₋₆₂rim in plagioclase macrocrysts. In the groundmass, olivine microcrysts have compositions of Fo₆₂₋₆₄, plagioclase of An₃₈₋₅₇, and clinopyroxene of En₄₅₋₅₇.

c) *JV031219-4*

Two zones are recognized: a light and a dark one that is generated between the vesicles and is less crystalline than the light zone (Fig. 22 C). The light zone has compositions of En₄₈₋₈₀core and En₄₂₋₈₄rim in orthopyroxene macrocrysts and An₁₁₋₂₆core and An₂₃₋₂₈rim in plagioclase macrocrysts. In the groundmass, orthopyroxene microcrysts have compositions of En₃₇₋₇₄ and plagioclase of An₆₋₃₇. The dark zone has compositions of En₃₂₋₃₃core and En₃₁rim in orthopyroxene macrocrysts and An₄₇₋₆₄core and An₄₇₋₆₀rim in plagioclase macrocrysts. In the groundmass, orthopyroxene microcrysts have compositions of En₃₇₋₅₁ and plagioclase of An₉₋₂₀.

d) *JV051219-8*

In this sample at least two zones are recognized, a first one where the groundmass is darker and has bigger crystals and a second one where the crystals in groundmass are smaller (Fig. 22 D). The light zone has compositions of Fo₇₆₋₈₆core and Fo₆₆₋₇₆rim in olivine macrocrysts and An₆₂₋₆₉core and An₆₃₋₇₃rim in plagioclase macrocrysts. In the groundmass, olivine microcrysts have compositions of Fo₆₂₋₈₇, plagioclase of An₃₆₋₆₅, and clinopyroxene of En₃₇₋₄₆. The dark zone has compositions of Fo₇₉₋₈₇core and Fo₆₉₋₇₇rim in olivine macrocrysts and An₆₇₋₇₁core and An₅₇₋₇₂rim in plagioclase macrocrysts. In the groundmass, olivine microcrysts have compositions of Fo₆₆₋₈₁, plagioclase of An₄₉₋₆₅, and clinopyroxene of En₃₄₋₄₈.

e) *JV240220-2*

At least two zones are recognized: a light and a dark one, where the vesicles are more abundant (Fig. 22 E). The light zone has compositions of Fo₇₆₋₈₉core and Fo₆₈₋₈₀rim in olivine macrocrysts and An₆₆₋₇₀core and An₆₄₋₇₂rim in plagioclase macrocrysts. In the groundmass, olivine microcrysts have compositions of Fo₆₆₋₈₀, plagioclase of An₅₂₋₆₈, and clinopyroxene of En₄₀₋₅₆. The dark zone has compositions of Fo₈₀₋₈₅core and Fo₆₈₋₈₁rim in olivine macrocrysts and An₇₁₋₇₃core and An₆₅₋₇₀rim in plagioclase macrocrysts. In the

groundmass, olivine microcrysts have compositions of Fo₆₆₋₆₈, plagioclase of An₅₃₋₇₀, and clinopyroxene of En₃₇₋₄₃.

2.5.4. Major elements

A large majority of the studied rocks are petrographically fresh and their Loss On Ignition (LOI) values range from slightly negative to ca. 2 wt.%. According to the TAS diagram (Total Alkalis-Silica) proposed by Le Bas et al. (1986) shown in Fig. 23, they are mostly basalts although a sample plots in the trachyte field (JV031219-4). The basalts are plotted in both alkaline and sub-alkaline series.

The bivariate plots (Fig. 24) show the relationship of major oxides and their variation with the magnesium number [$Mg\# = 100 * MgO / (MgO + FeO)$ where $FeO(\% wt) = Fe_2O_3^T(\% wt) * 1.1113$]. Considering the basalts and trachyte there is a pattern of decreasing CaO and Al₂O₃ content as Mg# decreases. K₂O and Na₂O contents increase as Mg# decreases. All other oxides such as TiO₂ and P₂O₅ show a steep increase as Mg# decreases, but then there is a change in the pattern to the trachytic sample where these oxides decrease in content.

However, between the more primitive samples (Fig. 25), looking at the x-axis, there is a significant variation in the magnesium number, not so on the y-axis where the oxide content has a minimum variation. The more significant change is in CaO, but it is still a small decrease. So the patterns are just linear with some fluctuations without a clear evolutionary pattern.

As a complementary tool, the CIPW norm (Table 2) introduced by Cross et al. (1902) has been calculated to classify the igneous rocks. For this purpose, it has been used an Excel program developed by Kurt Hollocher from the Geology Department of Union College, where the inputs correspond to oxide contents and some trace elements.

As expected, only the trachyte (sample JV031219-4) has normative quartz. All the remaining samples have normative olivine. All samples contain normative hypersthene, except sample JV051219-2. None of the samples contain normative nepheline and all of them contain normative diopside. Therefore, it is possible to classify sample JV031219-4 as silica oversaturated due to the presence of quartz and hypersthene. The rest of the samples that present hypersthene and olivine can be classified as silica saturated.

2.5.5. Minor and trace-element features

Incompatible trace element abundance patterns normalized to the composition of Primitive Mantle (Sun & McDonough, 1989) are shown in Fig. 26 A. The first group, which does not include sample JV031219-4 (trachyte, to be discussed separately) are depleted in Li, with a positive Pb and Sr anomaly. Within this first group, it is possible to see certain differences in the behavior of the elements, specifically in the more incompatible elements. The first subgroup (Fig. 26 B) has Ba positive anomaly and a little Nb negative anomaly, a second subgroup (Fig. 26 C) has an important Nb negative anomaly (most primitive samples), a third subgroup (Fig. 26 D) is depleted in Th and Nb, and the fourth subgroup (Fig. 26 E) with a little Th negative anomaly.

In general, Murta basalts display slightly LILE and LREE-enriched patterns. The sample JV031219-4 displays a general enrichment in all elements compared with the first group, except for the Sr which presents a large depletion. Also, presents a depletion in Nb but slightly lower than the first group, and a Pb and Zr positive anomaly. In contrast with the first group, the trachytic sample is more enriched in incompatible elements (Rb, Ba, Th, and U).

On the other hand, rare earth element abundance patterns normalized to the composition of Chondrite (Sun & McDonough, 1989) are shown in Fig. 27. The samples from the first group show an enriched LREE pattern and a relatively flat HREE pattern. The samples JV031219-2A, JV230220-2, and JV250220-1 have a slightly Eu positive anomaly. The sample JV031219-4 displays a general enrichment in all elements compared with the first group, except for a more horizontal behavior in the HREE elements.

The first group has $(La/Yb)_N$ from 2.7 to 5, while the sample JV031219-4 has a $(La/Yb)_N$ of 6.8, slightly higher.

2.5.6. Sr and Nd isotopic data

The isotopic compositions of the studied lavas are shown in Table 3 and plotted in Fig. 28. Owing to the young age of the examined lavas here the measured isotopic ratios were not corrected for in situ decay, and hence they are representative of the initial values. Strontium isotopic ratios $^{87}Sr/^{86}Sr$ are scattered between 0.70347 and 0.70465 ± 0.00005 and corresponding $^{143}Nd/^{144}Nd$ between 0.512672 and 0.512921 ± 0.000017 . The samples plotted

between MORB and Bulk Silicate Earth (BSE) closest to PREMA (prevalent mantle) and HIMU except for sample JV031219-4 which is more differentiated. In general, the Murta basalts plot within the mantle array defining a descending line.

2.6. DISCUSSION

The Murta basalts have geochemical characteristics at the transition from sub-alkaline to alkaline composition, whereas the majority of the SVZ volcanoes show a typical calc-alkaline affinity. In this section, the magma source and the processes that affected the magma through crustal ascent are described in relation to the geodynamic context.

2.6.1. Origin of the Murta basalts

As the samples plot in the mantle array (Sr-Nd isotope diagram), but specifically above the CHUR ($\epsilon_{Nd} > 0$), they are in the middle of a depleted mantle source and an enriched one. For modeling purposes, an enriched source (E-type MORB) from Mertz et al. (2001) was used, which corresponds to a MORB source enriched by 8% metasomatic melt. This source was chosen to model, in an REE diagram, the high LREE element content of the more primitive samples, whereas a depleted source would not model. Specifically, using a depleted mantle from Salters & Stracke (2004), the resulting pattern has a very low LREE content with an incremental curve to higher HREE contents that does not resemble the behavior of the Murta basalts.

REE patterns of the samples indicate that the Murta basalts are derived from a high degree of partial melting of the mantle source because of its relatively flat shape.

A Ni-Y plot (Fig. 29) has been used to model the Murta basalts, where Ni is a highly compatible and Y a highly incompatible element. The samples have similar Ni and Y content except for sample JV031219-4 which has the lowest Ni. The model was constructed using the enriched source aforementioned as the start point and then applying batch melting equations as in Rollinson & Pease (2021) for modal melting (the minerals contribute to the melt in proportion to their concentration in the rock) and non-modal melting (the phases in the host rock do not contribute to the melt in their modal proportions).

$$C_L = C_o/[D_{RS} + F(1 - D_{RS})] \text{ (Modal melting)}$$

$$C_L = C_o/[D_o + F(1 - P)] \text{ (Non-modal melting)}$$

$$D_{RS_i} = d_1D_1 + d_2D_2 + d_3D_3 + \dots$$

$$P_i = p_1D_1 + p_2D_2 + p_3D_3 + \dots$$

Where C_L is the concentration of a trace element in the melt. C_o is the concentration in the unmelted source. D_{RS} is the bulk partition coefficient of the residual solid, D_{RS_i} is the bulk partition coefficient for element i , and d_1 and D_1 are the percentage proportion and partition coefficient for element i in mineral 1, respectively. F is the weight fraction of melt produced. P is the bulk distribution coefficient of the minerals which are contributing to the melt, P_i is the bulk distribution coefficient for element i , p_1 is the weight normative fraction of mineral 1 in the melt and D_1 is the mineral-melt distribution coefficient for a given trace element for mineral 1.

The K_d 's were taken from Gorryng & Kay (2001). The source mineral mode (58% ol, 30% opx, 10% cpx, and 2% sp), and the phase proportions entering the melt (10% ol, 20% opx, 65% cpx, and 5% sp) are those used in Guivel et al. (2006) for spinel lherzolite (Table 4).

The results of applying these equations are the green lines in Fig. 29. The most primitive samples of Murta basalts (JV031219-1, JV031219-3, and JV051219-3) appear to have crystallized from a parental magma generated by a high percentage of melting (~18-25%) of an enriched mantle source using a batch melting model.

It is not possible to reconstruct the basalts through direct partial melting and some fractionation is needed. In the same figure, two blue lines have been plotted showing the olivine fractionation for modal and non-modal batch melting, using the equation for Rayleigh fractionation (Rollinson & Pease, 2021).

$$C_L = C_oF^{(D-1)} \text{ (Rayleigh fractionation)}$$

Where C_o is the initial concentration of a trace element in the initial melt obtained by batch melting (at 18% and 25% for modal and non-modal melting, respectively). F is the fraction of melt remaining. D is the bulk partition coefficient of the fractionating assemblage.

The most primitive samples of Murta basalts are reconstructed by nearly 20% of olivine fractionation in both cases.

The same modeling was replied for comparison with the REE (Fig. 30) using the same procedure explained above, obtaining a good correlation with the Ni-Y plot. The most primitive samples of the Murta basalts are reconstructed by almost 20-30% of olivine fractionation in both cases. Sample JV051219-3 fits better for modal batch melting (Fig. 30 A) and sample JV031219-3 for non-modal melting (Fig. 30 B).

2.6.2. Fractional crystallization

The Murta basalts have been divided into 4 subgroups and trachyte, as shown in chapter 2.5.5. And based on the available ages provided by Guivel et al. (2006) and Quiroz & Belmar (2010) it is possible to know what comes first (Fig. 31). The group composed by JV051219-7, JV051219-8, and JV031219-3 (subgroup 3) and JV051219-1, JV051219-2, and JV051219-3 (subgroup 4) are the oldest deposits with quite similar ages of 0.90 ± 0.08 and 0.85 ± 0.10 Ma, respectively. While the younger ones are located in the northern part of the study area with 0.16 ± 0.06 and 0.07 ± 0.03 Ma including the samples JV031219-1 and JV240220-2 (subgroup 2) and samples JV031219-2A and JV230220-2 (part of subgroup 1), respectively. The remaining samples are not correlated with the existing ages, but it is proposed that they are younger than subgroup 3 due to their stratigraphic position.

A fractional crystallization model for each subgroup allows the reconstruction of the more evolved samples, using the Rayleigh fractionation equation (Rollinson & Pease, 2021), mentioned in the previous chapter 2.6.1, for trace elements in a N-MORB normalized spider diagram.

$$C_L = C_o F^{(D-1)} \text{ (Rayleigh fractionation)}$$

$$D_i = x_1 D_1 + x_2 D_2 + x_3 D_3 + \dots$$

Where C_o is the initial melt concentration (in this case, the chosen samples as starting points). F is the fraction of melt remaining. D is the bulk partition coefficient of the fractionating assemblage (50% ol, 20% plg, 29% cpx, and 1% sp), D_i is the bulk partition coefficient for element i , and x_1 and D_1 are the percentage proportion and partition coefficient for element i

in mineral 1, respectively. The K_d 's were taken from several authors and are available in Table 5.

The results of applying these equations are the gray lines in Fig. 32, Fig. 33 and Fig. 34. From the sample JV031219-3 (Fig. 32) with 10-20% fractionation of olivine, clinopyroxene, plagioclase, and spinel sample JV051219-7 is obtained with a small Ba anomaly. From the sample JV051219-3 (Fig. 33) with 10-20% fractionation of the same phases and rates used before, samples JV051219-1 and JV051219-2 are obtained with a small Rb anomaly. If the previous subgroups are considered as a single group with JV031219-3 as the starting point, it is possible to reconstruct both, but now with 10-30% fractionation and a small Ta anomaly. In any case, the samples can be related to each other.

Instead, the samples in the northern part of the study area are partially reconstructed from the sample JV031219-1 (Fig. 34) with a strong Ba positive anomaly and a little Eu positive anomaly that is not possible to replicate with simple fractional crystallization. The rest of the elements are reconstructed with 10-20% fractionation using a variety of phase proportions combinations but is inferred that plagioclase didn't play an important role during fractionation because of the positive Eu anomaly. So, in this case, and possibly associated with the younger age of these deposits, other factors may be interacting with the system producing Ba anomaly. In fact, according to Keshavarzi et al. (2014), positive anomalies in Pb and Ba could be attributed to metasomatism of mantle wedge by fluids derived from the subducted slab or/and contamination with continental crust.

According to subgroup 1 (JV021219-1 and JV250220-1), the patterns do not fit with the fractional crystallization models presenting non-parallel and interlocking patterns using JV031219-3 and JV051219-3 as starting points, assigning to it the possibility of contamination and the participation of other external agents in the generation of these basalts (not shown).

It is important to note that assimilation may have occurred but in a minuscule amount compared to fractionation.

2.6.3. Crustal contamination

To evaluate crustal contamination in the Murta basalts, it has been utilized the Th-Nb proxy (Fig. 35). Th and Nb are highly incompatible elements that remain their ratios nearly constant during mantle melting. However, Th and Nb have significantly different characteristics which cause them to be decoupled during subduction (Pearce, 2014). The adaptation of Pearce (2008) who plots Th/Yb versus Nb/Yb was used, where lavas that are in a different environment than subduction are plotted along a diagonal that includes MORB and OIB. While the lavas derived from the mantle, but modified by fluids derived from subduction, move upwards to higher Th contents due to the mobility of this element mentioned above (Volcanic arc array). It is precisely in this last zone where the Murta basalts studied here are located, indicating the possibility of some effect of crustal contamination.

Also, negative Nb anomalies on spider diagrams are characteristic of the continental crust and may be an indicator of crustal involvement in magma processes (Rollinson, 1993).

Attempting to reconstruct the sample JV031219-4 an AFC model was made. It was Bowen (1928) who first proposed that the latent heat of crystallization generated during fractional crystallization may lead to wall rock assimilation in the magma chamber. The process of crustal assimilation is likely to be important in understanding the geochemistry of magmas that erupted through the continental crust (Rollinson & Pease, 2021). There is direct evidence of the presence of crustal xenoliths in the basalts.

DePaolo (1981) was the first who described the concentration of trace elements, and stable and radiogenic isotope ratios, in a melt relative to the composition of the original magma. An AFC model has been performed, using the equation proposed by DePaolo (1981), with $^{87}\text{Sr}/^{86}\text{Sr}$ vs Th, where the sample JV051219-3 was considered as a parent and the assimilated wall rock was taken from Pankhurst et al. (1999) who studied granitoids of the North Patagonian batholith in Aysén and has concentrations of Río Murta pluton (IBA43, IBA44, and IBA45).

$$C_L = C_o f' + \left[\frac{r}{r-1+D} \right] * \left[\frac{C_A}{C_o} * (1 - f') \right] \text{ (AFC equation)}$$

Where r is the assimilation rate/crystallization rate, D is the bulk partition coefficient, C_L is the element concentration in the contaminated magma, C_A is the concentration of the trace element in the assimilated wall rock and $f' = F^{-(r-1+D)/(r-1)}$ in which F is the fraction of magma remaining. The parameters are the same used before in chapter 2.6.2 and are available in Table 5. The fractional phases considered were 50% ol, 20% plg, 29% cpx, and 1% sp.

Fig. 36 shows the results of the modeling. Two cases were analyzed a) $r=0.5$ and b) $r=0.8$. The sample JV031219-4 is possible to reconstruct with 40-45% assimilated and fractionated mass and $r=0.5$. So, more is fractionated than assimilated.

The same modeling was replied using a N-MORB spider diagram (Fig. 37). The sample JV051219-3 was considered as starting point and JV240220-2x as the assimilated wall rock. Most of the elements are adjusted to $\pm 40\%$ assimilated and fractionated mass, at least the most incompatible elements. Then, it would agree with what is shown only with Th.

2.6.4. Origin of the crystals

Taking into account the differences within the same sample related to colors, textures, vesicles, and crystals, an equilibrium test was performed for the mafic minerals (olivine and pyroxene macrocrysts and microcrysts) using Rhodes diagram.

For each sample was calculated the range of olivine compositions in equilibrium with the observed whole-rock Mg#, using $K_D(\text{Fe-Mg})^{\text{ol-liq}} 0.30 \pm 0.03$ (Putirka, 2008) and the equation of Roeder & Emslie (1970). The distribution of olivine composition is in Fig. 38 A and as shown there are some crystals (macrocrysts and microcrysts) that are above the equilibrium zone, so they are not in equilibrium with liquids like the whole-rock compositions, indicating that they represent inherited crystals.

Clinopyroxene compositions in equilibrium with the observed whole-rock Mg# were calculated using $K_D(\text{Fe-Mg})^{\text{ol-liq}} 0.28 \pm 0.08$ (Putirka, 2008). The distribution of clinopyroxene composition is in Fig. 38 B and as shown all the crystals are under or in the equilibrium zone.

Orthopyroxene equilibrium was calculated using $K_D(\text{Fe-Mg})^{\text{ol-liq}} 0.29 \pm 0.06$ (Putirka, 2008) and the distribution is in Fig. 38 C and, as shown, most of the crystals are above the equilibrium zone, so they are not in equilibrium with liquids similar to the whole-rock compositions, indicating that they represent inherited crystals too. Apparently, the crystals in

the light zone are inherited and the crystals in the dark zone are in equilibrium (sample JV031219-4).

The olivine macrocryst cores generally show more primitive compositions than the macrocryst rims. But this is not always the case for microcrysts, where some microcrysts are even more primitive than the macrocryst cores. The same applies to orthopyroxene macrocrysts, where there are even more primitive rims than the core, whereas the clinopyroxene macrocrysts and microcrysts appear to have the expected behavior, with all the crystals below or within the equilibrium curve.

Some olivine and orthopyroxene macrocryst cores and microcrysts, plot significantly above the equilibrium curve, so probably they are non-cogenetic crystals (antecrysts) in disequilibrium with the host rock. Olivine macrocryst cores are in equilibrium with host rocks of Mg# 35-82, reaching much more primitive values than the higher Mg# sample. Orthopyroxene macrocryst cores are in equilibrium with host rocks of Mg# 20-58. On the other hand, olivine microcrysts are in equilibrium with host rocks < Mg# 80 and orthopyroxene microcrysts with host rocks of < Mg# 52. According to these results, some macrocrysts and microcrysts crystallized from more primitive melts than others, based on the intersection of the values.

Olivine macrocryst rims generally fall within or below the equilibrium curve owing to progressive fractionation of the magma, whereas orthopyroxene macrocryst rims do not.

The olivine antecrysts are characterized by being either crystals with cores in disequilibrium surrounded by rims in equilibrium with the host rock or completely inherited crystals with cores and rims in disequilibrium. Also, some crystals from the groundmass seems to be inherited from a melt in equilibrium with the antecrysts or even more primitive.

The orthopyroxene antecrysts are characterized by completely inherited crystals with cores and rims in disequilibrium with the host rock. Whereas the are microcrysts either in equilibrium or in disequilibrium with the host rock.

2.6.5. Origin of trachyte mineralogy

The presence of orthopyroxene macrocrysts and microcrysts in the trachyte is interesting, because the rest of the basalts contain only clinopyroxene in their mineralogy. Although the

presence of amphibole (especially oxidized acicular crystals) is not ruled out, the optical properties of orthopyroxene (presence of basal faces and characteristic cleavage) are undeniable.

Several alternatives for the presence of orthopyroxene in trachyte are proposed. Firstly, the assimilation of the wall rock composed by quartz, plagioclase, K-feldspar and oxides, without mafic phases. Only in one of the granitic xenolith samples it was possible to recognize chlorite as secondary mineralogy giving clues of the possible presence of mafic phases before. This was compared with Pankhurst et al. (1999) where there is an extensive characterization of the Patagonian Batholith including the intrusives that outcrop in the sector of Murta, Ibáñez and Chiflón rivers. The plutonic bodies that outcrop there, according to the authors, belong to the Early and Middle Cretaceous, and correspond to hornblende-biotite granodiorites, tonalites, diorites and gabbros. The difference in mineralogy with the literature is mainly attributed to the size of the xenoliths within the basalts. These are only a few centimeters long, which does not allow a complete characterization of the assimilated wall rock.

Secondly, the mixing textures could be responsible for the arrival of these mafic crystals from the secondary fluid that has modified the chemistry of this rock and, in addition, contributed to its mineralogy.

It is important to note that the presence of orthopyroxene is not exclusive in the area for the Murta basalts. The Hudson volcano, located about 20 km to the northwest, has had several episodes in which it has erupted trachyte characterized by the presence of orthopyroxene as phenocrysts, derived from a mafic source that has undergone fractional crystallization and magma mixing episodes (Kratzmann et al., 2010).

2.6.6. Mixing

The great number of high-magnesium olivine present in Murta samples indicates that some crystals are anomaly Mg-rich to have grown from the host magma, and thus are probably antecrysts. Therefore, the Mg# whole-rock is probably overestimated because of the presence of these antecrysts that are probably in equilibrium with a more primitive magma.

This behavior is expected for samples that present different textures and clear mixing evidence, but there are some samples like JV051219-1, JV230220-2, and JV250220-1 that do not show this evidence, although the chemistry reveals disequilibrium.

In the groundmass is where the different crystal composition allows us to group them into more primitive and evolved phases. For example, in sample JV021219-1 (Fig. 39) at least two different zones are recognized, a dark one and a light one, in the light one appears the most primitive olivine with up to Fo₉₂, whereas the dark one just contains olivine with an average of Fo₇₄. So, the light zone could represent the primitive member, and the dark zone the evolved member of the mixing, possibly being the first one the youngest injection into the system.

The sample JV031219-4 (Fig. 40, trachyte) has two zones, wherein the light one appears the most primitive pyroxene with up to En₈₀, whereas the dark one just contains pyroxene with an average of En₄₈₋₄₉, being the light zone the primitive member, and the dark zone the evolved member of the mixing.

On the other hand, the sample JV051219-1 (Fig. 41) has no evidence of mixing textures but exhibits olivine and plagioclase macrocrysts with reverse zonation. The first one, has cores with Fo₇₀ and rims with Fo₈₀, while plagioclase have cores with An₅₀ and rims with An₇₀, approximately. In this sample, the groundmass contains olivine with even more evolved compositions than the primitive rims of some macrocrysts.

In general terms, the macrocrysts do not show clear evidence of differences in composition to group them, although the great variation between the core and rim composition up to 20% of forsterite, indicates an abrupt change in the system. Probably, some primitive olivine macrocrysts were rapidly integrated into the system re-equilibrating their rims to the newly evolved compositions.

Also, there are segments within each sample where the different zones coexist, so the mineral composition in these parts is variable and it is not possible to attribute them to a specific band with certainty.

The high-Fo composition (>Fo₇₀) along with major elements measurements indicate the mixing occurred between at least two different magmas but very similar to each other and in

different degrees, whereas the samples that show mixing textures have a less effective mix than the samples do not present these textures.

Another evidence that mixing has occurred is the high variation in magnesium number observed in the bivariate plots (Fig. 25), but the little variation they show in the major oxides, which could be attributed to the arrival of multiple magma batches that do not allow the system to evolve and generate fluctuating patterns, without a clear evolution within the samples. Something similar has been described by Larrea et al. (2019) and Larrea et al. (2021), where they observed reversals in Mg# but almost no variations in some elements attributing them to mafic recharges during the differentiation of the magmas.

As previously proposed, the mixing could have occurred in an open system with the interaction of two similar magmas or in a closed system, not requiring direct involvement of another more mafic magma, caused by convection within a single magma body that is heated at the base of the chamber (Couch et al. 2001). This concept of self-mixing allows to explain the composition of minerals in disequilibrium with the system and the rock textures. In particular, the arrival of a hottest body at the bottom of the chamber generates overgrowth rims and a higher-temperature groundmass, as occurred in some Murta samples, where the groundmass is even more primitive than the macrocrysts.

According to the isotopic composition (Fig. 28) two samples overlap (JV051219-1 and JV051219-3), so their evolution could have occurred in a closed system. However, the variability of the isotopic composition makes it more likely that the system is open than closed. Although it cannot be ruled out that this applies for certain groups of samples. Further isotopic analysis would be required to prove this hypothesis.

On the other hand, some samples do not present antecrysts and the chemistry says the phenocrysts and microcrystals are in equilibrium with the whole-rock composition or are the result of differentiation. In fact, these rocks could represent the more primitive end member of this mix (JV031219-1 and JV240220-2) making it clear that they show slighter mixing textures but not so evident as other samples.

2.6.7. Geodynamic implications

The fact that the Murta basalts are inserted into a particular environment characterized by the development of a slab window beneath the continent cannot be denied. Russo et al. (2010) performed a study to determine the lithosphere and upper mantle structure in the vicinity of the subducting Chile Ridge using seismometers and analyzing the wave's time travel and velocities.

First-order evidence that the slab window exists is the P-wave very low velocities present at the depth projections, which could represent a most likely relatively warm zone. On the other hand, the splitting shear wave directions rotate from NW-SE trends, north of the slab window, to ENE-WSW inside the slab, Russo et al. (2010) interpret that the gap between the Nazca and Antarctic slabs allows asthenospheric upper mantle to flow into the separation between the subducted lithospheres.

The CTJ (Chile triple junction) along the Chilean margin is also characterized by a large negative Bouguer anomaly (Murdie et al., 2000) possibly generated by ridge subduction and the opening of the asthenospheric window. This allows the hot mantle to reach sublithospheric regions, producing first doming and then a weakening of the crust (Lagabrielle et al., 2007). The negative gravity anomaly reflects anomalously thin lithosphere in this region by the upward migration of the lithosphere-asthenosphere boundary (Fairhead, 1979). This is consistent with the abnormally high heat flow values in southern Patagonia shown by Ávila & Dávila (2018). They concluded that a hot buoyant asthenospheric mantle rises the isotherm of ~ 1300 °C and, consequently, the lithosphere-asthenosphere boundary would place shallower than in those areas out of the window.

Therefore, the presence of a slab window could be responsible that little pockets of primitive magma quickly ascent through the system, probably because the extension produced, and disturbed the more evolved and shallow magma. These pockets would be the more primitive member of the mixing episodes.

Even when the slab window is considered a plausible theory, a second possibility for the origin of the Murta basalts could be a tectonic one, due to the distribution of the deposits along the valleys and bordering the main rivers (Cajón, Ibáñez and Chiflón). Also, the lack

of recognizable eruptive centers along the Cajón River, supports the idea of a fissure eruption and structural control in the origin of the Murta basalts. This possibility does not exclude the existence of the slab window, and both may even be influencing the emplacement of the deposits.

2.6.8. Magmatic evolution

Given that the samples are very similar petrographically and geochemically they are considered cogenetic, derived from very similar parental magmas, but not the same. That is why all the models were made considering all the samples and the more primitive as parental.

The proposed evolution model has four stages: the first stage (t1 and t2 in Fig. 31) considers the emplacement of the oldest basalts along the Cajón and Murta rivers with little arc and subduction components. These samples are related by fractional crystallization and because of the mixing textures and the reverse zoning, the potential trigger was a magma mixing between at least two similar end members. The pillow lavas found also indicate a subaquatic/subglacial origin.

The second stage (t3 in Fig. 31) is the emplacement of the columnar basalts in the northern part of the study area. These basalts have more subduction and crustal components, because of the granitic xenoliths, but they are still very primitive. Mixing textures are also present, indicating mixing processes prior to eruption.

The third stage (t4 and white symbols in Fig. 31) considers three samples correlated by geochemistry, because of the lack of available ages. They have a large mantle wedge and crustal participation due to the large Ba anomaly, and minor slab window effects. These samples have clearly mixing textures and embayed olivine macrocrysts, indicating a major change in the system or a mixing with a more primitive magma.

The last stage (t5 in Fig. 31) is the emplacement of the trachytic sample from one of the most primitive samples, along with strong interaction with the crust through assimilation and also fractional crystallization. This sample shows mixing textures, indicating a mixing process prior to eruption. According to the available ages, this event would correspond to the second stage, but considering the well preserve eruptive centers and the deposits, the age would be much younger.

The preserved mixing textures provide evidence for the existence of a shallow magma chamber where all these processes took place. In the ascending magma, recharge from more primitive magmas is necessary to provide the antecrysts and part of the groundmass.

2.7. CONCLUDING REMARKS

Summarizing, the Murta basalts results from a series of process that were modifying the primary magmas derived from the asthenospheric window. The involved processes included fractional crystallization, assimilation, and at least one mixing/mingling episode.

The models indicate the mixing occurred, in an open system, between at least two different but similar magmas because resultant lavas are basalts according to the TAS diagram, the mineral chemical composition, in particular the mafic ones (high Mg# values), and trace elements resulting in parallel patterns between the samples where the mix is implicit. Or by self-mixing, in a closed system, due to the presence of a hot body at the base of the chamber.

The Murta basalts are located just in the northern limit of the asthenospheric window. So, they must be influenced directly by the window, but also by fluids and melts derived from the subducted oceanic slab. That's why the basalts are not as primitive as previously thought. Even the most primitive sample needs some fractionation to be modeled.

Furthermore, the subduction influence varies among the samples in two ways. The first one is that the samples increment the negative Nb anomaly northward, and it is known that negative Nb anomalies are characteristic of magmas derived by subduction-related melting of the mantle wedge in SSZ settings. The second one is that the older samples have a less Nb anomaly or are purely absent.

The basalts are all related to each other by fractionation of roughly similar parental magmas over time. Some assimilation may have occurred but in low quantity in comparison to the fractionated amount ($R=0.1-0.2$). The only sample that needs the greatest amount of assimilation is the trachyte. Trachyte is possible to reconstruct through AFC models, using as parental magma one of the oldest basalts and assimilating the Patagonian batholith, which

has an important role in the generation of the Murta basalts, due to the presence of intrusive xenoliths inside them.

2.8. ACKNOWLEDGEMENTS

The present study was funded by FONDAP-ANID project 15090013/15200001 and ACE210005 “Centro de Excelencia en Geotermia de Los Andes (CEGA)”. We are grateful to the Chilean National Geology and Mining Service (SERNAGEOMIN) for their help with transport and during the fieldwork (Pituso, Franco, and Álvaro). Also, for allowing us to use the facilities of your laboratory, sample storage, and for the realization of thin sections. We thank Petrus Le Roux and Christel Tinguely (Cape Town University) for their help with minor, trace, and isotope analyses and Activation Laboratories (ActLabs) for the major elements analyses.

2.9. REFERENCES

- Ávila, P., & Dávila, F. M. (2018). Heat flow and lithospheric thickness analysis in the Patagonian asthenospheric windows, southern South America. *Tectonophysics*, 747-748, 99-107. doi:10.1016/j.tecto.2018.10.006
- Bowen, N. L. (1928). *The evolution of the igneous rocks*. Princeton University Press.
- Breitsprecher, K., & Thorkelson, D. J. (2009). Neogene kinematic history of Nazca-Antarctic-Phoenix slab windows beneath Patagonia and the Antarctic Peninsula. *Tectonophysics*, 464(1-4), 10-20. doi:10.1016/j.tecto.2008.02.013
- Cande, S. C., & Leslie, R. B. (1986). Late Cenozoic tectonics of the southern Chile Trench. *Journal of Geophysical Research*, 91(B1), 471-496. doi:10.1029/JB091iB01p00471
- Cembrano, J., Hervé, F., & Lavenu, A. (1996). The Liquiñe Ofqui fault zone: a long-lived intra-arc fault system in southern Chile. *Tectonophysics*, 259(1-3), 55-66. doi: 10.1016/0040-1951(95)00066-6
- Corgne, A., Maury, R., Lagabrielle, Y., Bourgois, J., Suarez, M., Cotten, J., & Bellon, H. (2001). La diversité des basaltes de Patagonie à la latitude du point triple du Chili (468–478 lat. S): données complémentaires et implications sur les conditions de la subduction. *Earth and Planetary Sciences*, 333(7), 363-371. doi: 10.1016/S1251-8050(01)01641-X
- Couch, S., Sparks, R. S., & Carroll, M. R. (2001). Mineral disequilibrium in lavas explained by convective self-mixing in open magma chambers. *Nature*, 411(6841), 1037-1039. doi:10.1038/35082540
- Cross, W., Iddings, J., Pirsson, L., & Washington, H. (1902). A Quantitative Chemico-Mineralogical Classification and Nomenclature of Igneous Rocks. *The Journal Of Geology*, 10(6), 555-690. doi: 10.1086/621030
- D'Orazio, M., Innocenti, F., Manetti, P., Tamponi, M., Tonarini, S., González-Ferrán, O., Lahsen, A., & Omarini, R. (2003). The Quaternary calc-alkaline volcanism of the Patagonian Andes close to the Chile triple junction: geochemistry and petrogenesis of volcanic rocks from the Cay and Maca volcanoes (~45°S, Chile). *Journal Of South American Earth Sciences*, 16(4), 219-242. doi: 10.1016/s0895-9811(03)00063-4

Demant, A., Belmar, M., Hervé, F., Pankhurst, R. J., & Suárez, M. (1998). Pétrologie et géochimie des basaltes de Murta: une éruption sousglaciaire dans les Andes patagoniennes (468 lat. S.). Relation avec la subduction de la ride du Chili. *Earth and Planetary Science*, 327(12), 795-801. doi: 10.1016/S1251-8050(99)80053-6

Demant, A., Hervé, F., Pankhurst, R. J., & Magnette, B. (1994). Alkaline and calc-alkaline Holocene basalts from minor volcanic centres in the Andes of Aysén, Southern Chile. VII Congreso Geológico Chileno, Concepción, Actas vol. II, 1326-1330.

DePaolo, D. J. (1981). Trace Element and Isotopic Effects of Combined Wallrock Assimilation and Fractional Crystallization. *Earth and Planetary Science Letters*, 53, 189-202. doi: 10.1016/0012-821X(81)90153-9

Espinoza, F., Morata, D., Pelleter, E., Maury, R., Suárez, M., & Lagabrielle, Y., Polvé, M., Bellon, H., Cotten, J., De la Cruz, R., & Guivel, C. (2005). Petrogenesis of the Eocene and Mio-Pliocene alkaline basaltic magmatism in Meseta Chile Chico, southern Patagonia, Chile: Evidence for the participation of two slab windows. *Lithos*, 82(3-4), 315-343. doi: 10.1016/j.lithos.2004.09.024

Fairhead, J. (1979). A gravity link between the domally uplifted Cainozoic volcanic centres of North Africa and its similarity to the East African Rift System anomaly. *Earth And Planetary Science Letters*, 42(1), 109-113. doi: 10.1016/0012-821x(79)90195-x

Georgieva, V., Gallagher, K., Sobczyk, A., Sobel, E., Schildgen, T., Ehlers, T., & Strecker, M. (2019). Effects of slab-window, alkaline volcanism, and glaciation on thermochronometer cooling histories, Patagonian Andes. *Earth and Planetary Science Letters*, 511, 164-176. doi:10.1016/j.epsl.2019.01.030

Gorring, M., & Kay, S. (2001). Mantle processes and sources of Neogene slab window magmas from southern Patagonia, Argentina. *Journal of Petrology*, 42(6), 1067-1094. doi: 10.1093/petrology/42.6.1067

Gorring, M. L., Kay, S. M., Zeitler, P. K., Ramos, V. A., Rubiolo, D., Fernandez, M. L., & Panza, J. L. (1997). Neogene Patagonian plateau lavas: continental magmas associated with ridge collision at the Chile triple junction. *Tectonics*, 16(1), 1-17. doi: 10.1029/96TC03368

Guivel, C., Morata, D., Pelleter, E., Espinoza, F., Maury, R., Lagabrielle, Y., Polvé, M., Bellon, H., Cotten, J., Benoit, M., Suárez, M., & De la Cruz, R. (2006). Miocene to Late Quaternary Patagonian basalts (46–47°S): Geochronometric and geochemical evidence for slab tearing due to active spreading ridge subduction. *Journal Of Volcanology And Geothermal Research*, 149(3-4), 346-370. doi: 10.1016/j.jvolgeores.2005.09.002

Gutiérrez, F., Gioncada, A., González Ferran, O., Lahsen, A., & Mazzuoli, R. (2005). The Hudson Volcano and surrounding monogenetic centres (Chilean Patagonia): An example of volcanism associated with ridge–trench collision environment. *Journal Of Volcanology And Geothermal Research*, 145(3-4), 207-233. doi: 10.1016/j.jvolgeores.2005.01.014

Harris, C., Le Roux, P., Cochrane, R., Martin, L., Duncan, A. R., Marsh, J. S., Le Roex, A. P., & Class, C. (2015). The oxygen isotope composition of Karoo and Etendeka picrites: High $\delta^{18}\text{O}$ mantle or crustal contamination? *Contributions to Mineralogy and Petrology*, 170, 1-24. doi: 10.1007/s00410-015-1164-1

Hickey-Vargas, R., Holbik, S., Tormey, D., Frey, F., & Moreno Roa, H. (2016). Basaltic rocks from the Andean Southern Volcanic Zone: Insights from the comparison of along-strike and small-scale geochemical variations and their sources. *Lithos*, 258-259, 115-132. doi: 10.1016/j.lithos.2016.04.014

Hickey, R., Frey, F., Gerlach, D., & Lopez-Escobar, L. (1986). Multiple sources for basaltic arc rocks from the southern volcanic zone of the Andes (34°–41°S): Trace element and isotopic evidence for contributions from subducted oceanic crust, mantle, and continental crust. *Journal Of Geophysical Research*, 91(B6), 5963-5983. doi: 10.1029/jb091ib06p05963

Hole, M. J., Rogers, G., Saunders, A. D., & Storey, M. (1991). Relation between alkalic volcanism and slab-window formation. *Geology*, 19, 657-660. doi: 10.1130/0091-7613(1991)019<0657:RBAVAS>2.3.CO;2

Irvine, T., & Baragar, W. (1971). A Guide to the Chemical Classification of the Common Volcanic Rocks. *Canadian Journal of Earth Sciences*, 8(5), 523-548. doi: 10.1139/e71-055

Kay, S., MaksaeV, V., Moscoso, R., Mpodozis, C., Nasi, C., & Gordillo, C. (1988). Tertiary andean magmatism in Chile and Argentina between 28°S and 33°S: Correlation of magmatic

chemistry with a changing Benioff zone. *Journal Of South American Earth Sciences*, 1(1), 21-38. doi: 10.1016/0895-9811(88)90013-2

Kay, S. Mahlburg, MaksaeV, V., Mpodozis, C., Moscoso, R., & Nasi, C. (1987). Probing the evolving Andean lithosphere: Mid-late Tertiary magmatism in Chile (29-30.5°S) over the zone of subhorizontal subduction. *Journal of Geophysical Research*, 92(B7), 6173-6189. doi: 10.1029/JB092iB07p06173

Keshavarzi, R., Esmaili, D., Kahkhaei1, M., Mokhtari, M., & Jabari, R. (2014). Petrology, Geochemistry and Tectonomagmatic Setting of Neshveh Intrusion (NW Saveh). *Open Journal of Geology*, 4, 177-189. doi: 10.4236/ojg.2014.45013

Kratzmann, D. J., Carey, S., Scasso, R. A., & Naranjo, J. A. (2010). Role of cryptic amphibole crystallization in magma differentiation at Hudson volcano, Southern Volcanic Zone, Chile. *Contribution to Mineralogy and Petrology*, 159, 237-264. doi: 10.1007/s00410-009-0426-1

Lagabrielle, Y., Suárez, M., Malavieille, J., Morata, D., Espinoza, F., Maury, R. C., Scalabrino, B., Barbero, L., De la Cruz, R., Rossello, E. A., & Bellon, H. (2007). Pliocene extensional tectonics in the Eastern Central Patagonian Cordillera: geochronological constraints and new field evidence. *Terra Nova*, 19, 413-424. doi: 10.1111/j.1365-3121.2007.00766.x

Lagabrielle, Y., Suárez, M., Rosselló, E. A., Hérail, G., Martinod, J., Régnier, M., & De la Cruz, R. (2004). Neogene to Quaternary tectonic evolution of the Patagonian Andes at the latitude of the Chile triple junction. *Tectonophysics*, 385, 211-241. doi: 10.1016/j.tecto.2004.04.023

Larrea, P., Albert, H., Ubide, T., Costa, F., Colás, V., Widom, E., & Siebe, C. (2021). From explosive vent opening to effusive outpouring: Mineral constraints on magma dynamics and timescales at Parícutin Monogenetic Volcano. *Journal of Petrology*, 62(4), 1-19. doi:10.1093/petrology/egaa112

- Larrea, P., Widom, E., Siebe, C., Salinas, S., & Kuentz, D. (2019). A re-interpretation of the petrogenesis of Parícutin volcano: Distinguishing crustal contamination from mantle heterogeneity. *Chemical Geology*, 504, 66-82. doi:10.1016/j.chemgeo.2018.10.026
- Le Bas, M., Maitre, R., Streckeisen, A., & Zanettin, B. (1986). A Chemical Classification of Volcanic Rocks Based on the Total Alkali-Silica Diagram. *Journal of Petrology*, 27(3), 745-750. doi: 10.1093/petrology/27.3.745
- Lopez-Escobar, L., Kilian, R., Kempton, P., & Tagiri, M. (1993). Petrography and geochemistry of Quaternary rocks from the Southern Volcanic Zone of the Andes between 41°30' and 46°00'S, Chile. *Revista Geológica de Chile*, 20(1), 33-55. doi: 10.5027/andgeoV20n1-a04
- Mertz, D., Weinrich, A., Sharp, W., & Renne, P. (2001). Alkaline Intrusions in a Near-Trench Setting, Franciscan Complex, California: Constraints from Geochemistry, Petrology, and 40AR/39AR Chronology. *American Journal of Science*, 301(10), 877-911. doi: 10.2475/ajs.301.10.877
- Murdie, R., Styles, P., Prior, D., & Daniel, A. (2000). A new gravity map of southern Chile and its preliminary interpretation. *Revista Geológica De Chile*, 27(1), 49-63. doi: 10.4067/s0716-02082000000100004
- Murdie, R. E., & Russo, R. M. (1999). Seismic anisotropy in the region of the Chile margin triple junction. *Journal of South American Earth Sciences*, 12(3), 261-270. doi: 10.1016/S0895-9811(99)00018-8
- Norrish, K., & Hutton, J. (1969). An accurate X-ray spectrographic method for the analysis of a wide range of geological samples. *Geochimica et Cosmochimica Acta*, 33, 431-453. doi: 10.1016/0016-7037(69)90126-4
- Pankhurst, R. J., Weaver, S. D., Hervé, F., & Larrondo, P. (1999). Mesozoic-Cenozoic evolution of the North Patagonian Batholith in Aysen, southern Chile. *Journal of the Geological Society*, 156(4), 673-694. doi: 10.1144/gsjgs.156.4.0673
- Pearce, J. (2014). Immobile Element Fingerprinting of Ophiolites. *Elements*, 10(2), 101-108. doi: 10.2113/gselements.10.2.101

- Pearce, J. (2008). Geochemical fingerprinting of oceanic basalts with applications to ophiolite classification and the search for Archean oceanic crust. *Lithos*, 100(1-4), 14-48. doi: 10.1016/j.lithos.2007.06.016
- Putirka, K. (2008). Thermometers and Barometers for Volcanic Systems. *Reviews In Mineralogy And Geochemistry*, 69(1), 61-120. doi: 10.2138/rmg.2008.69.3
- Quiroz, D., & Belmar, M. (2010). Geología del Área Bahía Murta-Cerro Sin Nombre, Región Aisén del General Carlos Ibáñez del Campo. Servicio Nacional de Geología y Minería, Carta Geológica de Chile, Serie Geología Básica 125: 36 p., 1 mapa escala 1: 100.000.
- Roeder, P., & Emslie, R. (1970). Olivine-liquid equilibrium. *Contributions To Mineralogy And Petrology*, 29(4), 275-289. doi: 10.1007/bf00371276
- Rollinson, H. R., & Pease, V. (2021). *Using Geochemical Data To Understand Geological Processes*. Cambridge University Press.
- Rollinson, H. R. (1993). *Using geochemical data: evaluation, presentation, interpretation*. Harlow, Essex, England: Longman Scientific & Technical.
- Russo, R., VanDecar, J., Comte, D., Mocanu, V., Gallego, A., & Murdie, R. (2010). Subduction of the Chile Ridge: Upper mantle structure and flow. *GSA Today*, 20(9), 4-10. doi: 10.1130/gsatg61a.1
- Salters, V. J. M., & Stracke, A. (2004). Composition of the depleted mantle. *Geochemistry Geophysics Geosystems*, 5(5), Q05B07. doi:10.1029/2003GC000597
- Scalabrino, B., Lagabrielle, Y., Rupelle, A., Malavieille, J., Polvé, M., Espinoza, F., Morata D., & Suárez, M. (2009). Subduction of an Active Spreading Ridge Beneath Southern South America: A Review of the Cenozoic Geological Records from the Andean Foreland, Central Patagonia (46–47°S). *Subduction Zone Geodynamics*, 227-246. doi: 10.1007/978-3-540-87974-9_12
- Somoza, R. (1998). Updated Nazca (Farallon)-South America relative motions during the last 40 My: implications for mountain building in the central Andean region. *Journal Of South American Earth Sciences*, 11(3), 211-215. doi: 10.1016/s0895-9811(98)00012-1

- Streckeisen, A. (1979). Classification and nomenclature of volcanic rocks, lamprophyres, carbonatites, and melilitic rocks: Recommendations and suggestions of the IUGS Subcommittee on the Systematics of Igneous Rocks. *Geology*, 7(7), 331-335. doi: 10.1130/0091-7613(1979)7<331:CANOVR>2.0.CO;2
- Streckeisen, A. (1976). To each plutonic rock its proper name. *Earth-Science Reviews*, 12(1), 1-33. doi: 10.1016/0012-8252(76)90052-0
- Suárez, M., & De La Cruz, R. (2000). Tectonics in the eastern central Patagonian Cordillera (45°30'–47°30'S). *Journal Of The Geological Society*, 157(5), 995-1001. doi: 10.1144/jgs.157.5.995
- Sun, S., & McDonough, W. F. (1989). Chemical and isotopic systematics of oceanic basalts; implications for mantle composition and processes. *Geological Society*, 42, 313-345. doi: 10.1144/GSL.SP.1989.042.01.19
- Tanaka, T., Togashi, S., Kamioka, H., Amakawa, H., Kagami, H., Hamamoto, T., Yuhara, M., Orihashi, Y., Yoneda, S., Shimizu, H., Kunimaru, T., Takahashi, K., Yanagi, T., Nakano, T., Fujimaki, H., Shinjo, R., Asahara, Y., Tanimizu, M., & Dragusanu, C. (2000). JNdi-1: a neodymium isotopic reference in consistency with LaJolla neodymium. *Chemical Geology*, 168, 279-281. doi: 10.1016/S0009-2541(00)00198-4
- Thomson, S. F., Hervé, F., & Stockhert, B. (2001). Mesozoic–Cenozoic denudation history of the Patagonian Andes (southern Chile) and its correlation to different subduction processes. *Tectonics*, 20, 693-711. doi: 10.1029/2001TC900013
- Thorkelson, D. J., & Breitsprecher, K. (2005). Partial melting of slab window margins: Genesis of adakitic and non-adakitic magmas. *Lithos*, 79, 25-41. doi: 10.1016/j.lithos.2004.04.049
- Thorkelson, D. J. (1996). Subduction of diverging plates and the principles of slab window formation. *Tectonophysics*, 255(1-2), 47-63. doi: 10.1016/0040-1951(95)00106-9
- Waight, T., Baker, J., & Peate, D. (2002). Sr isotope ratio measurements by double-focusing MC-ICPMS: techniques, observations and pitfalls. *International Journal of Mass Spectrometry*, 221, 229-244. doi: 10.1016/S1387-3806(02)01016-3

2.10. FIGURES

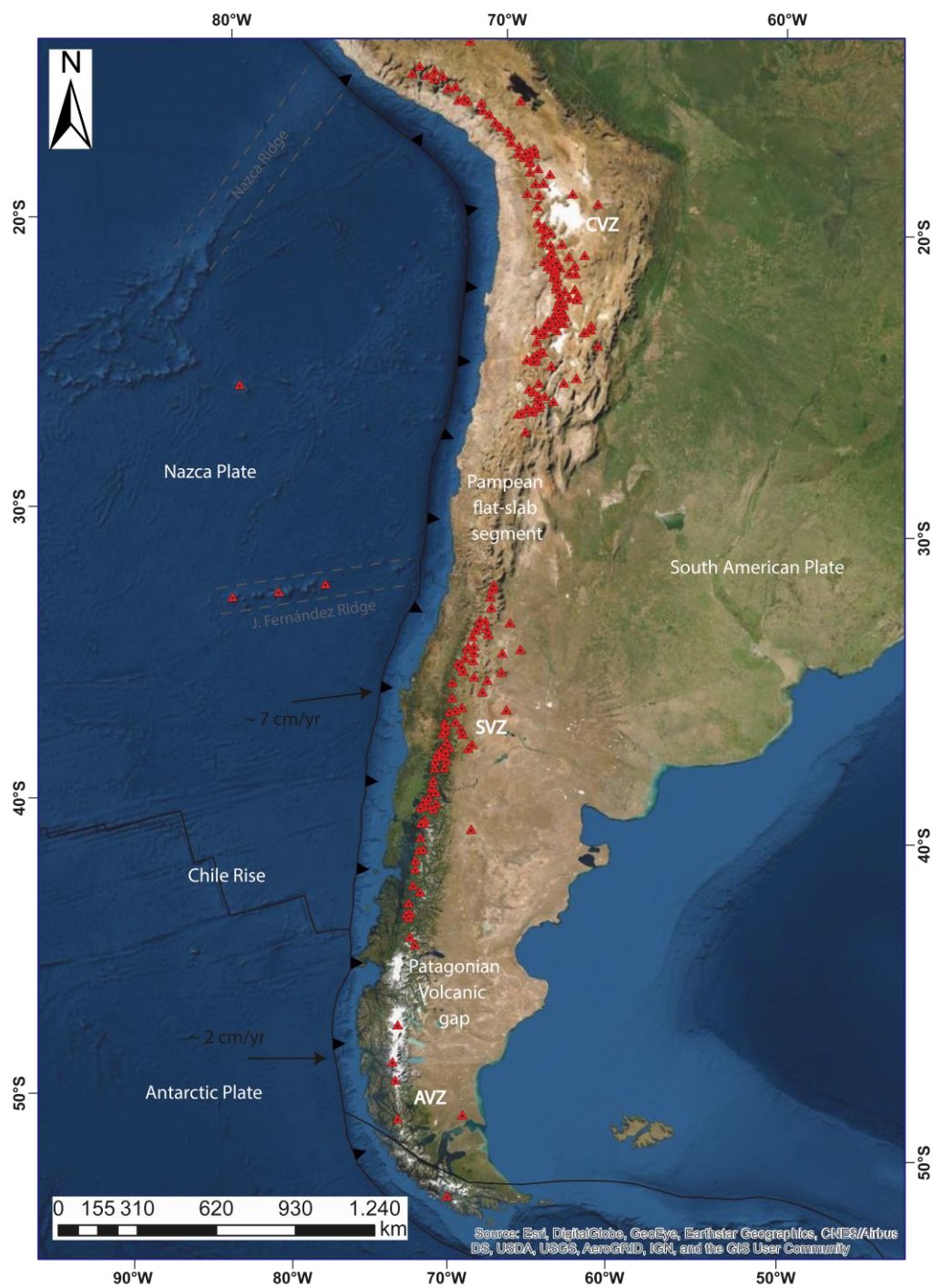


Fig. 6. Volcanic and nonvolcanic segments (Pampean flat-slab segment and Patagonian volcanic gap) along the Andes. Red triangles represent the Holocene and Pleistocene volcanoes available in the Smithsonian Global Volcanism Program. CVZ = Central Volcanic Zone, SVZ = Southern Volcanic Zone and AVZ = Austral Volcanic Zone.

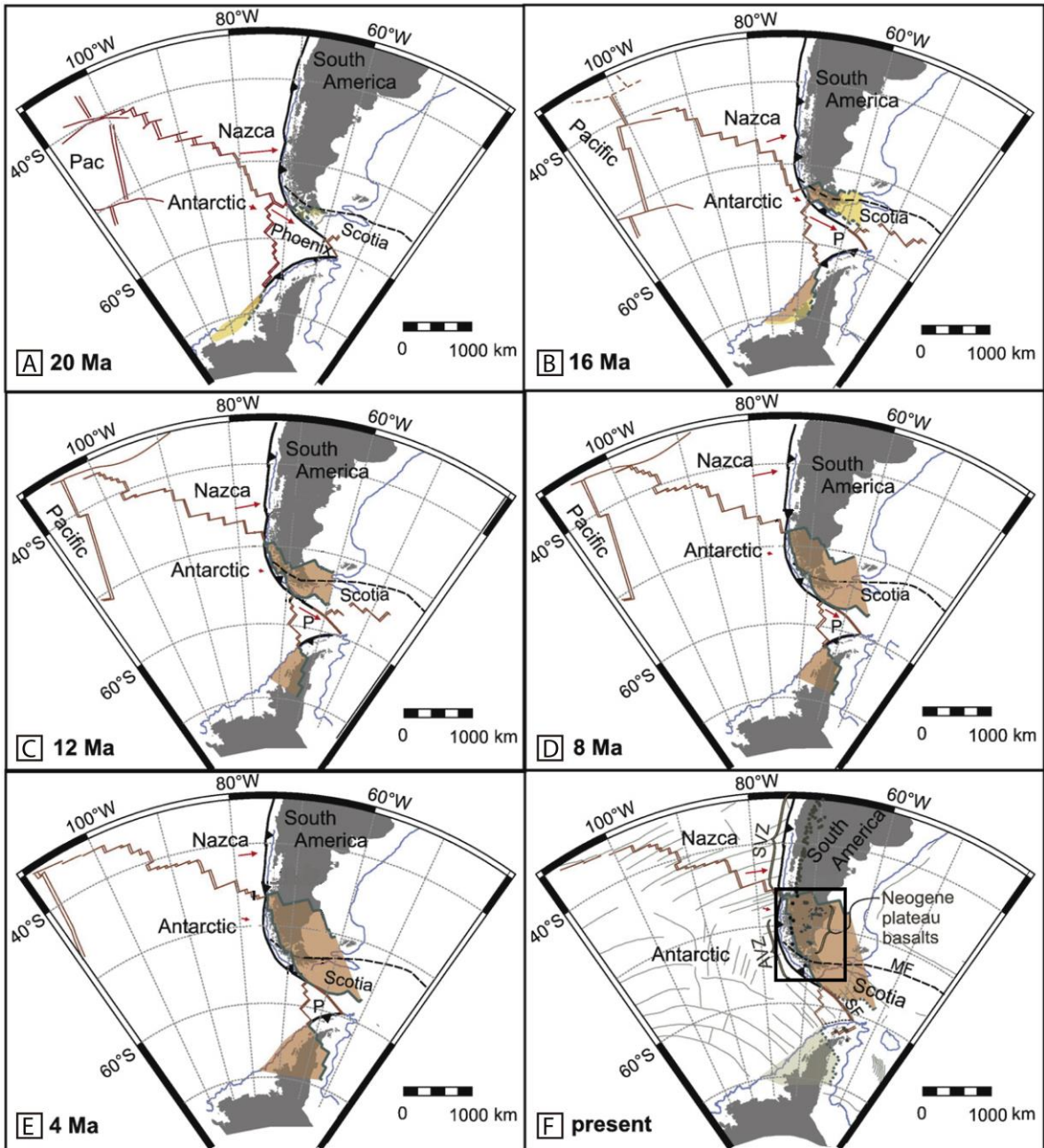


Fig. 7. Kinematic evolution of the Patagonia and Antarctic slab windows from 20 Ma to present. Rectangle in (F) indicates location of Fig. 8. AVZ = Austral Volcanic Zone; MF = Magallanes–Fagnano Fault; P = Phoenix; SF = Shackleton Fault; SVZ = Southern Volcanic Zone. All references used for the figure are detailed in Fig. 3 in Breitsprecher & Thorkelson (2009). Modified from Breitsprecher & Thorkelson (2009).

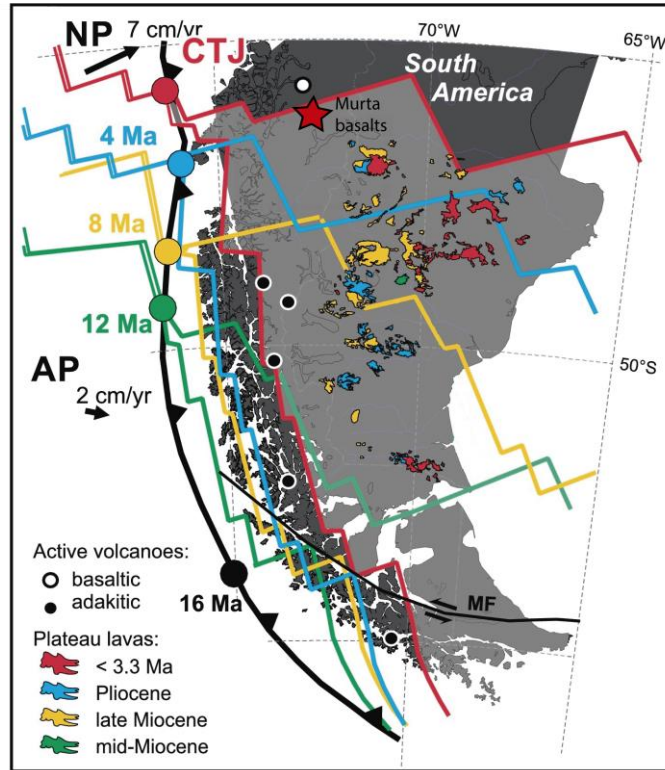


Fig. 8. Evolution of the Patagonia slab window through time. The colored points indicate the CTJ position from 12 Ma to present. The red star represents the Murta basalts location. MF = Magallanes–Fagnano Fault. All references used for the figure are detailed in Fig. 5 in Breitsprecher & Thorkelson (2009). Modified from Georgieva et al. (2019) after Breitsprecher & Thorkelson (2009).

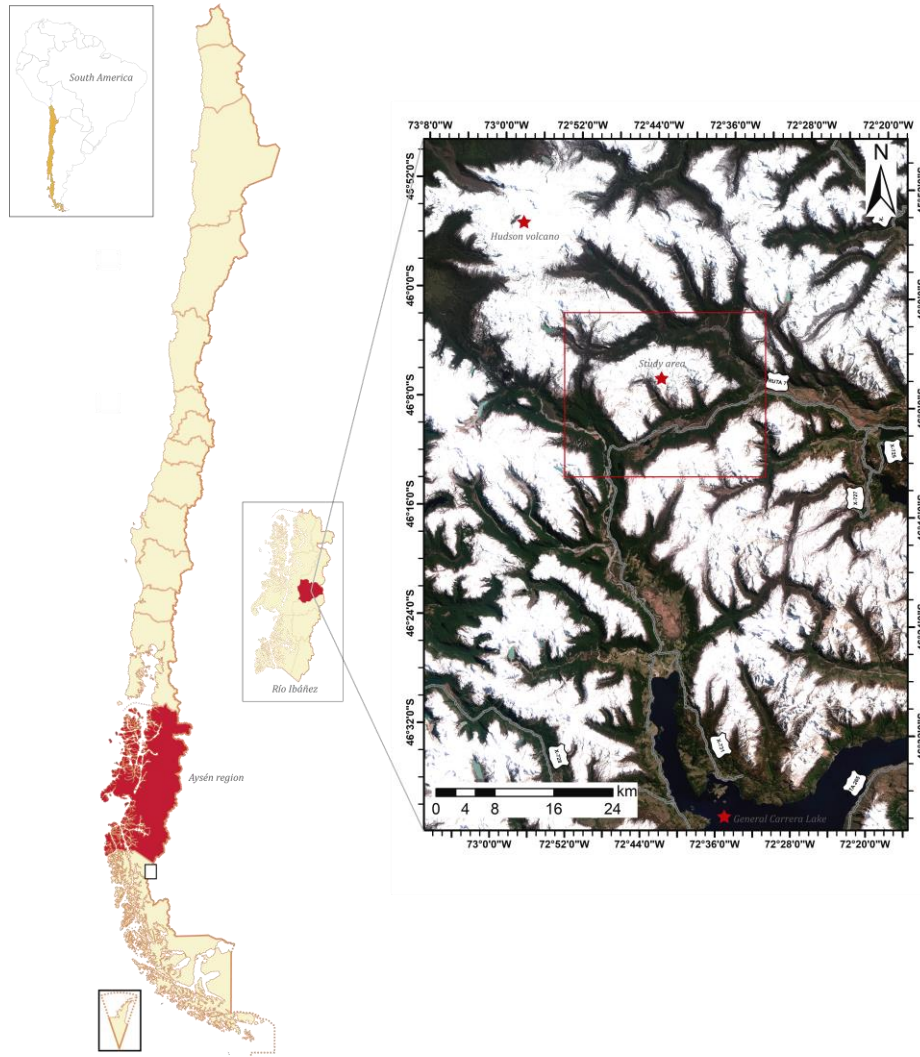


Fig. 9. Location of the Murta basalts in a red square. Red stars highlight some sites of interest near the Murta basalts, such as Hudson Volcano to the north and General Carrera Lake to the south.

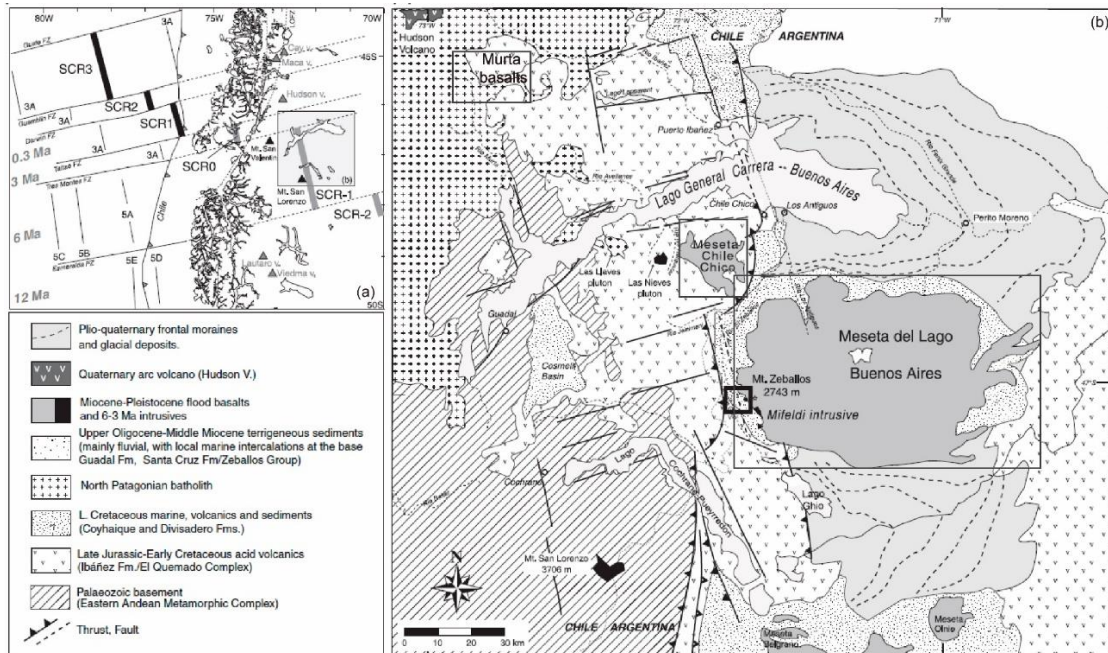


Fig. 12. Geological context of the study area. (a) Plate tectonic frame of the subduction of the South Chile Ridge (SCR), its transform faults zones (FZ), and active segments (SCR1 to SCR 4) with collision ages. (b) Geology of the region around the Lago General Carrera-Buenos Aires showing the location of Murta basalts, Meseta de Chile Chico, and Lago Buenos Aires in frames. Modified from Lagabrielle et al. (2007).

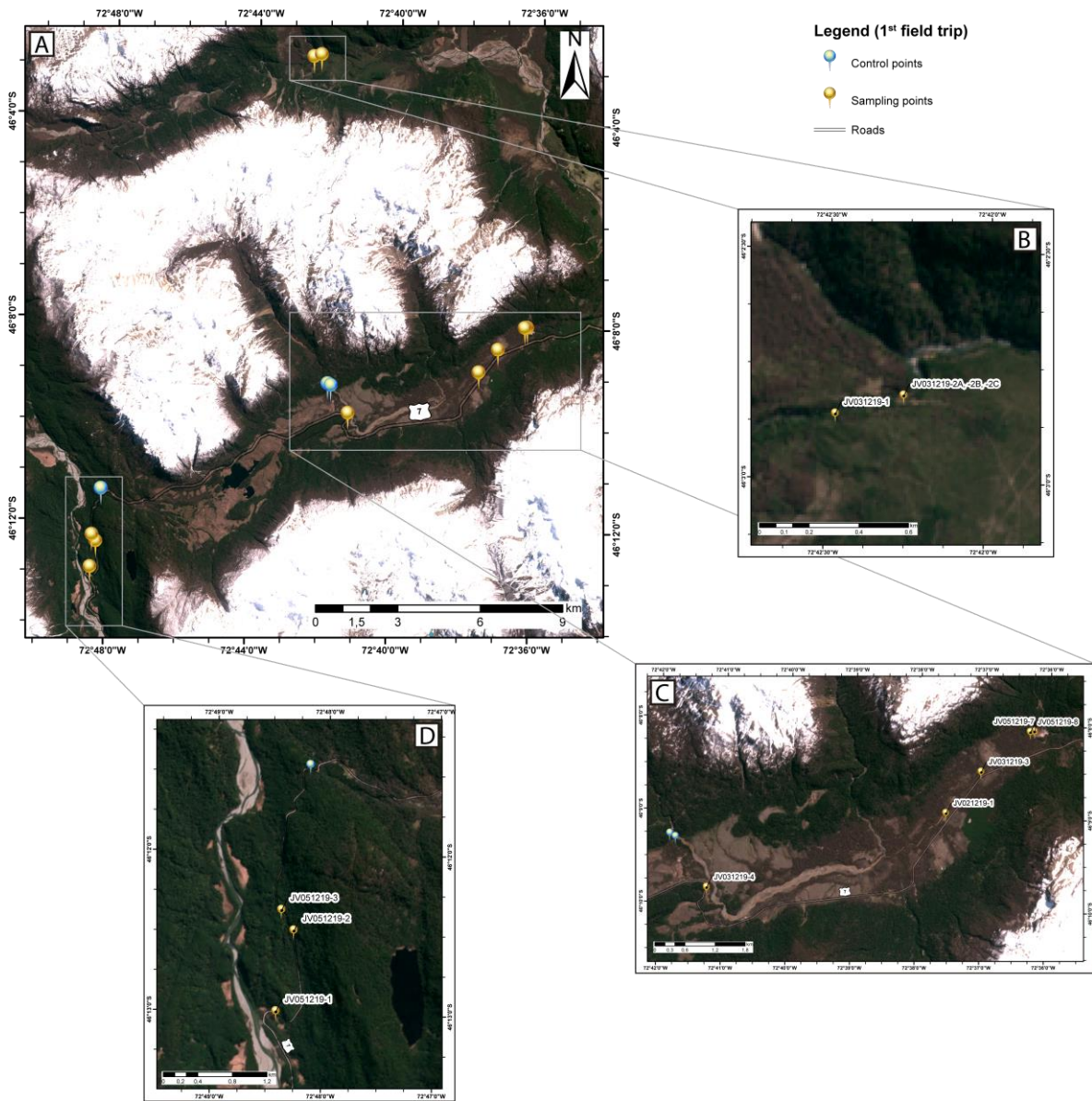


Fig. 13. (A) First field trip with the sampling and control points. (B), (C) and (D) Zoom to the northern (Ibáñez-Chiflón rivers), central (Cajón River) and southern (Murta River) parts of the study area.

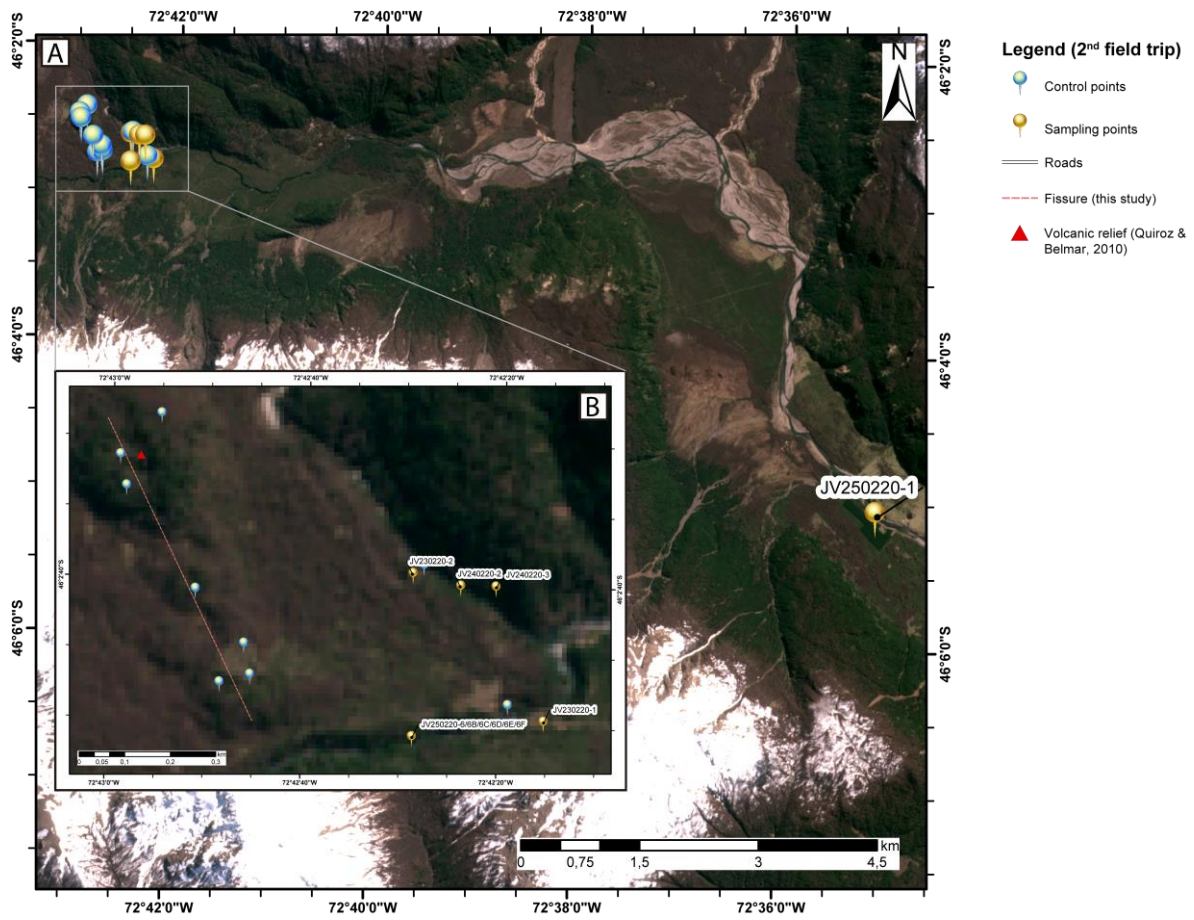


Fig. 14.(A) Second field trip with the sampling and control points. (B) Zoom to the northern (Ibáñez-Chiflón rivers) part of the study area.

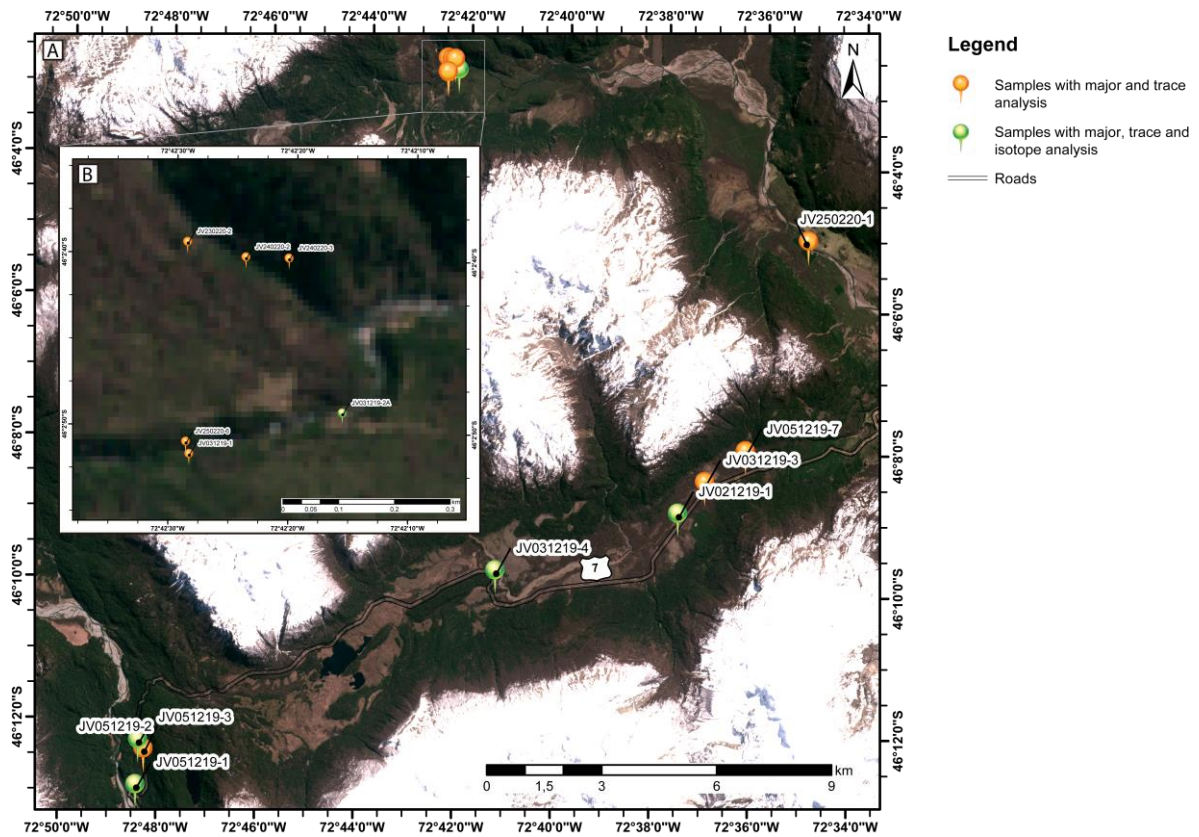


Fig. 15. (A) Samples with major, trace and isotope analysis. (B) Zoom to the northern (Ibáñez-Chiflón rivers) part of the study area.



Fig. 16. Images of the deposits found in the Cajón and Murta rivers. (A) Basalts with prismatic jointing located in the Cajón River. (B) Pillow lavas found in deposits near the Murta River. (C) Lighter-colored lavas with prismatic jointing, very thick with a fall deposit at the top. (D) Sample of lava near the Murta River with centimetric plagioclase macrocrysts.



Fig. 17. Deposits mapped at the intersection of the Ibáñez and Chiflón rivers. (A) Columnar basalts in Chiflón River. (B) Massive and highly vesiculated lavas. (C) Xenoliths within columnar basalts described in A.

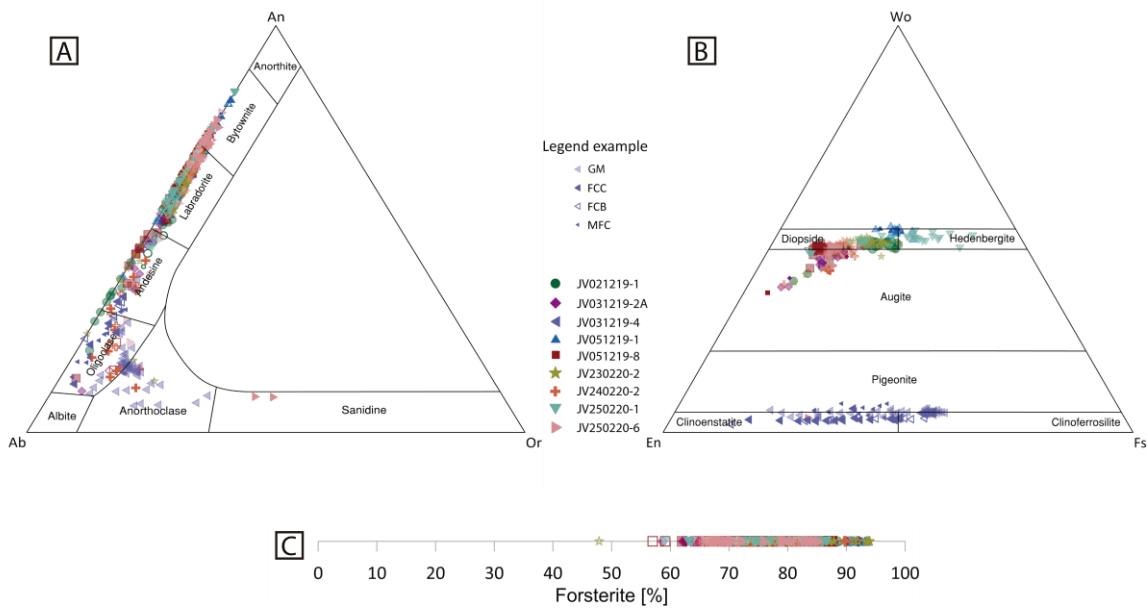


Fig. 18. Summary of Murta basalts mineral composition illustrating the compositional evolution of macrocrysts, microphenocrysts, and groundmass crystals. As shown in the legend, dark filled symbol corresponds to center macrocrysts/phenocrysts (FCC), white symbols correspond to border macrocrysts/phenocrysts (FCB), tiny dark-filled symbol corresponds to microphenocrysts (MFC), and light-filled symbol corresponds to groundmass crystals (GM). (A) Feldspar (An-Ab-Or), (B) pyroxene (En-Wo-Fs), and (C) olivine (Fo).

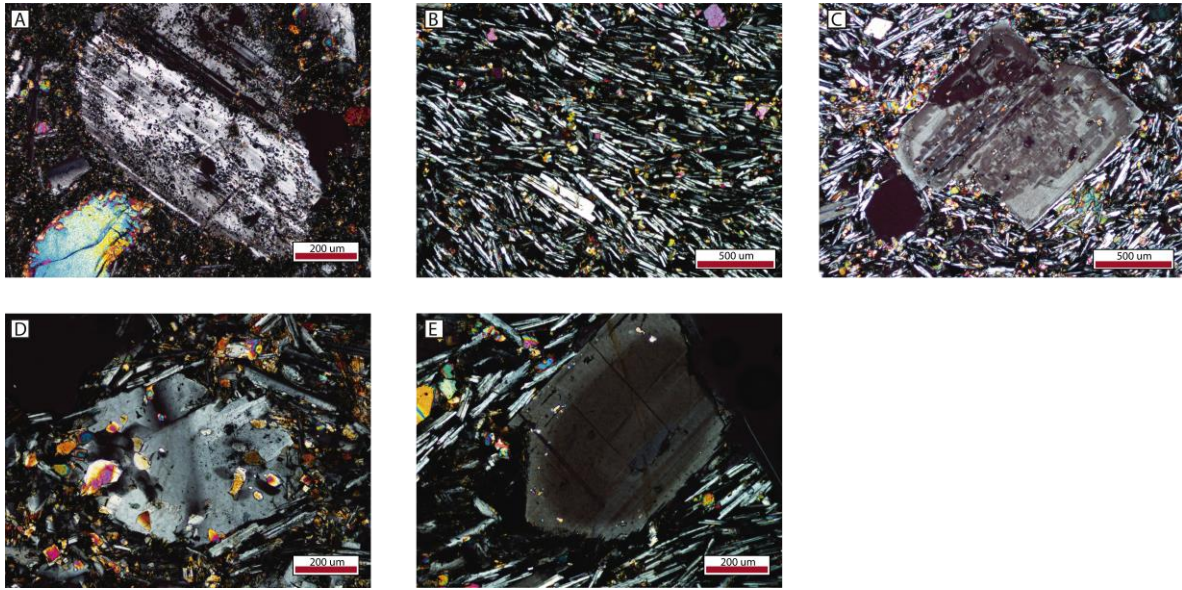


Fig. 19. Main textures observed in the plagioclase macrocrysts and microcrysts in the thin sections. (A) JV031219-1 showing sieve texture. (B) JV021219-1 showing pilotaxitic texture with oriented plagioclase. (C) JV03121919-3 showing patchy texture. (D) JV230220-2 showing poikilitic texture. (E) JV021219-1 showing diffuse zoning.

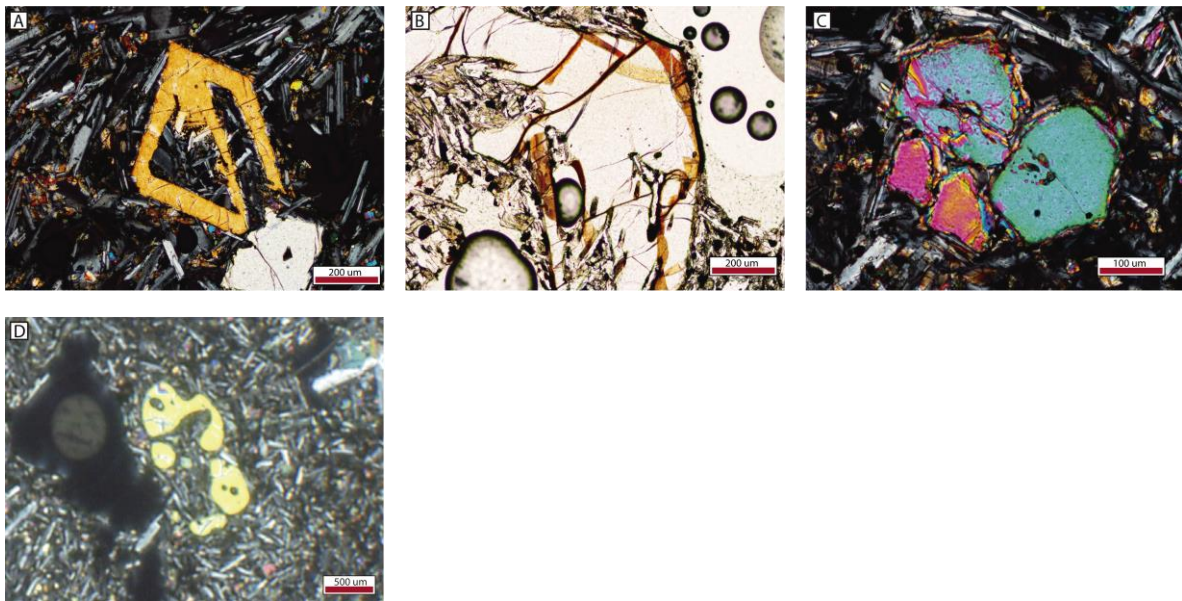


Fig. 20. Main photographs of the olivine macrocrysts observed in the thin sections. (A) JV230220-2 showing olivine with skeletal form. (B) JV031219-2A showing alteration of olivine on edge by iddingsite. (C) JV03121919-2A showing glomeroporphyritic texture where olivine macrocrysts are clustered. (D) JV250220-1 showing olivine with resorption.

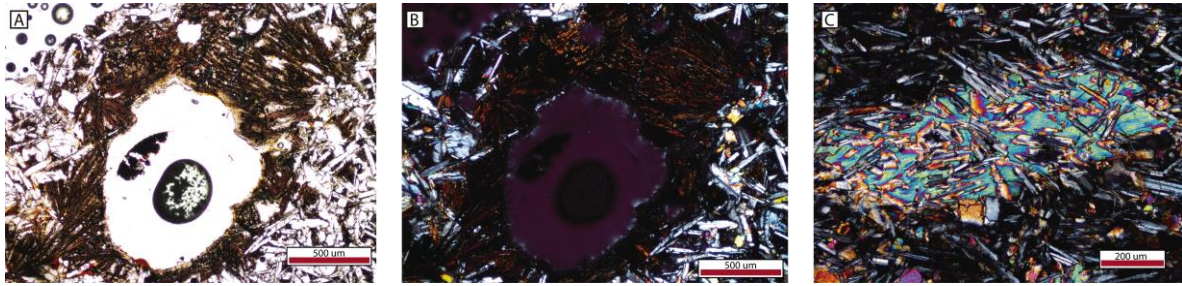


Fig. 21. Main textures observed in the pyroxene microphenocrysts in the thin sections. (A) JV051219-1 image of PPL showing a radial shape of pyroxene. (B) JV051219-1 XPL image of (A). (C) JV031219-3 showing subophitic texture of pyroxene partially enclosing smaller plagioclase.

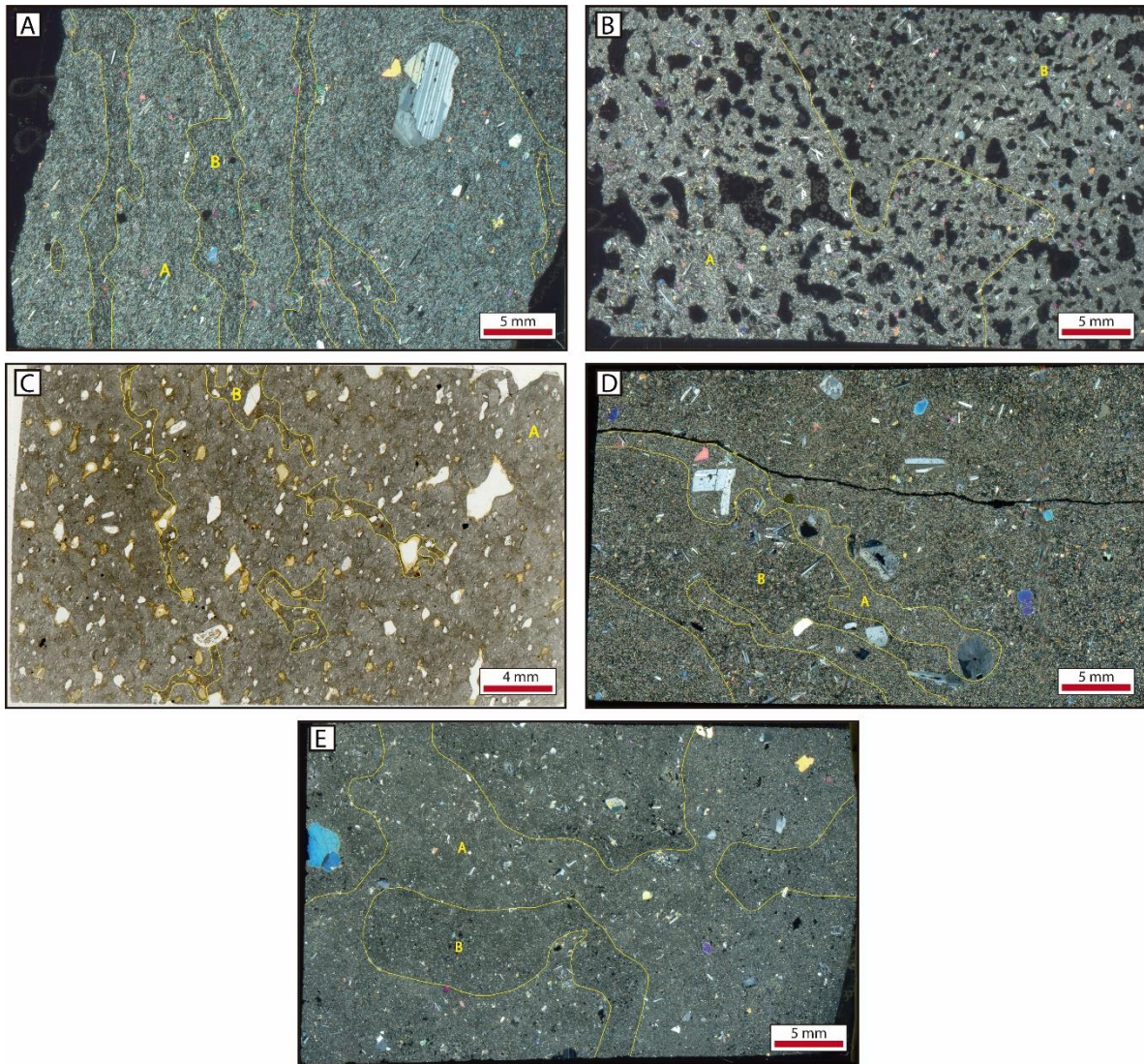


Fig. 22. Thin sections of samples (A) JV021219-1 (XPL), (B) JV031219-2A (XPL), (C) JV031219-4 (PPL), (D) JV051219-8 (XPL) and (E) JV240220-2 (XPL). Yellow lines highlight some examples of areas that are different from the rest of the groundmass. Letter A represents the light zones and B the dark zones.

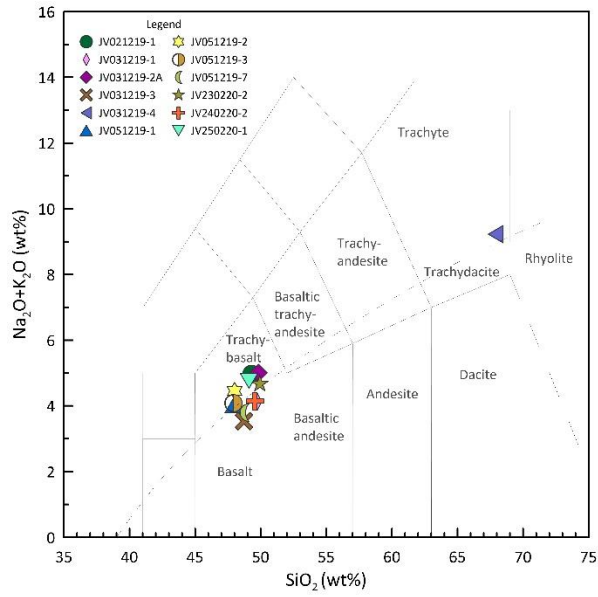


Fig. 23. Total alkali–silica classification diagram based on Le Bas et al. (1986) for the Murta Basalts recalculated to 100 wt. %, anhydrous basis. The dotted line represents the boundary between the alkaline and sub-alkaline series (Irvine and Baragar, 1971).

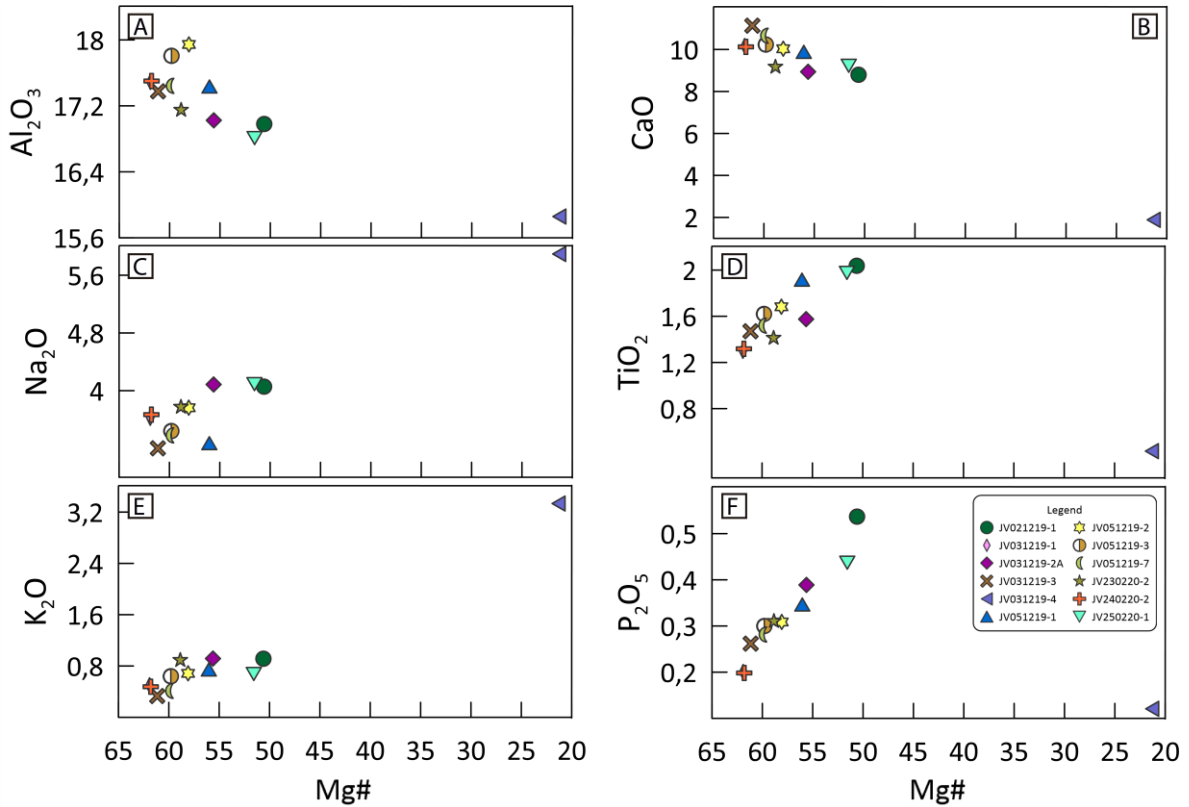


Fig. 24. Major element bivariate diagrams against magnesium number ($Mg\#$) for basalts and trachyte.

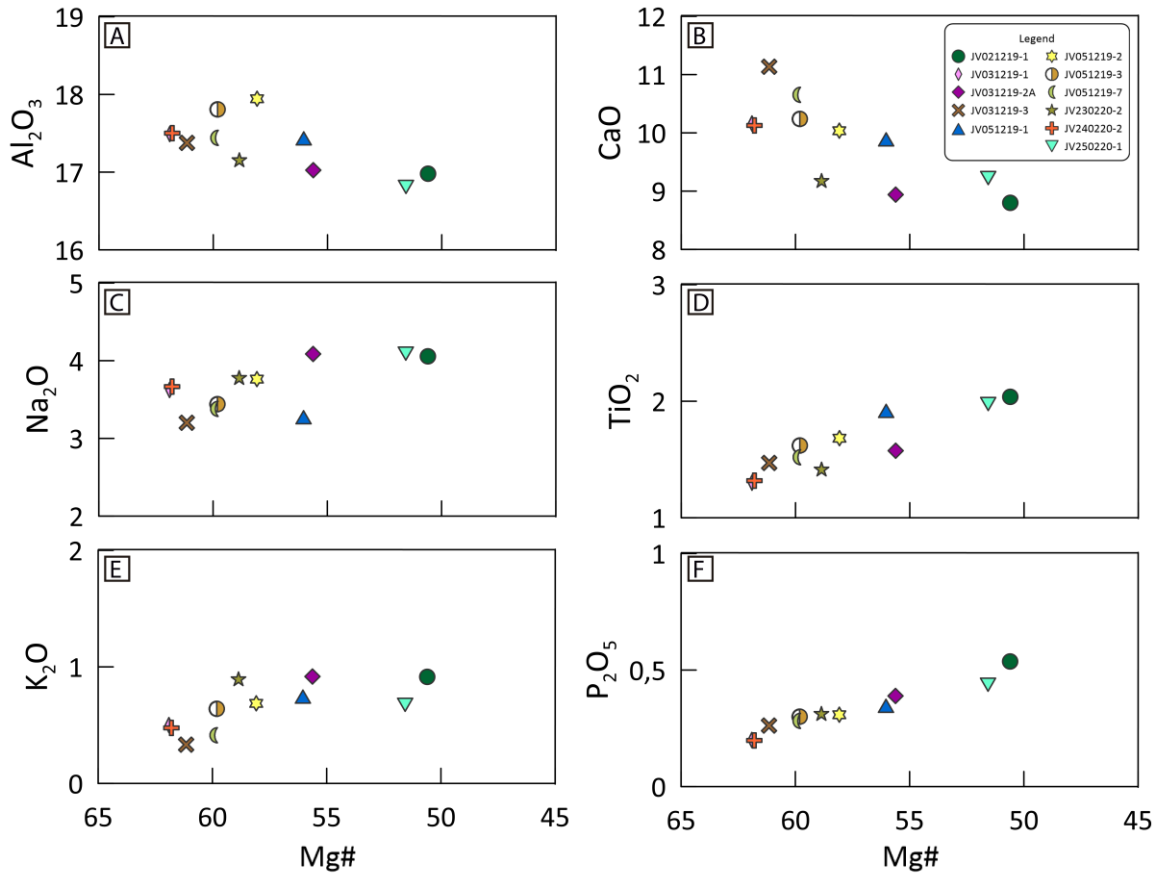


Fig. 25. Zoom to major element bivariate diagrams against magnesium number (Mg#) for basalts.

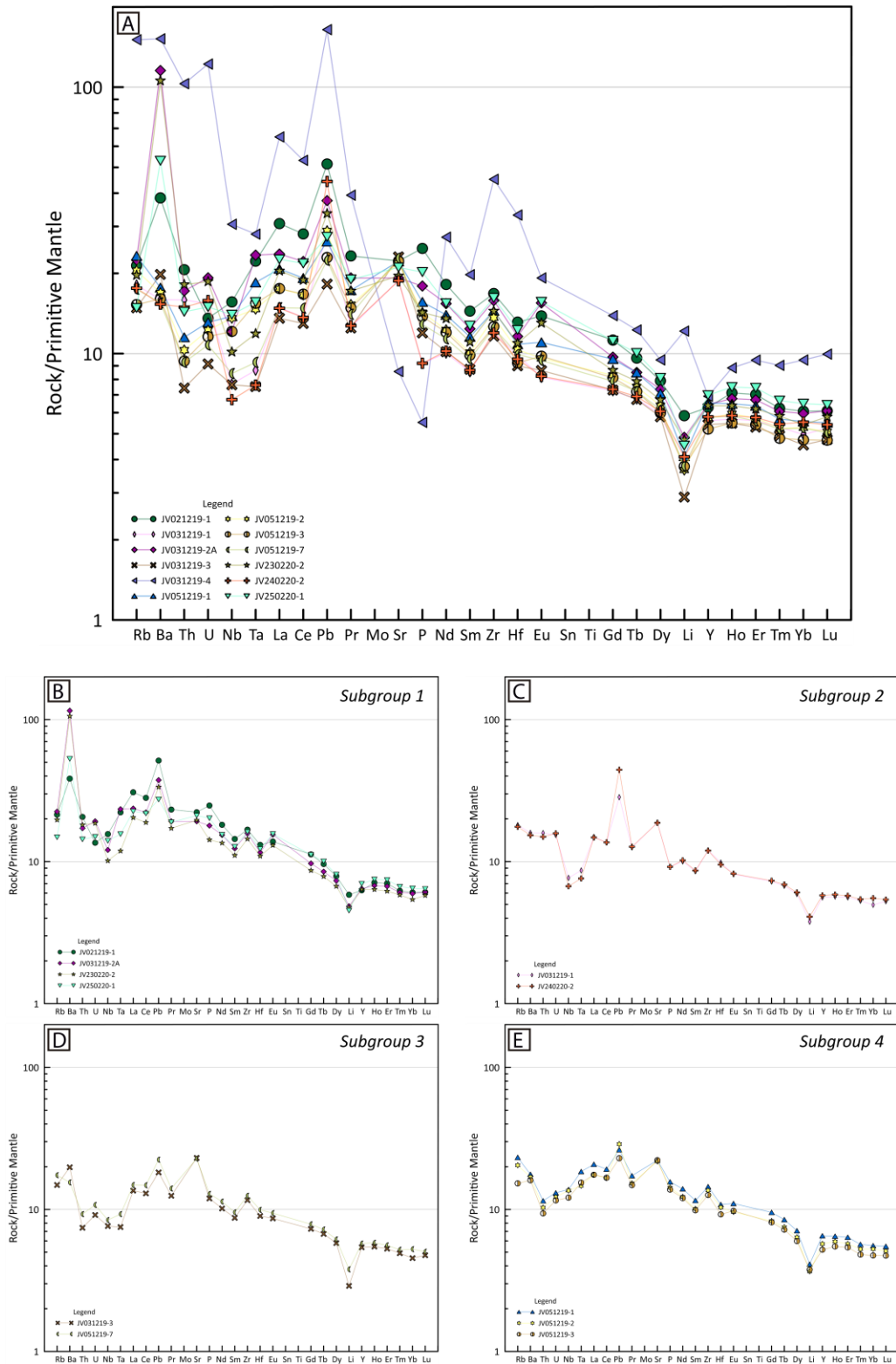


Fig. 26. Primitive mantle normalized (Sun & McDonough, 1989) spider diagram. (A) All samples plotted. (B), (C), (D) and (E) correspond to the different subgroups defined in chapter 2.5.5.

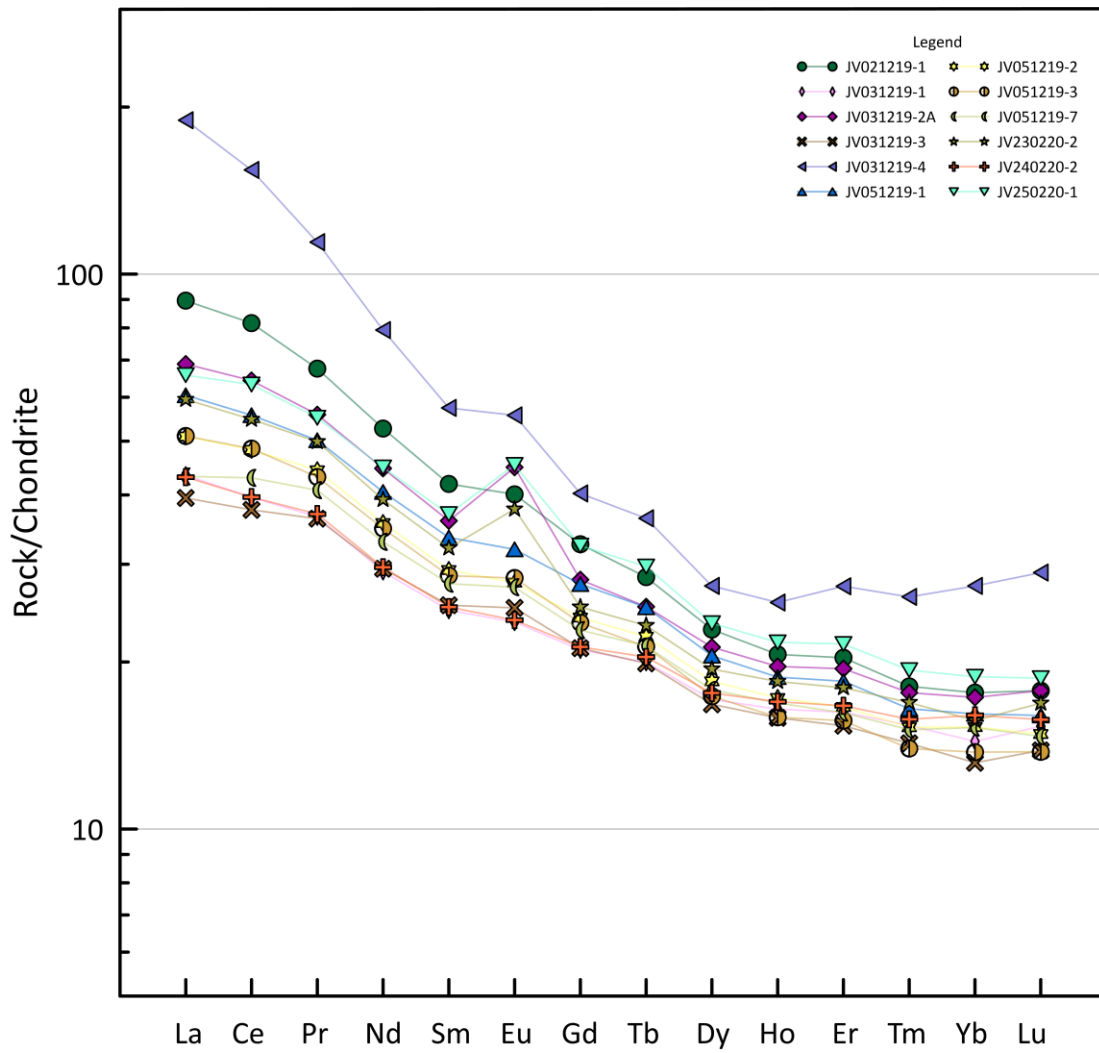


Fig. 27. Chondrite normalized (Sun & McDonough, 1989) REE diagram.

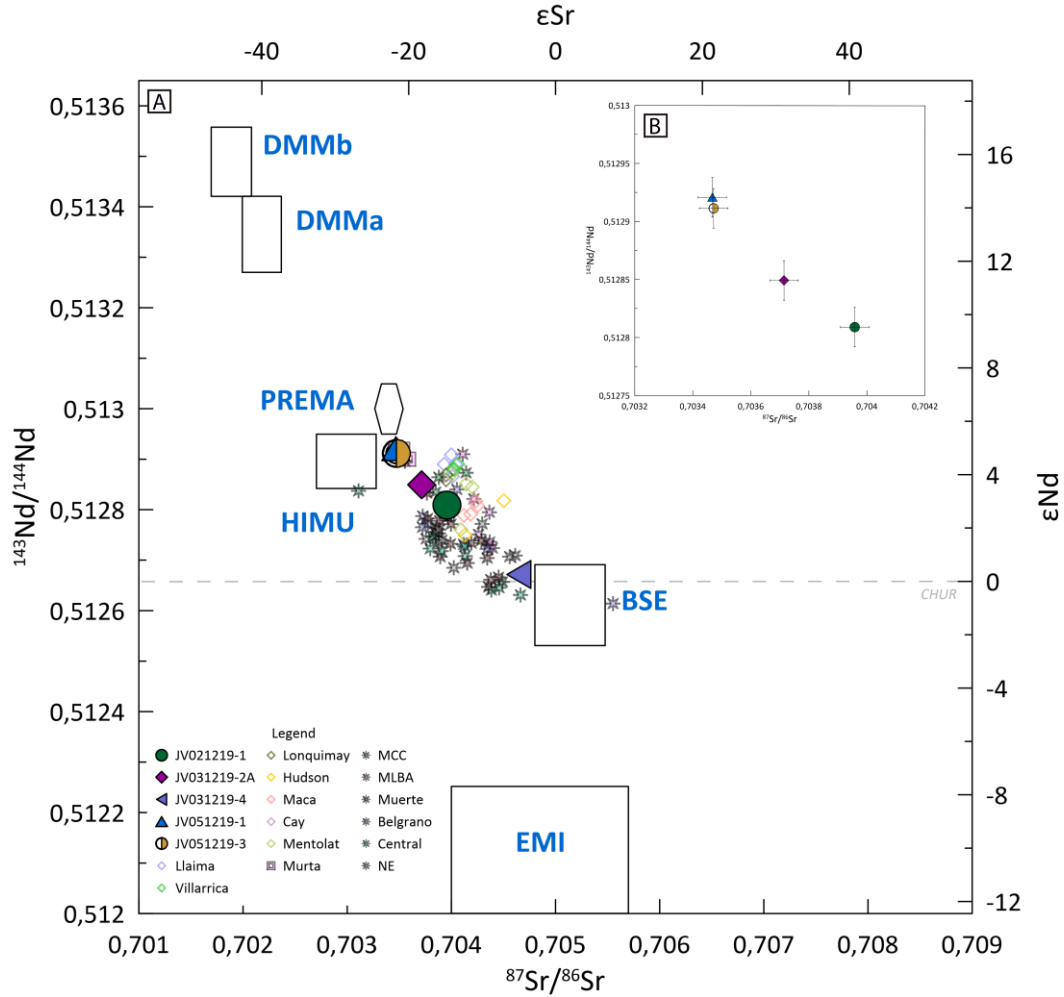


Fig. 28. Plot of $^{87}\text{Sr}/^{86}\text{Sr}$ against $^{143}\text{Nd}/^{144}\text{Nd}$ for (A) the studied lavas (symbol size bigger than the error bars), some SVZ and AVZ volcanoes, and Neogene Patagonian plateau lavas for comparison. Llaima data extracted from Hickey et al. (1986) and Hickey et al. (2016), Villarrica from Hickey et al. (1986), Lonquimay from Hickey et al. (2016), Hudson from Lopez-Escobar et al. (1993), Maca and Cay from Lopez-Escobar et al. (1993) and D'Orazio et al. (2003), Mentolat from Lopez-Escobar et al. (1993), Murta from Guivel et al. (2006) and Demant et al. (1998), Meseta Chile Chico (MCC) from Guivel et al. (2006) and Espinoza et al. (2005), Meseta Lago Buenos Aires (MLBA) from Guivel et al. (2006) and Muerte, Belgrano, Central and NE from Goring & Kay (2001). These include the depleted mantle (DM), bulk silicate Earth (BSE), enriched mantle (EM1), high- μ (U/Pb) (HIMU), and the 'prevalent mantle' (PREMA) fields. (B) Zoom to more primitive samples with error bars.

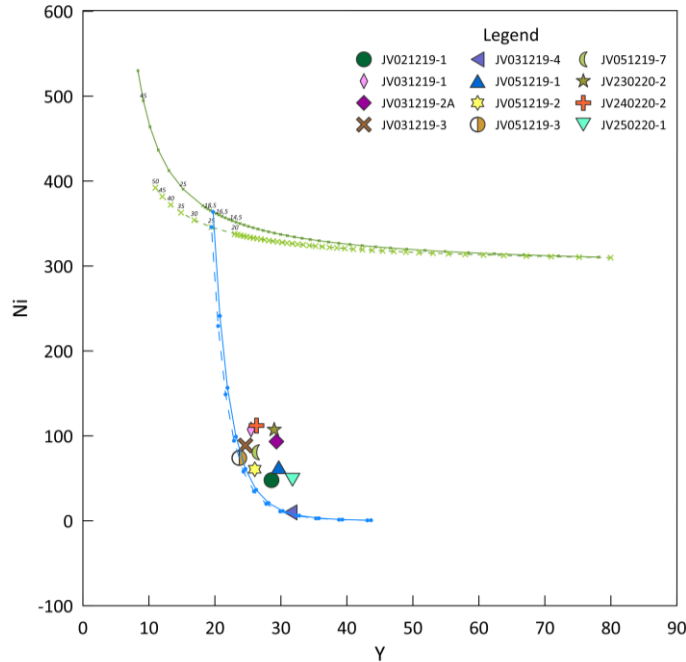


Fig. 29. The petrogenetic model based on Ni vs Y. Batch melting models are in green. The modal melting model is in a solid line and the non-modal melting model is in a dotted line. The E-MORB mantle's starting composition were taken from Mertz et al. (2001) and the K_D from Gorrying & Kay (2001) and are available in Table 4. Source mineral mode: 58% ol, 30% opx, 10% cpx, and 2% sp. Melt mineral mode: 10% ol, 20% opx, 65% cpx, and 5% sp. Two other curves in blue represent olivine fractionation trends with points marking increments of 5% olivine fractionation.

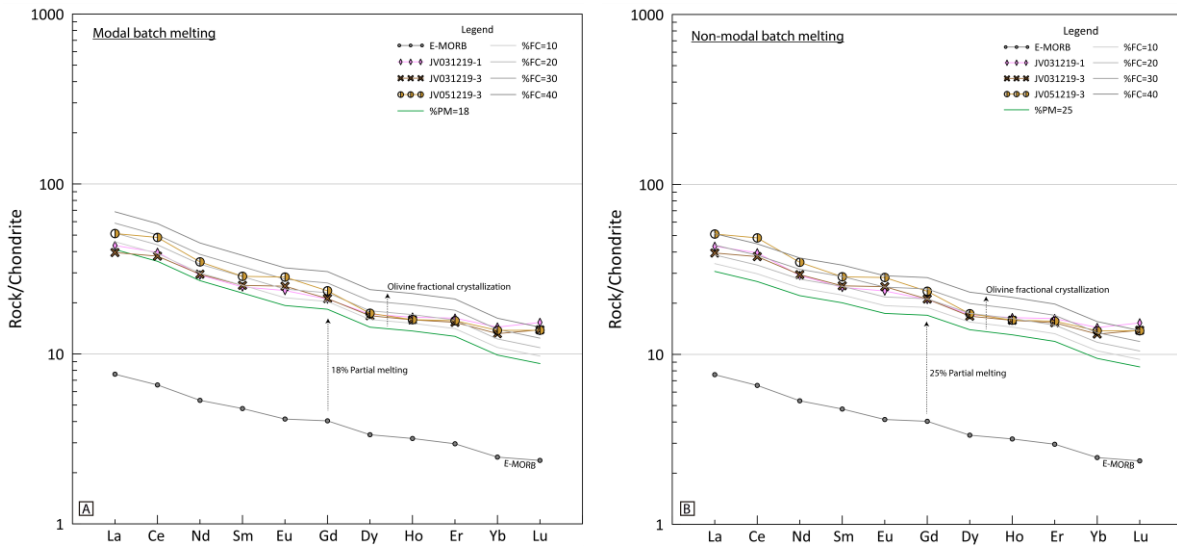


Fig. 30. The petrogenetic model using batch melting models and fractional crystallization on a Chondrite normalized (Sun & McDonough, 1989) REE diagram. (A) Modal melting model and (B) Non-modal melting model. The E-MORB mantle's starting composition were taken from Mertz et al. (2001) and the K_D from Gorrying & Kay (2001) and are available in Table 4. Source mineral mode: 58% ol, 30% opx, 10% cpx, and 2% sp. Melt mineral mode: 10% ol, 20% opx, 65% cpx, and 5% sp. The gray lines represent olivine fractionation trends with increments of 10% olivine fractionation. The green lines represent the partial melting percentage for each model used as a starting point for the fractionation models.

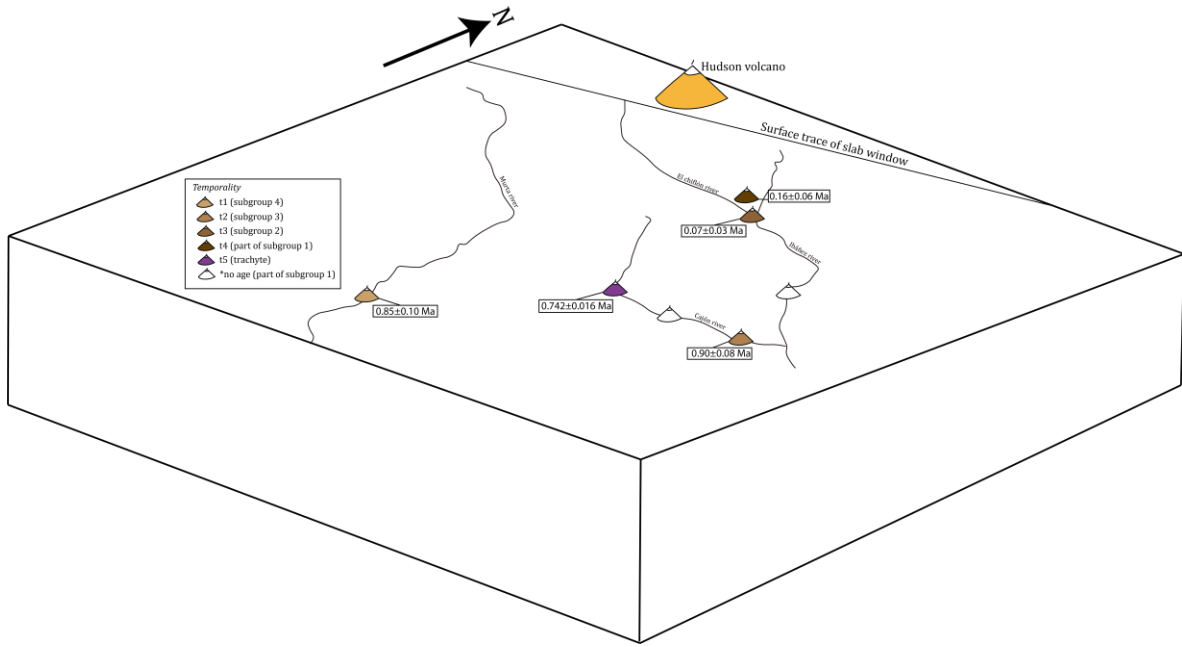


Fig. 31. Simplified scheme with the location of the analyzed samples grouped according to geochemical behavior and approximate ages. Subgroups 3 and 4 ages are from Guivel et al. (2006) and subgroups 1, 2 and trachyte are from Quiroz & Belmar (2010). According to temporality, t1 represents the oldest rocks and t5 the younger ones.

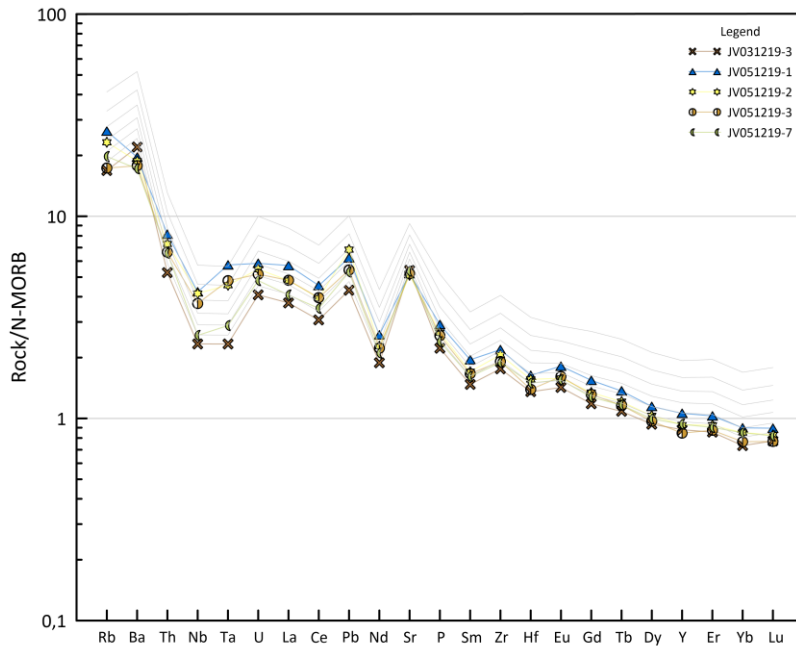


Fig. 32. N-MORB normalized (Sun & McDonough, 1989) fractional crystallization models using JV031219-3 as parental magma fractionating olivine, clinopyroxene, plagioclase, and spinel (50:29:20:1). Gray lines represent the proportion of liquid remaining with 10% increments. The K_d 's are available in Table 5.

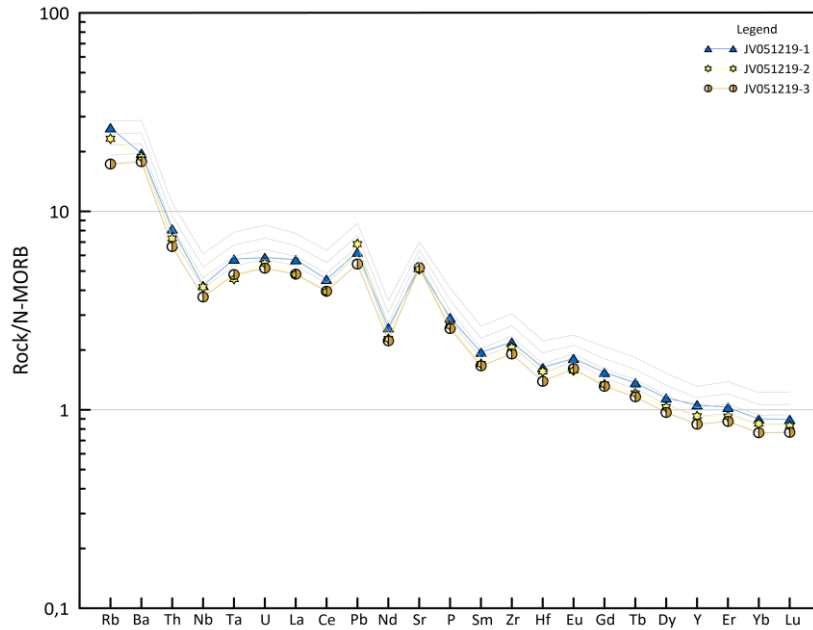


Fig. 33. N-MORB normalized (Sun & McDonough, 1989) fractional crystallization models using JV051219-3 as parental magma fractionating olivine, clinopyroxene, plagioclase, and spinel (50:29:20:1). Gray lines represent the proportion of liquid remaining with 10% increments. The K_d 's are available in Table 5.

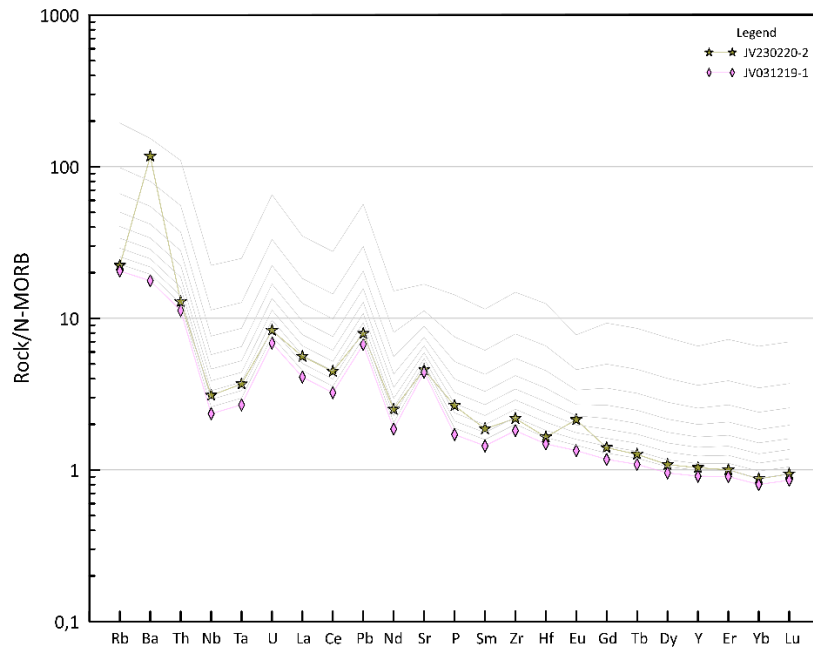


Fig. 34. N-MORB normalized (Sun & McDonough, 1989) fractional crystallization models using JV031219-1 as parental magma fractionating olivine, clinopyroxene, plagioclase, and spinel (50:29:20:1). Gray lines represent the proportion of liquid remaining with 10% increments. The K_d 's are available in Table 5.

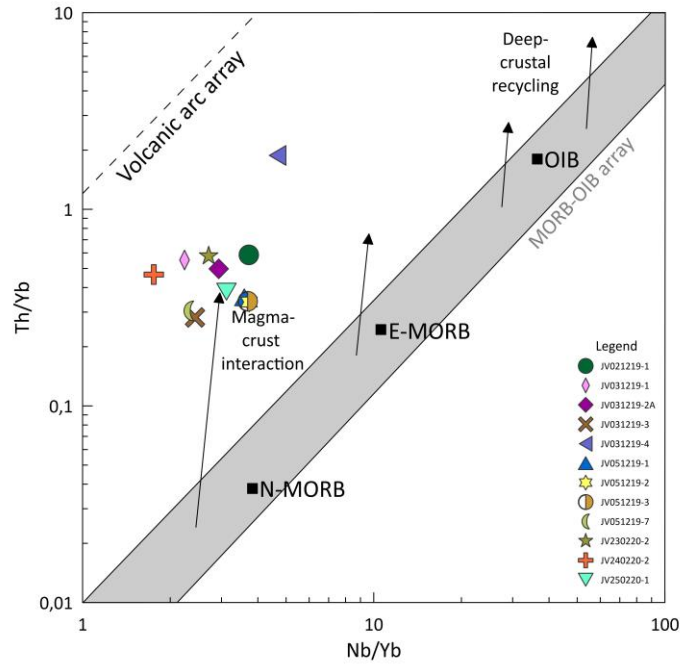


Fig. 35. Th–Nb proxy for crustal input based on Pearce (2008). Oceanic basalts (intraplate islands, plume-distal ocean ridges, and oceanic plateau) predominantly plot within the MORB–OIB array (shaded) while volcanic arc basalts plot above the array.

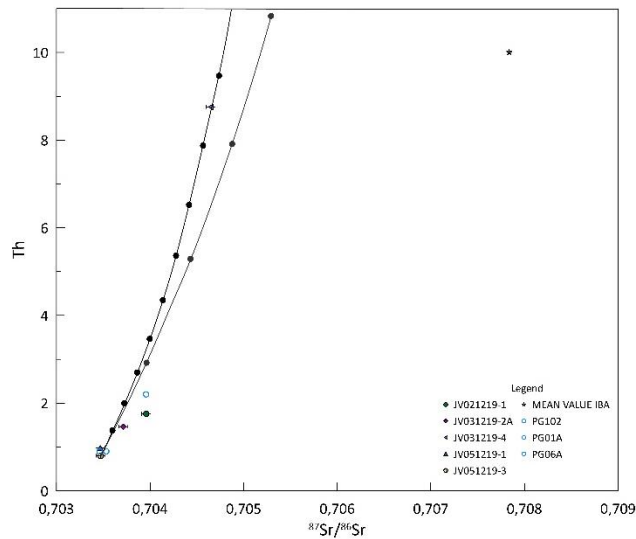


Fig. 36. AFC model between $^{87}\text{Sr}/^{86}\text{Sr}$ vs Th. Lines from left to right are $r=0.5$ and $r=0.8$, respectively. r is the assimilation rate (the mass assimilated/mass crystallized). The $^{87}\text{Sr}/^{86}\text{Sr}$ composition of the assimilated wall rock was taken from Pankhurst et al. (1999) and the average from three samples was used and Th=10 ppm. The partition coefficients are available in Table 5. Every point represents F with increments of 0.05.

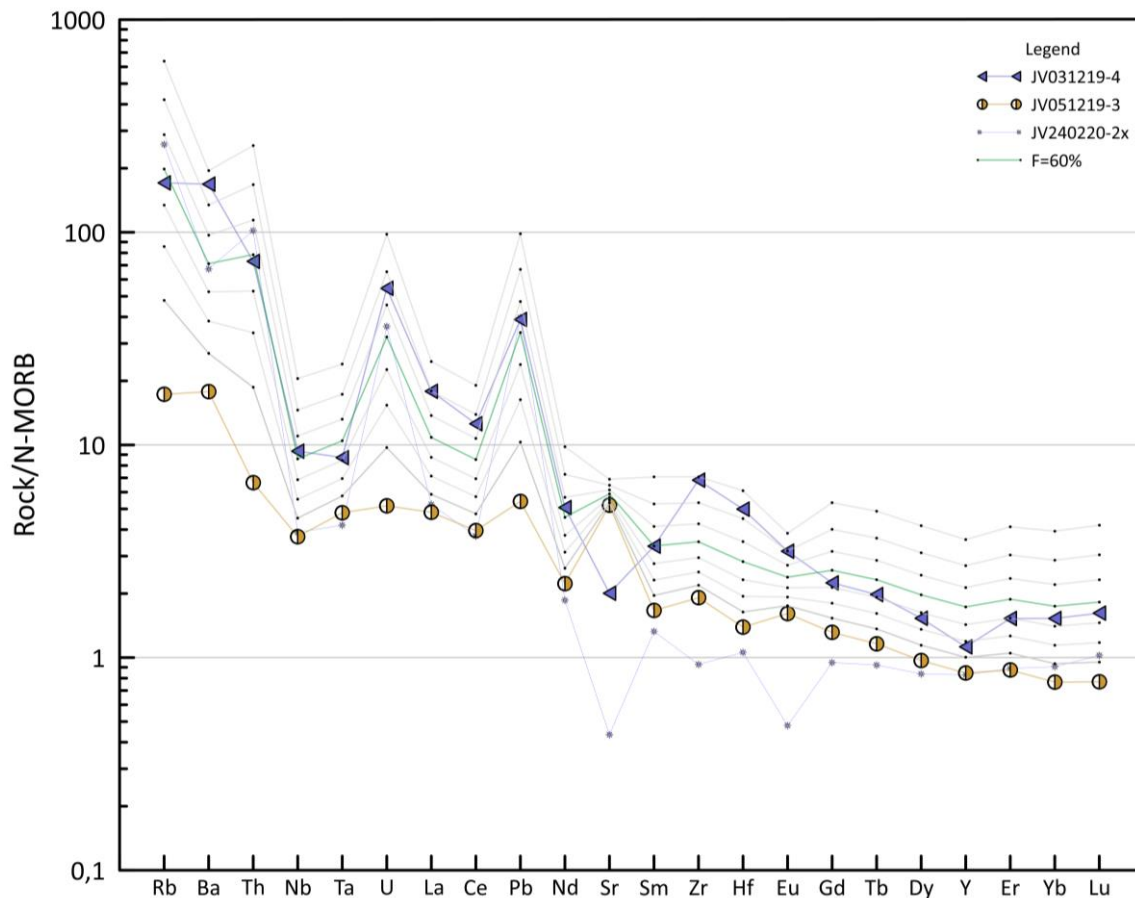


Fig. 37. N-MORB normalized (Sun & McDonough, 1989) AFC model for trace elements. $r=0.5$. The composition of the assimilated wall rock used was the sample JV240220-2x. The partition coefficients are available in Table 5. Every gray line represents F with increments of 10%. In green line $F=60\%$.

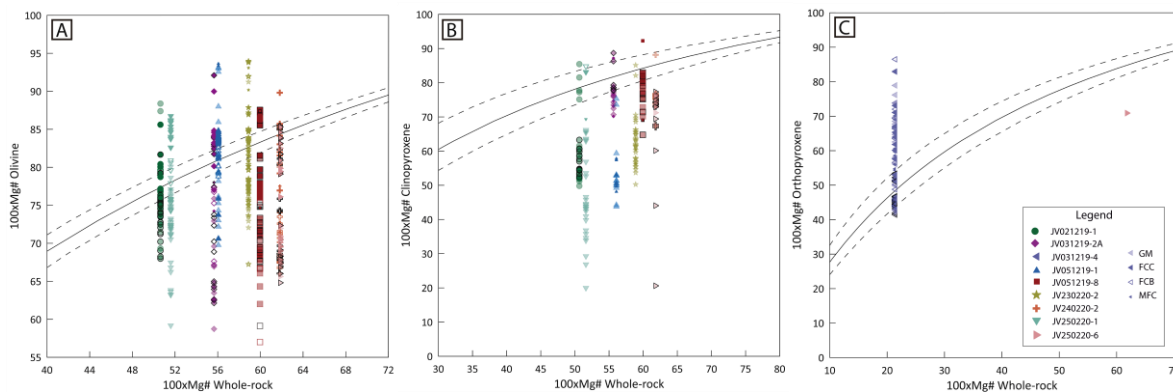


Fig. 38. Rhodes' diagram for testing (A) olivine/whole-rock equilibrium using $K_D(Fe-Mg)^{ol-liq} 0.30 \pm 0.03$, (B) clinopyroxene/whole-rock equilibrium using $K_D(Fe-Mg)^{ol-liq} 0.28 \pm 0.08$ and (C) orthopyroxene/whole-rock equilibrium using $K_D(Fe-Mg)^{ol-liq} 0.29 \pm 0.06$. As shown in the legend, dark filled symbol corresponds to center macrocrysts/phenocrysts (FCC), white symbols correspond to border macrocrysts/phenocrysts (FCB), tiny dark-filled symbol corresponds to microphenocrysts (MFC), and light-filled symbol corresponds to groundmass crystals (GM). Black borders represent the darker zones in thin sections equivalent to zone B in Fig. 22.

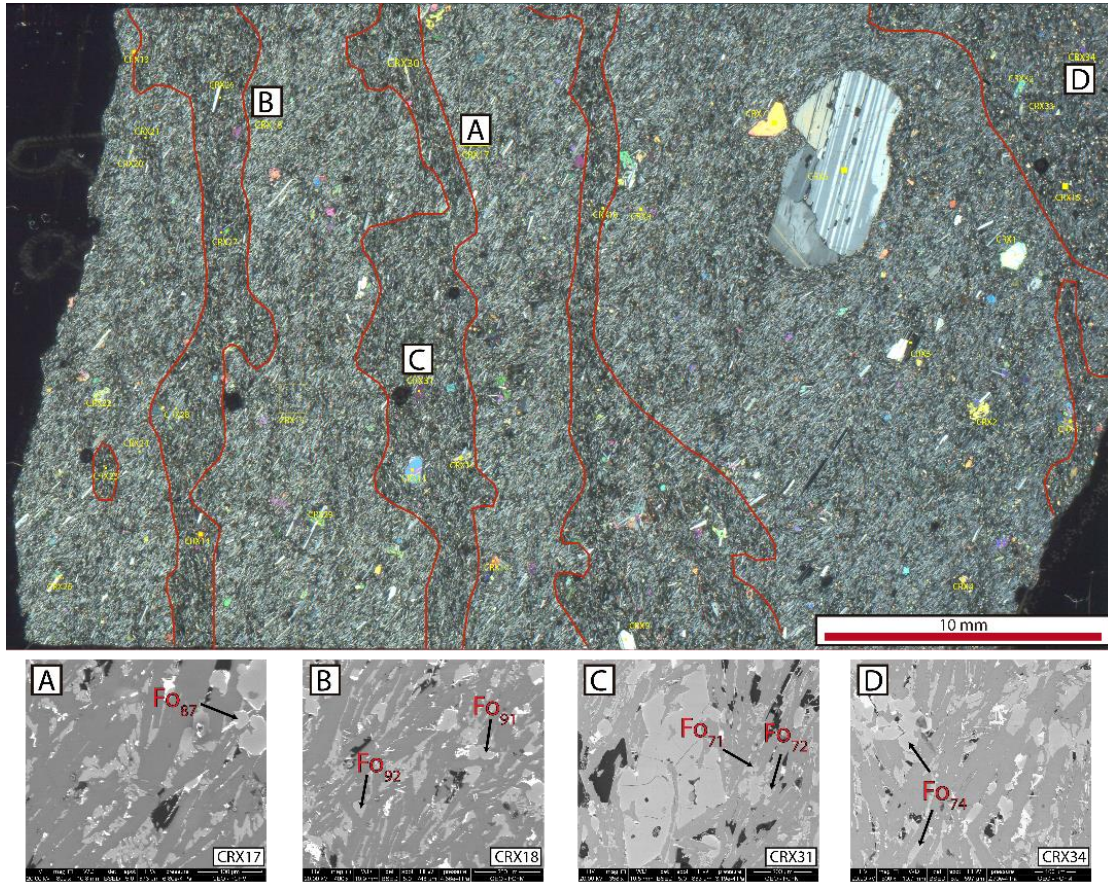


Fig. 39. Sample JV021219-1 (Cross-polarized light, XPL) with some SEM images and olivine compositions in the groundmass. A and B correspond to the light zone and C and D to the dark zone.

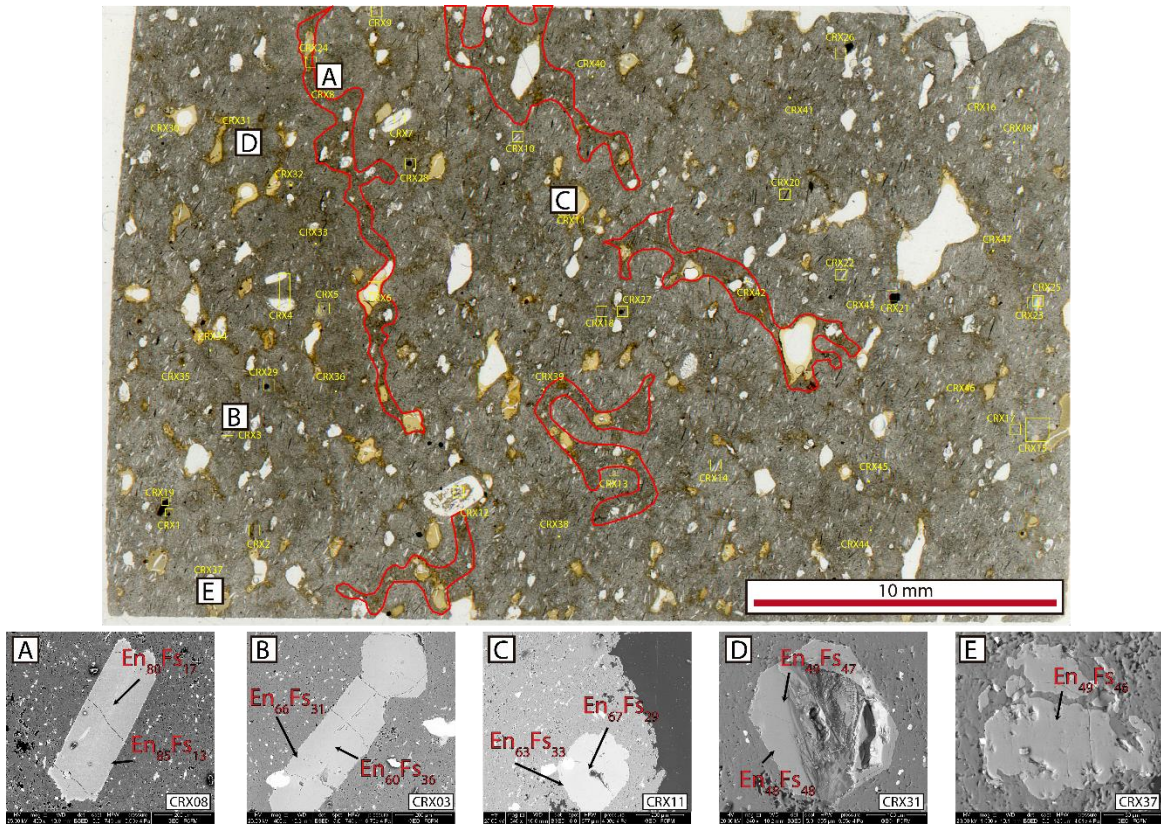


Fig. 40. Sample 031219-4 (Plane-polarized light, PPL) with some SEM images and pyroxene macrocrysts compositions. A, B and C correspond to the light zone and D and E to the dark zone.

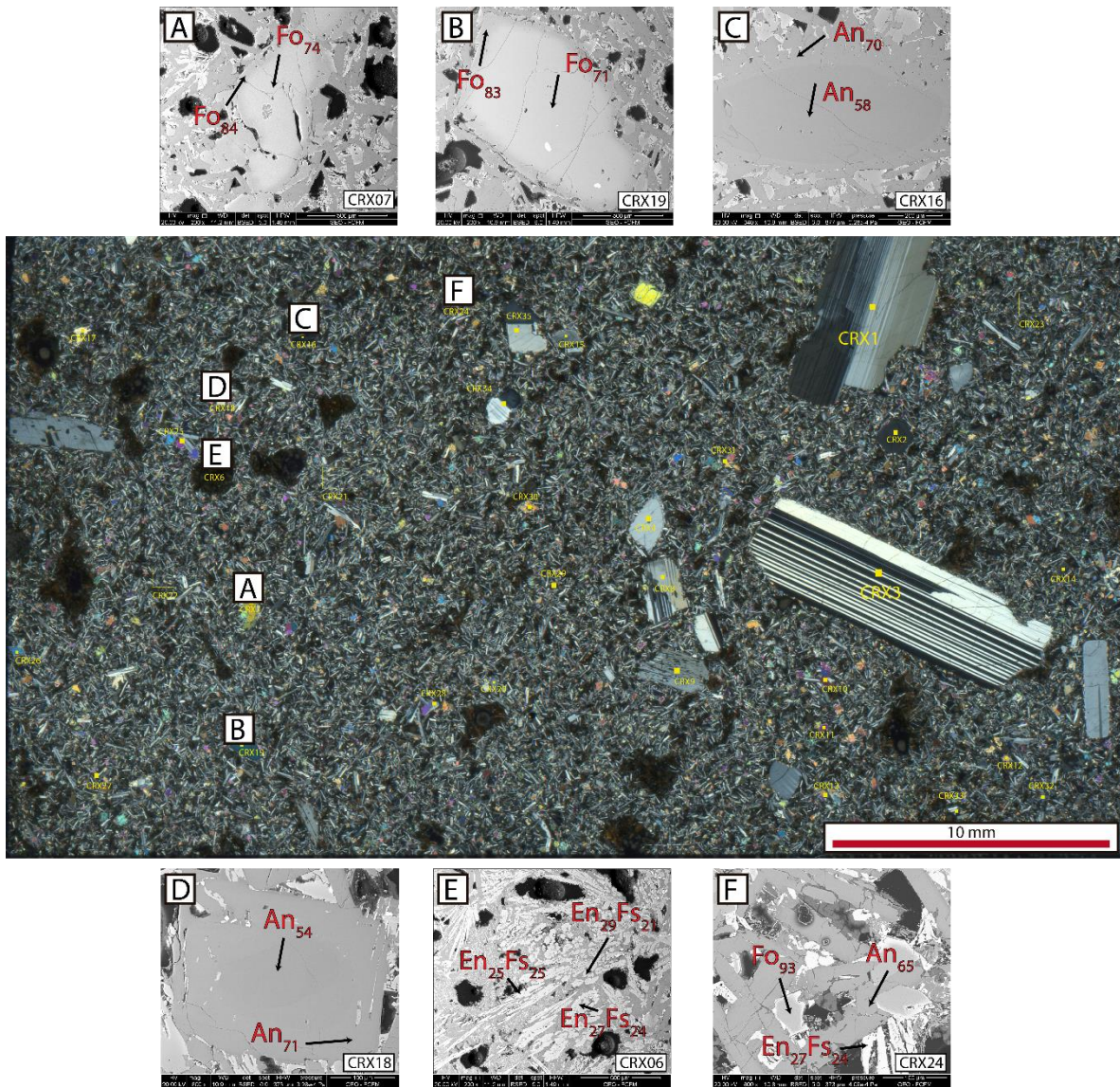


Fig. 41. Sample JV051219-1 (Cross-polarized light, XPL) with some SEM images and olivine, plagioclase, and pyroxene compositions. A-D macrocrysts and E-F microcrysts.

	Sample	Lat. °S	Long. °W	Rock type	Loc	#Mg	87Sr/86Sr	143Nd/144Nd	εNd
1	JV021219-1	46°08'58,8"	72°37'34,7"	Extrusive	Murta	50.60	0.70396	0.512809	-14.78
2	JV031219-2A	46°02'49,1"	72°42'15,9"	Extrusive	Ibáñez river	55.62	0.70371	0.512849	-18.24
3	JV031219-4	46°09'51"	72°41'14,9"	Extrusive	Murta	21.30	0.70465	0.512672	-5.01
4	JV051219-1	46°13'0,3"	72°48'25,4"	Extrusive	Murta	56.04	0.70347	0.512921	-21.74
5	JV051219-3	46°12'22,2"	72°48'23,7"	Extrusive	Murta	59.81	0.70347	0.512911	-21.68

Table 3. Sr and Nd isotopic data for Murta basalts.

	Element	Kd's				Source E-MORB
		Olivine	Orthopyroxene	Clinopyroxene	Spinel	[ppm]
R E E	<i>La</i>	0.000007	0.0005	0.0536	0.0006	1.8
	<i>Ce</i>	0.00001	0.0009	0.0858	0.0006	4.02
	<i>Nd</i>	0.00007	0.009	0.1873	0.0006	2.49
	<i>Sm</i>	0.0007	0.02	0.291	0.0006	0.73
	<i>Eu</i>	0.00095	0.03	0.3288	0.0006	0.24
	<i>Gd</i>	0.0012	0.04	0.367	0.0006	0.83
	<i>Dy</i>	0.004	0.06	0.442	0.0015	0.85
	<i>Ho</i>	0.0065	0.065	0.4145	0.0023	0.18
	<i>Er</i>	0.009	0.07	0.387	0.003	0.49
	<i>Yb</i>	0.023	0.1	0.43	0.0045	0.42
	<i>Lu</i>	0.035	0.15	0.433	0.0045	0.06
	<i>Ni</i>	9	0.97	3	10	1858.12
	<i>Y</i>	0.005	0.005	0.467	0.01	4.38

wt%	<i>d_i</i>	58	30	10	2
		<i>p_i</i>	10	20	65

Table 4. Partition coefficients used in the batch melting and fractionation model extracted from Gorryng & Kay (2001). E-MORB source is from Mertz et al. (2001). The source mineral mode (*d_i*) and the phase proportions entering the melt (*p_i*) are those used in Guivel et al. (2006) for spinel lherzolite.

		Olivine	Clinopyroxene	Plagioclase	Spinel
MULTI-ELEMENT	<i>Rb</i>	0.00018	0.011	0.1	0.029
	<i>Ba</i>	0.0000013	0.0035	0.3	0.0006
	<i>Th</i>	0.0001	0.00026	0.05	0.01
	<i>Nb</i>	0.01	0.05	0.01	0.0006
	<i>Ta</i>	0.03	0.04	0.04	0.0004
	<i>U</i>	0.0001	0.00036	0.11	0.014
	<i>La</i>	0.0004	0.054	0.27	0.01
	<i>Ce</i>	0.0005	0.098	0.2	0.01
	<i>Pb</i>	0.0001	0.0102	0.36	0.0005
	<i>Nd</i>	0.001	0.21	0.14	0.01
	<i>Sr</i>	0.00019	0.067	2	0.0047
	<i>P</i>	0.1	0.05	0.071	0
	<i>Sm</i>	0.0013	0.26	0.11	0.01
	<i>Zr</i>	0.06	0.195	0.0022	0.0081
	<i>Hf</i>	0.01	0.233	0.01	0.003
	<i>Eu</i>	0.0016	0.31	0.73	0.01
	<i>Gd</i>	0.0015	0.3	0.066	0.01
	<i>Tb</i>	0.0015	0.31	0.06	0.01
	<i>Dy</i>	0.0017	0.33	0.055	0.01
<i>Y</i>	0.0036	0.467	0.0227	0.002	
<i>Er</i>	0.0015	0.3	0.041	0.01	
<i>Yb</i>	0.0015	0.28	0.031	0.01	
<i>Lu</i>	0.0015	0.28	0.025	0.01	

REE	<i>La</i>	0.0004	0.054	0.27	0.01
	<i>Ce</i>	0.0005	0.098	0.2	0.01
	<i>Pr</i>	0.0008	0.15	0.17	0.01
	<i>Nd</i>	0.001	0.21	0.14	0.01
	<i>Sm</i>	0.0013	0.26	0.11	0.01
	<i>Eu</i>	0.0016	0.31	0.73	0.01
	<i>Gd</i>	0.0015	0.3	0.066	0.01
	<i>Tb</i>	0.0015	0.31	0.06	0.01
	<i>Dy</i>	0.0017	0.33	0.055	0.01
	<i>Ho</i>	0.0016	0.31	0.048	0.01
	<i>Er</i>	0.0015	0.3	0.041	0.01
	<i>Tm</i>	0.0015	1.09	0.036	0.01
	<i>Yb</i>	0.0015	0.28	0.031	0.01
<i>Lu</i>	0.0015	0.28	0.025	0.01	

wt%	x_i	50	29	20	1
-----	-------	----	----	----	---











REFERENCES	
	Beattie (1994)
	McKenzie & O'Nions (1991)
	Villemant et al. (1981)
	Bindeman & Davis (2000)
	Nielsen et al. (1992)
	Hauri et al. (1994)
	Brunet & Chazot (2001)
	Hart & Dunn (1993)
	Matsui et al. (1977)
	Elkins et al. (2008)

Table 5. Partition coefficients used in the fractionation and crustal assimilation models. The sources from which the data were extracted are shown on the right, representing the background color of each box. The elements are divided into two groups: elements used for spider diagrams and rare earth elements. X_i is the modal proportion in which the phases are fractionated.

3. DISCUSIONES

3.1. Origen basaltos y traquita

La evidencia petrográfica y química de los basaltos de Murta permite distinguir variados procesos en la formación de estos. Procesos fundamentados en base a modelos de fusión, mezcla, fraccionamiento y asimilación, de los que se pudo inferir que los basaltos se pueden relacionar entre sí a través de fraccionamiento, pero que no corresponderían a fluidos que ascendieron directamente del manto como se ha propuesto y pensado. Si bien, no se puede negar la posición geodinámica en la cual están emplazados estos depósitos, esta no sería la característica más importante.

En cuanto a la presencia de un único depósito evolucionado coexistiendo con lavas predominantemente basálticas, se ahondará a continuación. Resulta llamativa la presencia de una traquita entre basaltos, con una potencia y espesor considerable que permite hasta distinguirla y seguirla, usando imágenes satelitales, por unos cuantos kilómetros. Esta muestra es posible de reconstruir a partir de fraccionamiento y asimilación, usando como magma parental una de las muestras más primitivas y antiguas de los basaltos de Murta y como asimilante una muestra del Plutón del Río Murta (propia y extraída de Pankhurst et al. (1999)). Lo particular que llama la atención es la presencia de escasos fenocristales y microcristales de ortopiroxeno en la traquita, siendo que el resto de los basaltos solo contienen clinopiroxeno dentro de su mineralogía. Si bien, no se descarta la presencia de anfíbol (en particular cristales aciculares oxidados en todo el corte), las propiedades ópticas son innegablemente de ortopiroxeno (presencia de caras basales y clivaje característico).

Se proponen varias alternativas para la presencia de ortopiroxeno en la traquita. En primer lugar, la asimilación de la roca caja, donde las muestras que fueron recogidas durante el terreno se caracterizan por contener en su mineralogía cuarzo, plagioclasas, feldespatos potásicos y óxidos, sin ningún máfico predominante. Solo en una de las muestras de xenolitos corticales fue posible reconocer clorita como mineralogía secundaria dando pistas de la posible presencia de fases máficas con anterioridad. Esto, fue comparado con la bibliografía, en particular, con Pankhurst et al. (1999) en donde se tiene una caracterización extensa del Batolito Patagónico incluidos los intrusivos que afloran en el sector de río Murta, Ibáñez y Chiflón. Los cuerpos plutónicos que allí afloran, según los autores, pertenecen al Cretácico

temprano y medio, y corresponden a granodioritas de hornblenda-biotita, tonalitas, dioritas y gabros. La diferencia en la mineralogía con la bibliografía se atribuye principalmente al tamaño de los xenolitos dentro de los basaltos. Estos solo presentan tamaños de pocos centímetros que no hace posible la caracterización exhaustiva del asimilante.

La segunda posibilidad se asocia a que la presencia de texturas de mezcla dentro de la traquita sea la responsable de la llegada de estos cristales máficos a partir del fluido secundario que haya modificado la química de esta roca y, además, aportado en su mineralogía.

Es importante mencionar que la presencia de ortopiroxeno no es exclusiva en la zona para los basaltos de Murta, si no que el volcán Hudson, ubicado al noroeste a unos 20 kilómetros de distancia, ha tenido variados episodios en los que ha expulsado traquidacitas caracterizadas por la presencia de ortopiroxeno como fenocristales y que han sido derivadas de una fuente máfica que ha atravesado episodios de cristalización fraccionada y mezcla de magmas (Kratzmann et al., 2010).

3.2. Fisura río Ibáñez-Chiflón

Debido a que la fisura descrita en el texto se escapa del alcance de la investigación, en este capítulo se darán a conocer algunas características tectónicas que apoyan la presencia de esta posible estructura en la zona, dejando en claro que falta información y estudio de esta fisura para poder caracterizarla completamente.

Es sabido que en la Zona Volcánica Sur el volcanismo tiene una íntima relación con la tectónica, pero el área de estudio, aparentemente, se encontraría en una zona carente de grandes estructuras mapeadas y alejada de la principal zona de falla como es la Liquiñe-Ofqui.

En cuanto a deformación neotectónica en la zona, se puede mencionar que la subducción de la dorsal de Chile bajo el continente ha generado diversas hipótesis con respecto a sus efectos en la corteza. En Scalabrino et al. (2010) se menciona una inversión tectónica, donde fallas inversas se reactivarían como fallas normales debido a un régimen extensional que a su vez generó colapsos localizados. Pero hay otros autores, como Stevens Goddard y Fosdick (2019), que a través de análisis termo-cronológicos proponen más bien un engrosamiento

cortical y un acortamiento. Independiente de la teoría que se considere como válida, se puede desprender que debido a la subducción de la dorsal de Chile se producen efectos importantes en la configuración tectónica de la zona que sobreyace.

Evidencia de actividad neotectónica en la zona y cercano al área de estudio, sería la zona de falla Exploradores, en el valle Exploradores al oeste del Lago General Carrera y al norte del Monte San Valentín, de cinemática inversa, que ha sido descrita por Georgieva et al. (2016) y datada con el uso de apatito en He por Persico (2021) resultando las edades más jóvenes en 1.5 a 2.4 Ma. Este último autor, también ha descrito la falla Bosque Muerto al oeste de la Villa Cerro Castillo, también de cinemática inversa. Ambas fallas de aparente actividad Cuaternaria darían cuenta que en la zona podría haber otro tipo de actividad tectónica similar y por esto lo interesante del estudio de la fisura encontrada en las intersecciones del río Ibáñez y Chiflón, que en este caso estaría facilitando el ascenso magmático y el emplazamiento de los centros eruptivos.

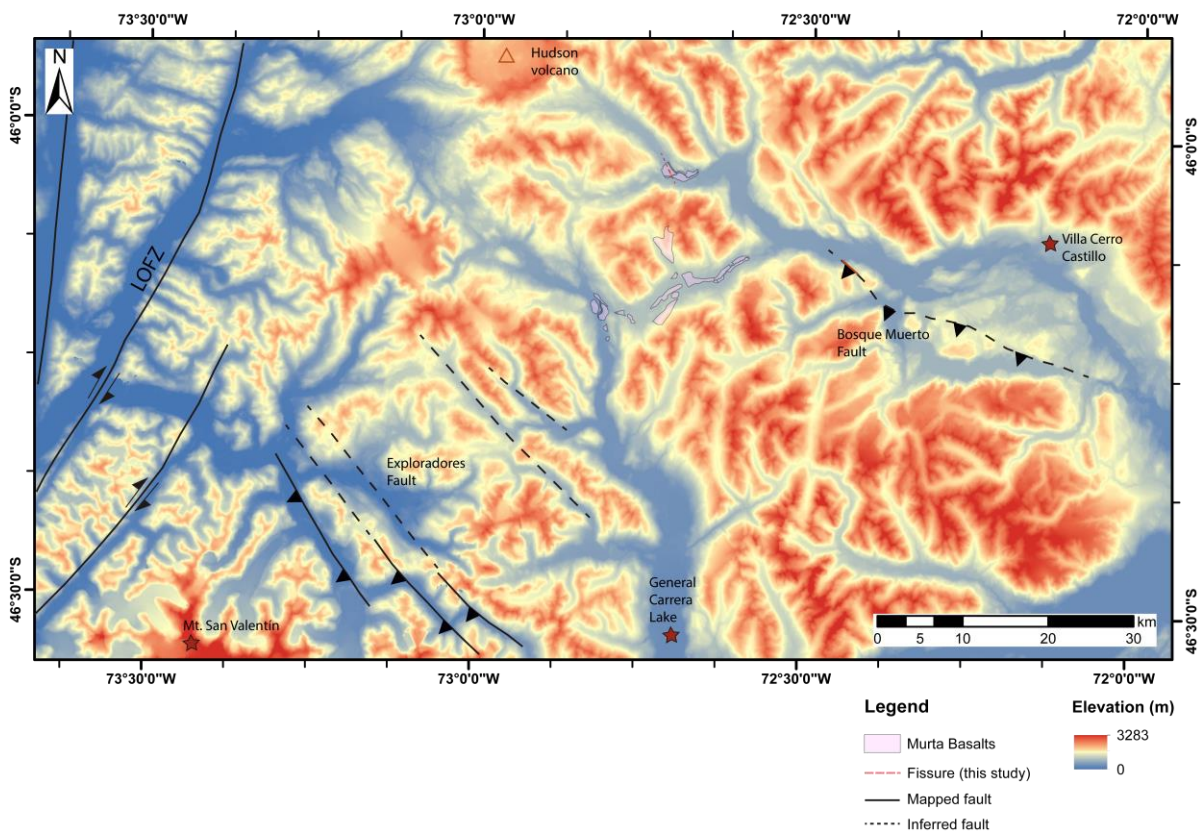


Fig. 42. Mapa topográfico con las principales estructuras descritas en el texto. Basaltos de Murta en polígonos rosados y fisura descrita en este estudio en línea punteada roja. Falla Exploradores de Georgieva et al. (2016) y Falla Bosque Muerto de Persico (2021). LOFZ de Cembrano y Lara (2009) y los autores citados en él. Algunas localidades importantes se marcan con estrellas rojas y el volcán Hudson con triángulo rojo. LOFZ: Zona de falla Liquiñe-Ofqui.

3.3. Importancia turística y peligro asociado

Finalmente, me gustaría notar la vulnerabilidad del área donde se encuentran ubicados los basaltos de Murta. No debemos olvidar la importancia del lugar en términos de conectividad y turismo, así como la presencia de pequeños centros eruptivos jóvenes, debido a su alta preservación, dentro del área. Es por esto que es importante mantener estas zonas estudiadas y monitoreadas. Más aún, la única carretera que conecta el sur de la Patagonia con el resto del país está ubicada muy cerca de algunos centros de emisión y, por lo mismo, el impacto de una erupción en localidades aisladas, turismo y acceso a parques nacionales sería altamente significativo.

4. CONCLUSIONES

Durante esta contribución se han podido cumplir los objetivos planteados en la introducción de esta tesis, llevando a cabo la metodología propuesta, con el propósito de comprobar o refutar la hipótesis planteada.

Los basaltos de Murta resultaron ser más complejos de lo que se suponía al comienzo. Se pensaba que correspondían a fluidos provenientes directamente del manto con muy leve aporte cortical en su evolución, siendo facilitado su ascenso por la generación de una ventana astenosférica bajo el continente producida por la subducción del *ridge* chileno conformado por la unión de las placas Nazca y Antártica.

Durante esta tesis se ha podido comprobar que los basaltos de Murta no provienen directamente de la fusión del manto, si no que han debido pasar por una serie de procesos de cristalización fraccionada y de asimilación para poder reconstruir todos los depósitos. Incluso, se han visto afectados por procesos de mezcla entre al menos dos fluidos bastante similares entre sí.

Si bien, no podemos negar que los basaltos de Murta se asocien a la ventana astenosférica por su ubicación geográfica, estos se encuentran en una zona conflictiva justo al borde norte de la delimitación de la actual apertura, lo que los hace ser susceptibles a la participación tanto de fluidos primitivos y más bien alcalinos, como también de una fuerte participación de fluidos derivados del slab propios de ambientes de subducción y que están relacionados al volcanismo de la zona volcánica sur.

Se propone como complemento a esta investigación la realización de mediciones en microsonda para una caracterización cuantitativa y exhaustiva de las fases minerales presentes, así como la realización de perfiles químicos en los cristales para determinar variaciones a escala microscópica y para el cálculo de tiempos de residencia, en particular en las plagioclasas de gran tamaño encontradas en las muestras.

Además, se propone volver a realizar dataciones a las muestras con métodos más actuales y confiables para poder ordenar, temporalmente, de mejor manera las muestras y respaldar el modelo evolutivo con fuentes certeras.

Y, por último, nuevas campañas de terreno son necesarias para trazar más detalladamente la continuidad y extensión de la traquita y para buscar los centros eruptivos responsables de los basaltos, que han sido propuestos por autores pero que no se han confirmado fehacientemente en terreno. Además, se ha dejado propuesto el estudio en detalle de la fisura encontrada en la intersección de los ríos Ibáñez y Chiflón y su vínculo con el volcanismo circundante. Y para ello, se propone el uso el uso local de herramientas geofísicas, como la magnetotelúrica para conocer el comportamiento de la corteza somera y la relación de esta posible estructura con el magmatismo de la zona.

BIBLIOGRAFÍA

- Andersen, D., & Lindsley, D. (1985). New (and final!) models for the Ti–magnetite/ilmenite geothermometer and oxygen barometer. *American Geophysical Union*, 66(18), 416.
- Anderson, A. (1968). Oxidation of the LaBlache Lake titaniferous magnetite deposit, Quebec. *The Journal of Geology*, 76(5), 528-547. doi: 10.1086/627358
- Bacon, C., & Hirschmann, M. (1988). Mg/Mn partitioning as a test for equilibrium between Fe-Ti oxides. *American Mineralogist*, 73(1-2), 57-61.
- Bangs, N., Cande, S., Lewis, S., & Miller, J. (1992). Structural framework of the Chile margin at the Chile Ridge Collision Zone. *Proceedings of the Ocean Drilling Program*, 141 Initial Reports. doi: 10.2973/odp.proc.ir.141.102.1992
- Buddington, A., & Lindsley, D. (1964). Iron-Titanium Oxide Minerals and Synthetic Equivalents. *Journal Of Petrology*, 5(2), 310-357. doi: 10.1093/petrology/5.2.310
- Carmichael, I. (1967). The iron–titanium oxides of salic volcanic rocks and their associated ferromagnesian silicates. *Contributions to Mineralogy and Petrology*, 14(1), 36-64. doi: 10.1007/BF00370985
- Cembrano, J., & Lara, L. (2009). The link between volcanism and tectonics in the Southern Volcanic Zone of the Chilean Andes: A Review. *Tectonophysics*, 471(1-2), 96-113. doi:10.1016/j.tecto.2009.02.038
- Demant, A., Hervé, F., Pankhurst, R. J., & Magnette, B. (1994). Alkaline and calc-alkaline Holocene basalts from minor volcanic centres in the Andes of Aysén, Southern Chile. VII Congreso Geológico Chileno, Concepción, Actas vol. II, 1326-1330
- Demant, A., Belmar, M., Hervé, F., Pankhurst, R. J., & Suárez, M. (1998). Pétrologie et géochimie des basaltes de Murta: une éruption sousglaciaire dans les Andes patagoniennes (468 lat. S.). Relation avec la subduction de la ride du Chili. *Earth and Planetary Science*, 327(12), 795-801. doi: 10.1016/S1251-8050(99)80053-6
- Dickinson, W. R., & Snyder, W. S. (1979). Geometry of subducted slabs related to San Andreas Transform. *The Journal of Geology*, 87(6), 609-627. doi: 10.1086/628456

Georgieva, V., Melnick, D., Schildgen, T. F., Ehlers, T. A., Lagabrielle, Y., Enkelmann, E., & Strecker, M. R. (2016). Tectonic control on rock uplift, exhumation, and topography above an oceanic ridge collision: Southern Patagonian Andes (47°S), Chile. *Tectonics*, 35(6), 1317-1341. doi:10.1002/2016tc004120

Gorring, M. L., Kay, S. M., Zeitler, P. K., Ramos, V. A., Rubiolo, D., Fernandez, M. L., & Panza, J. L. (1997). Neogene Patagonian plateau lavas: continental magmas associated with ridge collision at the Chile triple junction. *Tectonics*, 16(1), 1-17. doi: 10.1029/96TC03368

Guivel, C., Morata, D., Pelleter, E., Espinoza, F., Maury, R., Lagabrielle, Y., Polvé, M., Bellon, H., Cotten, J., Benoit, M., Suárez, M., & De la Cruz, R. (2006). Miocene to Late Quaternary Patagonian basalts (46–47°S): Geochronometric and geochemical evidence for slab tearing due to active spreading ridge subduction. *Journal Of Volcanology And Geothermal Research*, 149(3-4), 346-370. doi: 10.1016/j.jvolgeores.2005.09.002

Gutiérrez, F., Gioncada, A., González Ferran, O., Lahsen, A., & Mazzuoli, R. (2005). The Hudson Volcano and surrounding monogenetic centres (Chilean Patagonia): An example of volcanism associated with ridge–trench collision environment. *Journal Of Volcanology And Geothermal Research*, 145(3-4), 207-233. doi: 10.1016/j.jvolgeores.2005.01.014

Haggerty, S. (1991). Oxide Textures - A Mini-Atlas. In: Lindsley, D. H. (ed.) Oxide minerals: petrologic and magnetite significance. *Review in Mineralogy*, 25, 129-219.

Hole, M. J., Rogers, G., Saunders, A. D., & Storey, M. (1991). Relation between alkalic volcanism and slab-window formation. *Geology*, 19, 657-660. doi: 10.1130/0091-7613(1991)019<0657:RBAVAS>2.3.CO;2

Hou, T., Botcharnikov, R., Moulas, E., Just, T., Berndt, J., Koepke, J., Zhang, Z., Wang, M., Yang, Z., & Holtz, F. (2020). Kinetics of Fe–Ti Oxide Re-equilibration in Magmatic Systems: Implications for Thermo-oxybarometry. *Journal of Petrology*, 61(11-12), 1-24. doi: 10.1093/petrology/egaa116

Kratzmann, D. J., Carey, S., Scasso, R. A., & Naranjo, J. A. (2010). Role of cryptic amphibole crystallization in magma differentiation at Hudson volcano, Southern Volcanic Zone, Chile. *Contribution to Mineralogy and Petrology*, 159, 237-264. doi: 10.1007/s00410-009-0426-1

- Lindsley, D., & Spencer, K. (1982). Fe–Ti oxide geothermometry: Reducing analyses of coexisting Ti-magnetite (Mt) and ilmenite (Ilm). *Trans Amer Geophys Un (EOS)*, 63, 471.
- Murdie, R. E., & Russo, R. M. (1999). Seismic anisotropy in the region of the Chile margin triple junction. *Journal of South American Earth Sciences*, 12(3), 261-270. doi: 10.1016/S0895-9811(99)00018-8
- Pankhurst, R. J., Weaver, S. D., Hervé, F., & Larrondo, P. (1999). Mesozoic-Cenozoic evolution of the North Patagonian Batholith in Aysen, southern Chile. *Journal of the Geological Society*, 156(4), 673-694. doi: 10.1144/gsjgs.156.4.0673
- Persico Blanco, M. (2021). Neotectonics and crustal fault characterization in the Aysén Region (~44°-47°S), Northern Patagonian Andes, Chile. [Unpublished]. University of Chile.
- Powell, R., & Powell, M. (1977). Geothermometry and oxygen barometry using coexisting iron–titanium oxides: a reappraisal. *Mineralogical Magazine*, 41, 257-263. doi: 10.1180/minmag.1977.041.318.14
- Quiroz, D., & Belmar, M. (2010). Geología del Área Bahía Murta-Cerro Sin Nombre, Región Aisén del General Carlos Ibáñez del Campo. Servicio Nacional de Geología y Minería, Carta Geológica de Chile, Serie Geología Básica 125: 36 p., 1 mapa escala 1: 100.000.
- Russo, R., VanDecar, J., Comte, D., Mocanu, V., Gallego, A., & Murdie, R. (2010). Subduction of the Chile Ridge: Upper mantle structure and flow. *GSA Today*, 20(9), 4-10. doi: 10.1130/gsatg61a.1
- Scalabrino, B., Lagabriele, Y., Malavieille, J., Dominguez, S., Melnick, D., Espinoza, F., Suárez, M., & Rossello, E. (2010). A morphotectonic analysis of central Patagonian Cordillera: Negative inversion of the Andean belt over a buried spreading center? *Tectonics*, 29(2). doi:10.1029/2009tc002453
- Scalabrino, B., Lagabriele, Y., Rupelle, A., Malavieille, J., Polvé, M., Espinoza, F., Morata D., & Suárez, M. (2009). Subduction of an Active Spreading Ridge Beneath Southern South America: A Review of the Cenozoic Geological Records from the Andean Foreland, Central Patagonia (46–47°S). *Subduction Zone Geodynamics*, 227-246. doi: 10.1007/978-3-540-87974-9_12

- Spencer, K., & Lindsley, D. (1981). A solution model for coexisting iron–titanium oxides. *American Mineralogist*, 66, 1189-1201.
- Stevens Goddard, A. L., & Fosdick, J. C. (2019). Multichronometer thermochronologic modeling of migrating spreading ridge subduction in southern Patagonia. *Geology*, 47(6), 555-558. doi:10.1130/g46091.1
- Stormer, J. (1983). The effects of recalculation on estimates of temperature and oxygen fugacity from analyses of multicomponent–iron–titanium oxides. *American Mineralogist*, 68, 586-594.
- Thomson, S. F., Hervé, F., & Stockhert, B. (2001). Mesozoic–Cenozoic denudation history of the Patagonian Andes (southern Chile) and its correlation to different subduction processes. *Tectonics*, 20, 693-711. doi: 10.1029/2001TC900013
- Thorkelson, D., Madsen, J., & Sluggett, C. (2011). Mantle flow through the Northern Cordilleran slab window revealed by volcanic geochemistry. *Geology*, 39(3), 267-270. doi: 10.1130/g31522.1
- Thorkelson, D. J., & Breitsprecher, K. (2005). Partial melting of slab window margins: Genesis of adakitic and non-adakitic magmas. *Lithos*, 79, 25-41. doi: 10.1016/j.lithos.2004.04.049
- Thorkelson, D. J. (1996). Subduction of diverging plates and the principles of slab window formation. *Tectonophysics*, 255(1-2), 47-63. doi: 10.1016/0040-1951(95)00106-9
- Thorkelson, D. J., & Taylor, R. P. (1989). Cordilleran slab windows. *Geology*, 17(9), 833. doi:10.1130/0091-7613(1989)0172.3.co;2
- Yavuz, F. (2021). WinMIgob: A Windows program for magnetite-ilmenite geothermometer and oxygen barometer. *Journal Of Geosciences*, 66(1), 51-70. doi: 10.3190/jgeosci.319

ANNEXES

Annex A

A.1 Trabajo de terreno

El trabajo de terreno se realizó en 2 etapas. La primera campaña se realizó entre los días 2 y 6 de diciembre del 2019 y la segunda entre los días 23 y 26 de febrero del 2020. En las Table 6 y Table 7 adjuntas se indican las paradas realizadas, junto con las muestras y fotos tomadas.

Day	Time	Control Point	Lat. °S	Long. °W	Sample	Photos
02-12-2019	19:40	1	46°08'58,8"	72°37'34,7"	JV021219-1(D)	F101-2429/2431
03-12-2019	12:15	1	46°02'51,7"	72°42'28,6"	JV031219-1(D)	J100-4171/4180
03-12-2019	13:35	2	46°02'49,1"	72°42'15,9"	JV031219-2A	J100-4183/4184
03-12-2019	13:35	2	46°02'49,1"	72°42'15,9"	JV031219-2B	J100-4194
03-12-2019	13:35	2	46°02'49,1"	72°42'15,9"	JV031219-2C	J100-4195
03-12-2019	16:31	3	46°08'31,5"	72°37'3,1"	JV031219-3(D)	J100-4202/4210
03-12-2019	18:36	4	46°09'51"	72°41'14,9"	JV031219-4(D)	J100-4222/4225
05-12-2019	11:15	1	46°13'0,3"	72°48'25,4"	JV051219-1(D)	J100-4262/4280
05-12-2019	12:21	2	46°12'29,8"	72°48'16,8"	JV051219-2(D)	J100-4288/4297
05-12-2019	12:58	3	46°12'22,2"	72°48'23,7"	JV051219-3(D)	J100-4301/4316
05-12-2019	13:30	4	46°11'27,6"	72°48'10,1"	N/A	J100-4317/4325
05-12-2019	14:22	5	46°09'16,8"	72°41'50,3"	N/A	N/A
05-12-2019	15:12	6	46°09'18,8"	72°41'45"	N/A	N/A
05-12-2019	16:39	7	46°08'4,4"	72°36'14,6"	JV051219-7(D)	J100-4331/4341
05-12-2019	17:01	8	46°08'4,9"	72°36'18,6"	JV051219-8(D)	J100-4342/4347

Table 6. Detalles de las paradas realizadas durante la primera campaña de terreno a Bahía Murta.

Day	Time	Control Point	Lat. °S	Long. °W	Sample	Photos
23-02-2020	16:00	1a	46°02'49,7"	72°42'15,5"	JV230220-1 (+BOLON)	J100-4547/4553
23-02-2020	16:30	1b	46°02'48,6"	72°42'19,2"	N/A	J100-4554/4564
23-02-2020	17:45	2	46°02'39,4"	72°42'29,2"	JV230220-2	J100-4567/4573
24-02-2020	N/A	1	46°02'38,8"	72°42'28,1"	N/A	N/A
24-02-2020	N/A	2	46°02'40,2"	72°42'24,3"	JV240220-2	J100-4599/4612
24-02-2020	N/A	3	46°02'40,2"	72°42'20,7"	JV240220-3	J100-4613/4615
24-02-2020	N/A	4a	46°02'28,5"	72°42'55,3"	N/A	J100-4632/4636
24-02-2020	N/A	4b	46°02'31,5"	72°42'59,4"	N/A	J100-4637/4642
24-02-2020	N/A	4c	46°02'33,7"	72°42'58,7"	N/A	N/A
25-02-2020	N/A	1	46°05'05,6"	72°35'05,7"	JV250220-1	J100-4643/4652
25-02-2020	N/A	2	46°02'47,5"	72°42'48,7"	N/A	J100-4653/4654
25-02-2020	N/A	3	46°02'46,9"	72°42'45,6"	N/A	J100-4655/4656
25-02-2020	N/A	4	46°02'44,7"	72°42'46,3"	N/A	N/A
25-02-2020	N/A	5	46°02'40,9"	72°42'51,4"	N/A	N/A
25-02-2020	N/A	6	46°02'51"	72°42'28,9"	JV250220-6/6B/6C/6D/6E/6F	J100-4659/4668

Table 7. Detalles de las paradas realizadas durante la primera campaña de terreno a Río Ibáñez-Chiflón.

Annex B

B.1 Descripción de cortes transparentes

▪ Corte 021219-1

Mineralogía primaria

Mineral	%	Forma	Estructuralidad	Integridad	Tamaño
Fenocristales [10%]					
Olivino	33	granular	anhedral-subhedral	media-alta	0.4 mm-1.6 mm
Plagioclasa	63	tabular	subhedral-euhedral	media-alta	0.4 mm-7.5 mm
Clinopiroxeno	4	granular alargado	anhedral	media-alta	0.4 mm-0.5 mm
Masa fundamental [90%]					
Plagioclasas	-	tabular	euhedral	alta	<0.4 mm
Olivino	-	granular	anhedral	alta	<0.4 mm
Óxidos de Fe	-	-	-	-	<0.4 mm
Piroxenos	-	granular	anhedral	alta	<0.4 mm

Texturas

Textura	Descripción y minerales involucrados
Pilotaxítica	Plagioclasas orientadas
Cumuloporfídica	Cúmulos de plagioclasa con olivino
Porfídica	Fenocristales de plagioclasa, olivino y piroxeno en masa fundamental
Vesicular	Pequeñas vesículas y poco abundantes
Sieve	Inclusiones vítreas dentro de plagioclasa u oquedades
Zonación	En plagioclasa difusa

Clasificación QAP Andesita/Basalto

Nombre de la roca Basalto de olivino

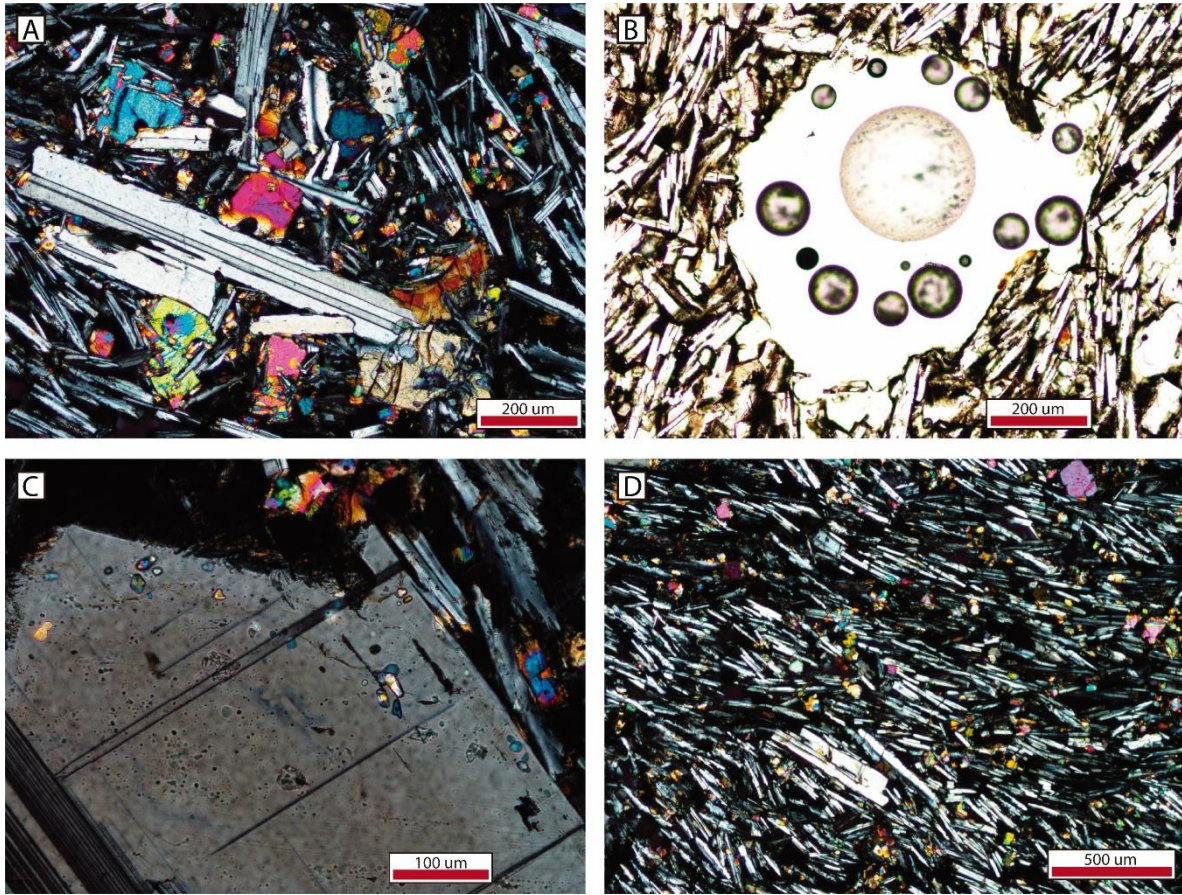


Fig. 43. Principales texturas observadas. (A) NX cúmulo de plagioclasas con olivinos, (B) NP vesícula, (C) NX plagioclasa con zonación difusa y (D) NX plagioclasas orientadas en masa fundamental.

▪ **Corte 031219-1**

Mineralogía primaria

Mineral	%	Forma	Estructuralidad	Integridad	Tamaño
Fenocristales [12%]					
Plagioclasa	72	tabular	subhedral-euhedral	media-baja (algunas rellenas de MF)	0.4-2.2 mm
Olivino	25	granular-prismático	subhedral-anhedral	media-alta	0.4-2.1 mm

Clinopiroxeno	3	granular alargado	anhedral- subhedral	alta	0.4 mm
Masa fundamental [88%]					
Plagioclasa	-	tabular	euhedral	alta	<0.4 mm
Olivino	-	granular	anhedral	alta	<0.4 mm
Óxidos de Fe	-	-	-	-	<0.4 mm
Piroxeno		granular	anhedral	alta	<0.4 mm

Texturas

Textura	Descripción y minerales involucrados
Porfídica	Fenocristales de olivino, plagioclasa y piroxeno en masa fundamental
Cumuloporfídica	Cúmulos de plagioclasa con olivino
Intergranular	Masa fundamental con cristales de plagioclasa aleatorios con cristales entre ellos
Sieve	Plagioclasas con abundantes inclusiones vítreas
Vesicular	Pequeñas vesículas y poco abundantes
Zonación	Escasa y poco notoria

Clasificación QAP Basalto/Andesita

Nombre de la roca Basalto de olivino

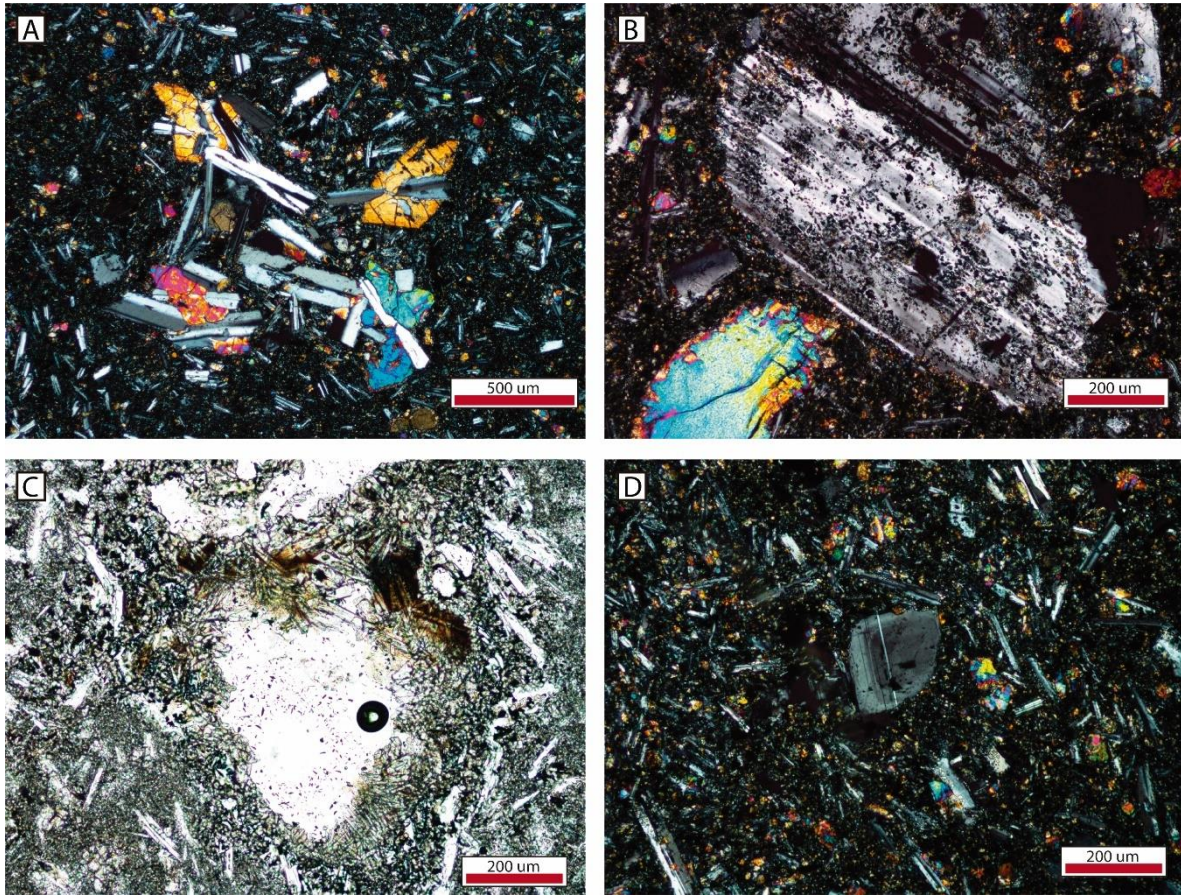


Fig. 44. Principales texturas observadas. (A) NX cúmulo de plagioclasas con olivinos, (B) NX abundancia de inclusiones en plagioclasa, (C) NP vesícula con crecimiento cristalino en sus paredes y (D) NX plagioclasa con zonación.

▪ **Corte 031219-2A**

Mineralogía primaria

Mineral	%	Forma	Estructuralidad	Integridad	Tamaño
Fenocristales [15%]					
Plagioclasa	54	tabular	euhedral	media-alta	0.4 mm-2 mm
Olivino	31	granular y prismático	anhedral-subhedral	media-baja	0.4 mm-1.2 mm
Clinopiroxeno	15	granular y alargado	anhedral-subhedral	media-alta	<0.5 mm
Masa fundamental [85%]					

Plagioclasa	-	tabular	euهدral	media-alta	<0.4 mm
Piroxeno	-	granular	anhedral	media-alta	<0.4 mm
Óxidos de Fe	-	-	-	-	<0.4 mm
Olivino	-	granular	anhedral	media-alta	<0.4 mm

Mineralogía secundaria

Mineral	Mineral y/o zona en que se encuentra
Iddingsita	En olivino

Texturas

Textura	Descripción y minerales involucrados
Vesicular	Abundantes vesículas irregulares (32%)
Intergranular	Plagioclasas no orientadas con cristales entre ellas
Porfídica	Fenocristales de plagioclasa, olivino y piroxeno en masa fundamental con abundante piroxeno
Cumuloporfídica	Cúmulo de plagioclasas con olivino
Glomeroporfídica	Cúmulo de olivinos
Subofítica	Plagioclasas encerradas parcialmente por piroxeno
Sieve	Inclusiones vítreas dentro de plagioclasas

Clasificación QAP Andesita/Basalto

Nombre de la roca Basalto de olivino

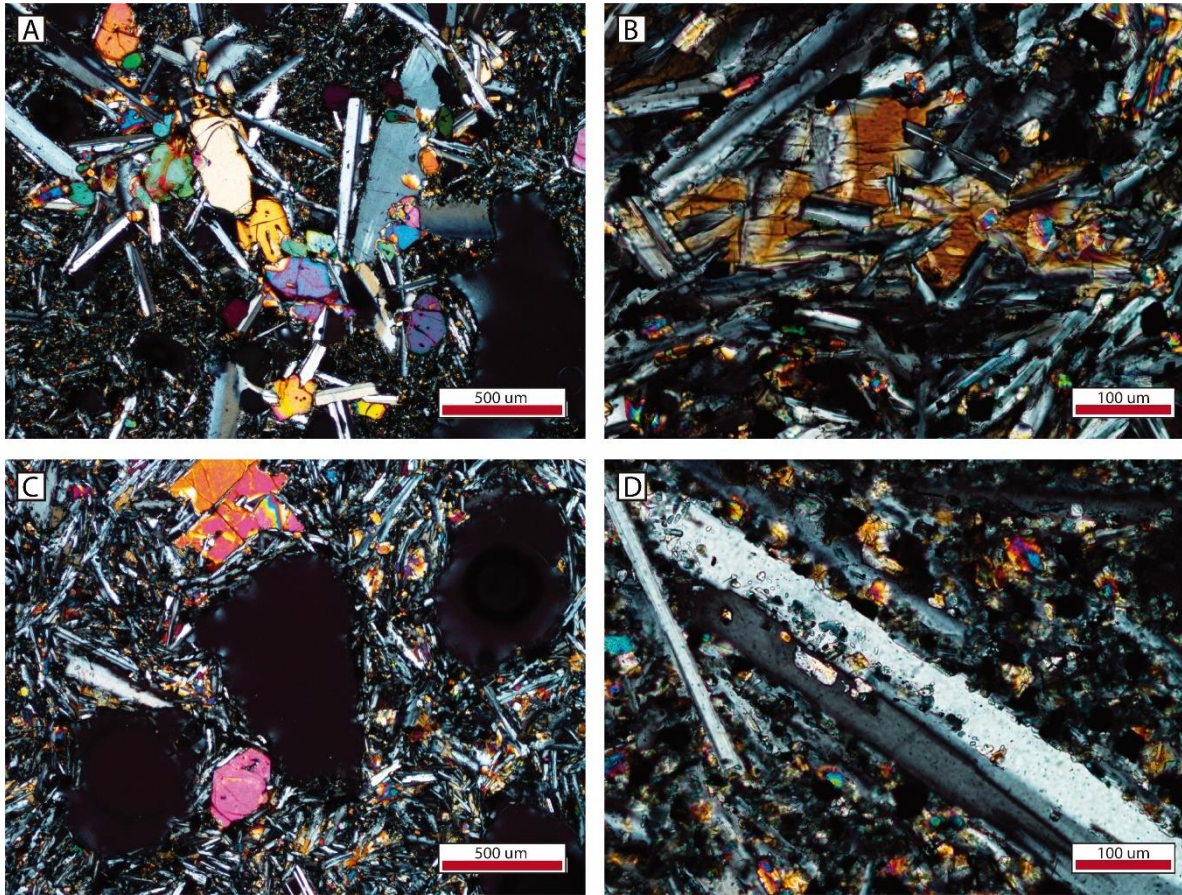


Fig. 45. Principales texturas observadas. (A) NX cúmulo de plagioclasas con olivinos, (B) NX plagioclasas encerradas parcialmente por piroxenos, (C) NX vesículas y (D) NX plagioclasa con inclusiones.

▪ Corte 031219-3

Mineralogía primaria

Mineral	%	Forma	Estructuralidad	Integridad	Tamaño
Fenocristales [24%]					
Plagioclasa	36	tabular	euhedral	media-baja	0.4 mm-2 mm
Olivino	8	granular y prismático	anhedral-subhedral	media-baja	0.4 mm-1.2 mm
Clinopiroxeno	56	granular y alargado	anhedral-subhedral	media	0.4 mm-2.3 mm
Masa fundamental [76%]					

Plagioclasa	-	tabular	euهدral	media	<0.4 mm
Piroxeno	-	granular	anhedral	media-alta	<0.4 mm
Olivino	-	granular	anhedral	media-alta	<0.4 mm
Óxido de Fe	-	-	-	-	<0.4 mm

Texturas

Textura	Descripción y minerales involucrados
Subofítica	Plagioclasa parcialmente rodeada de piroxeno
Sieve	En plagioclasas inclusiones vítreas
Porfídica	Plagioclasa, olivino y piroxeno en masa fundamental
Parche	Variaciones composicionales en plagioclasa
Cumuloporfídica	Cúmulos de plagioclasa con olivino
Vesicular	Poco abundantes y pequeñas
Pilotaxítica	Leve orientación plagioclasas
Poikilítica	Cristales de plagioclasa encerrando a unos más pequeños de piroxeno u olivino
Zonación	Poco marcada en plagioclasa

Clasificación QAP Andesita/Basalto

Nombre de la roca Basalto de olivino

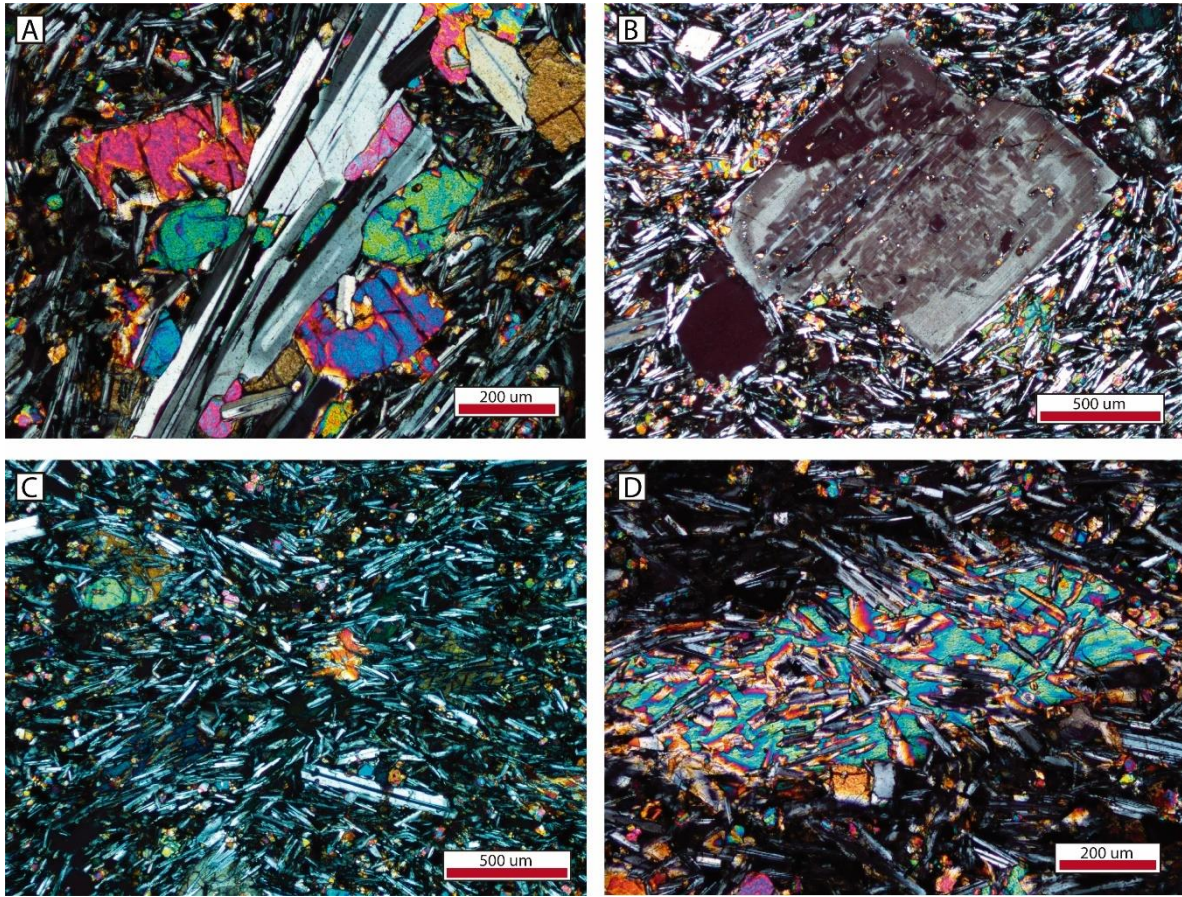


Fig. 46. Principales texturas observadas. (A) NX cúmulo de plagioclasas con olivinos, (B) NX plagioclasa con variación composicional e inclusiones, (C) NX leve orientación de plagioclasas en masa fundamental y (D) NX plagioclasas encerradas parcial o totalmente por piroxenos.

▪ **Corte 031219-4**

Mineralogía primaria

Mineral	%	Forma	Estructuralidad	Integridad	Tamaño
Fenocristales [9%]					
Feldespatos	86	tabular	euedral	alta	0.3-9 mm
Ortopiroxeno	14	granular	anhedral	alta	0.3-3.3 mm
Masa fundamental [91%]					
Feldespatos	-	tabular	euedral	alta	<0.3 mm
Piroxenos	-	granular	anhedral	alta	<0.3 mm
Óxidos de Fe	-	-	-	-	<0.3 mm

Texturas

Textura	Descripción y minerales involucrados
Vesicular	Vesículas abundantes redondeadas rellenas de mineral secundario (9%)
Intergranular	Solo cristales de feldspatos y piroxenos en la masa fundamental
Sieve	Inclusiones u oquedades en plagioclasas

Clasificación QAP Basalto/traquita

Nombre de la roca Basalto/traquita

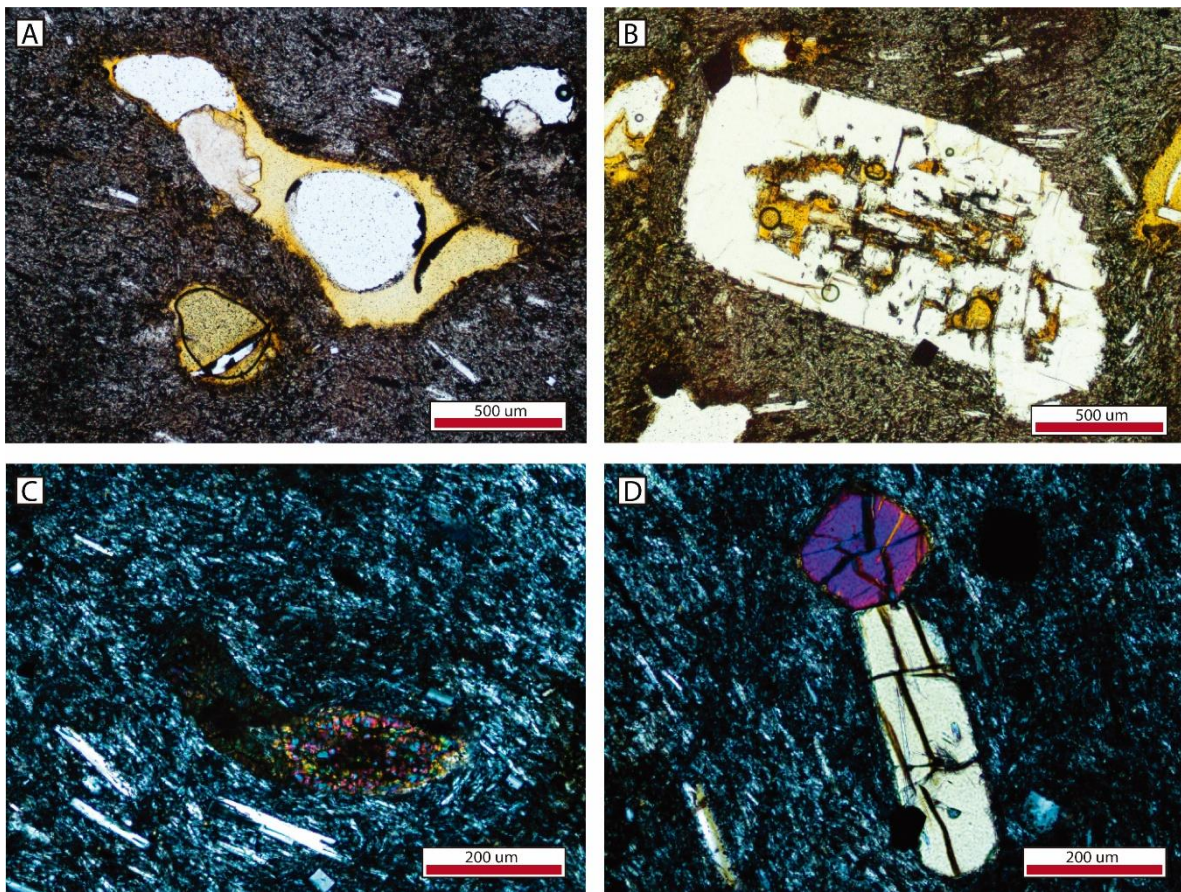


Fig. 47. Principales texturas observadas. (A) NP vesículas con crecimiento secundario, (B) NP inclusiones y oquedades en plagioclasas, (C) NX cúmulo de piroxenos microcristalino y (D) NX fenocristales de piroxenos observados.

▪ **Corte 051219-1**

Mineralogía primaria

Mineral	%	Forma	Estructuralidad	Integridad	Tamaño
Fenocristales [32%]					
Plagioclasa	68	tabular	euهدral	alta	0.4-11.8 mm
Olivino	23	granular	anhedral	alta	0.4-1.6 mm
Clinopiroxeno	9	radial alargado	euهدral	alta	0.4-1.3 mm
Masa fundamental [68%]					
Plagioclasas	-	tabular	euهدral	alta	<0.4mm
Piroxeno	-	granular	anhedral	alta	<0.4 mm
Olivino	-	granular	anhedral	alta	<0.4mm
Óxidos de Fe	-	-	-	-	<0.4mm

Texturas

Textura	Descripción y minerales involucrados
Intergranular	Masa fundamental de plagioclasas aleatorias con cristales en medio
Sieve	Inclusiones vítreas en plagioclasas
Vesicular	Vesículas pequeñas y poco abundantes
Poikilítica	Plagioclasas con inclusiones cristalinas
Cúmulo porfídica	Cúmulos de plagioclasa con olivino
Zonación	Poco marcada en plagioclasa

Clasificación QAP Basalto/Andesita

Nombre de la roca Basalto de olivino

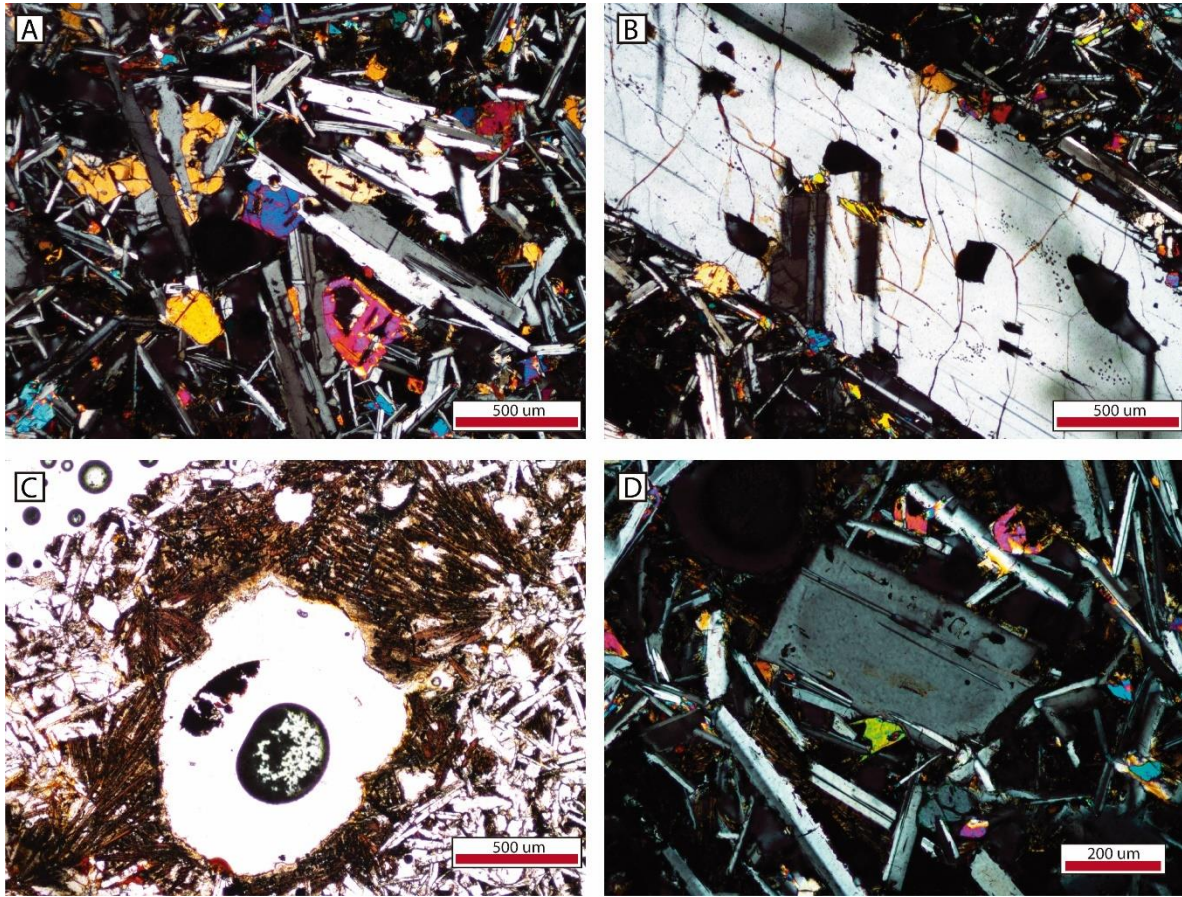


Fig. 48. Principales texturas observadas. (A) NX cúmulo de plagioclasas con olivinos, (B) NX abundancia de inclusiones y oquedades en plagioclase, (C) NP vesícula con crecimiento de piroxenos aciculares en borde y (D) NX plagioclase con zonación.

▪ Corte 051219-2

Mineralogía primaria

Mineral	%	Forma	Estructuralidad	Integridad	Tamaño
Fenocristales [30%]					
Plagioclase	74	tabular	euhedral	media-alta	0.3-8.8 mm
Clinopiroxeno	16	alargado-granular	anhedral-subhedral	alta	0.3-3.6 mm
Olivino	10	granular	anhedral	alta	0.3-1.5 mm
Masa fundamental [70%]					
Plagioclase	-	tabular	euhedral	alta	<0.2 mm

Olivino	-	granular	anhedral	alta	<0.2 mm
Piroxeno	-	granular	anhedral	alta	<0.2 mm
Óxidos de Fe	-	-	-	-	<0.1 mm

Mineralogía secundaria

Mineral	Mineral y/o zona en que se encuentra
Desconocido	En tonos rosados relleno de posibles vesículas

Texturas

Textura	Descripción y minerales involucrados
Intergranular	Masa fundamental de plagioclasas aleatorias con cristales en medio
Vesicular	Vesículas pequeñas y poco abundantes
Poikilítica	Inclusiones cristalinas en plagioclasa
Sieve	Inclusiones vítreas en plagioclasa
Zonación	Irregular, no sigue los bordes rectos

Clasificación QAP Basalto/Andesita

Nombre de la roca Basalto de olivino

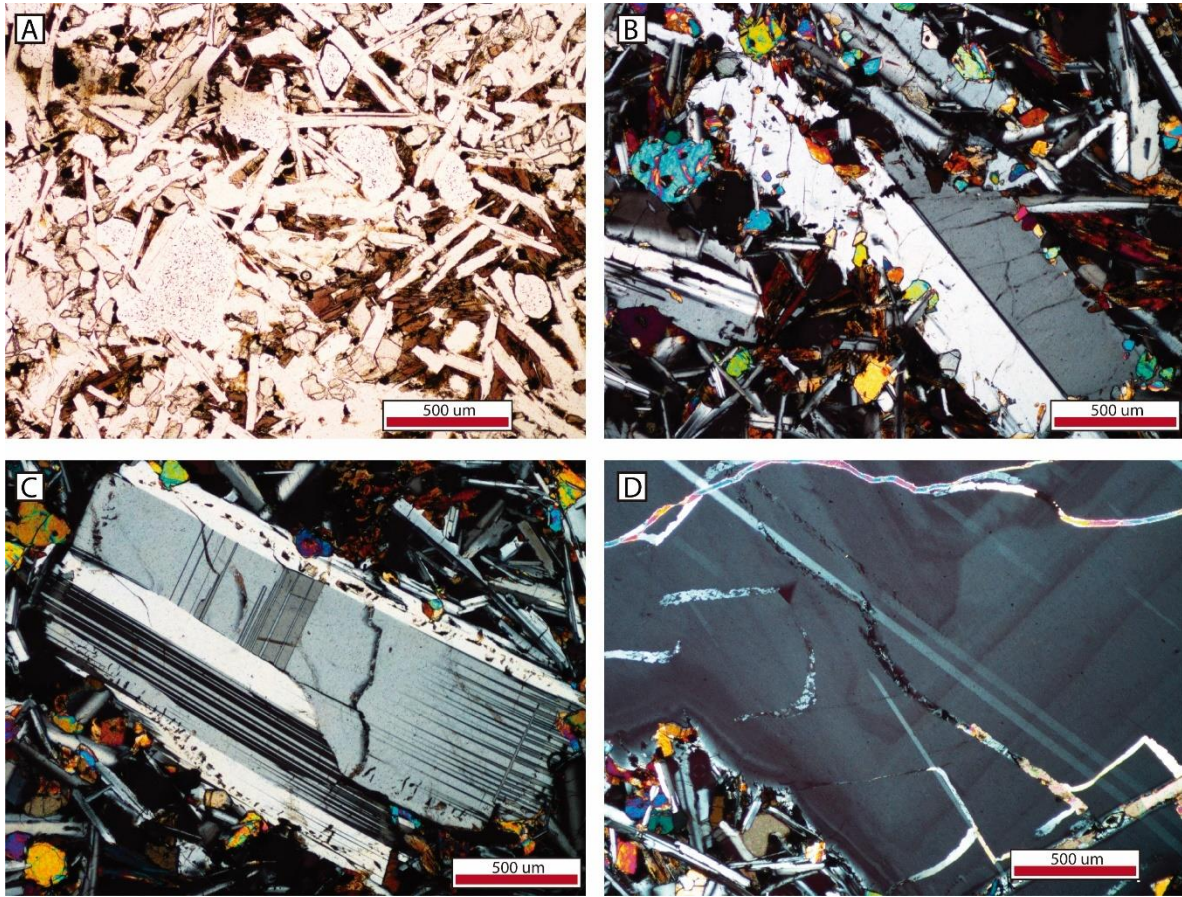


Fig. 49. Principales texturas observadas. (A) NP pequeñas vesículas, (B) NX abundancia de inclusiones cristalinas en plagioclasa, (C) NX inclusiones vítreas en borde plagioclasa y (D) NX plagioclasa con zonación.

▪ **Corte 051219-3**

Mineralogía primaria

Mineral	%	Forma	Estructuralidad	Integridad	Tamaño
Fenocristales [20%]					
Plagioclasa	60	tabular	subhedral-euhedral	media-alta	0.3-4.7 mm
Olivino	28	granular y prismático	anhedral-subhedral	alta	0.3-5 mm
Clinopiroxeno	12	radial alargado	euhedral	alta	<1 mm
Masa fundamental [80%]					

Plagioclasa	-	tabular	euهدral	alta	<0.2 mm
Piroxeno	-	granular	anhedral	alta	<0.2 mm
Olivino	-	granular	anhedral	alta	<0.2 mm
Óxidos de Fe	-	-	-	-	<0.2 mm

Mineralogía secundaria

Mineral	Mineral y/o zona en que se encuentra
Zeolitas	En algunas vesículas

Texturas

Textura	Descripción y minerales involucrados
Vesicular	Grandes vesículas y abundantes (12%)
Cúmulo porfídica	Cúmulos de plagioclasas con olivino
Sieve	Plagioclasas con inclusiones vítreas
Intergranular	Masa fundamental con plagioclasas y cristales entre medio
Zonación	En plagioclasas, pero no tan marcadas

Clasificación QAP Basalto/Andesita

Nombre de la roca Basalto de olivino

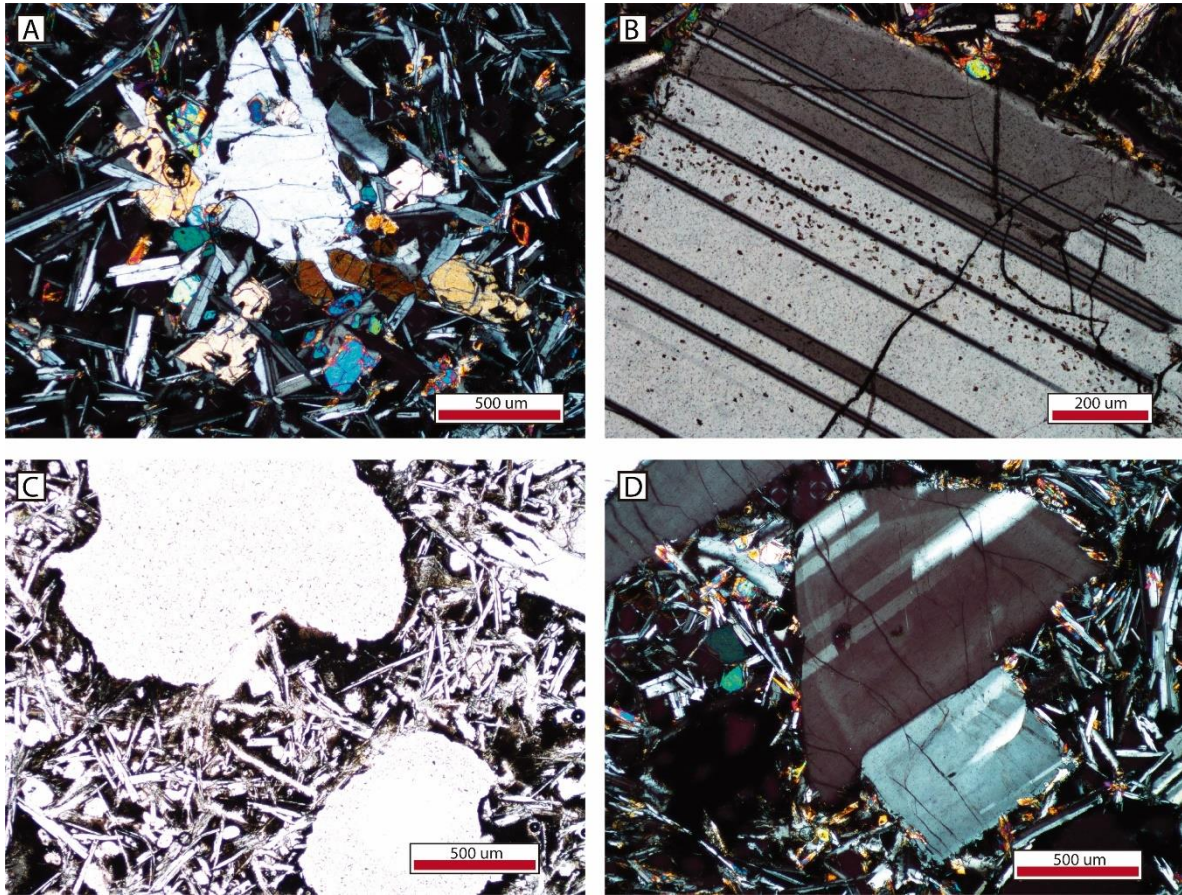


Fig. 50. Principales texturas observadas. (A) NX cúmulo de plagioclasas con olivinos, (B) NX abundancia de inclusiones en plagioclasa, (C) NP vesícula con óxidos en sus paredes y (D) NX plagioclasa con zonación.

▪ **Corte 051219-7**

Mineralogía primaria

Mineral	%	Forma	Estructuralidad	Integridad	Tamaño
Fenocristales [17%]					
Plagioclasa	62	tabular	subhedral-euhedral	media-baja (algunas rellenas de MF)	0.2-5.1 mm
Olivino	35	granular y prismático	anhedral-subhedral	alta	0.2-3.1 mm
Clinopiroxeno	3	granular y alargado	anhedral-subhedral	alta	0.2-0.4 mm

Masa fundamental [83%]					
Plagioclasa	-	tabular	euhedral	alta	<0.2 mm
Olivino	-	granular	anhedral	alta	<0.2 mm
Piroxeno	-	granular	anhedral	alta	<0.2 mm
Óxidos de Fe	-	-	-	-	

Texturas

Textura	Descripción y minerales involucrados
Sieve	En olivino y plagioclasas
Cúmulo porfídica	Cúmulos de plagioclasas con olivino
Poikilítica	Plagioclasas con cristales al interior
Intergranular	Masa fundamental con plagioclasas y cristales de piroxeno y olivino entre medio
Vesicular	Poco abundantes
Parche	Variación composicional dentro de plagioclasa
Zonación	No son tan notorias en plagioclasas

Clasificación QAP Basalto/Andesita

Nombre de la roca Basalto de olivino

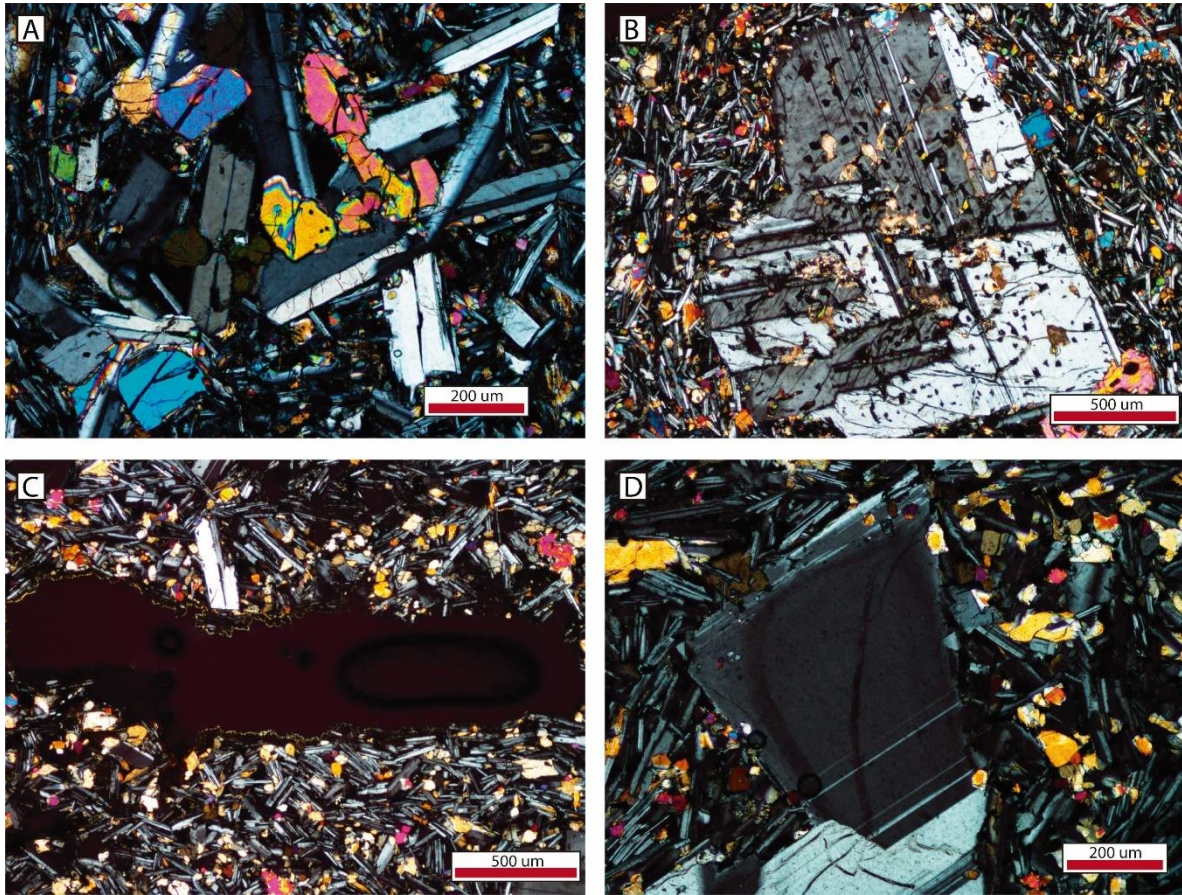


Fig. 51. Principales texturas observadas. (A) NX cúmulo de plagioclasas con olivinos, (B) NX abundancia de inclusiones en plagioclasa y variación composicional, (C) NX vesícula y (D) NX plagioclasa con zonación.

▪ **Corte 051219-8**

Mineralogía primaria

Mineral	%	Forma	Estructuralidad	Integridad	Tamaño
Fenocristales [19%]					
Plagioclasa	70	tabular	subhedral-euhedral	media-baja (re llenas con MF)	0.2-4.2 mm
Olivino	27	granular y prismático	anhedral-subhedral	alta	0.2-1.7 mm
Clinopiroxeno	3	granular y alargado	anhedral-subhedral	alta	0.2-0.5 mm
Masa fundamental [81%]					

Plagioclasa	-	tabular	euedral	alta	<0.2 mm
Olivino	-	granular	anhedral	alta	<0.2 mm
Piroxeno	-	granular	anhedral	alta	<0.2 mm
Óxidos de Fe	-	-	-	-	<0.2 mm

Texturas

Textura	Descripción y minerales involucrados
Poikilítica	Cristales dentro de plagioclasas
Sieve	Inclusiones vítreas en plagioclasas u oquedades
Intergranular	Masa fundamental con plagioclasas aleatorias y cristales de piroxeno y olivino entre medio
Cúmulo porfídica	Cúmulos cristalinos de plagioclasas con olivino
Parche	Variaciones composicionales dentro de plagioclasa irregulares
Zonación	Zonación difusa en plagioclasas

Clasificación QAP Basalto/Andesita

Nombre de la roca Basalto de olivino

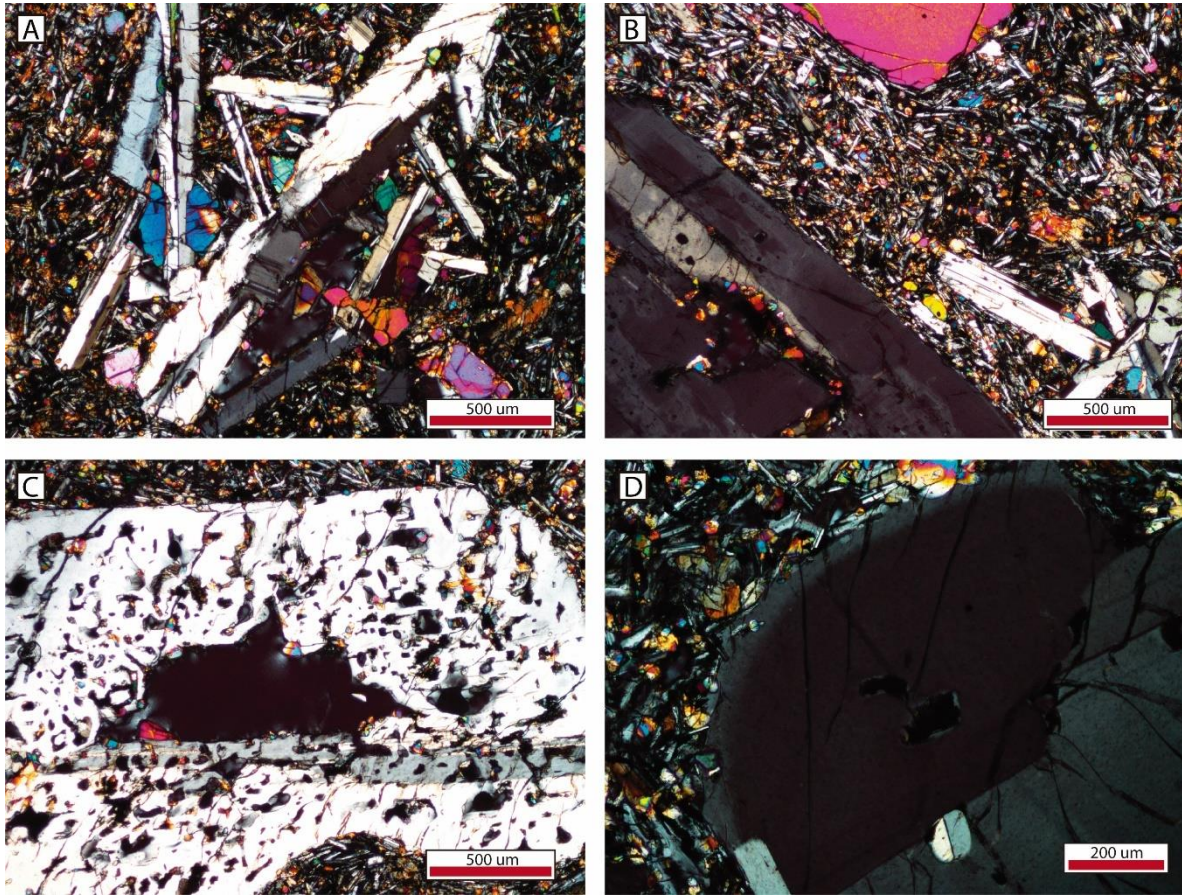


Fig. 52. Principales texturas observadas. (A) NX cúmulo de plagioclasas con olivinos, (B) NX masa fundamental intergranular y plagioclasea con variación composicional, (C) NX plagioclasea con abundantes inclusiones y oquedades y (D) NX plagioclasea con zonación.

▪ Corte 230220-2

Mineralogía primaria

Mineral	%	Forma	Estructuralidad	Integridad	Tamaño
Fenocristales [35%]					
Plagioclasea	72	tabular	subhedral-euhedral	alta	0.2-2.1 mm
Olivino	24	granular y prismático	euhedral-subhedral-anhedral	media (esqueletal algunos)	0.2-2.2 mm
Clinopiroxeno	4	granular alargado-radial	subhedral-euhedral	alta	0.2-0.5 mm

Masa fundamental [65%]					
Plagioclasa	-	tabular	euhedral	alta	<0.1 mm
Olivino	-	granular	anhedral	alta	<0.1 mm
Piroxeno	-	granular	anhedral	alta	<0.1 mm
Óxidos de Fe	-	-	-	-	<0.1 mm

Texturas

Textura	Descripción y minerales involucrados
Intergranular	Masa fundamental con plagioclasas aleatorias con cristales de piroxeno y olivino entre medio
Vesicular	Vesículas no tan abundantes, pero de gran tamaño
Cúmulo porfídica	Cúmulo de cristales de plagioclasa con olivino
Sieve	Inclusiones u oquedades en plagioclasas
Poikilítica	Inclusiones cristalinas en plagioclasas
Zonación	Difusa en plagioclasas

Clasificación QAP Basalto/Andesita

Nombre de la roca Basalto de olivino

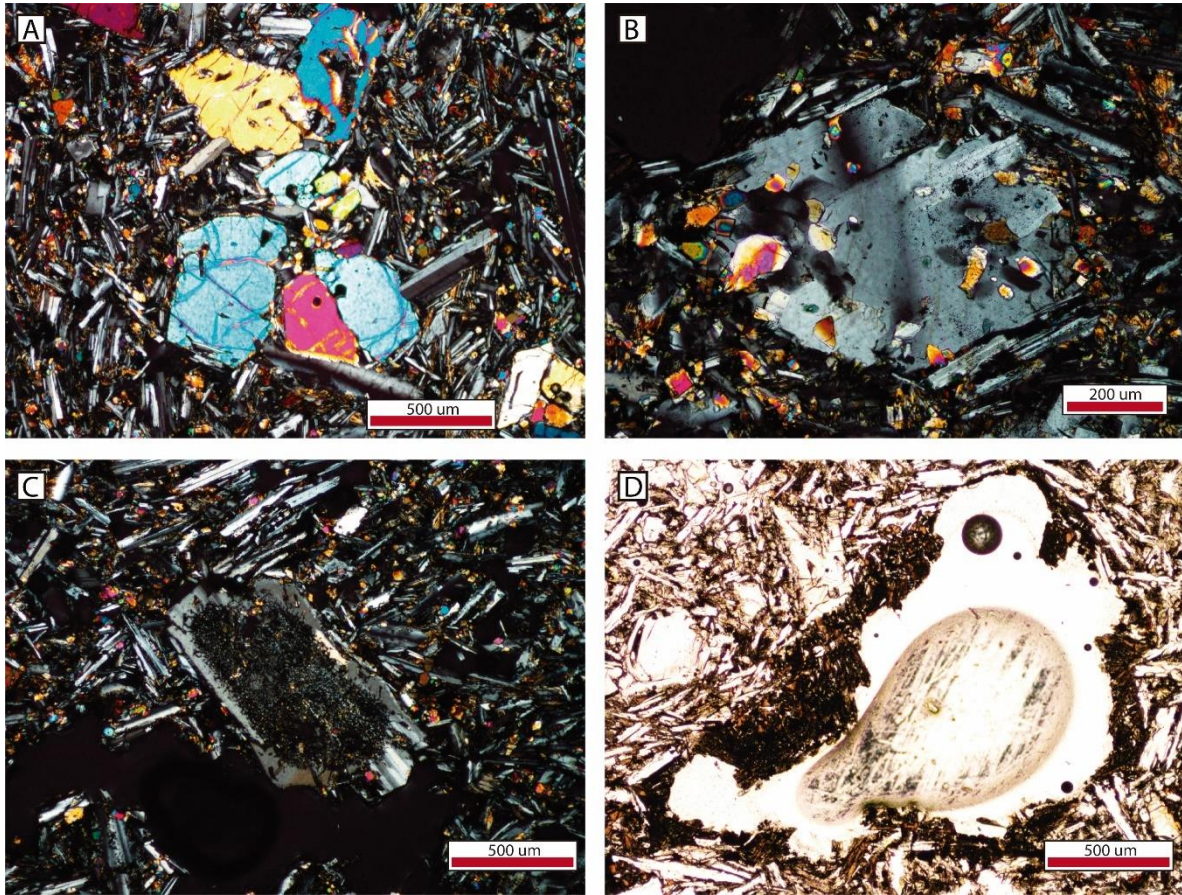


Fig. 53. Principales texturas observadas. (A) NX cúmulo de plagioclasas con olivinos, (B) NX plagioclasea con inclusiones cristalinas, (C) NX abundancia de inclusiones en plagioclasea y (D) NP vesícula con crecimiento cristalino en borde y óxidos.

▪ Corte 240220-2

Mineralogía primaria

Mineral	%	Forma	Estructuralidad	Integridad	Tamaño
Fenocristales [12%]					
Plagioclasea	62	tabular	subhedral-euhedral	media-alta (algunas con MF dentro)	0.2-1.4 mm
Olivino	32	granular y prismático	anhedral a subhedral	alta	0.2-3.8 mm
Clinopiroxeno	6	granular alargado	anhedral-subhedral	alta	0.2-0.6 mm

Masa fundamental [88%]					
Plagioclasa	-	tabular	euهدral	alta	<0.1 mm
Olivino	-	granular	anhedral	alta	<0.1 mm
Piroxeno	-	granular	anhedral	alta	<0.1 mm
Óxidos de Fe	-	-	-	-	<0.1 mm

Texturas

Textura	Descripción y minerales involucrados
Cúmulo porfídica	Cúmulos de plagioclasa con olivino
Intergranular	Masa fundamental de grano fino con plagioclasas aleatorias con cristales de piroxeno y olivino entre medio
Sieve	En plagioclasa, abundantes inclusiones vítreas
Vesicular	Pequeñas pero abundantes
Zonación	Difusa en plagioclasas
Parche	Variaciones composicionales en plagioclasas en forma de parche

Clasificación QAP Basalto/Andesita

Nombre de la roca Basalto de olivino

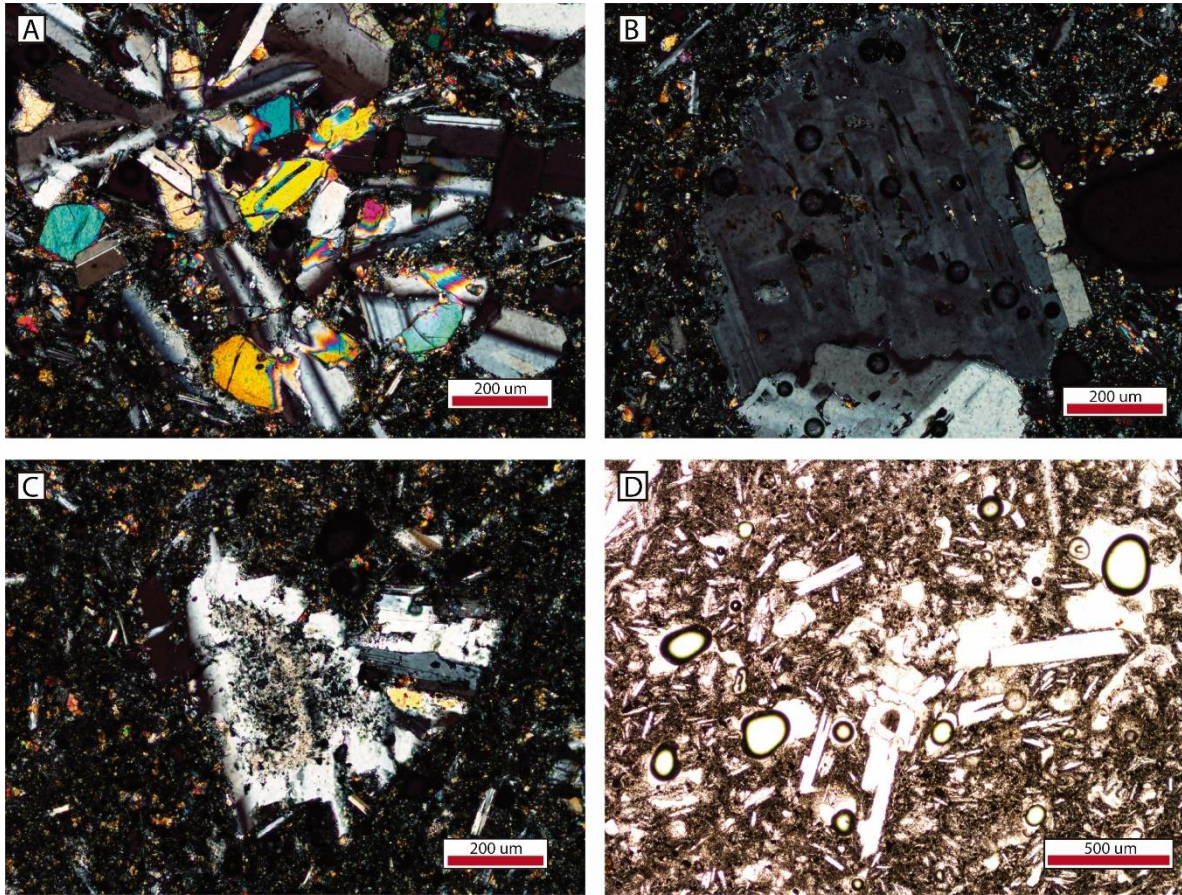


Fig. 54. Principales texturas observadas. (A) NX cúmulo de plagioclasas con olivinos, (B) NX plagioclasea con oquedades y variación composicional, (C) NX abundancia de inclusiones en plagioclasea y (D) NP vesículas.

▪ Corte 240220-2 xenolito

Mineralogía primaria

Mineral	%	Forma	Estructuralidad	Integridad	Tamaño
Cuarzo	37	granular	anhedral	media-alta	0.1-5.2 mm
Feld-k (ortoclasea)	63	granular- alargada	anhedral- subhedral	media-baja	<0.1-7.2 mm
Óxidos de Fe	-	-	-	-	-

Texturas

Textura	Descripción y minerales involucrados

Pertítica	Lamelas de exsolución poco abundantes en feldespatos
Fanerítica	Corte totalmente cristalino

Clasificación QAP Granito de feldespato alcalino

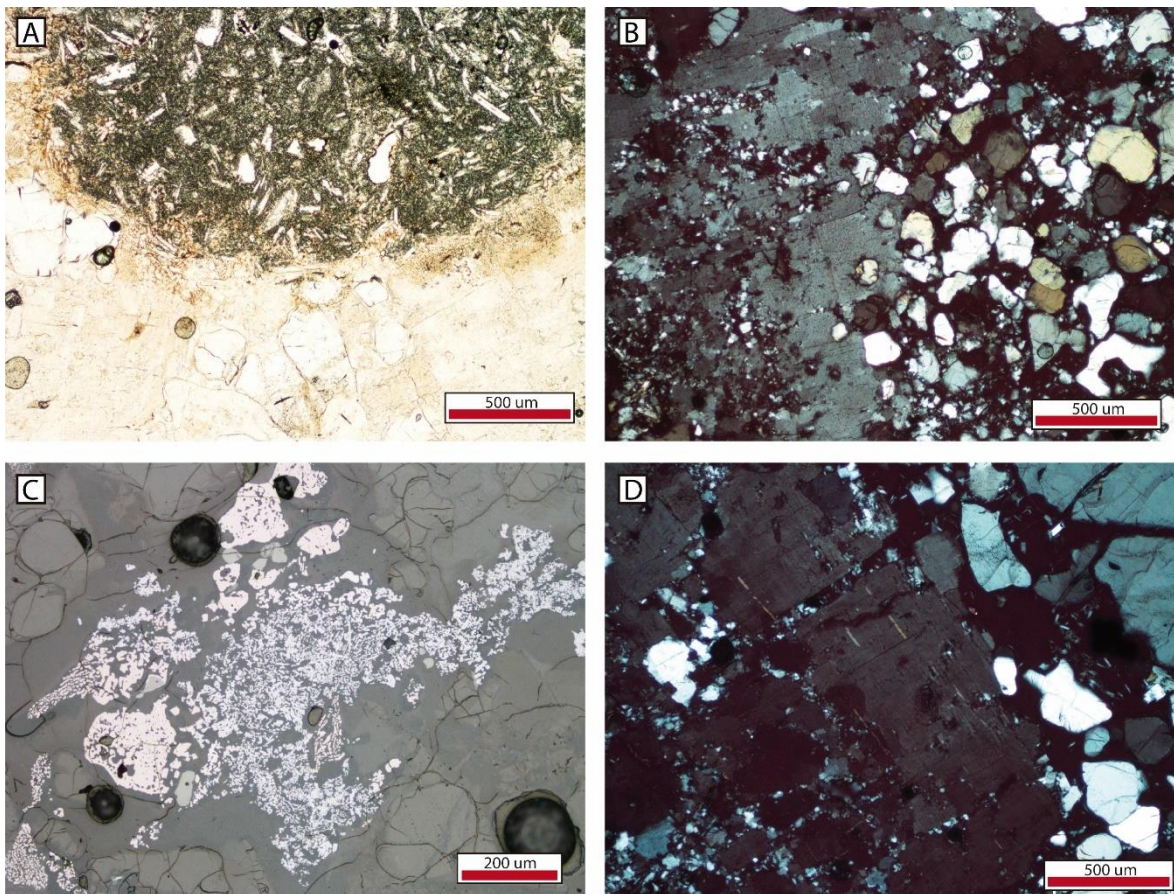


Fig. 55. Principales texturas observadas. (A) NP borde entre lava y xenolito granítico, (B) NX cristales de cuarzo granular y feldespato potásico, (C) LR óxidos en xenolito granítico y (D) NX lamelas de exsolución en feldespato potásico.

▪ **Corte 240220-3**

Mineralogía primaria

Mineral	%	Forma	Estructuralidad	Integridad	Tamaño
Cuarzo	42	granular	anhedral	media-alta	0.1-4.4 mm

Feld-K (ortoclasa)	20	granular alargado	anhedral- subhedral	baja	0.3-2.7 mm
Plagioclasa	38	tabular	euhedral	media	0.3-2.7 mm
Óxidos de Fe	-	-	-	-	-

Mineralogía secundaria

Mineral	Mineral y/o zona en que se encuentra
Clorita	Posible alteración de biotita por la forma planar que presenta
Epidota	Pequeños cristales con alto relieve y alta birrefringencia

Texturas

Textura	Descripción y minerales involucrados
Fanerítica	Corte cristalino
Pertítica	Lamelas de exsolución poco abundantes en feldespatos

Clasificación QAP Granito

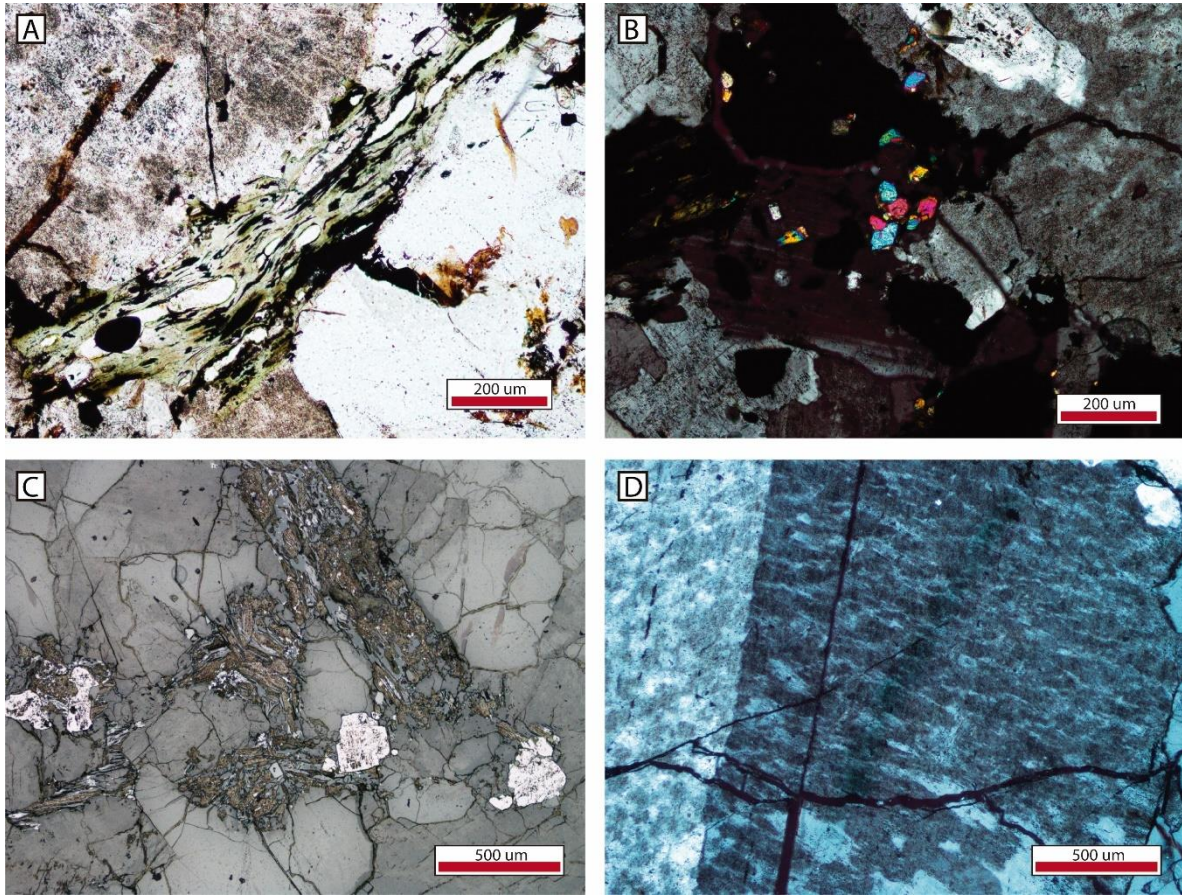


Fig. 56. Principales texturas observadas. (A) NP clorita mineralogía secundaria, (B) NX epidota mineralogía secundaria, (C) LR óxidos y (D) NX lamelas de exsolución en feldespato potásico.

▪ **Corte 250220-1**

Mineralogía primaria

Mineral	%	Forma	Estructuralidad	Integridad	Tamaño
Fenocristales [24%]					
Plagioclasa	79	tabular	subhedral-euhedral	media-baja (algunas rellenas con MF)	0.2-2 mm
Olivino	15	granular y prismático	anhedral-subhedral	alta	0.2-3.2 mm
Clinopiroxeno	6	granular alargado-radial	anhedral-subhedral	alta	0.2-4 mm

Masa fundamental [76%]					
Plagioclasa	-	tabular	euهدral	alta	<0.2 mm
Olivino	-	granular	anhedral	alta	<0.2 mm
Piroxeno	-	granular	anhedral	alta	<0.2 mm
Óxidos de Fe	-	-	-	-	<0.2 mm

Texturas

Textura	Descripción y minerales involucrados
Intergranular	Masa fundamental de plagioclasas aleatorias con minerales entre ellas
Vesicular	Grandes y abundantes (22%)
Cúmulo porfídica	Cúmulos de plagioclasas con olivino
Sieve	Inclusiones vítreas en plagioclasas
Zonación	Difusa en plagioclasas

Clasificación QAP Basalto/Andesita

Nombre de la roca Basalto de olivino

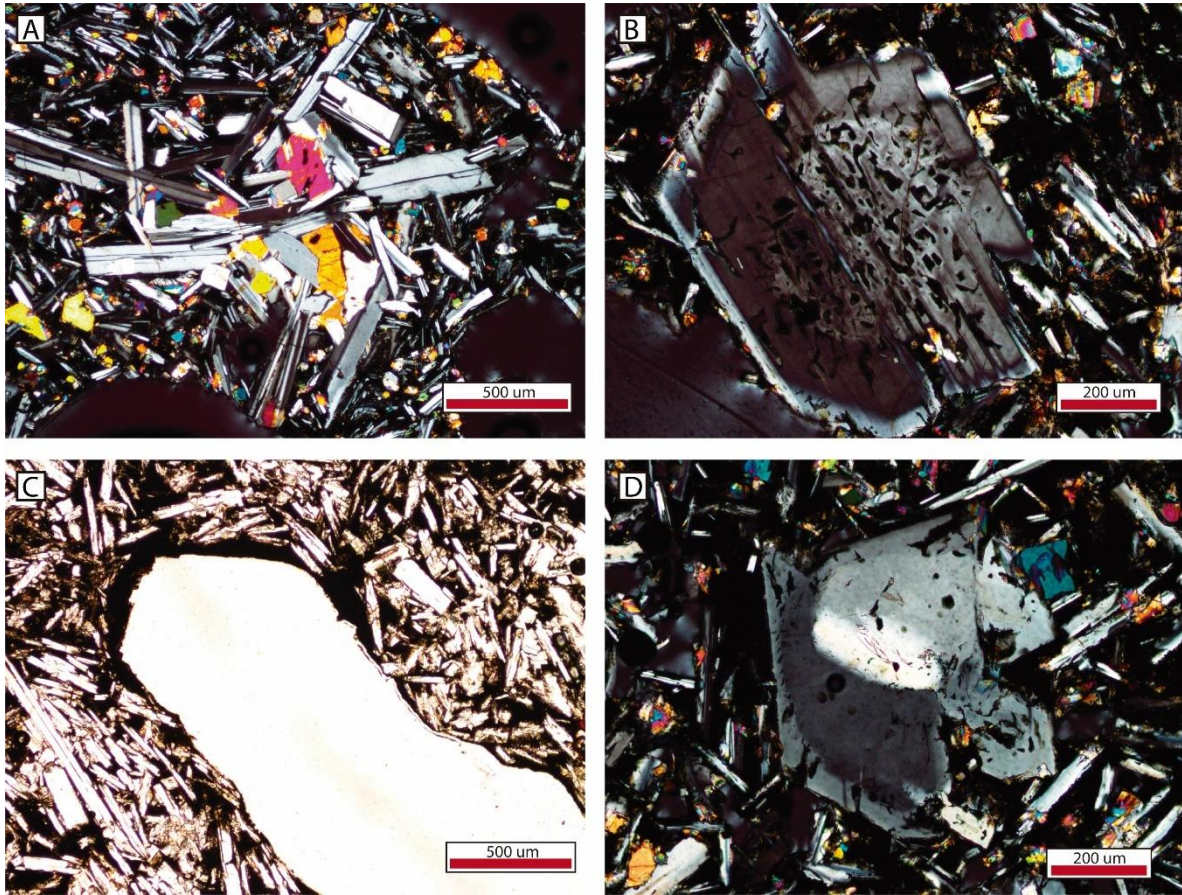


Fig. 57. Principales texturas observadas. (A) NX cúmulo de plagioclasas con olivinos, (B) NX abundancia de inclusiones en plagioclasa, (C) NP vesícula con óxidos en sus paredes y (D) NX plagioclasa con zonación.

▪ **Corte 250220-6t**

Mineralogía primaria

Mineral	%	Forma	Estructuralidad	Integridad	Tamaño
Cuarzo	24	granular	anhedral	alta	0.1-5.1 mm
Feld-k (ortoclasa)	76	granular alargado	subhedral- anhedral	media-baja	0.1-3 mm

Texturas

Textura	Descripción y minerales involucrados
Micrográfica	Intercrecimiento de cuarzo triangular con feld-k
Fanerítica	Corte cristalino

Vermicular	Crecimiento vermicular entre cristales de cuarzo y feld-k
------------	---

Clasificación QAP Granito de feldespato alcalino

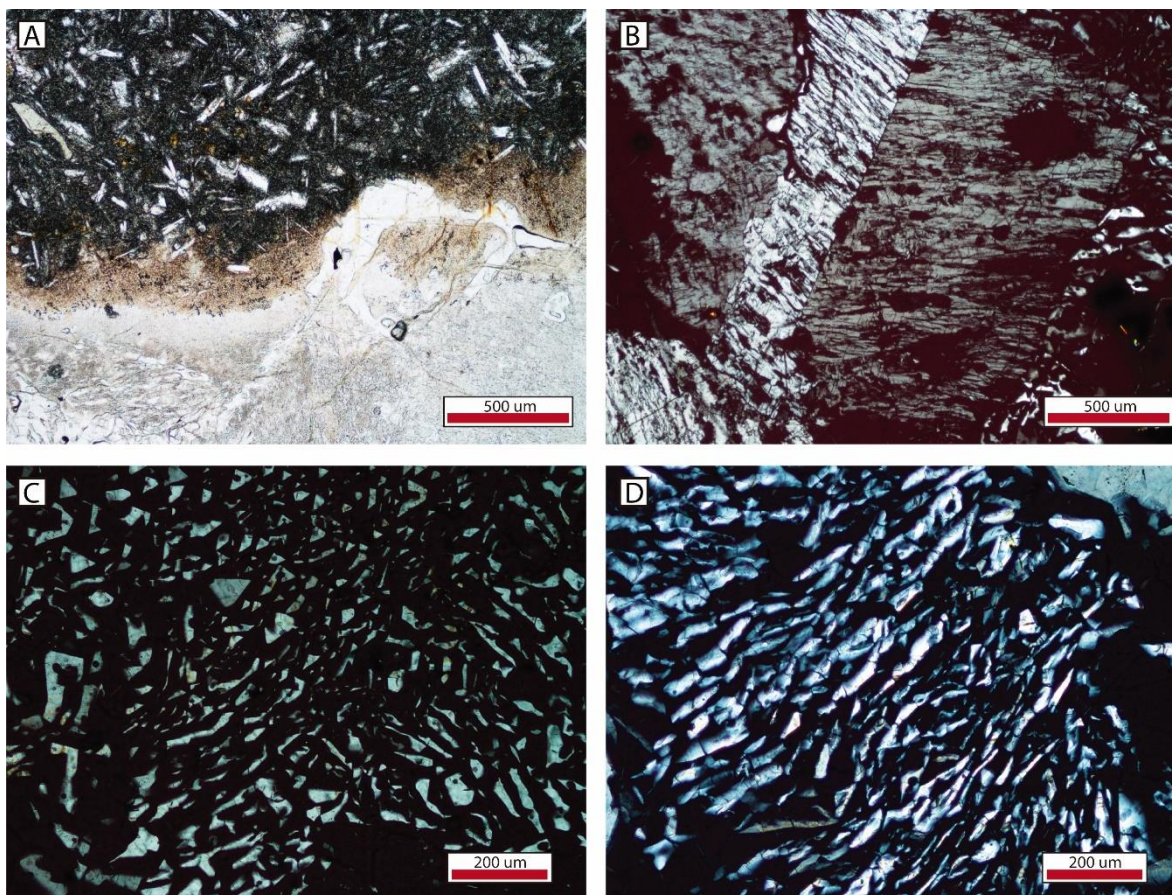


Fig. 58. Principales texturas observadas. (A) NP contacto entre lava y xenolito granítico, (B) NX textura de los feldespatos potásicos, (C) NX textura micrográfica en feldespato y (D) NX crecimiento vermicular entre cristales de cuarzo y feldespatos.

Annex C

C.1 Datos análisis SEM lavas

- **Mediciones puntuales realizadas en los fenocristales, microfenocristales y en masa fundamental, a las principales fases presentes en los basaltos y traquita: plagioclasa, olivino y piroxenos. Para orientación de los puntos de medición, se adjuntan imágenes a nícoles cruzados con los cristales enumerados. Número que aparece en la segunda fila de las tablas. El número entre paréntesis corresponde a la enumeración interna del SEM de los puntos de medición.**

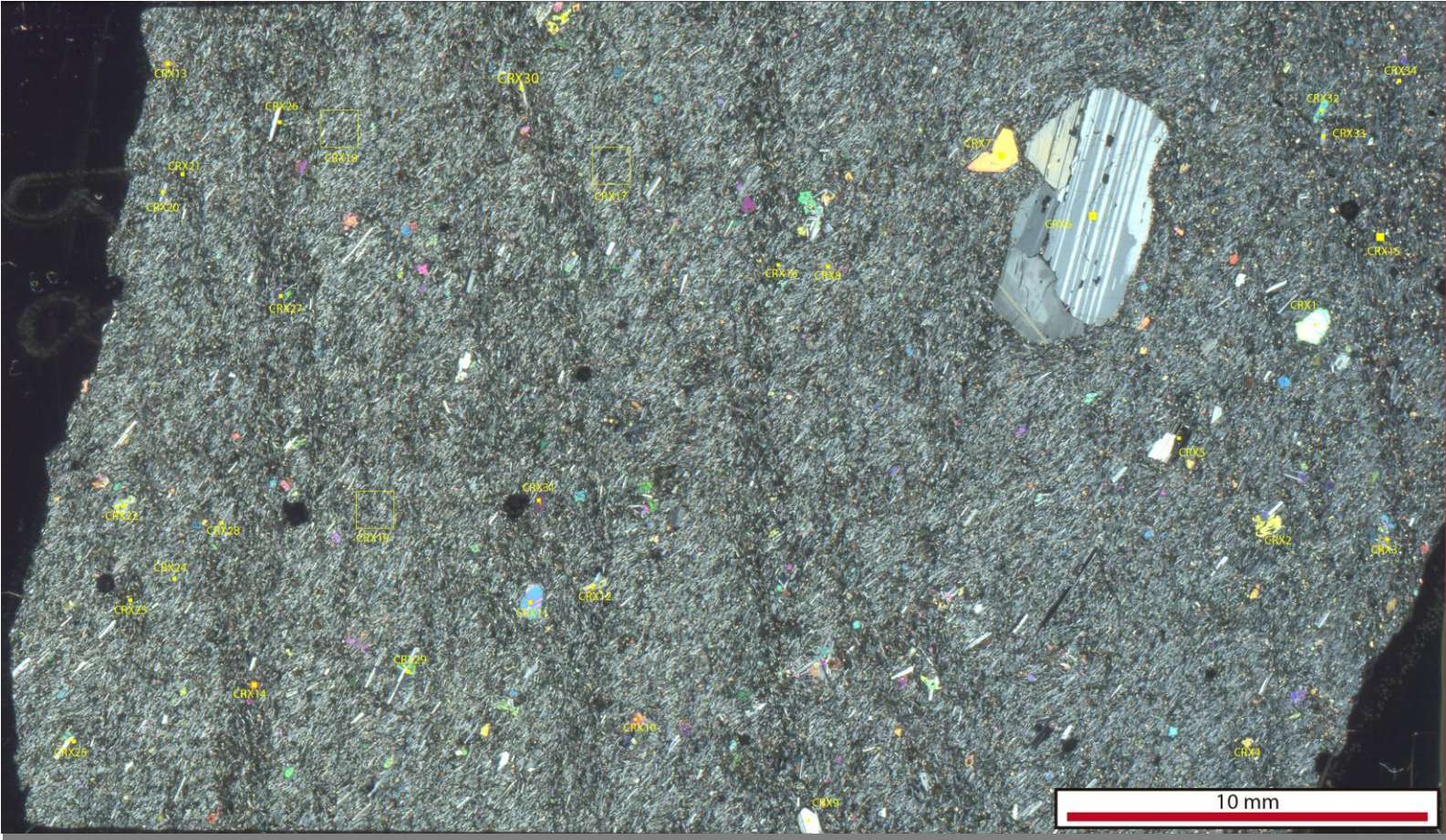


Fig. 59. Imagen a polarizadores cruzados de la muestra JV021219-1.

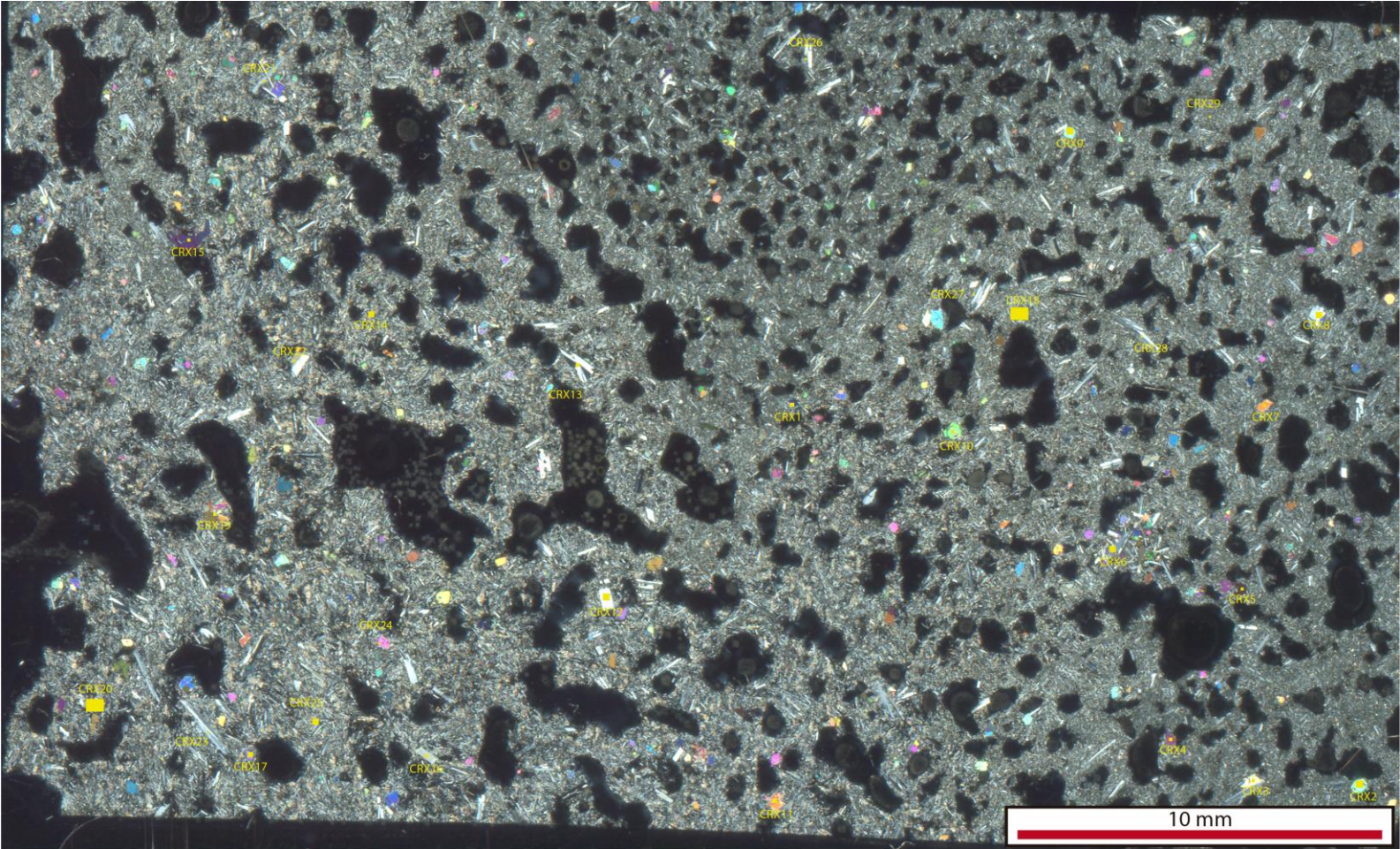


Fig. 60. Imagen a polarizadores cruzados de la muestra JV031219-2A.

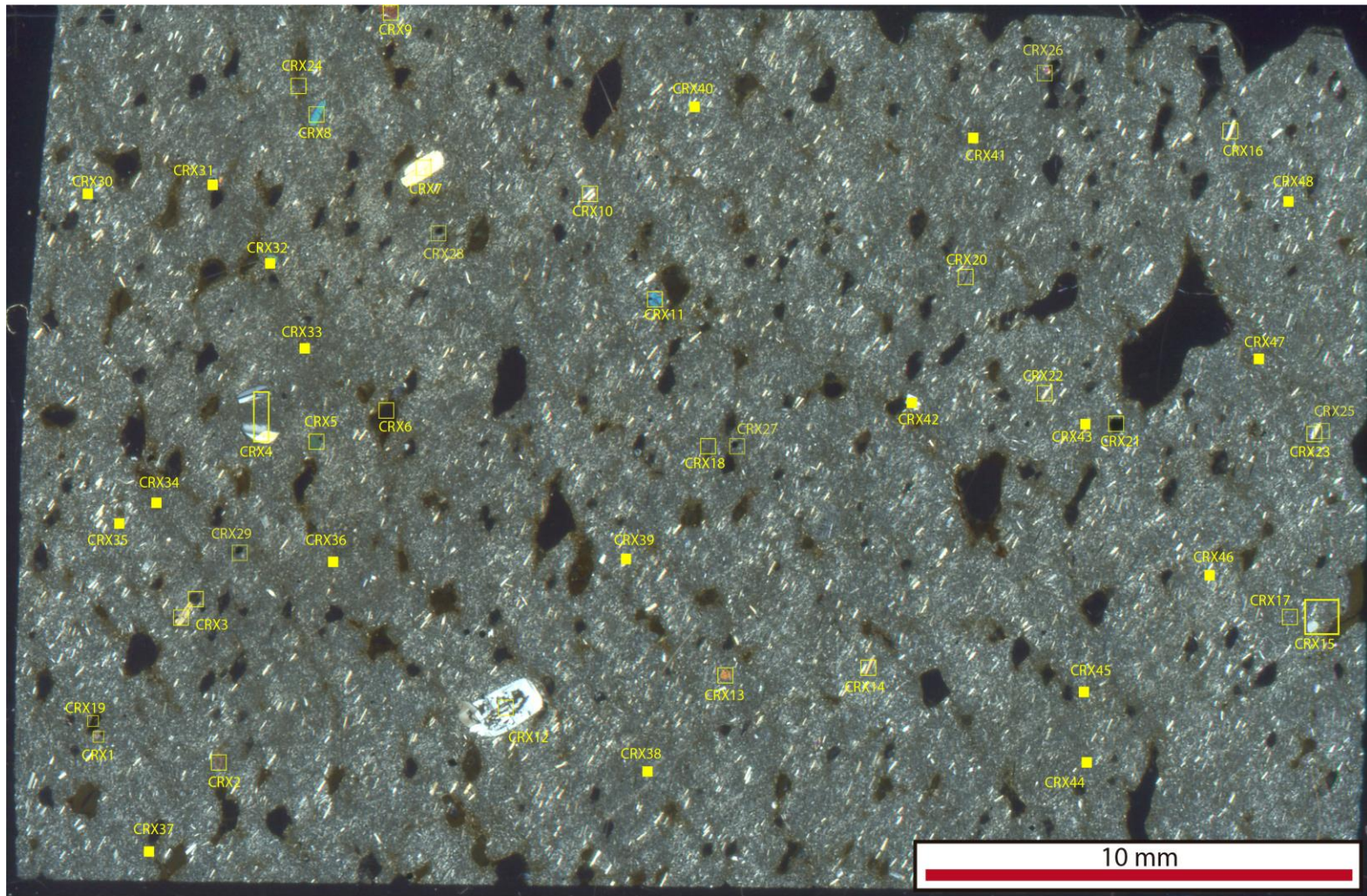


Fig. 61. Imagen a polarizadores cruzados de la muestra JV031219-4.

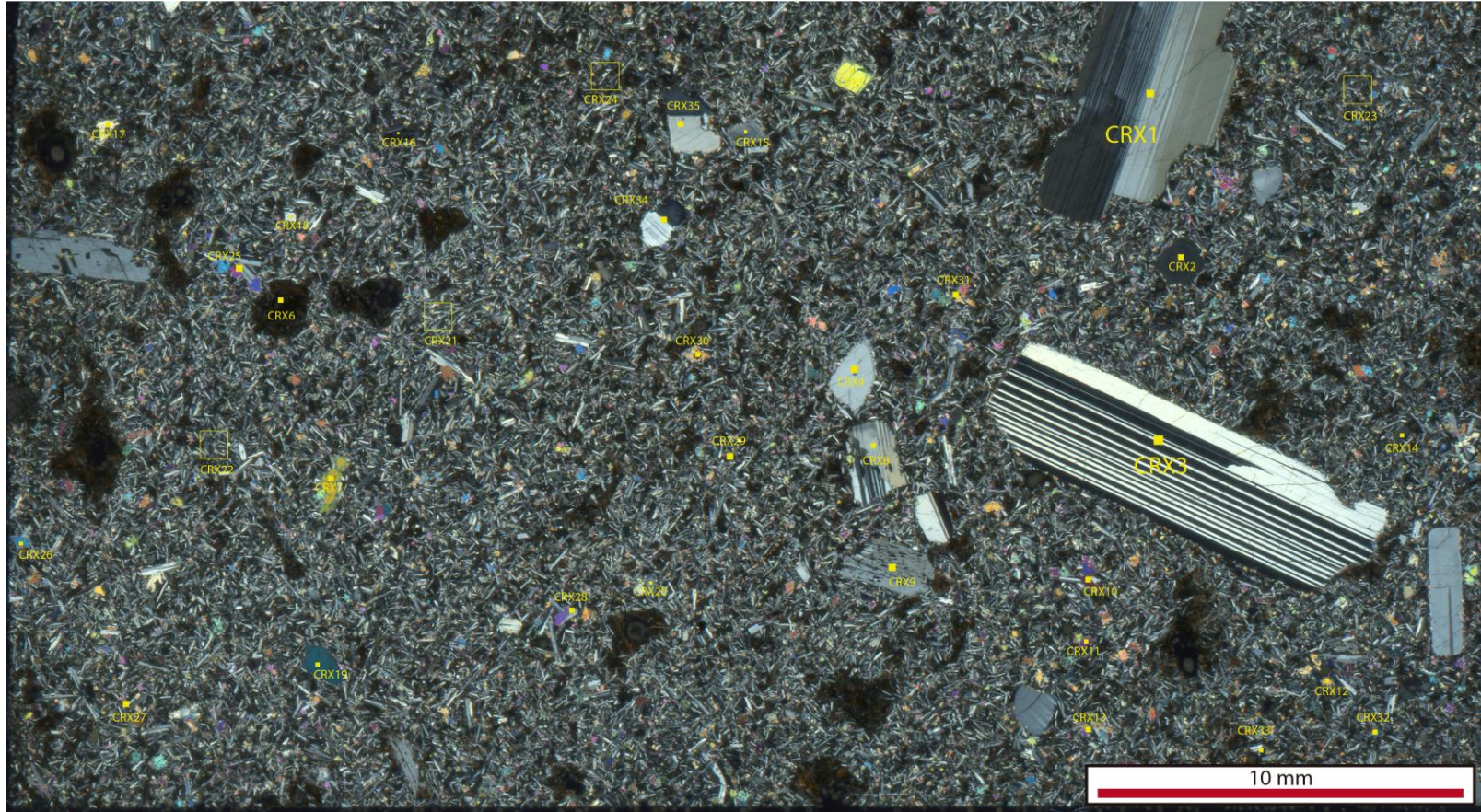


Fig. 62. Imagen a polarizadores cruzados de la muestra JV051219-1.



Fig. 63. Imagen a polarizadores cruzados de la muestra JV051219-8.

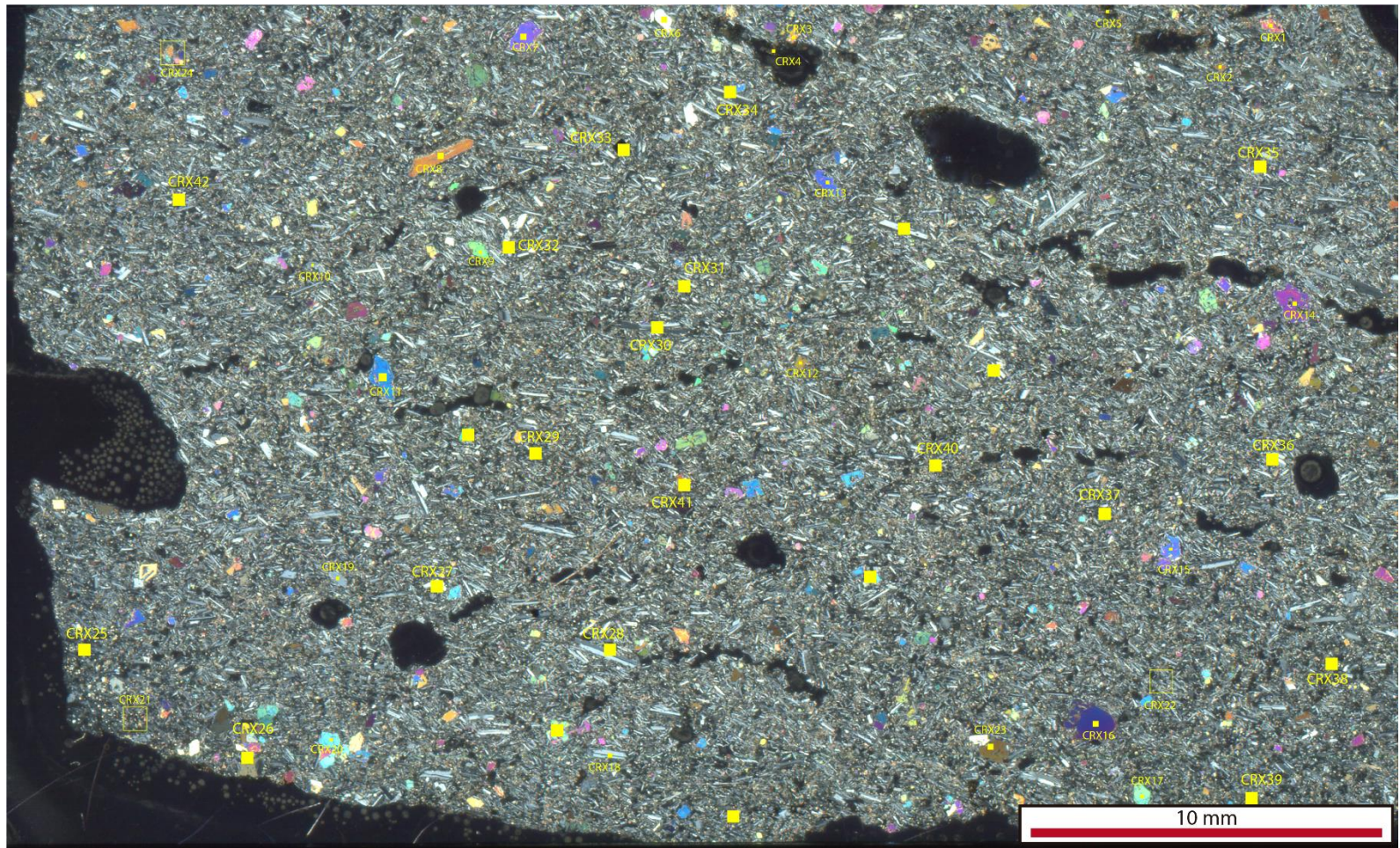


Fig. 64. Imagen a polarizadores cruzados de la muestra JV230220-2.

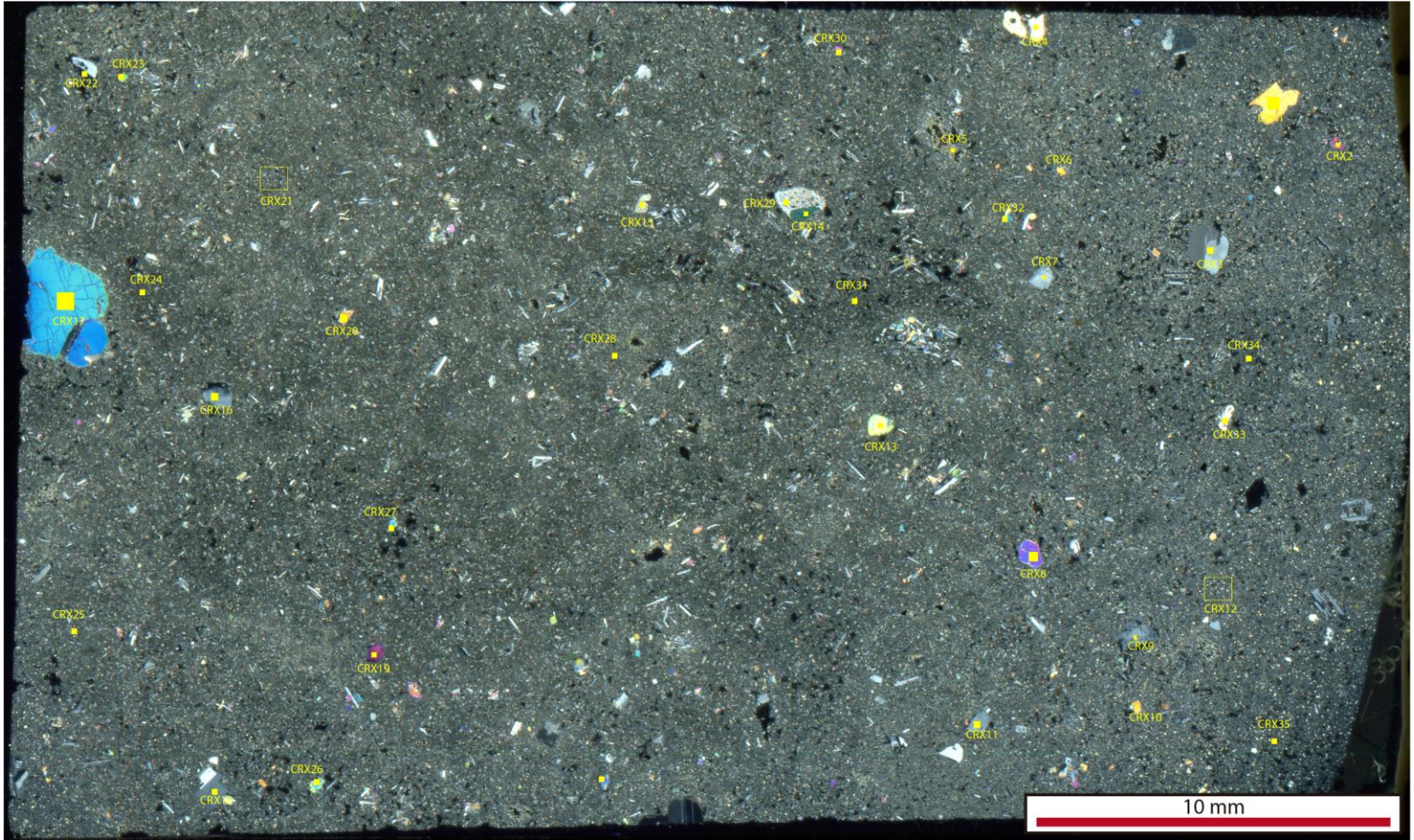


Fig. 65. Imagen a polarizadores cruzados de la muestra JV240220-2.

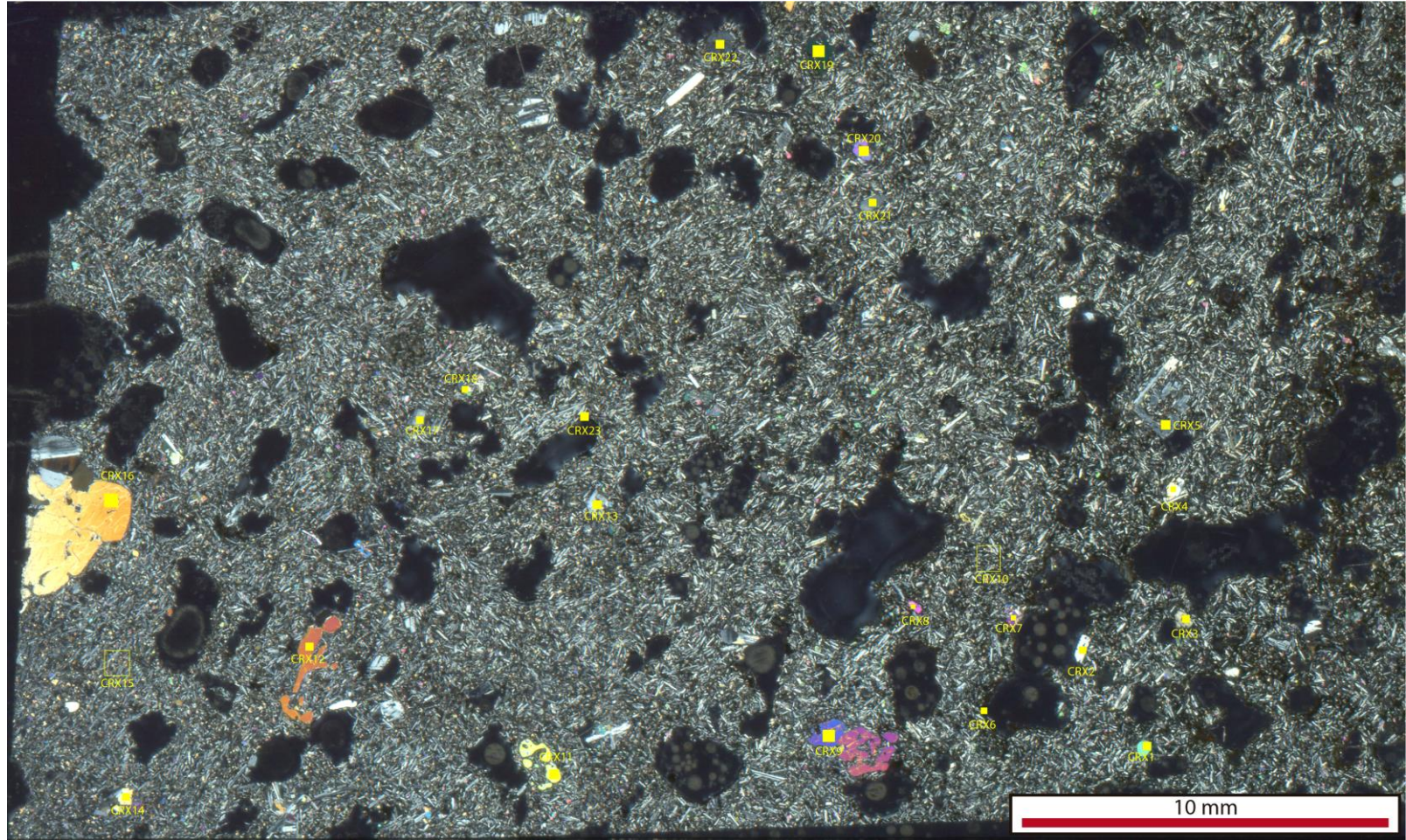


Fig. 66. Imagen a polarizadores cruzados de la muestra JV250220-1.

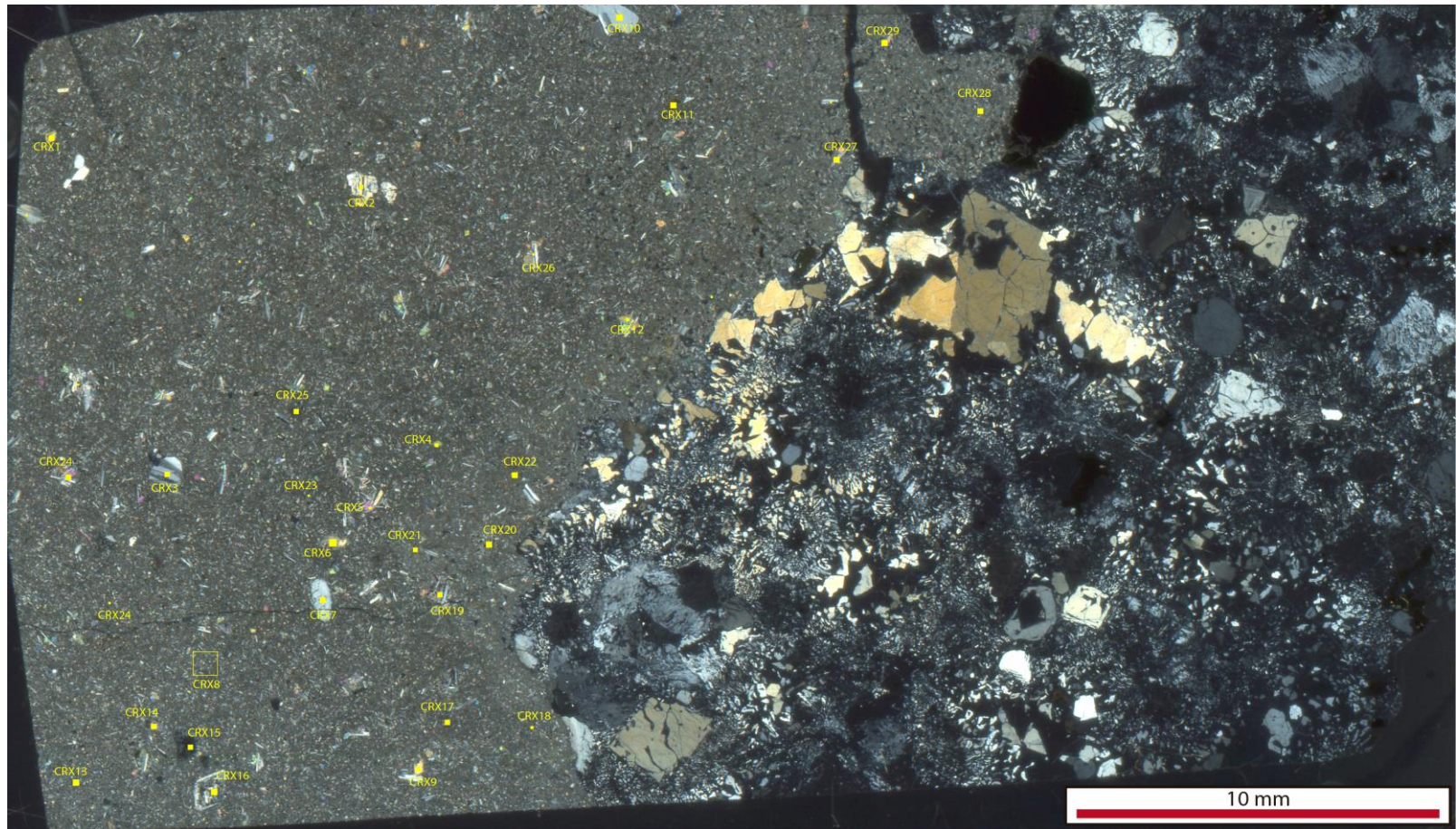


Fig. 67. Imagen a polarizadores cruzados de la muestra JV250220-6.

1. Plagioclasa

Sample Crystal/Zone [C: Core, R: Rim] Type [PC: phenocryst, MPC: microphenocryst, GM: groundmass]	021219-1	021219-1	021219-1	021219-1	021219-1	021219-1	021219-1	021219-1	021219-1	021219-1	021219-1	021219-1	021219-1	021219-1	021219-1
	CRX5 C (9)	CRX5 R (10)	CRX6 C (11)	CRX6 R (12)	CRX8 C (15)	CRX8 R (16)	CRX9 C (17)	CRX9 R (18)	CRX17 (1)	CRX17 (3)	CRX17 (4)	CRX17 (5)	CRX18 (7)	CRX18 (8)	CRX18 (9)
	PC	PC	PC	PC	PC	PC	PC	PC	GM	GM	GM	GM	GM	GM	GM
SiO2	53.65	53.71	54.02	52.58	54.70	58.29	53.11	55.27	58.10	56.91	58.29	59.52	56.49	57.68	58.49
Al2O3	29.98	29.78	29.69	30.51	28.94	25.62	30.32	28.28	28.23	29.14	28.46	26.46	29.93	29.00	28.61
FeO				0.32	0.45	1.06		0.53		0.42		0.40			
CaO	12.75	12.81	12.48	12.96	11.64	8.75	13.13	11.08	6.29	7.07	6.35	5.51	7.67	6.34	5.57
Na2O	3.62	3.70	3.81	3.62	4.27	5.90	3.44	4.59	7.38	6.46	6.89	8.11	5.90	6.98	7.33
K2O						0.38		0.24							
Total	1,699.96	100.00	100.00	99.99	100.00	100.00	100.00	99.99	100.00	100.00	99.99	100.00	99.99	100.00	100.00
An	66.06	65.67	64.41	66.42	60.10	44.02	67.84	56.32	32.02	37.69	33.74	27.30	41.81	33.42	29.57
Ab	33.94	34.33	35.59	33.58	39.90	53.71	32.16	42.22	67.98	62.31	66.26	72.70	58.19	66.58	70.43
Or	0.00	0.00	0.00	0.00	0.00	2.28	0.00	1.45	0.00	0.00	0.00	0.00	0.00	0.00	0.00

021219-1	021219-1	021219-1	021219-1	021219-1	021219-1	021219-1	021219-1	021219-1	021219-1	021219-1	021219-1	021219-1	021219-1	021219-1	021219-1
CRX18 (10)	CRX19 (18)	CRX19 (19)	CRX20 C (1)	CRX20 R (2)	CRX20 (10)	CRX20 (11)	CRX20 (12)	CRX21 (15)	CRX21 (19)	CRX21 (20)	CRX22 (25)	CRX22 (27)	CRX23 C (29)	CRX23 R (30)	
GM	GM	GM	PC	PC	GM	GM	GM	GM	GM	GM	GM	GM	GM	MPC	MPC
57.98	61.06	57.80	53.88	55.62	55.11	54.70	56.36	55.91	56.76	57.30	56.38	56.43	56.36	58.65	
29.59	24.40	28.33	29.38	28.06	27.97	28.68	27.64	27.94	27.10	26.59	27.02	27.45	26.95	25.45	
	0.40		0.44	0.62	0.76	0.66	0.63	0.73	0.56	0.81	0.68	0.61	0.79	0.96	
6.08	4.39	6.88	12.48	10.56	11.19	11.50	9.96	10.17	10.23	9.32	10.63	10.74	10.58	8.19	
6.35	9.29	6.76	3.82	4.89	4.69	4.46	5.10	4.96	5.11	5.65	5.03	4.77	5.03	6.24	
	0.46	0.22		0.24	0.28		0.30	0.29	0.23	0.33	0.26		0.30	0.52	
100.00	100.00	99.99	100.00	99.99	100.00	100.00	99.99	100.00	99.99	100.00	100.00	100.00	100.01	100.01	
34.60	20.18	35.51	64.35	53.62	55.92	58.76	50.96	52.18	51.79	46.75	53.04	55.44	52.80	40.74	
65.40	77.30	63.14	35.65	44.93	42.41	41.24	47.22	46.05	46.82	51.28	45.42	44.56	45.42	56.18	
0.00	2.52	1.35	0.00	1.45	1.67	0.00	1.83	1.77	1.39	1.97	1.54	0.00	1.78	3.08	

021219-1	021219-1	021219-1	021219-1	021219-1	021219-1	021219-1	021219-1	021219-1	021219-1	021219-1	021219-1	021219-1	021219-1	021219-1
CRX23 (35)	CRX24 (38)	CRX24 (41)	CRX25 C (44)	CRX25 R (45)	CRX26 C (48)	CRX26 R (49)	CRX26 (51)	CRX27 (56)	CRX28 C (59)	CRX28 R (60)	CRX28 (62)	CRX29 C (64)	CRX29 R (65)	CRX29 (68)
GM	GM	GM	PC	PC	PC	PC	GM	GM	PC	PC	GM	PC	PC	GM
56.28	55.56	56.39	53.63	54.62	53.74	56.08	56.32	56.60	53.76	55.04	53.93	54.06	53.21	56.33
27.79	27.83	27.07	29.72	28.84	29.38	27.84	27.40	27.25	29.30	28.41	28.88	28.93	29.73	26.62
0.59	0.59	0.65	0.45	0.53	0.50	0.70	0.66	0.75	0.57	0.67	0.67	0.56	0.59	1.20
10.60	11.24	10.73	12.49	11.50	12.45	10.56	10.24	10.22	12.46	11.34	12.27	12.47	12.62	10.42
4.47	4.57	4.87	3.69	4.26	3.94	4.81	5.09	4.96	3.91	4.32	4.05	3.98	3.84	4.93
0.28	0.21	0.27		0.25			0.29	0.22		0.23	0.20			0.51
100.01	100.00	99.98	99.98	100.00	100.01	99.99	100.00	100.00	100.00	100.01	100.00	100.00	99.99	100.01
55.72	56.88	54.02	65.16	58.95	63.59	54.82	51.73	52.52	63.78	58.36	61.85	63.39	64.49	52.23
42.52	41.85	44.37	34.84	39.52	36.41	45.18	46.53	46.13	36.22	40.23	36.95	36.61	35.51	44.72
1.75	1.27	1.62	0.00	1.53	0.00	0.00	1.74	1.35	0.00	1.41	1.20	0.00	0.00	3.04

021219-1	021219-1	021219-1	021219-1	021219-1	021219-1	021219-1	021219-1	021219-1
CRX30 C (71)	CRX30 R (72)	CRX30 (74)	CRX31 (81)	CRX32 (85)	CRX33 C (87)	CRX33 R (88)	CRX33 (91)	CRX34 (92)
PC	PC	GM	GM	GM	PC	PC	GM	GM
54.27	57.91	56.60	54.80	54.53	53.55	56.03	56.82	56.01
29.27	26.03	27.04	28.22	29.14	29.56	27.60	27.04	27.83
0.47	1.21	0.57	0.74	0.58	0.52	0.58	0.58	0.56
12.04	9.23	10.30	11.80	11.78	12.40	10.80	10.25	10.25
3.96	5.10	5.06	4.18	3.97	3.97	4.76	5.07	5.04
	0.52	0.43	0.25			0.22	0.24	0.29
100.01	100.00	100.00	99.99	100.00	100.00	99.99	100.00	99.98
62.69	48.38	51.58	60.01	62.12	63.32	54.89	52.00	51.99
37.31	48.37	45.86	38.47	37.88	36.68	43.78	46.55	46.26
0.00	3.25	2.56	1.51	0.00	0.00	1.33	1.45	1.75

Sample Crystal/Zone [C: Core, R: Rim] Type [PC: phenocryst, MPC: microphenocryst, GM: groundmass]	031219-2A	031219-2A	031219-2A	031219-2A	031219-2A	031219-2A	031219-2A	031219-2A	031219-2A	031219-2A	031219-2A	031219-2A	031219-2A	031219-2A	031219-2A
	CRX8 C (22)	CRX8 R (23)	CRX12 C (32)	CRX12 R (33)	CRX13 C (36)	CRX13 R (37)	CRX16 C (46)	CRX16 R (47)	CRX18 (6)	CRX18 (9)	CRX18 (10)	CRX19 (13)	CRX19 (16)	CRX19 (17)	CRX20 (20)
	PC	PC	PC	PC	PC	PC	PC	PC	GM	GM	GM	GM	GM	GM	GM
SiO2	54.14	54.61	54.76	54.02	54.13	55.11	53.97	55.76	56.39	59.21	56.44	55.87	56.33	56.60	63.05
Al2O3	28.83	28.54	28.79	29.22	28.92	28.16	29.24	27.98	28.59	25.49	28.28	28.28	28.52	28.58	21.83
FeO	0.51	0.43	0.45	0.40	0.48	0.53	0.40	0.56	0.41	0.66	0.59	0.65	0.58	0.56	0.43
CaO	12.48	12.02	11.49	12.40	12.26	11.47	12.43	10.93	8.89	7.75	9.25	10.29	8.77	8.52	2.43
Na2O	4.04	4.16	4.52	3.96	4.00	4.53	3.96	4.49	5.50	6.36	5.19	4.90	5.58	5.74	11.07
K2O		0.24			0.22	0.21		0.29	0.22	0.53	0.25		0.21		1.20
Total	1,700.05	100.00	100.01	100.00	100.01	100.01	100.00	100.01	100.00	100.00	100.00	99.99	99.99	100.00	100.01
An	63.06	60.60	58.42	63.38	62.04	57.59	63.43	56.34	46.53	38.96	48.84	53.71	45.87	45.06	10.17
Ab	36.94	37.96	41.58	36.62	36.63	41.16	36.57	41.88	52.10	57.86	49.59	46.29	52.82	54.94	83.85
Or	0.00	1.44	0.00	0.00	1.33	1.26	0.00	1.78	1.37	3.17	1.57	0.00	1.31	0.00	5.98

031219-2A	031219-2A	031219-2A	031219-2A	031219-2A	031219-2A	031219-2A	031219-2A	031219-2A	031219-2A	031219-2A	031219-2A	031219-2A	031219-2A	031219-2A	031219-2A
CRX20 (21)	CRX20 (23)	CRX21 C (1)	CRX21 R (2)	CRX21 (6)	CRX22 C (9)	CRX22 R (10)	CRX22 (13)	CRX23 C (14)	CRX23 R (15)	CRX23 (18)	CRX24 C (21)	CRX24 R (22)	CRX25 C (25)	CRX25 R (26)	
GM	GM	PC	PC	GM	PC	PC	GM	PC	PC	GM	GM	GM	GM	GM	
56.99	57.48	54.24	54.29	54.75	54.45	53.66	56.46	54.45	54.20	57.63	56.60	60.21	55.36	65.32	
27.02	27.74	29.19	29.04	28.77	29.26	29.69	27.39	29.24	29.51	26.68	27.39	24.92	28.59	20.95	
0.64	0.46	0.59	0.42	0.46	0.32	0.45	0.63	0.35	0.45	0.54	0.46	0.52	0.50	0.44	
9.45	7.82	11.87	12.01	11.28	11.92	12.37	10.25	11.85	11.78	9.23	10.30	6.99	10.92	3.12	
5.62	6.26	4.11	4.24	4.46	4.04	3.84	5.02	4.11	4.06	5.61	4.96	6.64	4.62	8.62	
0.29	0.25			0.28			0.24			0.31	0.28	0.72		1.55	
100.01	100.01	100.00	100.00	100.00	99.99	100.01	99.99	100.00	100.00	100.00	99.99	100.00	99.99	100.00	
47.33	40.21	61.48	61.02	57.30	61.98	64.03	52.24	61.44	61.59	46.73	52.53	35.19	56.64	15.17	
50.94	58.25	38.52	38.98	41.00	38.02	35.97	46.30	38.56	38.41	51.40	45.77	60.49	43.36	75.85	
1.73	1.53	0.00	0.00	1.69	0.00	0.00	1.46	0.00	0.00	1.87	1.70	4.32	0.00	8.97	

031219-2A	031219-2A	031219-2A	031219-2A	031219-2A	031219-2A	031219-2A	031219-2A	031219-2A	031219-2A	031219-2A
CRX26 C (29)	CRX26 R (30)	CRX26 (31)	CRX27 C (34)	CRX27 R (35)	CRX27 (38)	CRX28 C (39)	CRX28 R (40)	CRX28 (43)	CRX29 (44)	CRX29 (49)
PC	PC	GM	PC	PC	GM	PC	PC	GM	GM	GM
54.06	54.18	56.04	54.80	53.95	56.33	54.05	54.87	55.67	55.08	55.25
29.44	29.59	28.03	29.10	29.69	27.51	29.45	28.80	28.36	28.74	28.39
0.40	0.48	0.55		0.34	0.66	0.38	0.47	0.68	0.54	0.62
11.76	11.74	10.16	12.14	11.98	10.09	12.10	11.02	10.10	11.04	10.69
4.12	4.01	5.00	3.96	3.81	5.21	4.02	4.64	4.95	4.60	4.78
0.22		0.21		0.23	0.20		0.20	0.23		0.27
100.00	100.00	99.99	100.00	100.00	100.00	100.00	100.00	99.99	100.00	100.00
60.38	61.80	52.21	62.88	62.56	51.07	62.45	56.07	52.25	57.01	54.37
38.28	38.20	46.50	37.12	36.01	47.72	37.55	42.72	46.34	42.99	43.99
1.34	0.00	1.29	0.00	1.43	1.21	0.00	1.21	1.42	0.00	1.64

Sample Crystal/Zone [C: Core, R: Rim] Type [PC: phenocryst, MPC: microphenocryst, GM: groundmass]	031219-4	031219-4	031219-4	031219-4	031219-4	031219-4	031219-4	031219-4	031219-4	031219-4	031219-4	031219-4	031219-4	031219-4	031219-4
	CRX2 (8)	CRX14 C (15)	CRX14 R (16)	CRX14 C (17)	CRX14 R (18)	CRX7 C (23)	CRX7 R (24)	CRX10 (29)	CRX11 (32)	CRX11 (33)	CRX12 R (34)	CRX12 C (35)	CRX14 (39)	CRX14 (40)	CRX15 (45)
	GM	PC	PC	PC	PC	PC	PC	MPC	MPC	MPC	PC	PC	MPC	MPC	MPC
SiO2	62.14	61.83	62.24	62.02	62.12	59.01	60.83	62.76	61.89	62.10	61.76	61.97	62.12	70.73	62.10
Al2O3	23.96	24.13	24.01	24.06	24.08	25.62	25.53	23.85	23.79	23.77	24.32	24.47	24.00	17.33	23.88
FeO									0.43	0.32	0.31			0.41	0.23
CaO	5.64	6.60	6.24	6.37	6.15	4.82	4.79	5.16	5.99	5.93	5.64	5.33	4.09	2.56	5.00
Na2O	7.67	7.01	7.03	7.21	7.20	9.47	8.84	7.67	7.14	7.19	7.45	7.73	9.26	7.17	8.12
K2O	0.59	0.43	0.48	0.33	0.45	0.34		0.57	0.78	0.68	0.51	0.49	0.53	1.80	0.68
Total	100.00	100.00	100.00	99.99	100.00	99.26	99.99	100.01	100.02	99.99	99.99	99.99	100.00	100.00	100.01
An	27.89	33.34	31.95	32.16	31.19	21.55	23.04	26.17	30.19	30.02	28.59	26.78	19.04	14.48	24.39
Ab	68.64	64.08	65.13	65.86	66.09	76.64	76.96	70.39	65.13	65.88	68.33	70.29	78.02	73.40	71.67
Or	3.47	2.59	2.93	1.98	2.72	1.81	0.00	3.44	4.68	4.10	3.08	2.93	2.94	12.12	3.95

031219-4 CRX16 C (46)	031219-4 CRX16 R (47)	031219-4 CRX17 (1)	031219-4 CRX17 (2)	031219-4 CRX17 (9)	031219-4 CRX17 (10)	031219-4 CRX17 (16)	031219-4 CRX17 (17)	031219-4 CRX14 (20)	031219-4 CRX14 (21)	031219-4 CRX19 (30)	031219-4 CRX22 (42)	031219-4 CRX22 (43)	031219-4 CRX22 (44)	031219-4 CRX23 C (49)
MPC	MPC	GM	GM	MPC	GM	GM	GM	MPC	MPC	GM	MPC	MPC	MPC	PC
61.34	60.89	66.18	64.25	62.60	63.99	68.79	67.53	62.56	62.06	66.00	62.19	61.68	61.36	62.26
24.96	24.58	20.46	20.58	23.54	22.53	18.58	19.25	23.70	24.04	21.57	24.17	24.49	25.43	23.40
	0.17	0.31	1.69											
3.75	3.15	2.07	3.29	5.90	4.81	1.39	1.37	3.92	3.74	2.75	5.15	4.72	4.75	2.77
9.69	10.77	8.78	7.75	7.31	7.61	8.05	7.93	9.23	9.56	8.43	7.92	8.57	7.90	10.91
0.26	0.44	2.21	2.44	0.65	1.06	3.18	3.92	0.59	0.61	1.26	0.56	0.54	0.57	0.67
100.00	100.00	100.01	100.00	100.00	100.00	99.99	100.00	100.00	100.01	100.01	99.99	100.00	100.01	100.01
17.37	13.60	10.05	16.27	29.64	24.24	7.04	6.72	18.38	17.18	14.10	25.56	22.61	24.08	11.88
81.20	84.14	77.17	69.36	66.47	69.40	73.78	70.39	78.32	79.48	78.21	71.13	74.30	72.48	84.69
1.43	2.26	12.78	14.37	3.89	6.36	19.18	22.89	3.29	3.34	7.69	3.31	3.08	3.44	3.42
031219-4 CRX23 (51)	031219-4 CRX23 (52)	031219-4 CRX23 (54)	031219-4 CRX23 C (55)	031219-4 CRX23 (57)	031219-4 CRX23 (58)	031219-4 CRX8 (61)	031219-4 CRX8 (62)	031219-4 CRX30 (1)	031219-4 CRX30 (4)	031219-4 CRX31 (4)	031219-4 CRX32 (4)	031219-4 CRX33 (3)	031219-4 CRX33 (4)	031219-4 CRX34 (5)
GM	GM	GM	PC	GM	GM	GM	GM	GM	GM	GM	GM	GM	GM	GM
67.64	66.11	68.72	63.69	68.27	65.60	65.55	64.76	64.34	64.93	66.49	66.50	67.71	66.47	65.44
19.54	21.23	18.64	23.25	18.92	21.19	21.45	21.60	22.12	21.46	20.15	20.35	18.54	20.44	21.16
								0.38	0.55	0.36	0.64	1.51	0.57	0.67
1.32	2.93	2.03	4.73	2.07	2.65	2.01	2.40	4.78	3.74	2.93	2.87	1.61	3.12	3.69
8.42	7.79	7.58	7.43	8.28	9.13	9.62	9.80	7.31	7.70	7.66	7.51	5.87	7.56	7.44
3.08	1.94	3.03	0.90	2.47	1.43	1.38	1.43	1.06	1.62	2.40	2.13	4.75	1.84	1.60
100.00	100.00	100.00	100.00	100.01	100.00	100.01	99.99	99.99	100.00	99.99	100.00	99.99	100.00	100.00
6.53	15.15	10.49	24.58	10.35	12.69	9.54	10.99	24.80	19.08	14.91	15.11	9.00	16.43	19.36
75.34	72.90	70.87	69.86	74.94	79.15	82.65	81.21	68.65	71.08	70.55	71.54	59.38	72.04	70.64
18.13	11.95	18.64	5.57	14.71	8.16	7.80	7.80	6.55	9.84	14.54	13.35	31.62	11.54	10.00

031219-4	031219-4	031219-4	031219-4	031219-4	031219-4	031219-4	031219-4	031219-4	031219-4	031219-4	031219-4	031219-4	031219-4	031219-4
CRX34 (7)	CRX35 (1)	CRX35 (2)	CRX36 (3)	CRX36 (4)	CRX38 (8)	CRX38 (9)	CRX39 (3)	CRX39 (4)	CRX40 (4)	CRX40 (5)	CRX41 (6)	CRX41 (7)	CRX42 (1)	CRX42 (2)
GM	GM	GM	GM	GM	GM	GM	GM	GM	GM	GM	GM	GM	GM	GM
66.42	63.90	66.39	66.36	65.94	65.95	67.13	66.22	66.92	66.50	66.15	67.49	65.81	60.95	61.48
20.62	22.18	20.53	20.78	20.81	20.82	19.90	20.63	20.09	20.45	20.54	18.59	20.78	24.36	23.99
0.52	0.40	0.45	0.45	0.43	0.44	0.44	0.58	0.36	0.42	0.64	0.42	0.58	0.32	0.33
3.02	5.26	3.03	3.15	3.34	3.29	2.65	3.30	2.90	3.02	3.05	1.46	3.17	7.38	6.89
7.43	7.16	7.46	7.29	7.66	7.78	7.46	7.52	7.46	7.62	7.61	6.94	7.69	6.44	6.68
1.99	1.10	2.14	1.97	1.82	1.72	2.42	1.74	2.26	1.99	2.01	5.10	1.96	0.54	0.62
100.00	100.00	100.00	100.00	100.00	100.00	100.00	99.99	99.99	100.00	100.00	100.00	99.99	99.99	99.99
16.03	26.94	15.88	16.86	17.24	16.94	13.92	17.39	15.19	15.75	15.87	7.27	16.32	37.51	34.95
71.39	66.35	70.76	70.59	71.57	72.51	70.93	71.70	70.71	71.90	71.67	62.51	71.66	59.23	61.31
12.58	6.71	13.36	12.55	11.19	10.55	15.14	10.92	14.10	12.35	12.46	30.22	12.02	3.27	3.74

031219-4	031219-4	031219-4	031219-4	031219-4	031219-4	031219-4	031219-4	031219-4	031219-4	031219-4	031219-4	031219-4	031219-4	031219-4
CRX42 (4)	CRX43 (4)	CRX43 (5)	CRX44 (1)	CRX44 (2)	CRX44 (6)	CRX45 (1)	CRX45 (2)	CRX46 (5)	CRX46 (6)	CRX47 (3)	CRX47 (4)	CRX48 (4)	CRX48 (5)	
GM	GM	GM	GM	GM	GM	GM	GM	GM	GM	GM	GM	GM	GM	
63.82	66.11	66.61	66.21	66.80	66.31	65.29	67.49	65.66	66.37	65.22	65.45	66.16	66.40	
22.18	20.50	20.27	20.58	20.22	20.33	21.35	19.79	21.02	20.58	20.98	21.16	20.67	20.16	
0.59	0.34	0.47	0.56	0.33	0.54	0.43	0.39	0.50	0.34	0.46	0.46	0.46	0.55	
5.04	2.91	3.20	3.14	2.22	2.85	4.01	2.25	3.33	2.94	4.10	3.54	3.13	2.87	
7.39	7.61	7.60	7.59	7.10	7.91	7.52	7.13	7.83	7.84	7.48	7.75	7.82	7.64	
0.98	2.54	1.85	1.93	3.34	2.07	1.40	2.95	1.66	1.92	1.75	1.65	1.76	2.38	
100.00	100.01	100.00	100.01	100.01	100.01	100.00	100.00	100.00	99.99	99.99	100.01	100.00	100.00	
25.74	14.77	16.71	16.38	11.66	14.52	20.79	12.05	17.10	15.14	20.79	18.13	16.15	14.70	
68.30	69.88	71.80	71.64	67.46	72.92	70.56	69.13	72.75	73.08	68.64	71.81	73.03	70.79	
5.96	15.35	11.50	11.99	20.88	12.56	8.64	18.82	10.15	11.78	10.57	10.06	10.82	14.51	

Sample Crystal/Zone [C: Core, R: Rim] Type [PC: phenocryst, MPC: microphenocryst, GM: groundmass]	051219-1	051219-1	051219-1	051219-1	051219-1	051219-1	051219-1	051219-1	051219-1	051219-1	051219-1	051219-1	051219-1	051219-1	051219-1
	CRX1 C (1)	CRX1 R1 (2)	CRX1 R2 (3)	CRX2 C (4)	CRX2 R1 (5)	CRX2 R2 (6)	CRX3 C (7)	CRX3 R1 (8)	CRX3 R2 (9)	CRX4 C (10)	CRX4 R1 (11)	CRX4 R2 (12)	CRX8 C1 (1)	CRX8 R1 (2)	CRX8 R2 (3)
	PC	PC	PC	PC	PC	PC	PC	PC	PC	PC	PC	PC	PC	PC	PC
SiO2	52.66	53.75	53.94	53.95	53.65	53.76	55.06	55.19	54.95	52.75	53.15	53.60	48.74	51.80	52.06
Al2O3	30.19	29.25	29.23	29.17	29.37	29.36	28.20	28.04	28.58	30.13	29.95	29.73	32.41	30.29	30.12
FeO		0.50	0.34	0.40					0.32				0.27	0.41	0.39
CaO	13.72	12.99	12.75	12.89	13.23	12.75	12.00	12.72	12.07	13.89	13.43	13.36	16.55	14.15	13.95
Na2O	3.43	3.51	3.75	3.59	3.75	3.88	4.21	4.04	4.19	3.24	3.47	3.31	2.02	3.35	3.29
K2O						0.25	0.21		0.20						0.19
Total	100.00	100.00	100.01	100.00	100.00	100.00	100.00	99.99	99.99	100.01	100.00	100.00	100.00	100.00	100.00
An	68.85	67.16	65.26	66.49	66.10	63.53	60.40	63.50	60.68	70.32	68.14	69.04	81.88	70.04	69.33
Ab	31.15	32.84	34.74	33.51	33.90	34.99	38.34	36.50	38.12	29.68	31.86	30.96	18.12	29.96	29.54
Or	0.00	0.00	0.00	0.00	0.00	1.48	1.26	0.00	1.20	0.00	0.00	0.00	0.00	0.00	1.13

051219-1	051219-1	051219-1	051219-1	051219-1	051219-1	051219-1	051219-1	051219-1	051219-1	051219-1	051219-1	051219-1	051219-1	051219-1	051219-1
CRX8 C2 (4)	CRX8 R3 (5)	CRX9 C1 (6)	CRX9 R (7)	CRX9 C2 (8)	CRX14 C (25)	CRX14 R1 (26)	CRX14 R2 (27)	CRX15 C (28)	CRX15 R (29)	CRX16 C (30)	CRX16 R (31)	CRX16 (32)	CRX18 C (36)	CRX18 R1 (37)	
PC	PC	PC	PC	PC	PC	PC	PC	PC	PC	PC	PC	PC	MPC	PC	PC
49.37	48.87	50.27	50.92	51.17	53.54	53.12	52.78	55.45	52.73	55.89	52.50	54.33	56.64	53.83	
31.94	32.01	31.49	30.85	31.06	29.17	29.46	29.67	28.08	29.80	27.66	29.90	28.64	27.19	28.99	
0.43	0.41	0.22	0.36		0.37	0.50	0.50	0.33	0.46	0.43	0.42	0.54	0.30	0.35	
15.78	16.56	15.38	15.00	14.80	12.94	13.51	13.61	11.63	13.75	11.34	13.87	12.49	10.65	12.93	
2.48	2.15	2.65	2.87	2.97	3.78	3.41	3.29	4.29	3.27	4.46	3.31	3.84	4.88	3.72	
					0.20		0.15	0.22		0.22		0.17	0.34	0.17	
100.00	100.00	100.00	100.00	100.00	100.00	100.00	100.00	100.00	100.01	100.00	100.00	100.01	100.00	99.99	
77.88	80.94	76.22	74.25	73.39	64.64	68.65	68.94	59.17	69.91	57.64	69.84	63.59	53.56	65.09	
22.12	19.06	23.78	25.75	26.61	34.17	31.35	30.16	39.50	30.09	41.03	30.16	35.38	44.41	33.89	
0.00	0.00	0.00	0.00	0.00	1.19	0.00	0.90	1.33	0.00	1.33	0.00	1.03	2.04	1.02	

051219-1	051219-1	051219-1	051219-1	051219-1	051219-1	051219-1	051219-1	051219-1	051219-1	051219-1	051219-1	051219-1	051219-1	051219-1
CRX18 R2 (38)	CRX20 C (41)	CRX20 R (42)	CRX21 (1)	CRX21 (2)	CRX21 (3)	CRX22 (10)	CRX22 (11)	CRX22 (13)	CRX23 (18)	CRX23 (19)	CRX24 (22)	CRX24 (24)	CRX25 (9)	CRX25 C (12)
PC	PC	PC	GM	GM	GM	GM	GM	GM	GM	GM	GM	GM	GM	PC
52.43	54.71	53.09	55.05	57.21	55.75	56.88	55.46	56.97	57.32	55.70	55.39	53.60	55.43	52.92
29.95	28.58	29.54	29.84	28.31	30.34	29.55	30.92	29.19	29.07	30.22	31.26	30.08	27.81	29.92
0.53	0.39	0.48		0.43				0.33		0.30		0.54	0.72	
13.89	12.20	13.61	10.84	8.43	8.64	7.73	9.11	7.18	7.59	8.38	8.84	12.10	11.82	13.66
3.20	4.12	3.28	4.27	5.62	5.27	5.83	4.52	6.32	6.02	5.40	4.51	3.68	4.22	3.50
100.00	100.00	100.00	100.00	100.00	100.00	99.99	100.01	99.99	100.00	100.00	100.00	100.00	100.00	100.00
70.58	62.07	69.63	58.38	45.32	47.53	42.29	52.69	38.57	41.06	46.17	52.00	64.50	60.75	68.32
29.42	37.93	30.37	41.62	54.68	52.47	57.71	47.31	61.43	58.94	53.83	48.00	35.50	39.25	31.68
0.00	0.00	0.00	0.00	0.00	0.00	0.00	0.00	0.00	0.00	0.00	0.00	0.00	0.00	0.00

051219-1	051219-1	051219-1	051219-1	051219-1	051219-1	051219-1	051219-1	051219-1	051219-1	051219-1	051219-1	051219-1	051219-1	051219-1
CRX25 R (13)	CRX26 (3)	CRX27 (1)	CRX27 (2)	CRX28 (5)	CRX29 (3)	CRX29 (5)	CRX30 (3)	CRX31 (6)	CRX32 (3)	CRX33 (3)	CRX34 C (1)	CRX34 C (2)	CRX34 R (3)	CRX34 R (4)
PC	GM	GM	GM	GM	GM	GM	GM	GM	GM	GM	PC	PC	PC	PC
52.98	52.60	53.16	52.68	52.93	52.74	52.87	53.61	52.30	52.81	55.58	54.45	53.66	52.22	53.44
29.64	29.72	29.31	29.84	29.53	29.65	29.81	29.13	30.23	29.50	27.80	29.21	29.48	30.19	29.06
0.39	0.66	0.52	0.47	0.52	0.61	0.56	0.52	0.50	0.68	0.62			0.37	0.57
13.45	13.64	13.54	13.69	13.81	13.64	13.40	13.16	13.73	13.55	11.43	12.61	13.31	14.15	13.21
3.53	3.39	3.46	3.31	3.22	3.36	3.35	3.58	3.24	3.47	4.34	3.74	3.55	3.07	3.73
										0.23				
99.99	100.01	99.99	99.99	100.01	100.00	99.99	100.00	100.00	100.01	100.00	100.01	100.00	100.00	100.01
67.80	68.98	68.38	69.56	70.33	69.17	68.85	67.01	70.08	68.33	58.44	65.07	67.45	71.81	66.18
32.20	31.02	31.62	30.44	29.67	30.83	31.15	32.99	29.92	31.67	40.16	34.93	32.55	28.19	33.82
0.00	0.00	0.00	0.00	0.00	0.00	0.00	0.00	0.00	0.00	1.40	0.00	0.00	0.00	0.00

051219-1	051219-1	051219-1	051219-1
CRX35 C (1)	CRX35 R (2)	CRX35 C (3)	CRX35 R (4)
PC	PC	PC	PC
55.56	51.44	55.12	53.55
28.37	30.92	28.27	29.39
	0.39	0.45	0.45
11.57	14.23	11.74	13.07
4.50	3.02	4.41	3.54
100.00	100.00	99.99	100.00
58.69	72.25	59.53	67.11
41.31	27.75	40.47	32.89
0.00	0.00	0.00	0.00

Sample Crystal/Zone [C: Core, R: Rim] Type [PC: phenocryst, MPC: microphenocryst, GM: groundmass]	051219-8 CRX5 C (17)	051219-8 CRX5 R (18)	051219-8 CRX7 C (21)	051219-8 CRX7 R (22)	051219-8 CRX8 C (23)	051219-8 CRX8 R (24)	051219-8 CRX9 C (25)	051219-8 CRX9 R (26)	051219-8 CRX10 C (27)	051219-8 CRX10 R (28)	051219-8 CRX12 C (31)	051219-8 CRX12 R (32)	051219-8 CRX15 C (38)	051219-8 CRX15 R (39)	051219-8 CRX17 (2)
	PC	PC	PC	PC	PC	PC	PC	PC	PC	PC	PC	PC	PC	PC	GM
SiO2	54.27	54.67	52.82	52.93	52.79	51.64	51.96	54.63	52.54	52.58	54.46	53.21	53.29	52.78	55.74
Al2O3	28.84	28.55	29.90	29.76	29.60	30.35	30.19	28.45	29.96	29.97	28.60	29.46	29.56	29.60	29.95
FeO		0.37	0.27	0.30	0.43	0.42	0.42	0.54	0.46	0.37	0.36	0.57	0.28	0.37	0.45
MgO															
CaO	13.07	12.33	13.74	13.55	13.85	14.49	14.24	12.35	13.85	13.85	12.52	13.20	13.34	13.76	8.11
Na2O	3.81	4.09	3.28	3.47	3.33	3.10	3.19	4.04	3.18	3.23	4.06	3.56	3.53	3.47	5.76
K2O															
Total	99.99	100.01	100.01	100.01	100.00	100.00	100.00	100.01	99.99	100.00	100.00	100.00	100.00	99.98	100.01
An	65.47	62.49	69.83	68.33	69.68	72.09	71.15	62.82	70.65	70.32	63.02	67.20	67.62	68.66	43.76
Ab	34.53	37.51	30.17	31.67	30.32	27.91	28.85	37.18	29.35	29.68	36.98	32.80	32.38	31.34	56.24
Or	0.00	0.00	0.00	0.00	0.00	0.00	0.00	0.00	0.00	0.00	0.00	0.00	0.00	0.00	0.00

051219-8 CRX17 (3)	051219-8 CRX17 (4)	051219-8 CRX17 (5)	051219-8 CRX17 (6)	051219-8 CRX18 (8)	051219-8 CRX18 (9)	051219-8 CRX18 (10)	051219-8 CRX18 (13)	051219-8 CRX19 C (3)	051219-8 CRX19 R (4)	051219-8 CRX19 (6)	051219-8 CRX20 (10)	051219-8 CRX20 (13)	051219-8 CRX21 (18)	051219-8 CRX22 C (22)
GM	GM	GM	GM	GM	GM	GM	GM	PC	PC	GM	GM	GM	GM	PC
55.79	56.08	56.79	56.14	55.81	63.84	58.33	55.52	52.35	53.41	55.03	57.35	53.85	54.94	53.46
30.38	30.32	28.80	30.28	29.87	22.43	27.22	29.36	29.94	29.19	28.02	26.58	28.87	28.18	29.59
	0.37	0.46		0.35		0.52	0.63	0.53	0.53	0.73	0.80	0.71	0.78	
8.27	7.75	7.77	8.16	8.64	2.94	7.07	9.16	13.82	13.29	11.69	9.65	12.73	11.78	13.42
5.56	5.48	6.19	5.42	5.33	10.19	6.56	5.34	3.36	3.57	4.31	5.35	3.84	4.31	3.53
					0.60	0.30				0.23	0.27			
100.00	100.00	100.01	100.00	100.00	100.00	100.00	100.01	100.00	99.99	100.01	100.00	100.00	99.99	100.00
45.11	43.87	40.96	45.41	47.25	13.31	36.64	48.66	69.45	67.29	59.15	49.10	64.69	60.17	67.75
54.89	56.13	59.04	54.59	52.75	83.46	61.51	51.34	30.55	32.71	39.46	49.26	35.31	39.83	32.25
0.00	0.00	0.00	0.00	0.00	3.23	1.85	0.00	0.00	0.00	1.39	1.64	0.00	0.00	0.00
051219-8 CRX22 R (23)	051219-8 CRX22 (26)	051219-8 CRX23 (29)	051219-8 CRX24 C (32)	051219-8 CRX24 R (33)	051219-8 CRX25 R (38)	051219-8 CRX25 C (39)	051219-8 CRX26 (42)	051219-8 CRX26 R (44)	051219-8 CRX26 C (45)	051219-8 CRX27 (50)	051219-8 CRX28 (53)	051219-8 CRX28 (54)	051219-8 CRX29 (59)	051219-8 CRX30 (65)
PC	GM	GM	PC	PC	GM	GM	GM	GM	GM	GM	GM	GM	GM	GM
55.72	57.34	53.93	54.63	54.53	66.18	54.26	60.91	64.35	53.07	54.77	54.16	55.06	54.81	54.16
27.73	26.45	28.67	28.60	28.50	20.70	28.54	24.19	21.93	29.50	28.29	28.71	28.10	26.48	28.63
0.68	0.60	0.72	0.42	0.42	0.74	0.77	0.75	0.46	0.76	0.76	0.56	0.75	2.06	0.71
													1.09	
11.25	10.28	12.69	12.33	12.54	2.93	12.33	7.05	4.38	12.76	11.94	12.53	11.67	10.85	12.46
4.62	5.00	3.80	4.03	4.01	7.89	4.10	6.59	7.74	3.91	4.24	3.82	4.41	4.72	4.03
	0.33	0.20			1.56		0.50	1.15			0.22			
100.00	100.00	100.01	100.01	100.00	100.00	100.00	99.99	100.01	100.00	100.00	100.00	99.99	100.01	99.99
57.37	52.13	64.08	62.84	63.34	15.37	62.43	36.02	22.17	64.33	60.88	63.59	59.39	55.95	63.08
42.63	45.88	34.72	37.16	36.66	74.89	37.57	60.93	70.90	35.67	39.12	35.08	40.61	44.05	36.92
0.00	1.99	1.20	0.00	0.00	9.74	0.00	3.04	6.93	0.00	0.00	1.33	0.00	0.00	0.00

051219-8	051219-8	051219-8	051219-8	051219-8	051219-8	051219-8	051219-8	051219-8	051219-8	051219-8	051219-8	051219-8
CRX30 C (66)	CRX30 R (67)	CRX31 C (68)	CRX31 R (69)	CRX31 (71)	CRX32 (74)	CRX33 (78)	CRX34 (81)	CRX35 (83)	CRX36 (87)	CRX37 (93)	CRX38 (96)	CRX39 (99)
PC	PC	PC	PC	GM	GM	GM	GM	GM	GM	GM	GM	GM
52.56	51.83	54.42	54.11	53.80	54.03	53.61	54.17	54.62	55.12	53.81	53.64	53.87
29.70	30.52	28.73	29.07	28.90	28.83	28.84	28.09	28.58	27.94	29.13	29.20	29.08
0.38	0.50		0.46	0.63	0.52	0.76	0.78	0.70	0.58	0.60	0.54	0.48
13.90	14.26	12.77	12.52	12.90	12.74	12.76	12.30	11.99	11.93	12.61	12.84	12.87
3.46	2.89	4.07	3.83	3.77	3.87	4.03	4.45	4.12	4.43	3.85	3.78	3.71
							0.21					
100.00	100.00	99.99	99.99	100.00	99.99	100.00	100.00	100.01	100.00	100.00	100.00	100.01
68.94	73.17	63.42	64.37	65.41	64.53	63.63	59.70	61.66	59.81	64.41	65.24	65.72
31.06	26.83	36.58	35.63	34.59	35.47	36.37	39.09	38.34	40.19	35.59	34.76	34.28
0.00	0.00	0.00	0.00	0.00	0.00	0.00	1.21	0.00	0.00	0.00	0.00	0.00

Sample Crystal/Zone [C: Core, R: Rim] Type [PC: phenocryst, MPC: microphenocryst, GM: groundmass]	230220-2 CRX6 C (15)	230220-2 CRX6 R (16)	230220-2 CRX16 (42)	230220-2 CRX18 C (46)	230220-2 CRX18 R (47)	230220-2 CRX19 C (49)	230220-2 CRX19 R (50)	230220-2 CRX22 (1)	230220-2 CRX22 (2)	230220-2 CRX22 (3)	230220-2 CRX22 (7)	230220-2 CRX23 (13)	230220-2 CRX24 (20)	230220-2 CRX24 (21)	230220-2 CRX25 (1)
	PC	PC	GM	PC	PC	PC	PC	GM	GM	GM	GM	GM	GM	GM	GM
SiO2	53.69	52.73	55.69	53.18	53.56	52.65	56.35	58.19	56.14	57.72	54.44	55.34	57.47	56.91	52.87
TiO2															
Al2O3	29.56	29.71	27.58	29.49	29.18	29.79	26.89	28.51	30.20	28.73	27.66	31.36	29.05	29.28	29.51
FeO		0.54	0.61	0.42	0.56	0.40	0.55							0.37	0.49
CaO	13.22	13.65	11.30	13.40	12.96	13.78	11.05	6.93	7.95	7.65	5.85	8.07	7.60	7.39	13.78
Na2O	3.54	3.38	4.50	3.51	3.74	3.37	4.80	6.37	5.71	5.90	10.09	5.24	5.63	6.06	3.35
K2O			0.31				0.37							0.25	
Total	100.01	100.01	99.99	100.00	100.00	99.99	100.01	100.00	100.00	100.00	98.04	100.01	100.00	100.01	100.00
An	67.36	69.06	57.04	67.84	65.69	69.32	54.77	37.55	43.48	41.74	24.26	45.98	42.02	40.26	69.45
Ab	32.64	30.94	41.10	32.16	34.31	30.68	43.05	62.45	56.52	58.26	75.74	54.02	56.33	59.74	30.55
Or	0.00	0.00	1.86	0.00	0.00	0.00	2.18	0.00	0.00	0.00	0.00	0.00	1.65	0.00	0.00

230220-2	230220-2	230220-2	230220-2	230220-2	230220-2	230220-2	230220-2	230220-2	230220-2	230220-2	230220-2	230220-2	230220-2	230220-2
CRX25 (2)	CRX26 C (3)	CRX26 R (4)	CRX26 (6)	CRX27 C (1)	CRX27 R (2)	CRX27 C (3)	CRX27 R (4)	CRX27 (7)	CRX28 C (1)	CRX28 R (2)	CRX28 (3)	CRX29 (1)	CRX29 (2)	CRX30 C (1)
GM	PC	PC	GM	PC	PC	PC	PC	GM	PC	PC	GM	GM	GM	PC
53.65	53.30	54.73	53.46	53.02	54.96	52.86	55.32	53.99	53.52	54.53	55.41	54.83	54.56	53.41
29.10	29.35	28.19	28.94	29.40	27.98	29.65	27.57	28.58	29.09	28.45	27.53	28.05	28.24	29.22
0.43	0.50	0.58	0.56	0.42	0.61	0.46	0.67	0.52	0.50	0.49	0.79	0.60	0.56	0.50
13.20	13.45	12.14	13.19	13.57	11.99	13.73	11.97	12.89	13.24	12.33	11.60	12.17	12.35	13.46
3.63	3.41	4.14	3.68	3.43	4.21	3.30	4.22	3.80	3.64	3.98	4.40	4.10	4.04	3.41
		0.23	0.17	0.16	0.25		0.24	0.23		0.22	0.27	0.25	0.25	
100.01	100.01	100.01	100.00	100.00	100.00	100.00	99.99	100.01	99.99	100.00	100.00	100.00	100.00	100.00
66.77	68.55	60.99	65.78	67.96	60.23	69.69	60.17	64.32	66.78	62.29	58.34	61.20	61.88	68.57
33.23	31.45	37.64	33.21	31.09	38.27	30.31	38.39	34.31	33.22	36.39	40.04	37.31	36.63	31.43
0.00	0.00	1.38	1.01	0.95	1.50	0.00	1.44	1.37	0.00	1.32	1.62	1.50	1.49	0.00
230220-2	230220-2	230220-2	230220-2	230220-2	230220-2	230220-2	230220-2	230220-2	230220-2	230220-2	230220-2	230220-2	230220-2	230220-2
CRX30 R (2)	CRX30 (4)	CRX31 (1)	CRX31 C (2)	CRX31 R (3)	CRX32 C (1)	CRX32 R (2)	CRX32 (4)	CRX33 (5)	CRX34 C (1)	CRX34 R (2)	CRX34 (5)	CRX34 (6)	CRX35 (1)	CRX35 (2)
PC	GM	GM	GM	GM	PC	PC	GM	GM	PC	PC	GM	GM	GM	GM
52.78	54.64	54.90	54.81	66.92	52.53	55.37	56.50	54.07	53.00	54.62	52.83	54.29	53.54	53.99
				0.38										
29.58	28.23	28.19	28.17	19.86	29.81	27.76	27.00	28.60	29.49	28.29	29.68	28.52	29.20	28.67
0.48	0.57	0.50	0.51	0.58	0.41	0.45	0.61	0.65	0.47	0.51	0.52	0.55	0.50	0.63
13.65	12.33	12.16	12.13	2.33	13.93	11.76	10.84	12.54	13.64	12.31	13.72	12.50	13.19	12.72
3.34	4.01	4.03	4.13	6.95	3.34	4.33	4.74	3.92	3.39	4.02	3.25	3.92	3.57	3.74
0.17	0.22	0.23	0.25	2.99		0.32	0.32	0.22		0.24		0.23		0.24
100.00	100.00	100.01	100.00	100.01	100.02	99.99	100.01	100.00	99.99	99.99	100.00	100.01	100.00	99.99
68.60	62.12	61.64	60.95	12.62	69.74	58.87	54.75	63.03	68.98	61.95	70.00	62.92	67.12	64.33
30.38	36.56	36.97	37.55	68.10	30.26	39.22	43.32	35.65	31.02	36.61	30.00	35.70	32.88	34.23
1.02	1.32	1.39	1.50	19.28	0.00	1.91	1.92	1.32	0.00	1.44	0.00	1.38	0.00	1.45

230220-2	230220-2	230220-2	230220-2	230220-2	230220-2	230220-2	230220-2	230220-2	230220-2	230220-2	230220-2	230220-2	230220-2	230220-2
CRX36 C (1)	CRX36 R (2)	CRX36 (3)	CRX37 (1)	CRX37 (2)	CRX38 (1)	CRX38 (2)	CRX39 (1)	CRX39 (2)	CRX40 (1)	CRX40 (2)	CRX41 R (6)	CRX41 C (7)	CRX42 (1)	CRX42 (2)
PC	PC	GM	GM	GM	GM	GM	GM	GM	GM	GM	GM	GM	GM	GM
53.11	53.19	54.34	53.49	54.22	54.95	56.70	54.72	55.80	55.37	56.33	65.65	55.02	54.59	53.79
29.52	29.29	28.51	29.02	28.19	27.98	26.52	28.16	27.33	27.46	26.70	0.33	20.66	27.93	28.80
0.42	0.50	0.46	0.49	0.97	0.59	0.90	0.55	0.64	0.66	0.99	0.77	0.62	0.58	0.58
13.55	13.57	12.50	13.10	12.36	11.94	10.66	12.05	11.29	11.91	11.02	3.33	11.94	12.25	12.81
3.40	3.45	3.96	3.69	3.99	4.27	4.81	4.22	4.61	4.35	4.66	7.26	4.24	4.06	3.81
		0.23	0.21	0.28	0.27	0.42	0.30	0.34	0.24	0.31	1.99	0.26	0.23	0.22
100.00	100.00	100.00	100.00	100.01	100.00	100.01	100.00	100.01	99.99	100.01	99.99	100.01	100.00	100.01
68.77	68.49	62.69	65.41	62.07	59.73	53.66	60.12	56.35	59.35	55.60	17.68	59.93	61.65	64.16
31.23	31.51	35.94	33.34	36.26	38.66	43.82	38.10	41.63	39.23	42.54	69.74	38.51	36.97	34.53
0.00	0.00	1.37	1.25	1.67	1.61	2.52	1.78	2.02	1.42	1.86	12.58	1.55	1.38	1.31

Sample Crystal/Zone [C: Core, R: Rim] Type [PC: phenocryst, MPC: microphenocryst, GM: groundmass]	240220-2 CRX1 (3)	240220-2 CRX1 (4)	240220-2 CRX3 C (7)	240220-2 CRX3 R (8)	240220-2 CRX7 C (5)	240220-2 CRX7 R (6)	240220-2 CRX9 C1 (8)	240220-2 CRX9 C2 (9)	240220-2 CRX9 R1 (10)	240220-2 CRX9 R2 (11)	240220-2 CRX10 (35)	240220-2 CRX11 C1 (14)	240220-2 CRX11 C2 (17)	240220-2 CRX16 C1 (18)	240220-2 CRX16 C2 (19)
	GM	GM	PC	PC	PC	PC	PC	PC	PC	PC	GM	PC	PC	PC	PC
SiO2	54.10	52.59	53.55	52.98	64.79	62.61	65.32	65.10	63.50	62.29	52.73	63.96	62.61	59.87	59.82
Al2O3	29.06	29.70	29.42	29.71	22.07	23.44	21.47	21.65	22.49	23.44	29.89	22.49	23.45	25.68	25.37
FeO	0.47	0.66	0.37	0.51						0.50	0.70			0.34	0.36
MgO															
CaO	12.17	13.47	13.05	13.32	3.74	4.54	2.80	3.07	4.38	5.28	13.34	4.09	5.16	6.19	7.56
Na2O	4.20	3.56	3.61	3.49	8.74	8.39	8.70	8.38	8.30	7.68	3.34	8.35	7.90	7.64	6.50
K2O					0.66	1.01	1.72	1.79	1.32	0.82		1.10	0.88	0.28	0.39
Total	100.00	99.98	100.00	100.01	100.00	99.99	100.01	99.99	99.99	100.01	100.00	99.99	100.00	100.00	100.00
An	61.56	67.65	66.64	67.84	18.39	21.70	13.60	15.07	20.89	26.20	68.82	19.94	25.17	30.42	38.21
Ab	38.44	32.35	33.36	32.16	77.75	72.56	76.46	74.46	71.62	68.96	31.18	73.67	69.72	67.94	59.45
Or	0.00	0.00	0.00	0.00	3.86	5.75	9.95	10.47	7.49	4.84	0.00	6.39	5.11	1.64	2.35

240220-2	240220-2	240220-2	240220-2	240220-2	240220-2	240220-2	240220-2	240220-2	240220-2	240220-2	240220-2	240220-2	240220-2	240220-2
CRX16 R1 (20)	CRX16 R2 (21)	CRX18 C (56)	CRX18 R (57)	CRX20 C (24)	CRX20 R (25)	CRX21 (27)	CRX21 (28)	CRX21 (29)	CRX21 (33)	CRX22 C (1)	CRX22 R (2)	CRX22 (4)	CRX23 (9)	CRX24 (12)
PC	PC	PC	PC	PC	PC	GM	GM	GM	GM	PC	PC	GM	GM	GM
61.09	58.97	52.82	52.12	52.36	53.71	54.40	54.97	54.57	54.70	59.75	60.91	53.51	53.94	54.24
24.14	26.47	29.70	30.17	30.61	30.71	29.44	29.85	28.82	30.28	25.14	24.42	29.20	28.90	27.89
0.48	0.41	0.32	0.49	0.41	0.39	0.69	0.55	0.55	0.54	0.42	0.61	0.61	0.81	1.26
														0.47
6.05	6.77	13.69	14.18	13.53	11.61	10.66	9.73	11.18	10.08	8.27	6.97	12.56	12.41	11.57
7.84	7.04	3.47	3.04	3.09	3.57	4.57	4.62	4.67	4.39	5.95	6.41	3.88	3.93	4.24
0.40	0.33					0.24	0.28	0.22		0.46	0.69	0.23		0.33
100.00	99.99	100.00	100.00	100.00	99.99	100.00	100.00	100.01	99.99	99.99	100.01	99.99	99.99	100.00
29.21	34.02	68.56	72.05	70.76	64.25	55.48	52.81	56.20	55.92	42.23	35.94	63.26	63.57	58.92
68.49	64.01	31.44	27.95	29.24	35.75	43.04	45.38	42.48	44.08	54.98	59.82	35.36	36.43	39.08
2.30	1.97	0.00	0.00	0.00	0.00	1.49	1.81	1.32	0.00	2.80	4.24	1.38	0.00	2.00
240220-2	240220-2	240220-2	240220-2	240220-2	240220-2	240220-2	240220-2	240220-2	240220-2	240220-2	240220-2	240220-2	240220-2	240220-2
CRX25 (15)	CRX25 (18)	CRX26 C (21)	CRX26 R (22)	CRX26 (23)	CRX27 (29)	CRX28 (31)	CRX28 (36)	CRX29 C (37)	CRX29 C (38)	CRX29 R (39)	CRX29 R (40)	CRX30 (46)	CRX31 (48)	CRX31 (51)
GM	GM	PC	PC	GM	GM	GM	GM	PC	PC	PC	PC	GM	GM	GM
53.12	52.69	51.99	51.98	52.56	52.64	52.89	53.62	51.48	52.10	52.73	53.60	56.52	53.05	53.67
29.45	29.66	30.41	30.12	29.96	29.77	29.41	28.75	30.78	30.48	29.71	29.35	27.09	29.36	28.94
0.74	0.62	0.36	0.58	0.77	0.79	0.81	1.00	0.53	0.30	0.41	0.38	0.81	0.73	0.92
13.12	13.44	14.18	13.98	13.53	13.22	13.35	12.72	14.38	14.20	13.63	12.83	10.47	13.14	12.49
3.57	3.38	3.06	3.14	3.18	3.35	3.53	3.64	2.83	2.91	3.52	3.63	4.80	3.49	3.98
	0.21		0.19		0.22		0.27				0.20	0.31	0.22	
100.00	100.00	100.00	99.99	100.00	99.99	99.99	100.00	100.00	99.99	100.00	99.99	100.00	99.99	100.00
67.01	67.86	71.92	70.29	70.16	67.64	67.64	64.80	73.74	72.95	68.15	65.34	53.62	66.64	63.43
32.99	30.88	28.08	28.57	29.84	31.02	32.36	33.56	26.26	27.05	31.85	33.45	44.49	32.03	36.57
0.00	1.26	0.00	1.14	0.00	1.34	0.00	1.64	0.00	0.00	0.00	1.21	1.89	1.33	0.00

240220-2	240220-2	240220-2	240220-2	240220-2	240220-2
CRX34 (63)	CRX35 (65)	CRX9 C (67)	CRX9 C (68)	CRX9 C (69)	CRX9 R (70)
GM	GM	PC	PC	PC	PC
52.23	53.37	66.90	64.76	66.07	61.21
29.93	29.45	20.05	20.72	20.96	24.00
0.81	0.54				0.53
13.73	13.25	2.20	3.22	3.15	6.87
3.30	3.40	8.08	7.98	8.04	6.63
		2.78	2.59	1.78	0.77
100.00	100.01	100.01	99.27	100.00	100.01
69.69	68.29	10.93	15.52	15.89	34.72
30.31	31.71	72.63	69.61	73.41	60.64
0.00	0.00	16.44	14.87	10.69	4.63

Sample Crystal/Zone [C: Core, R: Rim] Type [PC: phenocryst, MPC: microphenocryst, GM: groundmass]	250220-1	250220-1	250220-1	250220-1	250220-1	250220-1	250220-1	250220-1	250220-1	250220-1	250220-1	250220-1	250220-1	250220-1	250220-1
	CRX1 (4)	CRX2 C (6)	CRX2 R (7)	CRX2 (8)	CRX3 C (9)	CRX3 R (10)	CRX4 C (13)	CRX4 R (14)	CRX5 R1 (15)	CRX5 C (17)	CRX10 (29)	CRX13 C1 (37)	CRX13 R1 (38)	CRX13 C2 (39)	CRX13 R2 (40)
	GM	PC	PC	GM	PC	PC	PC	PC	PC	PC	GM	PC	PC	PC	PC
SiO2	56.37	52.11	51.44	56.21	51.87	55.91	53.08	55.19	54.65	51.73	58.64	49.20	56.77	49.48	54.14
TiO2															
Al2O3	27.35	30.32	30.55	27.02	30.31	27.55	29.56	27.62	28.32	30.39	25.18	32.28	26.98	32.43	28.88
FeO	0.61	0.50	0.36	0.96	0.41	0.49		0.70	0.50	0.36	0.90	0.41	0.53		0.49
CaO	11.00	14.16	14.77	11.14	14.63	11.11	14.02	11.74	12.39	14.54	9.17	16.34	10.52	16.30	12.76
Na2O	4.67	2.90	2.89	4.66	2.78	4.73	3.34	4.53	4.15	2.98	5.79	1.77	4.91	1.78	3.73
K2O						0.21		0.22			0.33		0.28		
Total	100.00	99.99	100.01	99.99	100.00	100.00	100.00	100.00	100.01	100.00	100.01	100.00	99.99	99.99	100.00
An	56.55	72.96	73.85	56.92	74.41	55.77	69.88	58.12	62.26	72.95	45.76	83.61	53.30	83.50	65.40
Ab	43.45	27.04	26.15	43.08	25.59	42.97	30.12	40.58	37.74	27.05	52.28	16.39	45.01	16.50	34.60
Or	0.00	0.00	0.00	0.00	0.00	1.26	0.00	1.30	0.00	0.00	1.96	0.00	1.69	0.00	0.00

250220-1	250220-1	250220-1	250220-1	250220-1	250220-1	250220-1	250220-1	250220-1	250220-1	250220-1	250220-1	250220-1	250220-1	250220-1
CRX14 C (41)	CRX14 R (42)	CRX15 (48)	CRX17 C (51)	CRX17 R (52)	CRX21 C (61)	CRX21 R (62)	CRX22 C (63)	CRX22 R (64)	CRX24 (1)	CRX24 (4)	CRX25 (2)	CRX25 (6)	CRX26 C (1)	CRX26 R (2)
PC	PC	GM	PC	PC	PC	PC	PC	PC	GM	GM	GM	GM	PC	PC
51.38	57.92	55.66	52.35	56.20	53.84	55.81	52.37	55.40	52.28	53.86	55.85	58.79	53.93	53.47
31.00	26.31	27.79	30.32	27.18	29.34	27.74	30.16	27.73	30.07	29.08	27.78	25.62	29.10	29.27
	0.61	0.51		0.74		0.59	0.34	0.72	0.44	0.46	0.54	0.69		0.42
14.87	9.45	11.65	14.34	10.90	13.44	11.24	14.02	11.41	14.11	12.65	11.39	8.83	13.16	13.28
2.74	5.40	4.39	2.99	4.74	3.39	4.63	3.11	4.53	3.11	3.96	4.44	5.67	3.81	3.57
	0.31			0.23				0.21				0.40		
99.99	100.00	100.00	100.00	99.99	100.01	100.01	100.00	100.00	100.01	100.01	100.00	100.00	100.00	100.01
74.99	48.24	59.46	72.60	55.19	68.66	57.29	71.36	57.46	71.49	63.84	58.64	45.13	65.62	67.27
25.01	49.88	40.54	27.40	43.43	31.34	42.71	28.64	41.28	28.51	36.16	41.36	52.44	34.38	32.73
0.00	1.88	0.00	0.00	1.39	0.00	0.00	0.00	1.26	0.00	0.00	0.00	2.43	0.00	0.00
250220-1	250220-1	250220-1	250220-1	250220-1	250220-1	250220-1	250220-1	250220-1	250220-1	250220-1	250220-1	250220-1	250220-1	250220-1
CRX27 (2)	CRX27 C (5)	CRX28 (3)	CRX28 (4)	CRX29 (6)	CRX29 (7)	CRX30 (4)	CRX31 (2)	CRX31 (4)	CRX32 (3)	CRX32 (4)	CRX33 (3)	CRX33 (6)	CRX34 (5)	CRX34 (6)
GM	PC	GM	GM	GM	GM	GM	GM	GM	GM	GM	GM	GM	GM	GM
53.75	55.19	54.62	54.44	56.50	58.51	56.31	55.14	52.13	56.63	55.38	56.44	55.88	55.62	57.13
					0.33									
29.25	28.43	28.43	28.48	27.11	25.13	27.06	28.03	29.72	26.96	27.94	27.27	27.53	27.92	26.81
0.40	0.42	0.65	0.50	0.61	0.78	0.59	0.52	0.53	0.66	0.56	0.62	0.61	0.65	0.59
12.91	11.85	12.30	12.73	10.84	9.33	11.24	12.14	14.40	10.72	11.88	11.16	11.48	11.40	10.52
3.68	4.11	4.00	3.85	4.74	5.58	4.57	4.17	3.21	4.80	4.23	4.51	4.51	4.40	4.93
				0.20	0.34	0.23			0.22					
99.99	100.00	100.00	100.00	100.00	100.00	100.00	100.00	99.99	99.99	99.99	100.00	100.01	99.99	99.98
65.97	61.44	62.95	64.63	55.15	47.04	56.81	61.67	71.26	54.50	60.81	57.76	58.45	58.88	54.11
34.03	38.56	37.05	35.37	43.64	50.91	41.80	38.33	28.74	44.16	39.19	42.24	41.55	41.12	45.89
0.00	0.00	0.00	0.00	1.21	2.04	1.38	0.00	0.00	1.33	0.00	0.00	0.00	0.00	0.00

250220-1	250220-1	250220-1	250220-1	250220-1	250220-1	250220-1	250220-1	250220-1	250220-1	250220-1	250220-1
CRX35 (3)	CRX35 (4)	CRX36 (5)	CRX36 (6)	CRX37 C (1)	CRX37 R (2)	CRX37 R (3)	CRX37 C (4)	CRX38 C (1)	CRX38 R (2)	CRX39 C (4)	CRX39 R (5)
GM	GM	GM	GM	PC	PC	PC	PC	PC	PC	PC	PC
55.08	55.86	56.51	55.31	51.96	55.73	52.66	53.18	52.07	56.53	53.39	56.23
28.24	27.71	27.23	27.93	30.32	27.86	29.85	29.33	30.20	27.15	29.47	27.37
0.52	0.72	0.86	0.51	0.43	0.54	0.43	0.41	0.49	0.56	0.32	0.71
12.10	10.88	10.79	11.80	14.04	11.42	13.86	13.61	14.41	10.98	13.27	10.92
4.05	4.51	4.61	4.45	3.24	4.23	3.20	3.47	2.83	4.78	3.55	4.77
	0.32				0.22						
99.99	100.00	100.00	100.00	99.99	100.00	100.00	100.00	100.00	100.00	100.00	100.00
62.28	56.02	56.40	59.44	70.54	59.06	70.53	68.43	73.78	55.93	67.38	55.85
37.72	42.02	43.60	40.56	29.46	39.59	29.47	31.57	26.22	44.07	32.62	44.15
0.00	1.96	0.00	0.00	0.00	1.35	0.00	0.00	0.00	0.00	0.00	0.00

Sample Crystal/Zone [C: Core, R: Rim] Type [PC: phenocryst, MPC: microphenocryst, GM: groundmass]	250220-6	250220-6	250220-6	250220-6	250220-6	250220-6	250220-6	250220-6	250220-6	250220-6	250220-6	250220-6	250220-6	250220-6	250220-6
	CRX1 (3)	CRX2 C (4)	CRX2 R (5)	CRX2 (6)	CRX3 C1 (7)	CRX3 R1 (8)	CRX3 C2 (9)	CRX5 C (16)	CRX5 R (17)	CRX7 C (23)	CRX7 R (24)	CRX8 (27)	CRX10 C (33)	CRX10 R (34)	CRX13 (5)
	MPC	PC	PC	GM	PC	PC	PC	PC	PC	PC	PC	GM	PC	PC	GM
SiO2	52.32	51.27	52.14	52.57	53.82	51.64	52.24	51.86	52.54	52.94	52.22	53.27	52.95	52.29	51.69
TiO2														0.27	
Al2O3	30.04	31.12	30.33	29.92	29.20	30.62	30.41	30.32	29.86	29.61	30.27	29.35	29.88	29.68	30.22
FeO	0.67		0.33	0.66	0.30	0.39	0.31	0.48	0.49	0.41	0.49	0.71	0.25	0.43	0.64
MgO															
CaO	13.69	14.93	14.13	13.55	12.95	14.21	14.13	14.15	13.91	13.40	14.01	13.02	13.45	13.64	14.33
Na2O	3.28	2.68	3.07	3.31	3.73	2.92	2.91	3.18	3.20	3.46	3.01	3.64	3.46	3.53	3.12
K2O							0.23				0.17			0.18	
Total	100.00	100.00	100.00	100.01	100.00	100.01	100.00	99.99	100.00	99.99	100.00	99.99	99.99	100.02	100.00
An	69.76	75.48	71.78	69.35	65.74	71.88	72.85	71.09	70.61	67.46	72.01	66.40	68.24	67.38	71.74
Ab	30.24	24.52	28.22	30.65	34.26	26.73	27.15	28.91	29.39	31.52	27.99	33.60	31.76	31.56	28.26
Or	0.00	0.00	0.00	0.00	0.00	1.39	0.00	0.00	0.00	1.02	0.00	0.00	0.00	1.06	0.00

250220-6	250220-6	250220-6	250220-6	250220-6	250220-6	250220-6	250220-6	250220-6	250220-6	250220-6	250220-6	250220-6	250220-6	250220-6
CRX13 (6)	CRX14 (5)	CRX15 (6)	CRX15 (7)	CRX16 C (1)	CRX16 R (2)	CRX16 C (3)	CRX16 (7)	CRX17 (5)	CRX17 (6)	CRX18 (3)	CRX19 C (5)	CRX19 R (6)	CRX20 C (5)	CRX20 (6)
GM	GM	GM	GM	PC	PC	PC	GM	GM	GM	GM	PC	PC	PC	GM
53.03	53.79	64.28	62.98	50.92	49.95	51.05	52.27	54.06	58.01	56.43	51.95	52.98	72.92	52.07
29.52	28.76	21.77	22.80	31.29	31.73	31.10	30.07	28.58	25.53	27.16	30.18	29.68	12.66	30.08
0.62	0.64	0.53	0.53		0.51	0.53	0.44	0.76	0.78	0.98	0.55	0.65	3.68	0.64
13.39	12.82	4.37	5.46	15.25	15.47	14.82	13.88	12.38	9.45	10.69	14.06	13.12	1.18	13.82
3.44	3.77	7.43	7.18	2.54	2.33	2.50	3.35	3.91	5.38	4.31	3.02	3.33	3.47	3.12
	0.23	1.63	1.05					0.31	0.55	0.42	0.25	0.24	5.18	0.27
100.00	100.01	100.01	100.00	100.00	99.99	100.00	100.01	100.00	100.00	99.99	100.01	100.00	100.00	100.00
68.26	64.37	22.12	27.71	76.84	78.58	76.61	69.60	62.45	47.63	56.29	70.93	67.52	8.66	69.84
31.74	34.25	68.06	65.94	23.16	21.42	23.39	30.40	35.69	49.07	41.07	27.57	31.01	46.08	28.53
0.00	1.38	9.82	6.35	0.00	0.00	0.00	0.00	1.86	3.30	2.63	1.50	1.47	45.26	1.62
250220-6	250220-6	250220-6	250220-6	250220-6	250220-6	250220-6	250220-6	250220-6	250220-6	250220-6	250220-6	250220-6	250220-6	250220-6
CRX20 C (8)	CRX21 (5)	CRX21 (6)	CRX22 (5)	CRX22 (6)	CRX23 (1)	CRX23 (2)	CRX24 C (4)	CRX24 R (5)	CRX25 (3)	CRX26 C (1)	CRX26 R (2)	CRX27 C (1)	CRX27 R (2)	CRX28 (2)
PC	GM	GM	GM	GM	GM	GM	PC	PC	GM	PC	PC	PC	PC	GM
70.25	54.48	53.15	52.91	54.01	53.08	52.46	52.74	51.83	52.33	51.47	52.91	51.69	53.22	60.71
14.38	28.00	29.33	29.54	28.61	29.22	29.94	29.90	30.47	29.85	30.67	29.84	30.50	29.19	24.49
4.05	0.85	0.69	0.65	0.83	0.74	0.60	0.34	0.56	0.56	0.39	0.49	0.43	0.59	0.59
1.03														
1.27	12.01	13.17	13.31	12.80	13.02	13.91	13.83	14.20	13.98	14.69	13.68	14.56	13.29	7.39
3.97	4.25	3.37	3.31	3.55	3.68	3.10	3.19	2.95	3.05	2.58	3.08	2.83	3.48	5.92
5.06	0.41	0.30	0.29	0.21	0.25				0.23	0.20			0.23	0.90
100.01	100.00	100.01	100.01	100.01	99.99	100.01	100.00	100.01	100.00	100.00	100.00	100.01	100.00	100.00
8.77	59.49	67.11	67.75	65.73	65.17	71.26	70.55	72.68	70.70	74.96	71.05	73.98	66.91	38.54
49.62	38.09	31.07	30.49	32.99	33.34	28.74	29.45	27.32	27.91	23.82	28.95	26.02	31.71	55.87
41.61	2.42	1.82	1.76	1.28	1.49	0.00	0.00	0.00	1.38	1.22	0.00	0.00	1.38	5.59

250220-6	250220-6	250220-6
CRX29 (4)	CRX29 C (6)	CRX29 R (7)
GM	PC	PC
53.28	51.86	52.21
29.14	30.49	30.12
0.71	0.48	0.56
13.14	14.05	13.99
3.44	3.12	2.92
0.29		0.19
100.00	100.00	99.99
66.67	71.33	71.74
31.58	28.67	27.10
1.75	0.00	1.16

2. Olivino

Sample Crystal/Zone [C: Core, R: Rim] Type [PC: phenocryst, MPC: microphenocryst, GM: groundmass]	021219-1 CRX1 C (1)	021219-1 CRX1 R (2)	021219-1 CRX2 C (3)	021219-1 CRX2 R1 (4)	021219-1 CRX3 R (5)	021219-1 CRX3 C (6)	021219-1 CRX4 C1 (7)	021219-1 CRX4 C2 (8)	021219-1 CRX7 C (13)	021219-1 CRX7 R (14)	021219-1 CRX10 R (19)	021219-1 CRX10 C (20)	021219-1 CRX11 C (21)	021219-1 CRX11 R (22)	021219-1 CRX12 C (23)
	PC	PC	PC	PC	PC	PC	PC	PC	PC	PC	PC	PC	PC	PC	PC
SiO2	41.32	41.45	40.74	40.59	40.69	40.55	41.01	40.66	41.69	41.18	40.81	42.00	41.82	41.02	40.85
Al2O3															
FeO	17.76	18.29	20.62	20.85		20.97	21.10	21.34	17.93	18.54	21.08	18.24	16.54	18.62	20.21
MnO			0.42	0.40		0.45		0.41			0.35	0.36		0.39	0.38
MgO	40.91	40.26	38.22	37.73	37.77	37.70	37.56	37.26	40.37	40.29	37.39	38.78	41.34	39.96	38.19
CaO				0.42	0.40	0.33	0.33	0.33			0.38	0.62	0.30		0.37
Total	99.99	100.00	100.00	99.99	100.01	100.00	100.00	100.00	99.99	100.01	100.01	100.00	100.00	99.99	100.00
Fo	80.42	79.69	76.77	76.34	76.10	76.22	76.04	75.68	80.05	79.48	75.97	79.12	81.67	79.28	77.11
Fa	19.58	20.31	23.23	23.66	23.90	23.78	23.96	24.32	19.95	20.52	24.03	20.88	18.33	20.72	22.89

021219-1	021219-1	021219-1	021219-1	021219-1	021219-1	021219-1	021219-1	021219-1	021219-1	021219-1	021219-1	021219-1	021219-1	021219-1
CRX12 R (24)	CRX13 C (25)	CRX13 R (26)	CRX14 C (28)	CRX14 R (29)	CRX15 (30)	CRX15 (31)	CRX15 (32)	CRX15 (33)	CRX15 (34)	CRX15 (35)	CRX17 (2)	CRX18 (11)	CRX18 (12)	CRX18 (13)
PC	PC	PC	PC	PC	GM	GM	GM	GM	GM	GM	GM	GM	GM	GM
40.73	41.20	41.31	40.72	40.59	40.97	40.92	40.75	40.46	40.90	40.52	47.52	47.18	47.42	47.74
20.94	18.96	22.39	21.26	24.56	20.75	20.79	22.64	22.64	21.37	21.45	10.74	7.12	8.11	9.92
0.50	0.47	0.42	0.32	0.42	0.39			0.41		0.41				
37.83	39.36	35.52	37.31	34.08	37.58	37.81	36.22	36.11	37.42	37.24	41.74	45.38	44.14	42.33
		0.36	0.40	0.35	0.31	0.48	0.39	0.38	0.31	0.37		0.32	0.33	
100.00	99.99	100.00	100.01	100.00	100.00	100.00	100.00	100.00	100.00	99.99	100.00	100.00	100.00	99.99
76.31	78.73	73.88	75.78	71.21	76.35	76.43	74.04	73.98	75.74	75.58	87.39	91.91	90.66	88.38
23.69	21.27	26.12	24.22	28.79	23.65	23.57	25.96	26.02	24.26	24.42	12.61	8.09	9.34	11.62

021219-1	021219-1	021219-1	021219-1	021219-1	021219-1	021219-1	021219-1	021219-1	021219-1	021219-1	021219-1	021219-1	021219-1	021219-1
CRX 20 (3)	CRX 20 (4)	CRX 20 (5)	CRX 20 (6)	CRX 20 (9)	CRX 21 (14)	CRX 21 (16)	CRX 21 (21)	CRX 22 C (22)	CRX 22 R (23)	CRX 22 (24)	CRX 22 (28)	CRX 23 (31)	CRX 23 C (34)	CRX 23 (37)
GM	GM	MPC	GM	GM	GM	GM	GM	PC	PC	GM	GM	GM	MPC	GM
40.68	40.64	40.48	40.35	41.10	40.24	40.33	40.02	40.82	40.81	40.07	40.66	39.98	40.43	40.27
21.33	22.00	21.63	23.51	22.06	22.25	21.79	26.24	21.06	21.46	22.04	21.82	25.49	21.75	22.66
0.34	0.43	0.42	0.52		0.59	0.36	0.46	0.33	0.42	0.61	0.40	0.41	0.38	0.46
37.34	36.64	37.15	35.12	36.45	36.53	37.15	32.81	37.79	36.97	36.93	36.78	33.71	37.05	36.14
0.32	0.29	0.33	0.51	0.39	0.39	0.37	0.46		0.34	0.35	0.34	0.40	0.39	0.47
100.01	100.00	100.01	100.01	100.00	100.00	100.00	99.99	100.00	100.00	100.00	100.00	99.99	100.00	100.00
75.73	74.80	75.38	72.70	74.65	74.53	75.24	69.03	76.18	75.44	74.92	75.03	70.22	75.23	73.98
24.27	25.20	24.62	27.30	25.35	25.47	24.76	30.97	23.82	24.56	25.08	24.97	29.78	24.77	26.02

021219-1	021219-1	021219-1	021219-1	021219-1	021219-1	021219-1	021219-1	021219-1	021219-1	021219-1	021219-1	021219-1	021219-1	021219-1
CRX 24 (39)	CRX 24 (42)	CRX 25 C (46)	CRX 25 R (47)	CRX 26 (50)	CRX 27 C (53)	CRX 27 R (54)	CRX 27 (55)	CRX 27 (57)	CRX 28 (61)	CRX 28 (63)	CRX 29 C (66)	CRX 29 R (67)	CRX 29 (69)	CRX 30 (73)
GM	GM	PC	PC	GM	PC	PC	GM	GM	GM	GM	PC	PC	GM	GM
40.42	39.78	41.23	40.54	40.73	40.71	40.36	40.26	39.61	40.56	40.04	41.72	40.88	40.48	40.32
22.03	23.97	20.08	21.46	21.67	21.44	23.51	23.03	27.16	22.66	24.18	13.29	20.52	25.85	21.72
0.44	0.60	0.35	0.37	0.58	0.35	0.56	0.52	0.46	0.39	0.34	0.32		0.40	0.37
36.75	35.34	38.08	37.24	36.69	37.22	35.23	35.79	32.34	36.02	35.01	44.35	38.33	32.78	37.24
0.37	0.32	0.26	0.39	0.32	0.29	0.34	0.40	0.44	0.38	0.43	0.32	0.27	0.50	0.35
100.01	100.01	100.00	100.00	99.99	100.01	100.00	100.00	100.01	100.01	100.00	100.00	100.00	100.01	100.00
74.83	72.44	77.17	75.57	75.11	75.58	72.76	73.48	67.98	73.91	72.07	85.61	76.90	69.33	75.35
25.17	27.56	22.83	24.43	24.89	24.42	27.24	26.52	32.02	26.09	27.93	14.39	23.10	30.67	24.65

021219-1	021219-1	021219-1	021219-1	021219-1	021219-1	021219-1	021219-1	021219-1	021219-1	021219-1	021219-1
CRX 30 (75)	CRX 31 C (77)	CRX 31 R (78)	CRX 31 (79)	CRX 31 (80)	CRX 32 C (82)	CRX 32 R (83)	CRX 32 (84)	CRX 33 (89)	CRX 34 (93)	CRX 34 (95)	
GM	PC	PC	GM	GM	PC	PC	GM	GM	GM	GM	
39.77	39.89	40.15	40.09	39.78	40.73	40.69	40.60	40.69	41.35	40.47	
										0.44	
26.79	21.99	22.80	23.87	24.69	21.11	21.65	22.81	22.91	21.56	22.37	
0.65	0.46	0.56	0.42	0.41	0.42	0.38	0.57	0.37	0.41	0.41	
32.28	37.25	36.12	35.28	34.64	37.45	36.95	35.61	35.75	36.26	35.95	
0.50	0.41	0.37	0.34	0.49	0.28	0.34	0.42	0.28	0.44	0.37	
99.99	100.00	100.00	100.00	100.01	99.99	100.01	100.01	100.00	100.02	100.01	
68.23	75.12	73.85	72.49	71.44	75.98	75.26	73.57	73.56	74.99	74.13	
31.77	24.88	26.15	27.51	28.56	24.02	24.74	26.43	26.44	25.01	25.87	

Sample Crystal/Zone [C: Core, R: Rim] Type [PC: phenocryst, MPC: microphenocryst, GM: groundmass]	031219-2A CRX1 C1 (1)	031219-2A CRX1 R1 (2)	031219-2A CRX1 C2 (3)	031219-2A CRX1 R2 (4)	031219-2A CRX2 C (5)	031219-2A CRX2 R1 (6)	031219-2A CRX2 R2 (7)	031219-2A CRX3 C (8)	031219-2A CRX3 R1 (9)	031219-2A CRX3 R2 (10)	031219-2A CRX4 C (11)	031219-2A CRX4 R1 (12)	031219-2A CRX4 R2 (13)	031219-2A CRX5 C (14)	031219-2A CRX5 R (15)
	PC	PC	PC	PC	PC	PC	PC	PC	PC	PC	PC	PC	PC	PC	PC
SiO2	41.48	39.47	41.10	39.85	41.57	39.16	39.83	41.16	40.04	39.63	41.07	40.38	40.34	41.55	39.92
Al2O3	16.02	25.59	15.38	24.62	15.80	30.79	26.06	16.68	23.50	26.59	15.60	23.97	22.18	14.74	23.30
FeO	0.35	0.70	0.41	0.52	0.75	0.53	0.53	0.60	0.49	0.32	0.48	0.51	0.49	0.49	0.49
MnO	42.16	33.87	42.83	35.01	42.63	28.81	33.18	41.89	35.52	33.02	42.76	35.17	36.64	43.40	35.97
MgO		0.38	0.27			0.49	0.40	0.27	0.34	0.28	0.25	0.32	0.30	0.32	0.32
CaO															
Total	100.01	100.01	99.99	100.00	100.00	100.00	100.00	100.00	100.00	100.01	100.00	100.00	99.99	99.99	100.00
Fo	82.43	70.23	83.23	71.71	82.79	62.52	69.42	81.74	72.93	68.88	83.01	72.34	74.65	84.00	73.35
Fa	17.57	29.77	16.77	28.29	17.21	37.48	30.58	18.26	27.07	31.12	16.99	27.66	25.35	16.00	26.65

031219-2A CRX6 (16)	031219-2A CRX6 (17)	031219-2A CRX7 C1 (1)	031219-2A CRX7 C2 (3)	031219-2A CRX7 R (5)	031219-2A CRX7 (21)	031219-2A CRX9 C (24)	031219-2A CRX9 R (25)	031219-2A CRX10 C (26)	031219-2A CRX10 R (27)	031219-2A CRX11 C (28)	031219-2A CRX11 R (29)	031219-2A CRX11 (30)	031219-2A CRX11 (31)	031219-2A CRX12 (34)
MPC	MPC	PC	PC	PC	GM	PC	PC	PC	PC	PC	PC	GM	GM	GM
41.75	40.48	43.41	45.64	42.20	39.10	41.36	40.16	41.62	39.44	40.72	40.20	39.38	38.43	39.38
16.54	22.44	12.37	7.21	19.67	30.05	14.86	22.92	14.48	27.43	20.40	21.72	29.54	33.54	30.16
41.33	0.54	44.22	47.15	37.78	0.53	43.51	0.43	0.38	0.65	38.34	0.54	0.53	0.67	0.68
0.38	36.26	0.28	47.15	0.36	29.90	0.42	0.27	0.31	0.33	37.09	0.46	29.91	26.77	29.38
	0.28				0.27	0.27	0.31	0.33	0.34	0.46	0.50	0.41	0.41	0.40
100.00	100.00	100.00	100.00	100.01	100.00	100.00	99.99	100.00	99.99	100.00	100.00	100.00	100.00	100.00
81.67	74.23	86.44	92.10	77.40	63.95	83.92	73.77	84.17	67.62	77.01	75.27	64.35	58.73	63.46
18.33	25.77	13.56	7.90	22.60	36.05	16.08	26.23	15.83	32.38	22.99	24.73	35.65	41.27	36.54

031219-2A	031219-2A	031219-2A	031219-2A	031219-2A	031219-2A	031219-2A	031219-2A	031219-2A	031219-2A	031219-2A	031219-2A	031219-2A	031219-2A	031219-2A
CRX13 (39)	CRX15 C (43)	CRX15 R (44)	CRX15 (45)	CRX16 (48)	CRX17 C (50)	CRX17 R (51)	CRX18 (11)	CRX19 C1 (12)	CRX19 C2 (14)	CRX19 (15)	CRX20 (19)	CRX21 (5)	CRX21 C (7)	CRX21 R (8)
GM	PC	PC	GM	GM	PC	PC	MPC	PC	PC	GM	GM	GM	PC	PC
38.69	41.85	41.15	40.00	39.31	41.58	39.18	44.99	43.73	43.03	43.48	47.86	39.93	41.87	41.05
31.16	15.38	15.85	23.52	30.72	14.33	27.78	18.24	9.32	11.26	20.13	13.28	27.55	13.89	20.05
0.70			0.46	0.72		0.78	0.50			0.41		0.65	0.32	0.34
29.04	42.77	42.67	35.53	28.81	44.09	31.83	36.27	46.96	45.46	35.53	38.46	31.58	43.57	38.24
0.41		0.32	0.49	0.44		0.42			0.24	0.45	0.40	0.28	0.34	0.33
100.00	100.00	99.99	100.00	100.00	100.00	99.99	100.00	100.01	99.99	100.00	100.00	99.99	99.99	100.01
62.42	83.21	82.76	72.92	62.57	84.58	67.13	78.00	89.98	87.80	75.88	83.77	67.14	84.83	77.27
37.58	16.79	17.24	27.08	37.43	15.42	32.87	22.00	10.02	12.20	24.12	16.23	32.86	15.17	22.73

031219-2A	031219-2A	031219-2A	031219-2A	031219-2A	031219-2A	031219-2A	031219-2A	031219-2A	031219-2A	031219-2A	031219-2A
CRX22 (12)	CRX23 (17)	CRX24 C (19)	CRX24 R (20)	CRX24 (24)	CRX25 (28)	CRX26 (32)	CRX27 (36)	CRX28 (41)	CRX29 (45)	CRX29 (48)	
GM	GM	PC	PC	GM	GM	GM	GM	GM	GM	GM	
39.54	40.62	41.70	41.51	39.49	39.75	39.90	39.79	39.86	39.78	39.77	
						0.74					
27.91	25.61	17.66	20.24	30.71	30.47	30.33	29.40	29.12	28.90	30.44	
0.55	0.48	0.33	0.43	0.65	0.66	0.79	0.68	0.55	0.81	0.78	
31.69	32.89	39.97	37.47	28.75	28.67	27.91	29.68	30.01	30.08	28.56	
0.32	0.41	0.35	0.34	0.40	0.46	0.34	0.44	0.46	0.42	0.45	
100.01	100.01	100.01	99.99	100.00	100.01	100.01	99.99	100.00	99.99	100.00	
66.93	69.60	80.14	76.74	62.53	62.65	62.13	64.28	64.75	64.98	62.58	
33.07	30.40	19.86	23.26	37.47	37.35	37.87	35.72	35.25	35.02	37.42	

Sample	051219-1	051219-1	051219-1	051219-1	051219-1	051219-1	051219-1	051219-1	051219-1	051219-1	051219-1	051219-1	051219-1	051219-1	051219-1
Crystal/Zone [C: Core, R: Rim]	CRX5 C1 (13)	CRX5 C2 (14)	CRX5 R1 (15)	CRX5 R2 (16)	CRX7 C1 (26)	CRX7 R1 (27)	CRX7 R2 (28)	CRX7 R3 (29)	CRX7 C2 (30)	CRX10 C (9)	CRX10 R1 (10)	CRX10 R2 (11)	CRX11 C (12)	CRX11 R1 (13)	CRX11 R2 (14)
Type [PC: phenocryst, MPC: microphenocryst, GM: groundmass]	PC	PC	PC	PC	PC	PC	PC	PC	PC	PC	PC	PC	PC	PC	PC
SiO2	41.09	41.53	41.46	41.37	39.99	41.43	41.65	41.11	40.25	38.01	38.21	38.03	41.33	41.27	41.19
Al2O3	15.64	15.21	15.68	15.81	22.77	15.17	15.15	16.09	23.04	14.95	15.46	15.46	14.64	16.21	16.49
FeO	0.32	0.30		0.32	0.45					0.26	0.28	0.30		0.21	0.27
MnO	42.71	42.71	42.59	42.50	36.48	43.11	42.88	42.39	36.47	46.47	45.78	45.83	43.77	41.98	41.74
MgO	0.24	0.25	0.27		0.31	0.29	0.33	0.41	0.24	0.30	0.28	0.38	0.26	0.32	0.32
CaO															
Total	100.00	100.00	100.00	100.00	100.00	100.00	100.01	100.00	100.00	99.99	100.01	100.00	100.00	99.99	100.01
Fo	82.96	83.35	82.88	82.73	74.07	83.51	83.46	82.44	73.83	84.71	84.07	84.09	84.20	82.20	81.86
Fa	17.04	16.65	17.12	17.27	25.93	16.49	16.54	17.56	26.17	15.29	15.93	15.91	15.80	17.80	18.14

051219-1	051219-1	051219-1	051219-1	051219-1	051219-1	051219-1	051219-1	051219-1	051219-1	051219-1	051219-1	051219-1	051219-1	051219-1	051219-1
CRX12 C (15)	CRX12 R (16)	CRX12 (17)	CRX12 (18)	CRX13 C1 (19)	CRX13 C2 (20)	CRX13 C3 (21)	CRX13 R2 (22)	CRX13 R1 (23)	CRX13 R3 (24)	CRX17 C (33)	CRX17 R (34)	CRX19 C (39)	CRX19 R (40)	CRX21 (5)	
PC	PC	MPC	MPC	PC	PC	PC	PC	PC	PC	PC	PC	PC	PC	PC	GM
41.57	40.87	40.89	41.03 0.80	41.02	41.06	40.84	41.01	41.35	41.01	40.07	40.75	39.34	41.05	47.77	
14.86	17.86	17.61	18.63	16.94	16.98	17.87	16.59	16.14	16.68	21.38	17.90	25.46	15.86	11.52	
0.22	0.31	0.29	0.30	0.29	0.29	0.25	0.27	0.27	0.28	0.35	0.26	0.47	0.26		
43.02	40.62	40.84	38.83	41.51	41.43	40.83	41.85	41.88	41.65	37.92	40.77	34.47	42.61	39.87	
0.33	0.34	0.37	0.41	0.23	0.24	0.20	0.29	0.35	0.39	0.29	0.32	0.25	0.22	0.84	
100.00	100.00	100.00	100.00	99.99	100.00	99.99	100.01	99.99	100.01	100.01	100.00	99.99	100.00	100.00	
83.77	80.21	80.52	78.79	81.37	81.31	80.29	81.81	82.22	81.66	75.97	80.24	70.70	82.73	86.05	
16.23	19.79	19.48	21.21	18.63	18.69	19.71	18.19	17.78	18.34	24.03	19.76	29.30	17.27	13.95	

051219-1 CRX21 (8)	051219-1 CRX22 (9)	051219-1 CRX22 (12)	051219-1 CRX23 (14)	051219-1 CRX23 (15)	051219-1 CRX23 (20)	051219-1 CRX24 (21)	051219-1 CRX24 (23)	051219-1 CRX25 C (1)	051219-1 CRX25 R (2)	051219-1 CRX25 C (3)	051219-1 CRX25 R (4)	051219-1 CRX25 C (5)	051219-1 CRX25 R (6)	051219-1 CRX25 (7)
GM	MPC	GM	GM	MPC	GM	GM	GM	PC	PC	PC	PC	PC	PC	GM
42.77	45.42	45.17	45.30	44.83	45.11	45.41	43.77	41.82	41.59	41.75	41.02	41.58	41.54	41.45
16.27	6.09	6.39	6.73	5.93	8.26	6.20	10.85	13.92	14.87	14.31	16.18	14.98	14.64	16.58
40.65	48.48	48.44	47.69	49.24	46.31	48.07	45.04	43.98	43.21	43.57	42.07	42.87	43.27	41.71
0.30			0.28		0.31	0.33	0.34	0.28	0.33	0.38	0.37	0.27	0.25	0.26
99.99	99.99	100.00	100.00	100.00	99.99	100.01	100.00	100.00	100.00	100.01	100.00	100.00	100.01	100.00
81.66	93.42	93.11	92.66	93.67	90.90	93.25	88.10	84.92	83.82	84.44	82.25	83.61	84.05	81.77
18.34	6.58	6.89	7.34	6.33	9.10	6.75	11.90	15.08	16.18	15.56	17.75	16.39	15.95	18.23

051219-1 CRX25 (8)	051219-1 CRX26 C (1)	051219-1 CRX26 R (2)	051219-1 CRX26 (4)	051219-1 CRX27 (3)	051219-1 CRX27 (4)	051219-1 CRX28 C (1)	051219-1 CRX28 R (2)	051219-1 CRX28 C (3)	051219-1 CRX28 R (4)	051219-1 CRX28 (6)	051219-1 CRX29 (2)	051219-1 CRX29 (4)	051219-1 CRX30 C (1)	051219-1 CRX30 R (2)
GM	PC	PC	GM	GM	GM	PC	PC	PC	PC	GM	GM	GM	PC	PC
39.51	41.56	41.45	39.88	39.54	40.70	41.43	41.57	41.95	40.78	40.83	40.99	40.77	41.52	40.75
25.86	15.17	16.18	21.79	23.57	19.46	15.57	14.82	14.62	18.54	18.73	18.32	18.38	15.08	16.91
0.50			0.51	0.47					0.35		0.35	0.39		0.32
33.65	43.27	42.07	37.43	35.99	39.39	43.00	43.28	43.44	40.01	40.04	39.89	40.00	43.04	41.63
0.47		0.30	0.39	0.44	0.45		0.33		0.32	0.39	0.44	0.45	0.35	0.39
99.99	100.00	100.00	100.00	100.01	100.00	100.00	100.00	100.01	100.00	99.99	99.99	99.99	99.99	100.00
69.88	83.57	82.25	75.38	73.13	78.30	83.12	83.89	84.12	79.37	79.21	79.51	79.51	83.57	81.44
30.12	16.43	17.75	24.62	26.87	21.70	16.88	16.11	15.88	20.63	20.79	20.49	20.49	16.43	18.56

051219-1	051219-1	051219-1	051219-1	051219-1	051219-1	051219-1	051219-1	051219-1	051219-1	051219-1	051219-1
CRX30 (4)	CRX31 C (1)	CRX31 R (2)	CRX31 C (3)	CRX31 R (4)	CRX31 (5)	CRX31 (7)	CRX32 (1)	CRX32 C (4)	CRX32 R (5)	CRX33 (1)	
GM	PC	PC	PC	PC	GM	GM	GM	PC	PC	GM	
40.00	41.40	41.14	41.62	41.48	41.14	40.78	41.46	41.69	41.47	39.87	
24.12	15.04	18.86	15.27	15.27	16.99	20.87	16.89	14.72	15.30	22.44	
35.31	43.26	39.59	42.82	43.25	41.01	37.54	41.32	43.28	42.97	36.63	
0.57	0.30	0.40	0.29		0.39	0.37	0.33		0.25	0.57	
100.00	100.00	99.99	100.00	100.00	100.00	100.01	100.00	99.99	99.99	100.00	
72.30	83.68	78.91	83.33	83.47	81.14	76.23	81.35	83.98	83.35	74.42	
27.70	16.32	21.09	16.67	16.53	18.86	23.77	18.65	16.02	16.65	25.58	

Sample Crystal/Zone [C: Core, R: Rim] Type [PC: phenocryst, MPC: microphenocryst, GM: groundmass]	051219-8 CRX1 C (1)	051219-8 CRX1 R1 (2)	051219-8 CRX1 R2 (3)	051219-8 CRX1 (4)	051219-8 CRX2 (6)	051219-8 CRX2 (7)	051219-8 CRX3 C (10)	051219-8 CRX3 R (11)	051219-8 CRX4 C1 (12)	051219-8 CRX4 R1 (13)	051219-8 CRX4 R2 (14)	051219-8 CRX4 C2 (15)	051219-8 CRX6 C (19)	051219-8 CRX6 R (20)	051219-8 CRX11 C (29)
	PC	PC	PC	GM	MPC	GM	PC	PC	PC	PC	PC	PC	PC	PC	PC
SiO2	41.98	39.83	39.86	39.38	40.05	39.94	42.30	39.92	41.71	41.59	40.46	41.99	41.74	40.13	41.60
Al2O3				0.72											
FeO	13.12	22.09	22.32	24.36	22.24	23.87	11.84	21.13	13.43	17.31	20.65	13.98	11.74	20.77	12.86
MnO	0.33	0.49	0.39	0.55	0.53	0.58		0.37		0.38		0.35		0.36	0.23
MgO	44.57	37.30	36.97	34.51	36.76	35.14	45.51	38.06	44.58	40.72	38.49	43.28	46.28	38.31	44.94
CaO		0.30	0.45	0.48	0.41	0.47	0.35	0.52	0.28		0.40	0.41	0.24	0.43	0.37
Total	100.00	100.01	99.99	100.00	99.99	100.00	100.00	100.00	100.00	100.00	100.00	100.01	100.00	100.00	100.00
Fo	85.83	75.06	74.70	71.63	74.66	72.41	87.26	76.25	85.54	80.74	76.87	84.66	87.54	76.68	86.17
Fa	14.17	24.94	25.30	28.37	25.34	27.59	12.74	23.75	14.46	19.26	23.13	15.34	12.46	23.32	13.83

051219-8	051219-8	051219-8	051219-8	051219-8	051219-8	051219-8	051219-8	051219-8	051219-8	051219-8	051219-8	051219-8	051219-8	051219-8
CRX11 R (30)	CRX13 C (33)	CRX13 R1 (34)	CRX13 R2 (35)	CRX14 C (36)	CRX14 R (37)	CRX16 (40)	CRX16 (41)	CRX16 (42)	CRX16 (43)	CRX17 (1)	CRX17 (51)	CRX18 (11)	CRX18 (12)	CRX19 R (1)
PC	PC	PC	PC	PC	PC	GM	GM	GM	GM	GM	GM	GM	MPC	PC
40.25	41.70	41.44	40.27	41.56	40.16	39.84	39.59	39.09	39.37	46.19	39.07	45.23	44.90	39.97
21.11	12.45	14.45	19.79	12.65	20.77	23.33	23.93	26.99	24.57	11.00	27.00	15.91	11.20	21.78
0.45		0.30	0.38	0.22	0.38	0.46	0.47	0.52	0.51		0.51			0.38
37.73	45.56	43.45	39.18	45.27	38.25	35.96	35.49	32.89	35.02	42.81	32.96	38.48	43.54	37.45
0.46	0.29	0.36	0.38	0.30	0.44	0.41	0.52	0.51	0.53		0.46	0.38	0.37	0.42
100.00	100.00	100.00	100.00	100.00	100.00	100.00	100.00	100.00	100.00	100.00	100.00	100.00	100.01	100.00
76.11	86.71	84.28	77.92	86.45	76.65	73.32	72.56	68.48	71.76	87.40	68.51	81.17	87.39	75.40
23.89	13.29	15.72	22.08	13.55	23.35	26.68	27.44	31.52	28.24	12.60	31.49	18.83	12.61	24.60

051219-8	051219-8	051219-8	051219-8	051219-8	051219-8	051219-8	051219-8	051219-8	051219-8	051219-8	051219-8	051219-8	051219-8	051219-8
CRX19 C (2)	CRX19 (7)	CRX20 (9)	CRX20 (11)	CRX21 C (15)	CRX21 R (16)	CRX21 (17)	CRX22 C (20)	CRX22 R (21)	CRX22 (25)	CRX23 C (27)	CRX23 R (28)	CRX23 (30)	CRX25 C (34)	CRX25 R (35)
PC	GM	GM	GM	PC	PC	GM	PC	PC	GM	PC	PC	GM	PC	PC
40.23	38.96	39.33	38.85	40.43	39.02	38.46	40.96	39.66	39.61	40.46	39.93	38.60	40.10	38.82
21.21	27.53	26.95	28.30	20.11	28.27	30.10	18.24	25.05	26.53	19.99	24.12	28.87	20.66	27.49
0.36	0.40	0.58	0.52	0.37	0.54	0.62	0.31	0.45	0.54	0.34	0.57	0.53	0.45	0.51
37.74	32.66	32.66	31.94	38.72	31.71	30.44	40.16	34.37	32.81	38.81	34.95	31.50	38.27	32.73
0.46	0.45	0.48	0.41	0.37	0.45	0.38	0.33	0.47	0.51	0.40	0.44	0.50	0.52	0.45
100.00	100.00	100.00	100.02	100.00	99.99	100.00	100.00	100.00	100.00	100.00	100.01	100.00	100.00	100.00
76.03	67.89	68.36	66.80	77.44	66.66	64.32	79.69	70.98	68.79	77.58	72.09	66.04	76.76	67.97
23.97	32.11	31.64	33.20	22.56	33.34	35.68	20.31	29.02	31.21	22.42	27.91	33.96	23.24	32.03

051219-8	051219-8	051219-8	051219-8	051219-8	051219-8	051219-8	051219-8	051219-8	051219-8	051219-8	051219-8	051219-8	051219-8	051219-8
CRX25 (36)	CRX26 C (40)	CRX26 R (41)	CRX27 C (46)	CRX27 R (47)	CRX27 (49)	CRX28 C (51)	CRX28 R (52)	CRX29 C (56)	CRX29 R (57)	CRX29 (58)	CRX30 C (61)	CRX30 R (62)	CRX30 (64)	CRX31 (70)
GM	GM	GM	PC	PC	GM	GM	GM	PC	PC	GM	PC	PC	GM	GM
39.41	39.32	38.22	40.41	39.33	38.42	39.32	37.96	40.75	39.11	39.56	41.02	39.55	39.55	39.88
26.14	24.70	34.84	20.30	24.60	31.49	25.04	33.58	19.06	26.30	24.93	19.73	25.03	26.61	23.44
0.48	0.51	0.52		0.50	0.79	0.51	0.73		0.57	0.35		0.56	0.49	0.44
33.44	34.95	25.91	38.84	35.15	28.84	34.70	27.24	39.83	33.51	34.77	38.83	34.37	32.88	35.87
0.52	0.52	0.51	0.45	0.43	0.47	0.42	0.49	0.36	0.50	0.40	0.42	0.49	0.46	0.37
99.99	100.00	100.00	100.00	100.01	100.01	99.99	100.00	100.00	99.99	100.01	100.00	100.00	99.99	100.00
69.52	71.61	57.00	77.33	71.81	62.01	71.18	59.12	78.84	69.43	71.32	77.82	71.00	68.78	73.18
30.48	28.39	43.00	22.67	28.19	37.99	28.82	40.88	21.16	30.57	28.68	22.18	29.00	31.22	26.82

051219-8	051219-8	051219-8	051219-8	051219-8	051219-8	051219-8	051219-8	051219-8	051219-8	051219-8
CRX32 (73)	CRX33 (77)	CRX34 (80)	CRX35 (82)	CRX36 (86)	CRX37 C (89)	CRX37 R (90)	CRX37 (91)	CRX38 (95)	CRX39 (98)	
GM	GM	GM	GM	GM	PC	PC	GM	GM	GM	
39.96	39.91	39.40	39.76	39.50	41.65	40.06	39.26	40.24	39.65	
			0.45							
24.67	24.43	27.47	26.06	25.54	16.77	22.19	24.77	23.60	26.01	
0.61	0.46	0.38	0.46	0.53		0.34	0.47	0.37	0.57	
34.30	34.71	32.23	32.78	34.01	41.58	36.99	35.03	35.32	33.24	
0.47	0.48	0.51	0.48	0.41		0.42	0.47	0.47	0.53	
100.01	99.99	99.99	99.99	99.99	100.00	100.00	100.00	100.00	100.00	
71.25	71.69	67.65	69.16	70.36	81.55	74.82	71.60	72.74	69.49	
28.75	28.31	32.35	30.84	29.64	18.45	25.18	28.40	27.26	30.51	

Sample	230220-2	230220-2	230220-2	230220-2	230220-2	230220-2	230220-2	230220-2	230220-2	230220-2	230220-2	230220-2	230220-2	230220-2	230220-2
Crystal/Zone [C: Core, R: Rim]	CRX1 C (1)	CRX1 R (2)	CRX2 C (3)	CRX2 R (4)	CRX3 C (5)	CRX3 R (6)	CRX5 (13)	CRX7 C (17)	CRX7 R (18)	CRX8 C (19)	CRX8 R (20)	CRX9 C (21)	CRX9 R (22)	CRX10 (23)	CRX10 (25)
Type [PC: phenocryst, MPC: microphenocryst, GM: groundmass]	PC	PC	PC	PC	PC	PC	MPC	PC	PC	PC	PC	PC	PC	GM	GM
SiO2	41.18	40.46	41.66	40.59	41.36	40.55	40.29	42.47	40.44	41.49	41.50	42.18	41.00	40.44	40.37
Al2O3							0.52		0.45						
FeO	18.04	19.62	16.77	20.10	15.41	20.12	20.48	11.32	19.37	15.31	14.88	14.06	17.78	20.56	19.66
MnO		0.36			0.35	0.35	0.38		0.41					0.54	0.45
MgO	40.79	39.23	41.57	38.95	42.88	38.98	37.96	45.94	39.33	43.20	43.28	43.76	40.85	38.06	39.18
CaO		0.32		0.37			0.37	0.26				0.33	0.37	0.40	0.34
Total	100.01	99.99	100.00	100.01	100.00	100.00	100.00	99.99	100.00	100.00	99.99	100.00	100.00	100.00	100.00
Fo	80.12	78.09	81.55	77.55	83.22	77.55	76.77	87.86	78.35	83.42	83.83	84.73	80.38	76.74	78.03
Fa	19.88	21.91	18.45	22.45	16.78	22.45	23.23	12.14	21.65	16.58	16.17	15.27	19.62	23.26	21.97

230220-2	230220-2	230220-2	230220-2	230220-2	230220-2	230220-2	230220-2	230220-2	230220-2	230220-2	230220-2	230220-2	230220-2	230220-2	230220-2
CRX11 C (27)	CRX11 R (28)	CRX12 C (29)	CRX12 R (30)	CRX12 (32)	CRX13 C (33)	CRX13 R (34)	CRX14 C (35)	CRX14 R (36)	CRX15 C (37)	CRX15 R (38)	CRX16 C (39)	CRX16 R (40)	CRX16 (41)	CRX17 C (43)	
PC	PC	PC	PC	MPC	PC	PC	PC	PC	PC	PC	PC	PC	MPC	PC	
41.52	41.56	41.87	40.89	41.00	41.92	40.74	41.39	40.78	42.01	41.17	42.15	41.52	41.42	41.78	
14.12	16.16	13.93	19.15	19.53	13.88	18.37	16.77	17.32	12.20	15.96	11.97	15.00	17.41	14.01	
0.32			0.44			0.33		0.34							
43.71	42.28	43.91	39.19	39.03	44.19	40.24	41.54	41.20	45.50	42.87	45.59	43.12	41.17	44.21	
0.32		0.29	0.34	0.43		0.32	0.30	0.36	0.28		0.30	0.37			
99.99	100.00	100.00	100.01	99.99	99.99	100.00	100.00	100.00	99.99	100.00	100.01	100.01	100.00	100.00	
84.66	82.34	84.89	78.49	78.08	85.02	79.61	81.53	80.92	86.93	82.72	87.16	83.67	80.83	84.91	
15.34	17.66	15.11	21.51	21.92	14.98	20.39	18.47	19.08	13.07	17.28	12.84	16.33	19.17	15.09	

230220-2	230220-2	230220-2	230220-2	230220-2	230220-2	230220-2	230220-2	230220-2	230220-2	230220-2	230220-2	230220-2	230220-2	230220-2
CRX17 R (44)	CRX18 (48)	CRX20 C (52)	CRX20 R (53)	CRX21 (54)	CRX21 (55)	CRX21 (57)	CRX21 (58)	CRX22 (4)	CRX22 (5)	CRX23 C1 (8)	CRX23 R (9)	CRX23 C2 (10)	CRX24 C1 (16)	CRX24 R1 (17)
PC	GM	PC	PC	MPC	GM	MPC	MPC	GM	MPC	PC	PC	PC	PC	PC
41.06	40.76	41.39	40.34	41.21	39.81	40.23	39.93	45.64	45.36	43.64	44.44	45.51	44.49	45.70
18.30	20.38	14.20	21.61	15.01	23.06	20.54	21.64	7.96	6.39	9.66	7.52	5.75	5.71	7.31
40.27	38.07	44.13	37.24	43.51	36.11	38.50	37.54	46.40	48.25	46.41	48.04	48.73	49.80	46.99
0.37	0.37	0.28	0.45	0.27	0.50	0.40	0.45			0.28				
100.00	100.00	100.00	100.00	100.00	99.99	100.01	99.99	100.00	100.00	99.99	100.00	99.99	100.00	100.00
79.69	76.90	84.71	75.44	83.79	73.62	76.97	75.56	91.22	93.08	89.54	91.93	93.79	93.96	91.97
20.31	23.10	15.29	24.56	16.21	26.38	23.03	24.44	8.78	6.92	10.46	8.07	6.21	6.04	8.03

230220-2	230220-2	230220-2	230220-2	230220-2	230220-2	230220-2	230220-2	230220-2	230220-2	230220-2	230220-2	230220-2	230220-2	230220-2
CRX24 C2 (18)	CRX24 R2 (19)	CRX24 (23)	CRX25 (5)	CRX25 (6)	CRX25 C (8)	CRX25 R (9)	CRX26 C (1)	CRX26 R (2)	CRX26 (7)	CRX27 (5)	CRX28 (4)	CRX29 (3)	CRX29 (4)	CRX29 (6)
PC	PC	MPC	GM	GM	GM	GM	PC	PC	GM	GM	GM	GM	GM	GM
44.89	45.48	46.01	40.29	40.22	39.27	36.49	41.11	40.49	39.97	40.29	40.06	39.93	39.92	40.33
6.09	7.93	8.78	20.39	20.54	25.96	40.93	15.17	20.10	22.54	20.87	21.51	23.55	23.19	21.21
49.02	46.59	45.22	38.58	38.46	33.90	21.08	43.15	38.66	36.64	38.06	37.61	35.56	35.96	37.55
			0.36	0.38	0.42	0.59	0.29	0.35	0.42	0.39	0.39	0.51	0.46	0.49
100.00	100.00	100.01	99.99	100.01	100.00	100.00	100.00	100.00	100.00	100.01	100.00	100.01	100.00	100.00
93.48	91.28	90.18	77.13	76.95	69.95	47.86	83.53	77.42	74.34	76.48	75.71	72.91	73.43	75.94
6.52	8.72	9.82	22.87	23.05	30.05	52.14	16.47	22.58	25.66	23.52	24.29	27.09	26.57	24.06

230220-2 CRX30 (3)	230220-2 CRX31 (4)	230220-2 CRX31 (5)	230220-2 CRX32 (3)	230220-2 CRX33 (4)	230220-2 CRX34 (3)	230220-2 CRX35 (3)	230220-2 CRX35 (4)	230220-2 CRX36 (5)	230220-2 CRX37 (3)	230220-2 CRX37 (4)	230220-2 CRX38 (5)	230220-2 CRX38 (6)	230220-2 CRX39 (5)	230220-2 CRX39 (6)
GM	GM	GM	GM	GM	GM	GM	GM	GM	GM	GM	GM	GM	GM	GM
40.64	40.19	40.39	40.07	40.06	40.30	40.37	40.42	40.15	40.44	40.36	40.21	40.07	40.09	40.18
19.80	21.99	20.76	22.33	21.66	19.59	20.23	20.36	21.47	19.41	20.02	20.91	23.00	22.06	21.48
0.36	0.40	0.37	0.41	0.45	0.34	0.38	0.35	0.41	0.36	0.40	0.41	0.42	0.37	0.35
38.80	37.03	38.09	36.74	37.40	38.99	38.65	38.51	37.50	39.46	38.86	38.08	36.08	37.06	37.59
0.40	0.38	0.39	0.45	0.44	0.43	0.38	0.36	0.47	0.32	0.36	0.39	0.43	0.42	0.40
100.00	99.99	100.00	100.00	100.01	100.00	100.01	100.00	100.00	99.99	100.00	100.00	100.00	100.00	100.00
77.74	75.01	76.58	74.57	75.48	78.01	77.30	77.13	75.69	78.37	77.58	76.45	73.66	74.97	75.73
22.26	24.99	23.42	25.43	24.52	21.99	22.70	22.87	24.31	21.63	22.42	23.55	26.34	25.03	24.27

230220-2 CRX40 (5)	230220-2 CRX40 (6)	230220-2 CRX41 C (1)	230220-2 CRX41 R (2)	230220-2 CRX41 C (3)	230220-2 CRX41 R (4)	230220-2 CRX41 (5)	230220-2 CRX42 (3)	230220-2 CRX42 (4)
GM	GM	PC	PC	PC	PC	GM	GM	GM
39.99	40.59	41.25	40.07	41.62	39.68	39.84	40.47	40.38
22.08	19.43	16.31	22.08	14.73	27.61	24.24	19.58	20.50
0.41	0.37	0.27	0.38	0.28	0.54	0.49	0.36	0.36
37.12	39.23	41.92	37.10	43.12	31.77	35.04	39.24	38.42
0.40	0.38	0.25	0.37	0.25	0.41	0.39	0.35	0.34
100.00	100.00	100.00	100.00	100.00	100.01	100.00	100.00	100.00
74.98	78.26	82.08	74.97	83.92	67.23	72.04	78.13	76.96
25.02	21.74	17.92	25.03	16.08	32.77	27.96	21.87	23.04

Sample Crystal/Zone [C: Core, R: Rim] Type [PC: phenocryst, MPC: microphenocryst, GM: groundmass]	240220-2	240220-2	240220-2	240220-2	240220-2	240220-2	240220-2	240220-2	240220-2	240220-2	240220-2	240220-2	240220-2	240220-2	240220-2
	CRX1 C (1)	CRX1 R (2)	CRX2 C (5)	CRX2 R (6)	CRX3 (9)	CRX3 (10)	CRX4 C1 (11)	CRX4 C2 (12)	CRX4 R1 (13)	CRX4 R2 (14)	CRX6 C (20)	CRX6 R (21)	CRX6 (22)	CRX8 C (26)	CRX8 R (27)
	PC	PC	PC	PC	GM	GM	PC	PC	PC	PC	PC	PC	GM	PC	PC
SiO2	41.74	39.97	41.07	39.54	39.14	38.91	41.35	41.66	40.84	39.25	40.88	39.57	39.57	41.34	39.96
Al2O3										0.56					
FeO	13.76	22.76	16.94	24.96	27.64	27.71	15.25	14.65	19.63	23.91	16.55	24.77	26.83	15.50	23.23
MnO		0.49		0.50	0.68	0.60			0.39	0.44		0.67	0.59	0.35	0.40
MgO	44.50	36.49	41.99	34.57	32.12	32.43	43.10	43.68	39.14	35.51	42.28	34.62	32.57	42.53	36.11
CaO		0.29		0.43	0.42	0.35	0.31			0.34	0.30	0.38	0.45	0.28	0.29
K2O															
Total	100.00	100.00	100.00	100.00	100.00	100.00	100.01	99.99	100.00	100.01	100.01	100.01	100.01	100.00	99.99
Fo	85.22	74.08	81.55	71.17	67.44	67.60	83.44	84.16	78.04	72.58	81.99	71.36	68.39	83.03	73.48
Fa	14.78	25.92	18.45	28.83	32.56	32.40	16.56	15.84	21.96	27.42	18.01	28.64	31.61	16.97	26.52

240220-2	240220-2	240220-2	240220-2	240220-2	240220-2	240220-2	240220-2	240220-2	240220-2	240220-2	240220-2	240220-2	240220-2	240220-2	240220-2
CRX9 (30)	CRX9 (31)	CRX10 C (32)	CRX10 R (33)	CRX10 (34)	CRX11 (38)	CRX12 (40)	CRX12 (42)	CRX13 C (44)	CRX13 R (45)	CRX14 C (46)	CRX14 R (47)	CRX17 C (54)	CRX17 R (55)	CRX19 C (58)	
MPC	GM	PC	PC	GM	GM	GM	GM	PC	PC	PC	PC	PC	PC	PC	
39.89	39.05	42.13	39.16	39.25	39.16	38.93	38.75	40.37	39.42	41.59	40.11	41.94	40.83	41.50	
24.67	28.23	13.20	25.89	27.40	27.58	28.04	27.90	20.64	26.66	13.84	22.57	13.28	17.24	13.33	
0.47	0.58		0.51	0.58	0.69	0.73	0.67		0.43		0.48				
34.64	31.72	44.37	34.12	32.36	32.15	31.77	32.28	38.64	33.24	44.21	36.37	44.45	41.59	44.86	
0.33	0.42	0.30	0.31	0.41	0.42	0.53	0.40	0.36	0.25	0.36	0.47	0.33	0.34	0.30	
100.00	100.00	100.00	99.99	100.00	100.00	100.00	100.00	100.01	100.00	100.00	100.00	100.00	100.00	99.99	
71.45	66.70	85.70	70.14	67.80	67.51	66.88	67.35	76.94	68.97	85.06	74.18	85.65	81.13	85.71	
28.55	33.30	14.30	29.86	32.20	32.49	33.12	32.65	23.06	31.03	14.94	25.82	14.35	18.87	14.29	

240220-2	240220-2	240220-2	240220-2	240220-2	240220-2	240220-2	240220-2	240220-2	240220-2	240220-2	240220-2	240220-2	240220-2	240220-2
CRX19 R (59)	CRX9 (13)	CRX20 C (22)	CRX20 R (23)	CRX21 (30)	CRX21 (31)	CRX21 (34)	CRX22 (3)	CRX23 C (5)	CRX23 R (6)	CRX23 (8)	CRX24 (10)	CRX25 (13)	CRX25 (16)	CRX26 C (19)
PC	GM	PC	PC	MPC	MPC	GM	GM	PC	PC	GM	GM	GM	GM	PC
39.99	45.12	43.49	42.66	41.15	42.66	40.75	38.51	40.94	39.31	38.92	39.10	39.06	38.81	41.66
24.49	16.78	9.51	16.76	23.21	19.22	24.43	27.94	17.87	26.46	27.51	27.49	27.75	27.72	13.92
0.58			0.41	0.59	0.57	0.57	0.63		0.67	0.57	0.59	0.61	0.59	
34.61	37.74	47.00	38.89	34.65	37.17	33.80	32.48	40.90	33.03	32.57	32.35	32.22	32.51	44.12
0.33	0.36		0.28	0.39	0.38	0.44	0.44	0.29	0.53	0.42	0.47	0.36	0.38	0.31
100.00	100.00	100.00	99.00	99.99	100.00	99.99	100.00	100.00	100.00	99.99	100.00	100.00	100.01	100.01
71.58	80.04	89.81	80.53	72.69	77.52	71.15	67.45	80.31	68.99	67.85	67.72	67.42	67.64	84.96
28.42	19.96	10.19	19.47	27.31	22.48	28.85	32.55	19.69	31.01	32.15	32.28	32.58	32.36	15.04

240220-2	240220-2	240220-2	240220-2	240220-2	240220-2	240220-2	240220-2	240220-2	240220-2	240220-2	240220-2	240220-2	240220-2	240220-2	
CRX26 R (20)	CRX26 (24)	CRX27 C (26)	CRX27 R (27)	CRX27 (28)	CRX28 (33)	CRX28 (34)	CRX 30 C (41)	CRX 30 R (42)	CRX30 (44)	CRX31 (47)	CRX31 (49)	CRX 33 C (58)	CRX 33 R (59)	CRX34 (60)	CRX35 (64)
PC	GM	PC	PC	GM	GM	GM	PC	PC	GM	GM	GM	PC	PC	GM	GM
40.05	38.85	41.35	40.44	38.88	38.94	38.99	41.98	39.19	39.05	39.11	39.13	40.57	39.84	39.22	38.45
22.50	27.54	16.15	21.44	27.50	27.69	27.64	13.44	26.20	27.42	27.33	27.08	18.74	25.32	26.82	28.47
0.54	0.60			0.62	0.64	0.75		0.53	0.68	0.54	0.57	0.34	0.58	0.71	0.65
36.57	32.53	42.24	37.79	32.64	32.35	32.17	44.29	33.76	32.53	32.66	32.71	40.01	34.27	32.89	31.03
0.35	0.49	0.26	0.34	0.36	0.38	0.45	0.30	0.33	0.31	0.34	0.50	0.35		0.36	0.40
															0.23
100.01	100.01	100.00	100.01	100.00	100.00	100.00	100.01	100.01	99.99	99.98	99.99	100.01	100.01	100.00	99.23
74.34	67.80	82.34	75.86	67.91	67.56	67.48	85.45	69.67	67.90	68.05	68.29	79.19	70.70	68.61	66.02
25.66	32.20	17.66	24.14	32.09	32.44	32.52	14.55	30.33	32.10	31.95	31.71	20.81	29.30	31.39	33.98

Sample Crystal/Zone [C: Core, R: Rim] Type [PC: phenocryst, MPC: microphenocryst, GM: groundmass]	250220-1 CRX1 C (1)	250220-1 CRX1 R (2)	250220-1 CRX1 (5)	250220-1 CRX1 (5)	250220-1 CRX3 (12)	250220-1 CRX7 C (20)	250220-1 CRX7 R (21)	250220-1 CRX8 C (22)	250220-1 CRX8 R (23)	250220-1 CRX9 C (24)	250220-1 CRX9 R (25)	250220-1 CRX10 (28)	250220-1 CRX10 (30)	250220-1 CRX11 C1 (31)	250220-1 CRX11 C2 (32)
	PC	PC	GM	GM	GM	PC	PC	PC	PC	PC	PC	GM	GM	PC	PC
SiO2	41.66	39.53	38.12	40.21	39.11	41.93	39.90	42.11	40.17	42.10	41.33	38.71	38.21	41.32	41.44
TiO2													0.43		
Al2O3															
FeO	13.26	24.19	30.54	20.74	28.14	12.40	23.80	12.94	22.65	13.06	15.12	30.26	32.73	14.77	15.00
MnO		0.46	0.60	0.40	0.57	0.30	0.46		0.47			0.60	0.77	0.34	
MgO	44.79	35.36	29.33	38.27	31.63	45.07	35.41	44.94	36.71	44.84	43.30	29.82	26.50	43.17	43.21
CaO	0.28	0.46	0.70	0.39	0.55	0.31	0.43				0.25	0.61	1.36	0.40	0.35
Na2O															
P2O5			0.72												
Total	99.99	100.00	100.01	100.01	100.00	100.01	100.00	99.99	100.00	100.00	100.00	100.00	100.00	100.00	100.00
Fo	85.76	72.27	63.13	76.69	66.71	86.63	72.62	86.09	74.29	85.96	83.62	63.72	59.07	83.90	83.70
Fa	14.24	27.73	36.87	23.31	33.29	13.37	27.38	13.91	25.71	14.04	16.38	36.28	40.93	16.10	16.30

250220-1 CRX11 R (33)	250220-1 CRX11 C3 (34)	250220-1 CRX12 C (35)	250220-1 CRX12 R (36)	250220-1 CRX14 C (43)	250220-1 CRX14 R (44)	250220-1 CRX15 (47)	250220-1 CRX18 C (53)	250220-1 CRX18 R (54)	250220-1 CRX19 C (57)	250220-1 CRX19 R (58)	250220-1 CRX20 C (59)	250220-1 CRX20 R (60)	250220-1 CRX24 (2)	250220-1 CRX24 (3)
PC	PC	PC	PC	PC	PC	GM	PC	PC	PC	PC	PC	PC	GM	GM
40.47	41.76	42.12	40.76	42.19	40.95	39.40	42.18	40.51	41.74	40.82	40.07	40.27	40.60	40.46
									0.43					0.48
21.79	14.94	14.00	22.59	12.86	18.48	27.53	12.90	21.39	13.64	19.95	21.54	21.92	19.24	27.44
0.37						0.63		0.40			0.36		0.32	0.56
37.09	43.00	43.88	36.40	44.64	40.22	31.88	44.63	37.15	44.19	39.24	37.69	37.47	39.44	30.04
0.29	0.30		0.24	0.31	0.35	0.56	0.29	0.56			0.35	0.34	0.40	0.55
														0.46
100.01	100.00	100.00	99.99	100.00	100.00	100.00	100.00	100.01	100.00	100.01	100.01	100.00	100.00	99.99
75.21	83.69	84.82	74.18	86.09	79.51	67.37	86.05	75.59	85.24	77.81	75.72	75.29	78.51	66.12
24.79	16.31	15.18	25.82	13.91	20.49	32.63	13.95	24.41	14.76	22.19	24.28	24.71	21.49	33.88

250220-1	250220-1	250220-1	250220-1	250220-1	250220-1	250220-1	250220-1	250220-1	250220-1	250220-1	250220-1	250220-1	250220-1	250220-1	
CRX24 (5)	CRX24 (6)	CRX25 (1)	CRX25 (5)	CRX26 C (3)	CRX26 R (4)	CRX27 (1)	CRX27 (4)	CRX28 (1)	CRX28 (2)	CRX29 (1)	CRX29 C (2)	CRX29 R (3)	CRX30 C (1)	CRX30 R (2)	
GM	GM	GM	GM	PC	PC	GM	MPC	GM	GM	GM	GM	GM	PC	PC	
39.37	39.41	40.00	39.90	41.72	40.98	39.68	40.56	40.03	39.87	40.38	39.70	38.31	40.89	39.92	
23.61	25.55	24.06	24.37	14.29	17.61	24.98	20.32	22.25	24.87	21.15	24.46	30.66	15.88	24.25	
0.55	0.38	0.35	0.45		0.31	0.49	0.43	0.45	0.42	0.33	0.46	0.64	0.35	0.43	
36.03	34.10	35.12	34.80	43.73	40.77	34.39	38.30	36.87	34.39	37.71	34.94	29.94	41.96	35.02	
0.44	0.56	0.47	0.49	0.26	0.33	0.45	0.39	0.40	0.46	0.43	0.44	0.45	0.33	0.37	
													0.59		
100.00	100.00	100.00	100.01	100.00	100.00	99.99	100.00	100.00	100.01	100.00	100.00	100.00	100.00	99.99	
73.12	70.41	72.24	71.80	84.51	80.50	71.05	77.06	74.71	71.14	76.07	71.80	63.51	82.49	72.02	
26.88	29.59	27.76	28.20	15.49	19.50	28.95	22.94	25.29	28.86	23.93	28.20	36.49	17.51	27.98	
250220-1	250220-1	250220-1	250220-1	250220-1	250220-1	250220-1	250220-1	250220-1	250220-1	250220-1	250220-1	250220-1	250220-1	250220-1	
CRX30 (5)	CRX31 (1)	CRX31 (3)	CRX32 (5)	CRX32 (6)	CRX33 (4)	CRX33 (5)	CRX34 (2)	CRX34 (3)	CRX34 (4)	CRX35 (5)	CRX35 (6)	CRX36 (4)	CRX39 C (1)	CRX39 R (2)	CRX39 R (3)
GM	GM	GM	GM	GM	GM	GM	GM	GM	GM	GM	GM	GM	PC	PC	PC
41.16	40.18	40.01	40.29	40.00	39.94	39.76	37.94	40.11	40.07	40.14	39.92	40.80	41.40	41.30	41.10
18.08	21.03	24.09	22.11	23.57	23.94	25.05	30.77	21.75	22.39	22.53	24.54	20.31	15.07	17.39	18.44
40.47	0.33	0.43	0.44	0.37	0.58	0.39	0.56	0.37	0.44	0.46	0.38	0.37			
0.29	38.00	35.03	36.77	35.63	35.10	34.30	29.53	37.30	36.68	36.38	34.68	38.14	43.26	41.07	40.14
	0.45	0.43	0.39	0.44	0.44	0.50	0.61	0.48	0.42	0.48	0.48	0.37	0.28	0.24	0.32
							0.58								
100.00	99.99	99.99	100.00	100.01	100.00	100.00	99.99	100.01	100.00	99.99	100.00	99.99	100.01	100.00	100.00
79.96	76.31	72.16	74.78	72.93	72.33	70.94	63.11	75.35	74.49	74.22	71.58	77.00	83.65	80.81	79.51
20.04	23.69	27.84	25.22	27.07	27.67	29.06	36.89	24.65	25.51	25.78	28.42	23.00	16.35	19.19	20.49

Sample Crystal/Zone [C: Core, R: Rim] Type [PC: phenocryst, MPC: microphenocryst, GM: groundmass]	250220-6 CRX1 C (1)	250220-6 CRX1 R (2)	250220-6 CRX4 (12)	250220-6 CRX5 C (14)	250220-6 CRX5 R (15)	250220-6 CRX6 (18)	250220-6 CRX8 (25)	250220-6 CRX8 (29)	250220-6 CRX9 C (30)	250220-6 CRX9 R (31)	250220-6 CRX11 (37)	250220-6 CRX12 C (38)	250220-6 CRX12 R (39)	250220-6 CRX13 (1)	250220-6 CRX13 (2)
	PC	PC	GM	PC	PC	MPC	GM	GM	PC	PC	GM	PC	PC	GM	GM
SiO2	41.38	39.50	39.35	41.14	39.31	39.05	39.13	38.81	41.78	39.38	39.04	41.53	39.76	38.94	39.28
Al2O3											0.33				
FeO	14.95	26.47	27.59	17.21	27.00	27.70	27.59	28.63	13.54	26.15	27.65	14.74	25.38	27.52	28.53
MnO		0.40	0.53	0.36	0.53	0.51	0.54	0.53	0.24	0.47	0.51	0.29	0.42	0.56	0.55
MgO	43.27	33.22	32.01	40.95	32.68	32.34	32.25	31.48	44.15	33.59	31.95	43.12	34.04	32.55	31.09
CaO	0.40	0.41	0.51	0.35	0.48	0.41	0.48	0.55	0.28	0.41	0.51	0.33	0.40	0.43	0.54
Total	100.00	100.00	99.99	100.01	100.00	100.01	99.99	100.00	99.99	100.00	99.99	100.01	100.00	100.00	99.99
Fo	83.76	69.11	67.41	80.92	68.33	67.55	67.57	66.22	85.32	69.60	67.32	83.91	70.51	67.83	66.02
Fa	16.24	30.89	32.59	19.08	31.67	32.45	32.43	33.78	14.68	30.40	32.68	16.09	29.49	32.17	33.98

250220-6 CRX14 C (1)	250220-6 CRX14 C (2)	250220-6 CRX14 (3)	250220-6 CRX16 (4)	250220-6 CRX16 (5)	250220-6 CRX17 (1)	250220-6 CRX17 (2)	250220-6 CRX18 C (1)	250220-6 CRX18 R (2)	250220-6 CRX18 (5)	250220-6 CRX19 C (1)	250220-6 CRX19 R (2)	250220-6 CRX19 C (3)	250220-6 CRX19 R (4)	250220-6 CRX19 (8)
PC	PC	GM	GM	GM	GM	GM	PC	PC	GM	PC	PC	PC	PC	GM
40.61	40.81	39.18	39.39	39.08	39.52	39.15	39.96	39.57	40.47	40.62	39.77	41.37	39.65	39.20
									1.28					
18.81	18.46	27.51	27.34	27.65	27.74	27.75	24.11	25.64	24.93	21.16	25.35	18.06	25.14	26.90
0.33	0.39	0.65	0.46	0.50	0.54	0.38	0.41	0.61	0.40		0.58		0.53	0.59
39.96	39.94	32.17	32.38	32.31	31.59	32.22	35.27	33.73	31.97	37.83	33.86	40.16	34.23	32.85
0.29	0.40	0.49	0.43	0.46	0.61	0.50	0.26	0.45	0.94	0.39	0.43	0.41	0.45	0.47
100.00	100.00	100.00	100.00	100.00	100.00	100.00	100.01	100.00	99.99	100.00	99.99	100.00	100.00	100.01
79.11	79.41	67.58	67.86	67.56	67.00	67.42	72.28	70.11	69.57	76.12	70.42	79.85	70.82	68.52
20.89	20.59	32.42	32.14	32.44	33.00	32.58	27.72	29.89	30.43	23.88	29.58	20.15	29.18	31.48

250220-6 CRX20 (1)	250220-6 CRX20 (2)	250220-6 CRX20 (4)	250220-6 CRX20 (7)	250220-6 CRX21 (1)	250220-6 CRX21 (2)	250220-6 CRX22 (1)	250220-6 CRX22 (2)	250220-6 CRX23 (3)	250220-6 CRX23 (4)	250220-6 CRX24 C (1)	250220-6 CRX24 R (2)	250220-6 CRX24 C (3)	250220-6 CRX25 (4)	250220-6 CRX26 C (3)
GM	GM	GM	GM	GM	GM	GM	GM	GM	GM	PC	PC	PC	GM	GM
39.34	40.00	39.57	39.83	39.48	39.35	39.57	39.61	39.15	39.25	41.58	40.87	41.49	38.81	39.55
26.49	25.25	25.37	27.42	26.16	26.18	25.74	26.40	29.33	27.32	15.43	16.75	14.26	28.22	24.16
0.67	0.48	0.66	0.67	0.52	0.39	0.42	0.57	0.56	0.54				0.59	0.51
33.10	33.92	34.07	31.65	33.40	33.70	33.88	32.92	30.29	32.36	42.68	42.04	43.91	31.87	35.46
0.39	0.35	0.33	0.42	0.45	0.38	0.39	0.51	0.67	0.54	0.31	0.34	0.33	0.52	0.31
99.99	100.00	100.00	99.99	100.01	100.00	100.00	100.01	100.00	100.01	100.00	100.00	99.99	100.01	99.99
69.02	70.54	70.54	67.29	69.47	69.65	70.12	68.97	64.80	67.86	83.14	81.73	84.59	66.81	72.35
30.98	29.46	29.46	32.71	30.53	30.35	29.88	31.03	35.20	32.14	16.86	18.27	15.41	33.19	27.65

250220-6 CRX26 R (4)	250220-6 CRX27 C (3)	250220-6 CRX27 R (4)	250220-6 CRX28 (1)	250220-6 CRX28 (3)	250220-6 CRX29 C (1)	250220-6 CRX29 R (2)	250220-6 CRX29 (3)	250220-6 CRX29 (8)
GM	MPC	MPC	GM	GM	PC	PC	GM	GM
39.38	41.71	41.14	39.08	39.63	41.08	41.34	39.90	39.54
				0.75				
27.08	13.68	17.49	28.39	26.53	18.46	15.90	24.24	25.03
0.43		0.39	1.68	1.43		0.32	0.48	0.6
32.65	44.28	40.62	30.40	31.30	40.07	42.06	34.90	34.33
0.45	0.33	0.35	0.46	0.36	0.39	0.37	0.48	0.49
99.99	100.00	99.99	100.01	100.00	100.00	99.99	100.00	99.99
68.25	85.23	80.54	65.62	67.77	79.46	82.50	71.96	70.97
31.75	14.77	19.46	34.38	32.23	20.54	17.50	28.04	29.03

3. Piroxeno

Sample Crystal/Zone [C: Core, R: Rim] Type [PC: phenocryst, MPC: microphenocryst, GM: groundmass]	021219-1 CRX16 (36)	021219-1 CRX16 (37)	021219-1 CRX16 (38)	021219-1 CRX16 (39)	021219-1 CRX17 (6)	021219-1 CRX18 (14)	021219-1 CRX18 (15)	021219-1 CRX19 (16)	021219-1 CRX19 (17)	021219-1 CRX 20 (7)	021219-1 CRX 20 (8)	021219-1 CRX 20 (13)	021219-1 CRX 21 (17)	021219-1 CRX 21 (18)	021219-1 CRX 22 (26)
	GM	GM	GM	GM	GM	GM	GM	GM	GM	GM	GM	GM	GM	GM	GM
SiO2	47.88	47.14	48.52	50.43	56.80	56.11	57.07	55.53	58.14	48.24	50.52	50.31	47.46	49.61	49.58
TiO2	4.93	5.32	4.89	4.44	3.35	2.68	2.88	3.56	2.75	4.71	2.87	3.07	5.18	3.57	4.50
Al2O3	3.48	3.81	3.61	4.63	4.97	6.77	5.06	4.97	3.56	4.39	2.96	3.13	4.85	4.40	3.17
FeO	13.12	13.18	13.75	12.99	6.36	4.44	5.43	6.38	6.86	12.94	14.33	14.23	12.82	11.46	14.42
MnO										0.38	0.54	0.35	0.35		
MgO	8.92	8.79	8.77	7.93	12.10	14.62	13.46	12.52	11.63	8.69	8.66	8.67	8.66	9.95	8.03
CaO	19.97	19.85	19.56	17.79	14.91	14.11	14.68	15.91	15.51	19.74	19.38	19.40	19.78	20.33	19.21
Na2O	1.05	0.98	0.90	1.24	1.51	1.27	1.42	1.13	1.55	0.93	0.74	0.85	0.89	0.69	1.08
K2O				0.55											
P2O5	0.66	0.94													
Total	99.35	99.07	100.00	100.00	100.00	100.00	100.00	100.00	100.00	100.02	100.00	100.01	99.99	100.01	99.99
En	29.12	28.87	28.72	28.32	45.86	53.65	49.75	45.47	43.68	28.63	28.00	28.15	28.61	32.11	26.83
Fs	24.03	24.28	25.26	26.02	13.52	9.14	11.26	13.00	14.45	24.63	26.98	26.57	24.42	20.74	27.03
Wo	46.85	46.85	46.03	45.66	40.62	37.21	38.99	41.53	41.87	46.74	45.03	45.28	46.97	47.15	46.14

021219-1 CRX 23 (32)	021219-1 CRX 23 (33)	021219-1 CRX 23 (36)	021219-1 CRX 24 (40)	021219-1 CRX 24 (43)	021219-1 CRX 26 (52)	021219-1 CRX 27 (58)	021219-1 CRX 29 (70)	021219-1 CRX 30 (76)	021219-1 CRX 32 (86)	021219-1 CRX 33 (90)	021219-1 CRX 34 (94)
GM	GM	GM	GM	GM	GM	GM	GM	GM	GM	GM	GM
47.58	48.75	49.44	49.46	49.82	49.31	47.42	47.28	48.52	48.20	48.69	49.69
5.04	4.44	3.43	3.74	3.61	3.74	5.36	5.33	3.79	4.66	4.49	4.19
4.02	3.62	3.65	3.47	3.77	4.81	3.66	4.08	4.42	4.08	3.47	3.52
12.76	12.68	12.18	11.70	12.08	10.99	13.89	14.02	11.84	12.31	13.87	13.30
	0.34	0.32					0.38	0.32			
9.74	9.43	10.48	10.52	9.72	10.62	8.61	8.25	9.90	9.77	8.95	8.93
19.99	20.05	19.88	20.38	20.25	19.82	20.18	19.81	20.52	19.44	19.59	19.61
0.87	0.69	0.61	0.73	0.75	0.71	0.88	0.84	0.69	0.86	0.93	0.75
									0.69		
100.00	100.00	99.99	100.00	100.00	100.00	100.00	99.99	100.00	100.01	99.99	99.99
31.15	30.28	32.97	33.15	31.30	34.23	27.86	26.99	31.46	31.88	29.05	29.29
22.89	23.46	22.07	20.68	21.82	19.87	25.21	26.44	21.68	22.53	25.25	24.47
45.95	46.27	44.96	46.16	46.87	45.91	46.93	46.58	46.86	45.59	45.70	46.23

Sample	031219-2A	031219-2A	031219-2A	031219-2A	031219-2A	031219-2A	031219-2A	031219-2A	031219-2A	031219-2A	031219-2A	031219-2A	031219-2A	031219-2A	031219-2A
Crystal/Zone [C: Core, R: Rim]	CRX6 (18)	CRX13 (38)	CRX14 (40)	CRX14 (41)	CRX14 (42)	CRX16 (49)	CRX18 (7)	CRX18 (8)	CRX19 (18)	CRX21 (3)	CRX21 (4)	CRX21 (11)	CRX23 (16)	CRX24 (23)	CRX25 (27)
Type [PC: phenocryst, MPC: microphenocryst, GM: groundmass]	GM	MPC	MPC	MPC	MPC	GM	GM	GM	MPC	GM	GM	GM	GM	GM	GM
SiO2	53.91	51.66	51.90	54.21	50.60	51.88	57.92	57.79	55.49	52.10	52.75	51.98	52.46	52.92	52.03
TiO2	1.26	2.16	1.88	1.17	2.80	2.78	1.21	1.12	1.78	2.00	2.00	2.27	2.10	2.13	2.32
Al2O3	1.97	3.86	3.84	2.01	3.91	3.30	3.75	3.49	5.27	4.13	3.79	4.74	4.20	3.26	4.46
FeO	7.95	8.64	8.11	8.10	9.54	9.24	3.94	4.76	4.30	8.34	8.51	7.68	7.40	8.89	7.61
MnO			0.33		0.42										
MgO	14.48	13.23	13.44	15.02	12.58	12.50	17.32	16.80	16.42	13.53	13.21	13.58	13.95	13.13	13.61
CaO	20.02	19.79	20.03	19.49	19.25	19.71	15.07	15.14	16.00	19.39	19.22	19.37	19.35	19.04	19.41
Na2O	0.40	0.66	0.47		0.80	0.59	0.79	0.90	0.72	0.51	0.52	0.38	0.54	0.64	0.58
Total	99.99	100.00	100.00	100.00	99.90	100.00	100.00	100.00	99.98	100.00	100.00	100.00	100.00	100.01	100.02
En	43.45	40.96	41.26	44.74	39.31	39.25	57.05	55.35	54.14	42.09	41.54	42.69	43.58	41.29	42.76
Fs	13.38	15.01	14.54	13.54	17.47	16.28	7.28	8.80	7.95	14.55	15.01	13.54	12.97	15.68	13.41
Wo	43.17	44.03	44.20	41.72	43.23	44.48	35.67	35.85	37.91	43.35	43.44	43.76	43.45	43.03	43.83

031219-2A	031219-2A	031219-2A	031219-2A	031219-2A
CRX26 (33)	CRX27 (37)	CRX28 (42)	CRX29 (46)	CRX29 (47)
GM	GM	GM	GM	GM
54.75	54.12	53.75	54.14	53.99
1.01	1.18	1.38	1.30	1.12
3.24	2.11	3.29	2.68	3.24
7.21	7.70	7.14	7.61	6.93
	0.30			
14.76	15.27	14.72	14.84	14.91
18.37	18.81	19.29	18.94	19.37
0.66	0.50	0.44	0.50	0.43
100.00	99.99	100.01	100.01	99.99
46.11	45.89	45.17	45.35	45.57
12.64	13.49	12.29	13.05	11.88
41.25	40.62	42.54	41.60	42.55

Sample Crystal/Zone [C: Core, R: Rim] Type [PC: phenocryst, MPC: microphenocryst, GM: groundmass]	031219-4 CRX1 (1)	031219-4 CRX1 (2)	031219-4 CRX1 (3)	031219-4 CRX1 (4)	031219-4 CRX2 (5)	031219-4 CRX2 (6)	031219-4 CRX2 (7)	031219-4 CRX3 C (9)	031219-4 CRX3 R (10)	031219-4 CRX3 C (11)	031219-4 CRX3 C (14)	031219-4 CRX5 C (19)	031219-4 CRX5 R (20)	031219-4 CRX8 C (25)	031219-4 CRX8 R (26)
	MPC	MPC	MPC	MPC	MPC	MPC	MPC	PC	PC	PC	PC	PC	PC	PC	PC
SiO2	56.29	56.65	57.54	58.40	53.95	55.27	57.12	59.13	60.06	60.81	62.98	58.72	58.88	62.14	63.08
TiO2	0.43														
Al2O3								1.35	0.72					1.66	
FeO	22.16	21.39	21.93	19.66	25.43	23.89	21.11	19.25	16.34	16.11	12.00	18.24	19.63	9.34	7.84
MnO	1.69	1.46	1.48	1.68	1.67	1.69	1.50	1.15	0.95	1.06	0.83	0.93	1.03		
MgO	17.57	17.76	16.53	17.79	17.25	15.95	15.06	19.11	20.76	20.76	22.93	20.81	19.16	25.48	28.17
CaO	1.87	2.75	2.51	2.47	1.71	3.20	2.71	1.36	1.17	1.27	1.26	1.30	1.29	1.38	0.91
Na2O							0.79								
K2O							0.35								
P2O5															
Total	100.01	100.01	99.99	100.00	100.01	100.00	99.99	100.00	100.00	100.01	100.00	100.00	99.99	100.00	100.00
En	54.39	54.54	52.51	56.39	51.20	48.91	50.70	60.59	66.31	66.30	73.88	64.02	60.47	80.35	84.79
Fs	41.45	39.39	41.75	37.98	45.16	44.04	42.74	36.31	31.00	30.79	23.21	33.10	36.60	16.52	13.24
Wo	4.16	6.07	5.73	5.63	3.65	7.05	6.56	3.10	2.69	2.91	2.92	2.87	2.93	3.13	1.97

031219-4 CRX9 R (27)	031219-4 CRX9 C (28)	031219-4 CRX11 C (30)	031219-4 CRX11 R (31)	031219-4 CRX13 C (37)	031219-4 CRX13 R (38)	031219-4 CRX15 C (41)	031219-4 CRX15 R (42)	031219-4 CRX15 C (43)	031219-4 CRX15 R (44)	031219-4 CRX1 (1)	031219-4 CRX1 (2)	031219-4 CRX1 (3)	031219-4 CRX1 (4)	031219-4 CRX1 (5)
PC	PC	PC	PC	PC	PC	PC	PC	PC	PC	MPC	MPC	MPC	MPC	MPC
53.69	54.85	61.20	59.88	61.93	52.53	60.07	62.38	56.33	55.20	60.41	61.26	61.79	60.79	59.52
		0.95		0.76	0.30	0.81		0.48	0.27					
				2.27	2.27	0.81		0.59	0.59					
26.99	22.89	15.04	17.82	14.02	28.16	17.92	14.49	22.99	23.70	16.50	16.46	15.13	17.13	19.89
1.70	1.45	0.79	0.98	0.75	1.8	1.01	1.03	1.26	1.41	0.94	1.22	0.84	1.36	1.49
15.96	19.34	20.73	19.98	21.34	13.43	18.92	20.91	17.52	17.32	20.67	18.95	19.91	17.73	17.15
1.66	1.48	1.28	1.33	1.20	1.51	1.28	1.19	1.42	1.52	1.48	2.11	2.33	2.98	1.95
100.00	100.01	99.99	99.99	100.00	100.00	100.01	100.00	100.00	100.01	100.00	100.00	100.00	99.99	100.00
47.99	56.77	67.89	63.45	69.98	42.86	62.10	68.60	54.49	53.28	65.57	62.35	65.17	58.60	56.13
48.43	40.11	29.10	33.51	27.19	53.68	34.88	28.59	42.34	43.36	31.06	32.66	29.35	34.32	39.29
3.59	3.12	3.01	3.04	2.83	3.46	3.02	2.81	3.17	3.36	3.37	4.99	5.48	7.08	4.59

031219-4	031219-4	031219-4	031219-4	031219-4	031219-4	031219-4	031219-4	031219-4	031219-4	031219-4	031219-4	031219-4	031219-4	031219-4
CRX3 C (8)	CRX3 R (9)	CRX3 R (10)	CRX3 R (11)	CRX3 C (12)	CRX18 (1)	CRX18 (2)	CRX18 (5)	CRX18 (6)	CRX18 (7)	CRX17 (14)	CRX17 (15)	CRX14 (22)	CRX19 (24)	CRX19 (26)
PC	PC	PC	PC	PC	GM	GM	GM	GM	GM	GM	GM	GM	GM	GM
57.80	57.99	59.12	58.17	57.64	62.76	64.74	57.22	59.04	61.85	57.12	57.94	65.51	55.76	57.26
1.18			0.72	0.99	0.85				2.01					
19.52	19.58	18.18	19.23	20.54	15.71	12.59	24.26	21.14	16.67	23.89	23.12	11.65	25.73	22.83
1.22	1.29	1.21	0.72	1.18	0.92	1.13	1.64	1.45	1.29	1.89	1.74		1.95	1.25
17.72	19.62	20.12	19.89	18.11	17.67	19.84	14.82	16.37	15.61	15.18	15.01	20.89	14.36	16.38
2.55	1.52	1.38	1.27	1.54	2.08	1.69	2.06	2.00	1.77	1.92	2.19	1.95	2.20	2.29
									0.80					
99.99	100.00	100.01	100.00	100.00	99.99	99.99	100.00	100.00	100.00	100.00	100.00	100.00	100.00	100.01
56.80	60.50	62.88	62.16	57.66	62.00	68.99	48.05	53.69	57.89	48.91	49.14	72.47	45.61	51.93
37.32	36.13	34.02	34.99	38.82	32.76	26.79	47.15	41.60	37.40	46.64	45.70	22.67	49.37	42.85
5.87	3.37	3.10	2.85	3.52	5.25	4.22	4.80	4.71	4.72	4.45	5.15	4.86	5.02	5.22
031219-4	031219-4	031219-4	031219-4	031219-4	031219-4	031219-4	031219-4	031219-4	031219-4	031219-4	031219-4	031219-4	031219-4	031219-4
CRX19 (27)	CRX19 (28)	CRX20 (32)	CRX20 (33)	CRX20 (34)	CRX20 (35)	CRX22 (46)	CRX23 (50)	CRX17 (3)	CRX30 (2)	CRX30 (3)	CRX31 C (1)	CRX31 R (2)	CRX31 (3)	CRX32 C (1)
GM	GM	GM	GM	GM	GM	GM	GM	GM	GM	GM	PC	PC	GM	PC
57.07	58.88	64.75	63.35	67.03	66.52	61.80	67.81	56.63	53.22	53.78	53.22	53.29	52.86	53.34
	2.63			2.35					0.36	0.70	1.35	0.67	0.75	0.59
23.52	21.48	15.54	14.73	13.03	12.39	17.31	9.71	23.34	28.87	28.11	26.83	26.72	29.19	27.09
1.72	1.62		1.28			1.16		2.03	2.05	1.79	1.43	1.47	2.06	1.52
15.22	12.65	18.28	18.98	15.89	19.65	17.75	20.39	16.32	12.80	12.19	16.45	15.86	12.74	15.84
2.48	1.95	1.42	1.65	1.70	1.45	1.97	2.08	1.68	2.00	2.15	1.41	1.61	2.41	1.61
	0.79									0.63				
100.01	100.00	99.99	99.99	100.00	100.01	99.99	99.99	100.00	100.00	100.00	100.01	100.00	100.01	99.99
48.82	46.81	65.24	65.10	65.07	71.09	60.10	74.60	51.36	40.51	39.94	49.36	48.29	39.79	47.92
45.46	48.00	31.11	30.84	29.93	25.14	35.11	19.93	44.84	54.94	55.00	47.60	48.18	54.80	48.58
5.72	5.19	3.64	4.07	5.00	3.77	4.79	5.47	3.80	4.55	5.06	3.04	3.52	5.41	3.50

031219-4 CRX32 R (2)	031219-4 CRX33 (1)	031219-4 CRX33 (2)	031219-4 CRX34 (2)	031219-4 CRX34 (3)	031219-4 CRX34 (6)	031219-4 CRX35 (4)	031219-4 CRX36 (1)	031219-4 CRX36 (2)	031219-4 CRX36 (5)	031219-4 CRX37 C (1)	031219-4 CRX37 R (2)	031219-4 CRX37 R (3)	031219-4 CRX37 R (4)	031219-4 CRX38 (1)
PC	GM	GM	GM	GM	GM	GM	GM	GM	GM	PC	PC	PC	PC	GM
53.87	53.04	52.35 0.41	53.40	53.48	52.96	52.94	52.11 0.47	53.25	52.78	53.70	53.16	53.31	53.72	52.89 0.33
0.57		0.56					0.41 0.70					0.64		
25.91	29.51	30.25	29.32	29.24	29.68	29.10	29.79	29.72	30.65	26.52	27.82	26.95	28.09	29.00
1.49	2.06	2.26	2.18	2.12	2.13	1.89	1.93	2.19	1.94	1.5	1.67	1.51	1.7	2.01
16.61	13.24	12.02	13.06	12.95	13.00	13.46	13.03	12.69	12.39	16.77	15.75	16.06	15.00	13.79
1.54	2.15	2.14	2.04	2.21	2.24	2.20	1.95	2.14	2.24	1.51	1.59	1.52	1.48	1.97
99.99	100.00	99.99	100.00	100.00	100.01	100.00	99.98	99.99	100.00	100.00	99.99	99.99	99.99	99.99
50.18	40.73	37.78	40.54	40.29	40.04	41.49	40.42	39.48	38.36	49.93	47.09	48.48	45.75	42.28
46.47	54.52	57.38	54.91	54.77	55.00	53.63	55.24	55.74	56.65	46.84	49.50	48.22	51.01	53.38
3.34	4.75	4.83	4.55	4.94	4.96	4.87	4.35	4.78	4.98	3.23	3.42	3.30	3.24	4.34
031219-4 CRX38 (3)	031219-4 CRX38 (4)	031219-4 CRX38 (5)	031219-4 CRX38 (6)	031219-4 CRX38 (7)	031219-4 CRX39 (1)	031219-4 CRX39 (2)	031219-4 CRX40 (1)	031219-4 CRX40 (2)	031219-4 CRX40 (3)	031219-4 CRX41 (1)	031219-4 CRX41 (2)	031219-4 CRX41 (3)	031219-4 CRX41 (4)	031219-4 CRX42 (3)
GM	GM	GM	GM	GM	GM	GM	GM	GM	GM	GM	GM	GM	GM	GM
53.41	53.06 0.48	53.72	52.85	53.28	53.57	54.24	53.42	53.21	53.02	53.58	53.84	52.86	52.72	53.66
								0.46	0.48				0.47	
29.04	29.22	28.66	28.55	28.96	29.04	28.45	29.24	29.43	28.98	28.94	28.29	29.65	29.34	28.48
2.03	2.04	2.1	1.96	1.84	1.93	1.77	2.03	1.9	2.09	1.96	1.84	1.97	2.07	1.88
13.39	12.91	13.45	13.22	13.53	13.16	13.45	13.22	12.81	13.36	13.33	13.86	13.30	13.15	13.90
2.13	2.29	2.07	2.59	2.39	2.30	2.10	2.10	2.19	2.07	2.19	2.17	2.21	2.24	2.08
			0.84											
100.00	100.00	100.00	100.01	100.00	100.00	100.01	100.01	100.00	100.00	100.00	100.00	99.99	99.99	100.00
41.37	40.21	41.76	41.04	41.58	40.87	42.13	40.95	40.07	41.37	41.33	42.86	40.75	40.59	42.85
53.90	54.66	53.62	53.18	53.14	54.00	53.14	54.38	55.01	54.02	53.79	52.31	54.39	54.44	52.54
4.73	5.13	4.62	5.78	5.28	5.13	4.73	4.67	4.92	4.61	4.88	4.82	4.87	4.97	4.61

031219-4	031219-4	031219-4	031219-4	031219-4	031219-4	031219-4	031219-4	031219-4	031219-4	031219-4	031219-4
CRX43 (3)	CRX44 (3)	CRX44 (4)	CRX44 (5)	CRX45 (3)	CRX45 (4)	CRX46 (1)	CRX46 (4)	CRX47 (1)	CRX47 (2)	CRX48 (1)	CRX48 (2)
GM	GM	GM	GM	GM	GM	GM	GM	GM	GM	GM	GM
53.09	53.12	53.18	52.85	53.34	53.51	53.26	52.87	53.81	53.29 0.34	54.00	53.30
29.03	29.63	28.90	29.07	28.72	28.23	29.63	30.04	28.62	29.03	28.60	28.78
2.03	1.91	2.05	1.79	2.1	2.16	2.1	1.97	2.01	1.95	1.74	1.98
13.76	13.11	13.46	13.62	13.69	13.91	12.34	12.67	13.49	13.13	13.56	13.86
2.09	2.24	2.40	2.67	2.15	2.19	2.20	2.45	2.07	2.26	2.09	2.07
100.00	100.01	99.99	100.00	100.00	100.00	100.00	100.00	100.00	100.00	99.99	99.99
42.08	40.43	41.34	41.44	42.07	42.74	38.88	39.10	41.93	40.84	42.25	42.49
53.33	54.61	53.37	52.72	53.18	52.43	56.13	55.46	53.45	54.10	53.07	52.95
4.59	4.96	5.30	5.84	4.75	4.84	4.98	5.43	4.62	5.05	4.68	4.56

Sample Crystal/Zone [C: Core, R: Rim] Type [PC: phenocryst, MPC: microphenocryst, GM: groundmass]	051219-1 CRX6 (17)	051219-1 CRX6 (18)	051219-1 CRX6 (19)	051219-1 CRX6 (20)	051219-1 CRX6 (21)	051219-1 CRX6 (22)	051219-1 CRX6 (23)	051219-1 CRX21 (7)	051219-1 CRX23 (16)	051219-1 CRX23 (17)	051219-1 CRX24 (25)	051219-1 CRX26 (5)	051219-1 CRX26 (6)	051219-1 CRX27 (5)	051219-1 CRX27 (6)
	MPC	MPC	MPC	MPC	MPC	MPC	MPC	GM	GM	GM	GM	GM	GM	GM	GM
SiO2	44.84	45.72	44.64	43.96	44.13	45.65	45.47	46.66	52.54	52.88	49.88	44.35	45.17	43.75	43.76
TiO2	5.49	4.40	5.39	6.00	5.72	4.81	5.20	5.38	4.14	3.68	4.99	6.17	5.49	6.27	6.11
Al2O3	6.95	7.29	7.62	7.47	7.06	6.85	6.06	6.84	9.25	8.78	6.17	6.78	6.41	7.10	7.59
FeO	11.64	11.53	12.67	13.29	13.57	13.21	14.21	12.86	6.61	6.36	11.82	13.04	13.48	13.43	12.42
MnO															
MgO	8.82	8.90	8.06	7.60	7.55	7.67	7.43	7.44	10.44	11.01	7.56	7.76	7.41	7.63	7.91
CaO	21.46	21.46	20.80	20.82	21.10	21.20	20.83	19.95	15.50	16.16	18.59	21.07	21.19	21.11	21.43
Na2O	0.79	0.70	0.83	0.84	0.87	0.62	0.80	0.88	1.51	1.12	0.98	0.83	0.84	0.71	0.78
Total	99.99	100.00	100.01	99.98	100.00	100.01	100.00	100.01	99.99	99.99	99.99	100.00	99.99	100.00	100.00
En	28.66	28.90	26.76	25.32	24.89	25.30	24.46	25.66	41.28	42.04	27.44	25.68	24.54	25.15	26.12
Fs	21.22	21.01	23.60	24.84	25.11	24.44	26.25	24.88	14.66	13.62	24.07	24.21	25.04	24.84	23.01
Wo	50.12	50.09	49.64	49.85	50.00	50.26	49.29	49.45	44.05	44.34	48.49	50.11	50.43	50.01	50.87

051219-1	051219-1	051219-1	051219-1	051219-1	051219-1	051219-1
CRX28 (7)	CRX29 (1)	CRX29 (6)	CRX30 (5)	CRX31 (8)	CRX32 (2)	CRX33 (2)
GM	GM	GM	GM	GM	GM	GM
44.37	45.56	45.14	44.57	45.78	45.48	44.30
5.55	5.06	5.10	5.53	4.52	5.62	6.46
6.27	6.44	6.94	6.93	7.21	5.74	5.84
15.56	13.57	12.62	13.19	11.11	13.64	15.14
0.39		0.36	0.32			
6.99	7.65	7.99	7.91	9.19	7.89	6.67
20.09	21.06	21.12	20.89	21.52	20.78	20.81
0.79	0.65	0.73	0.66	0.67	0.84	0.79
100.01	99.99	100.00	100.00	100.00	99.99	100.01
23.01	25.17	26.24	25.93	29.75	25.89	22.15
29.46	25.04	23.92	24.85	20.18	25.11	28.20
47.53	49.79	49.84	49.22	50.07	49.00	49.66

Sample	051219-8	051219-8	051219-8	051219-8	051219-8	051219-8	051219-8	051219-8	051219-8	051219-8	051219-8	051219-8	051219-8	051219-8	051219-8
Crystal/Zone [C: Core, R: Rim]	CRX2 (5)	CRX2 (8)	CRX2 (9)	CRX16 (44)	CRX16 (45)	CRX17 (46)	CRX17 (47)	CRX17 (48)	CRX17 (49)	CRX17 (7)	CRX18 (14)	CRX19 (5)	CRX20 (8)	CRX20 (12)	CRX21 (19)
Type [PC: phenocryst, MPC: microphenocryst, GM: groundmass]	MPC	GM	MPC	GM	GM	GM	GM	MPC	GM	MPC	GM	GM	GM	GM	GM
SiO2	50.11	52.60	51.59	50.35	52.11	52.11	53.49	53.09	53.55	58.49	53.87	53.04	53.43	51.98	51.09
TiO2	2.84	1.46	1.75	2.16	1.36	1.25	0.98	1.20	1.03	0.75	2.42	1.12	1.08	1.45	2.48
Al2O3	4.48	3.27	4.96	4.78	4.29	3.69	2.55	3.12	2.66	3.60	5.75	3.15	2.15	4.16	3.80
Cr2O3			0.80	0.26	0.63		0.46	0.44	0.25			0.47		1.02	
FeO	9.63	6.48	6.21	7.41	6.65	7.42	5.98	5.94	5.88	2.87	5.89	6.46	6.56	6.03	8.54
MnO				0.22					0.21			0.30			
MgO	12.06	14.57	13.99	13.66	14.21	14.26	14.87	14.66	14.93	19.18	14.45	14.71	15.25	14.17	12.84
CaO	20.22	21.22	20.69	20.80	20.39	20.93	21.29	21.23	21.09	15.12	16.70	20.74	21.18	21.19	20.68
Na2O	0.66	0.39		0.37	0.37	0.34	0.37	0.34	0.42		0.93		0.34		0.58
Total	100.00	99.99	99.99	100.01	100.01	100.00	99.99	100.02	100.02	100.01	100.01	99.99	99.99	100.00	100.01
En	37.69	43.55	43.25	41.53	43.60	42.61	44.35	44.09	44.56	60.59	48.56	44.03	44.65	43.22	39.52
Fs	16.88	10.87	10.77	13.02	11.45	12.44	10.01	10.02	10.20	5.09	11.10	11.36	10.78	10.32	14.74
Wo	45.42	45.58	45.97	45.45	44.96	44.95	45.64	45.89	45.24	34.33	40.34	44.61	44.57	46.46	45.74

051219-8	051219-8	051219-8	051219-8	051219-8	051219-8	051219-8	051219-8	051219-8	051219-8	051219-8	051219-8	051219-8	051219-8	051219-8
CRX22 (24)	CRX23 (31)	CRX25 (37)	CRX26 (43)	CRX27 (48)	CRX28 (55)	CRX29 (60)	CRX30 (63)	CRX31 (72)	CRX32 (75)	CRX33 (76)	CRX34 (79)	CRX35 (84)	CRX36 (85)	CRX37 (92)
GM	GM	GM	GM	GM	GM	GM	GM	GM	GM	GM	GM	GM	GM	GM
53.69	54.26	53.28	49.48	51.71	51.61	53.76	52.58	53.10	52.62	54.25	53.28	48.85	51.50	52.13
0.95	0.97	0.98	3.30	1.30	1.93	1.01	1.23	1.17	1.56	0.89	1.07	3.80	1.90	2.04
2.75	2.26	2.68	4.49	4.38	4.02	2.59	3.24	2.92	3.24	2.12	2.96	4.65	4.08	2.05
	0.58	0.35		0.80		0.57	0.49	0.50		0.51	0.58			
5.90	6.06	5.96	9.29	6.16	7.44	5.73	6.32	5.92	6.96	5.66	5.88	10.63	7.92	9.48
														0.35
15.03	15.52	14.95	12.27	14.52	13.82	15.27	14.62	14.79	14.18	15.46	14.92	10.96	13.68	13.29
21.28	20.35	21.37	20.65	20.73	20.74	20.61	21.11	21.17	21.07	21.11	21.32	20.24	20.92	20.24
0.39		0.43	0.52	0.41	0.44	0.46	0.41	0.42	0.37			0.87		0.41
99.99	100.00	100.00	100.00	100.01	100.00	100.00	100.00	99.99	100.00	100.00	100.01	100.00	100.00	99.99
44.69	46.27	44.43	37.96	44.17	42.01	45.86	43.85	44.38	42.68	45.73	44.48	34.83	41.26	39.85
9.84	10.13	9.94	16.12	10.51	12.69	9.65	10.63	9.97	11.75	9.39	9.83	18.95	13.40	16.54
45.47	43.60	45.64	45.92	45.32	45.31	44.49	45.51	45.65	45.57	44.88	45.68	46.22	45.34	43.61

051219-8	051219-8
CRX38 (94)	CRX39 (97)
GM	GM
53.15	53.78
1.67	1.00
2.23	2.60
	0.40
8.25	5.70
14.02	15.23
20.67	21.30
99.99	100.01
41.85	45.14
13.81	9.48
44.34	45.38

Sample	230220-2	230220-2	230220-2	230220-2	230220-2	230220-2	230220-2	230220-2	230220-2	230220-2	230220-2	230220-2	230220-2	230220-2	230220-2
Crystal/Zone [C: Core, R: Rim]	CRX4 (7)	CRX4 (8)	CRX4 (9)	CRX4 (10)	CRX5 (11)	CRX5 (12)	CRX5 (14)	CRX10 (24)	CRX10 (26)	CRX12 (31)	CRX17 (45)	CRX19 (51)	CRX21 (56)	CRX21 (59)	CRX21 (60)
Type [PC: phenocryst, MPC: microphenocryst, GM: groundmass]	MPC	MPC	MPC	MPC	MPC	MPC	MPC	GM	GM	GM	GM	GM	GM	GM	GM
SiO2	48.59	48.91	49.91	48.51	49.30	48.32	48.38	48.80	50.43	50.60	49.68	49.42	48.12	49.25	48.71
TiO2	3.68	3.39	2.98	3.50	3.06	3.52	3.32	3.81	2.76	2.72	2.89	3.30	4.11	3.29	3.49
Al2O3	5.02	4.53	4.23	4.49	4.59	5.07	4.19	4.14	2.89	4.02	4.08	4.54	4.20	4.81	4.38
Cr2O3	0.38														
FeO	10.49	12.30	11.46	12.84	11.79	11.58	14.28	12.02	13.66	9.51	11.28	10.38	12.72	9.37	11.51
MnO		0.34		0.44		0.34	0.42		0.36		0.34		0.39		
MgO	10.95	9.88	10.46	9.29	10.14	9.97	9.12	10.24	10.13	11.99	10.94	10.75	9.80	12.09	10.41
CaO	20.39	20.12	20.50	20.31	20.42	20.59	19.56	20.34	19.07	20.69	20.27	21.10	20.15	20.69	20.39
Na2O	0.49	0.53	0.46	0.63	0.70	0.61	0.71	0.66	0.70	0.46	0.53	0.50	0.52	0.49	0.62
V2O5															0.49
Total	99.99	100.00	100.00	100.01	100.00	100.00	99.98	100.01	100.00	99.99	100.01	99.99	100.01	99.99	99.51
En	34.77	31.43	33.08	29.64	32.26	31.69	29.02	32.40	31.95	37.24	34.16	33.87	30.97	37.53	33.03
Fs	18.69	22.57	20.33	23.78	21.04	21.26	26.25	21.34	24.82	16.57	20.36	18.35	23.25	16.32	20.48
Wo	46.54	46.00	46.59	46.58	46.69	47.04	44.73	46.26	43.23	46.19	45.48	47.78	45.77	46.16	46.49

230220-2	230220-2	230220-2	230220-2	230220-2	230220-2	230220-2	230220-2	230220-2	230220-2	230220-2	230220-2	230220-2	230220-2	230220-2	230220-2
CRX21 (61)	CRX22 (6)	CRX24 (22)	CRX25 (3)	CRX25 (4)	CRX25 (7)	CRX26 (5)	CRX27 (6)	CRX28 (5)	CRX29 (5)	CRX30 (5)	CRX31 (6)	CRX31 (7)	CRX32 (5)	CRX33 (3)	
GM	GM	GM	GM	GM	GM	GM	GM	GM	GM	GM	GM	GM	GM	GM	GM
48.01	59.03	58.25	49.07	49.09	49.05	48.48	49.37	47.67	48.27	48.71	48.80	48.07	47.78	48.49	
4.11	1.91	2.40	3.30	3.33	3.24	3.60	3.38	4.36	3.72	3.50	3.59	4.43	4.21	3.55	
4.41	5.04	4.32	4.61	4.03	4.56	4.33	4.08	4.08	4.86	4.49	4.29	3.18	4.33	4.58	
12.45	4.55	5.34	10.07	11.52	10.10	12.48	10.80	13.40	10.95	11.18	11.45	14.67	12.51	12.14	
0.34			0.29	0.28	0.26	0.31	0.21	0.31	0.24	0.30	0.21	0.33	0.28	0.26	
9.43	14.60	13.73	11.10	10.28	11.10	9.63	10.64	9.04	10.45	10.23	10.27	8.31	9.57	10.06	
20.71	13.95	14.75	21.09	20.89	21.12	20.54	20.91	20.45	20.92	20.97	20.78	20.22	20.61	20.28	
0.53	0.92	1.22	0.46	0.57	0.56	0.62	0.61	0.70	0.59	0.63	0.60	0.79	0.71	0.64	
99.99	100.00	100.01	99.99	99.99	99.99	99.99	100.00	100.01	100.00	100.01	99.99	100.00	100.00	100.00	
29.94	53.72	50.24	34.61	32.21	34.59	30.50	33.41	28.76	32.90	32.23	32.35	26.58	30.32	31.84	
22.79	9.39	10.96	18.13	20.75	18.12	22.73	19.40	24.48	19.77	20.29	20.61	26.93	22.74	22.02	
47.26	36.89	38.79	47.26	47.04	47.30	46.76	47.19	46.76	47.33	47.48	47.04	46.49	46.94	46.13	

230220-2	230220-2	230220-2	230220-2	230220-2	230220-2	230220-2	230220-2	230220-2	230220-2	230220-2	230220-2	230220-2	230220-2	230220-2
CRX34 (4)	CRX35 (5)	CRX35 (6)	CRX36 (4)	CRX37 (5)	CRX37 (6)	CRX38 (3)	CRX38 (4)	CRX39 (3)	CRX39 (4)	CRX40 (3)	CRX40 (4)	CRX41 (8)	CRX42 (5)	CRX42 (6)
GM	GM	GM	GM	GM	GM	GM	GM	GM	GM	GM	GM	GM	GM	GM
49.22	47.18	48.69	48.80	48.68	48.96	48.39	49.09	48.30	48.80	49.66	48.57	49.87	49.24	49.21
2.90	4.28	3.37	3.61	3.76	3.30	3.80	3.20	3.55	3.39	2.85	3.72	2.66	3.14	3.19
4.94	5.07	3.85	3.61	4.34	5.07	4.70	4.22	4.00	4.23	5.03	3.69	4.13	4.84	4.51
										0.31			0.23	
10.37	12.94	12.98	13.37	10.59	9.13	10.70	11.69	13.23	11.40	8.86	13.80	10.24	9.42	10.22
0.26	0.28	0.33	0.31	0.27	0.23	0.22	0.24	0.37	0.28	0.30	0.30	0.27	0.22	0.27
10.94	9.31	9.53	9.31	10.94	11.80	10.35	10.38	9.27	10.34	11.92	8.97	10.98	11.50	10.94
20.84	20.23	20.29	20.35	20.78	21.03	21.24	20.58	20.33	21.02	20.88	20.36	21.26	20.91	21.07
0.52	0.71	0.70	0.64	0.64	0.50	0.60	0.61	0.63	0.56	0.50	0.60	0.58	0.49	0.58
		0.26						0.32						
99.99	100.00	100.00	100.00	100.00	100.02	100.00	100.01	100.00	100.02	100.01	100.01	99.99	99.99	99.99
34.31	29.78	30.18	29.45	34.22	36.68	32.61	32.57	29.42	32.31	37.37	28.46	34.14	36.01	34.22
18.71	23.72	23.65	24.28	19.06	16.33	19.30	21.01	24.22	20.48	15.58	25.11	18.34	16.94	18.41
46.98	46.50	46.17	46.27	46.72	46.99	48.09	46.42	46.37	47.21	47.05	46.43	47.51	47.05	47.37

Sample	240220-2	240220-2	240220-2	240220-2	240220-2	240220-2	240220-2	240220-2	240220-2	240220-2	240220-2	240220-2	240220-2	240220-2	
Crystal/Zone [C: Core, R: Rim]	CRX5 (15)	CRX5 (16)	CRX5 (17)	CRX5 (18)	CRX6 (23)	CRX11 (39)	CRX12 (41)	CRX12 (43)	CRX15 C (48)	CRX15 R (49)	CRX21 (32)	CRX23 (7)	CRX24 (11)	CRX25 (14)	CRX25 (17)
Type [PC: phenocryst, MPC: microphenocryst, GM: groundmass]	GM	GM	GM	GM	GM	GM	GM	GM	PC	PC	GM	GM	GM	GM	GM
SiO2	54.51	54.78	54.88	55.43	52.05	54.16	52.53	53.02	54.43	53.70	58.13	51.81	52.97	51.50	52.12
TiO2		0.73			2.23	0.76	1.76	1.78	0.53	0.91	1.17	2.33	1.56	1.99	2.03
Al2O3		1.56			3.40	0.86	2.53	2.58	1.20	2.10	2.41	3.49	2.47	3.29	2.82
FeO	11.03	8.43	11.19	10.77	8.22	9.15	8.02	7.81	8.81	8.66	4.22	8.05	7.84	8.35	7.96
MnO			0.35				0.38		0.66	0.55				0.31	
MgO	12.99	14.54	12.71	12.47	13.01	14.07	13.53	13.65	15.15	15.12	17.60	13.07	14.18	13.38	13.66
CaO	20.90	19.96	20.38	20.84	20.50	20.60	20.79	20.65	18.78	18.95	15.87	20.77	20.60	20.64	20.95
Na2O	0.57		0.50	0.49	0.59	0.40	0.45	0.52	0.45		0.60	0.48	0.39	0.54	0.47
Total	100.00	100.00	100.01	100.00	100.00	100.00	99.99	100.01	100.01	99.99	100.00	100.00	100.01	100.00	100.01
En	37.98	43.26	37.57	37.24	40.21	41.37	40.77	41.52	44.61	44.59	56.10	40.20	42.48	40.45	41.17
Fs	18.09	14.07	19.14	18.04	14.25	15.09	14.21	13.33	15.66	15.25	7.55	13.89	13.17	14.70	13.46
Wo	43.92	42.68	43.29	44.72	45.54	43.53	45.02	45.15	39.74	40.16	36.36	45.91	44.35	44.85	45.38

240220-2	240220-2	240220-2	240220-2	240220-2	240220-2	240220-2	240220-2	240220-2	240220-2	240220-2	240220-2	240220-2
CRX26 (25)	CRX27 (30)	CRX28 (32)	CRX28 (35)	CRX30 (45)	CRX31 (50)	CRX 32 C (53)	CRX32 R (54)	CRX32 (55)	CRX32 (56)	CRX32 (57)	CRX34 (61)	CRX35 (66)
GM	GM	GM	GM	GM	GM	PC	PC	GM	GM	GM	GM	GM
53.02	53.44	52.81	52.58	52.12	51.15	54.17	54.07	54.79	54.99	53.74	52.19	53.21
1.55	1.65	1.82	1.91	1.87	2.35	0.67	0.71	1.06	0.87	1.22	1.99	1.66
2.57	2.62	2.38	2.55	3.21	4.25	1.50	1.58	1.51	1.96	1.87	3.16	2.22
7.69	7.42	7.99	8.35	8.13	8.32	8.69	8.36	7.85	7.68	7.81	7.85	7.71
				0.29		0.44	0.45					0.32
13.71	13.65	13.67	13.53	13.18	12.62	15.28	15.33	14.21	14.00	14.52	13.65	13.59
20.99	20.57	20.80	20.51	20.64	20.71	18.90	19.06	20.58	19.91	20.37	20.66	20.67
0.46	0.65	0.53	0.57	0.55	0.59	0.35	0.44		0.59	0.47	0.51	0.62
99.99	100.00	100.00	100.00	99.99	99.99	100.00	100.00	100.00	100.00	100.00	100.01	100.00
41.41	41.88	41.30	41.06	40.26	39.23	44.96	45.12	42.54	42.92	43.29	41.49	41.24
13.03	12.77	13.54	14.21	14.43	14.51	15.08	14.56	13.18	13.21	13.06	13.38	13.68
45.56	45.35	45.16	44.73	45.31	46.27	39.97	40.32	44.28	43.87	43.65	45.13	45.08

Sample Crystal/Zone [C: Core, R: Rim] Type [PC: phenocryst, MPC: microphenocryst, GM: groundmass]	250220-1	250220-1	250220-1	250220-1	250220-1	250220-1	250220-1	250220-1	250220-1	250220-1	250220-1	250220-1	250220-1	250220-1	250220-1
	CRX3 (11)	CRX10 (26)	CRX10 (27)	CRX15 (45)	CRX15 (46)	CRX16 C (49)	CRX16 R (50)	CRX23 (65)	CRX23 (66)	CRX23 (67)	CRX23 (68)	CRX24 (7)	CRX25 (3)	CRX25 (4)	CRX27 (3)
	GM	GM	GM	MPC	MPC	PC	PC	GM	GM	GM	GM	GM	GM	GM	GM
SiO2	46.39	44.28	44.59	48.81	48.91	51.77	51.98	45.41	46.10	50.60	45.25	47.77	45.56	46.23	48.58
TiO2	4.27	6.73	5.99	3.64	3.69	1.00	0.82	6.35	6.34	3.56	7.19	5.02	6.39	5.44	3.73
Al2O3	5.42	3.65	4.86	5.01	5.19	6.14	6.58	4.15	4.66	3.67	2.89	5.08	4.11	4.08	4.58
Cr2O3					0.39	0.56	0.76								
FeO	14.24	16.38	16.50	10.41	9.22	5.50	4.83	17.93	17.27	18.72	20.73	13.64	15.81	16.70	10.40
MnO		0.36	0.41					0.50	0.36	0.57	0.61	0.34	0.34	0.37	0.32
MgO	9.13	6.70	6.06	11.04	11.62	14.95	14.83	4.11	5.07	3.81	2.86	6.10	6.86	6.43	11.07
CaO	19.90	20.09	19.15	20.61	20.41	19.56	19.64	19.10	18.70	16.83	19.26	18.41	20.13	19.71	20.76
Na2O	0.64	1.04	1.34	0.48	0.58	0.52	0.57	1.48	1.51	1.53	1.20	1.95	0.80	1.04	0.55
K2O			0.25					0.34		0.72		0.62			
P2O5		0.78	0.84					0.65				1.07			
Total	99.99	99.23	99.15	100.00	100.01	100.00	100.01	99.37	100.01	100.01	99.99	100.00	100.00	100.00	99.99
En	29.06	21.94	20.66	34.84	36.93	46.58	46.85	14.59	17.85	14.25	9.97	22.45	22.57	21.31	34.59
Fs	25.42	30.78	32.40	18.43	16.44	9.61	8.56	36.70	34.83	40.50	41.76	28.87	29.82	31.74	18.80
Wo	45.52	47.28	46.93	46.74	46.63	43.80	44.59	48.71	47.32	45.25	48.27	48.69	47.61	46.95	46.62

250220-1	250220-1	250220-1	250220-1	250220-1	250220-1	250220-1	250220-1	250220-1	250220-1	250220-1	250220-1	250220-1	250220-1	250220-1	250220-1
CRX27 (6)	CRX28 (5)	CRX28 (6)	CRX29 (4)	CRX29 (5)	CRX30 (3)	CRX31 (5)	CRX32 (1)	CRX32 (2)	CRX33 (1)	CRX33 (2)	CRX34 (1)	CRX35 (1)	CRX35 (2)	CRX36 (1)	CRX36 (2)
GM	GM	GM	GM	GM	GM	GM	GM	GM	GM	GM	GM	GM	GM	GM	GM
44.91	47.46	48.21	45.10	45.81	49.00	45.38	44.67	44.46	47.95	45.66	49.79	49.46	46.66	46.66	46.04
6.65	5.94	4.80	6.26	5.83	3.48	6.34	6.71	7.09	3.94	6.11	3.21	4.03	5.05	3.95	4.03
4.87	4.77	5.06	4.87	5.22	5.30	4.36	4.07	3.81	5.43	5.83	3.87	6.25	6.18	5.45	6.16
15.70	16.23	14.40	15.62	13.61	10.04	17.19	17.35	15.46	10.36	14.91	11.24	11.04	14.13	11.32	10.93
0.48	0.36						0.48		0.36						0.31
6.64	4.61	6.76	6.91	8.41	10.91	5.32	5.61	6.49	10.85	6.43	10.77	8.09	6.85	10.67	10.61
19.79	17.65	18.78	20.12	20.27	20.66	20.11	20.06	20.65	20.53	18.76	20.66	18.47	18.94	21.13	21.09
0.96	1.56	1.44	1.11	0.85	0.62	1.31	1.06	1.08	0.58	1.09	0.46	1.12	1.05	0.83	0.83
	0.72	0.55								0.54		0.80	0.46		
	0.70							0.96		0.67		0.75	0.70		
100.00	100.00	100.00	99.99	100.00	100.01	100.01	100.01	100.00	100.00	100.00	100.00	100.01	100.02	100.01	100.00
22.18	17.33	23.86	22.93	27.47	34.76	18.09	18.68	21.63	34.31	22.74	33.74	29.36	24.13	33.10	33.04
30.32	34.99	28.51	29.08	24.94	17.94	32.78	33.32	28.91	19.03	29.58	19.75	22.47	27.92	19.80	19.76
47.50	47.68	47.63	47.99	47.59	47.30	49.13	48.00	49.46	46.66	47.68	46.51	48.17	47.95	47.11	47.20

Sample Crystal/Zone [C: Core, R: Rim] Type [PC: phenocryst, MPC: microphenocryst, GM: groundmass	250220-6	250220-6	250220-6	250220-6	250220-6	250220-6	250220-6	250220-6	250220-6	250220-6	250220-6	250220-6	250220-6	250220-6	250220-6
	CRX4 C (10)	CRX4 R (11)	CRX4 (13)	CRX6 R (20)	CRX6 C2 (21)	CRX6 C3 (22)	CRX8 (26)	CRX8 (28)	CRX11 (35)	CRX11 (36)	CRX13 (3)	CRX13 (4)	CRX14 (4)	CRX16 (6)	CRX17 (3)
	PC	PC	GM	PC	PC	PC	GM	GM	MPC	MPC	GM	GM	GM	GM	GM
SiO2	53.04	53.56	53.34	53.63	55.64	55.73	51.07	50.88	54.98	55.19	51.55	51.59	51.04	52.48	52.01
TiO2	1.20	0.99	1.49	1.14	0.36	0.34	2.20	2.42	0.67	0.56	2.48	2.15	2.05	1.92	2.11
Al2O3	2.45	1.84	2.20	1.94	0.51	0.57	4.38	3.81	0.68	0.36	3.91	3.90	4.77	2.59	3.23
Cr2O3							0.26	0.26							
FeO	9.11	8.96	7.75	8.02	17.22	17.18	8.35	8.18	7.94	8.12	8.44	7.84	7.44	7.75	8.15
MnO	0.33	0.30	0.26	0.27	1.02	1.05	0.23	0.23	0.29	0.27					
MgO	14.41	14.83	14.15	14.52	23.56	23.44	13.22	12.92	14.37	14.59	12.78	13.46	13.34	13.88	13.32
CaO	19.06	19.13	20.42	20.09	1.69	1.68	20.17	20.76	20.75	20.60	20.26	20.63	20.91	20.95	20.72
Na2O	0.40	0.39	0.41	0.38			0.35	0.54	0.31	0.31	0.58	0.43	0.44	0.44	0.46
Total	100.00	100.00	100.02	99.99	100.00	99.99	100.00	100.00	99.99	100.00	100.00	100.00	99.99	100.01	100.00
En	43.14	43.91	42.47	43.20	67.29	67.20	40.80	39.68	42.39	42.78	39.84	41.18	40.99	41.70	40.63
Fs	15.86	15.39	13.49	13.84	29.24	29.34	14.46	14.49	13.62	13.81	14.76	13.46	12.83	13.06	13.95
Wo	41.01	40.71	44.04	42.96	3.47	3.46	44.74	45.82	43.99	43.41	45.40	45.36	46.18	45.24	45.42

250220-6	250220-6	250220-6	250220-6	250220-6	250220-6	250220-6	250220-6	250220-6	250220-6	250220-6	250220-6	250220-6	250220-6	250220-6
CRX17 (4)	CRX18 (4)	CRX19 (7)	CRX20 (3)	CRX21 (3)	CRX21 (4)	CRX22 (3)	CRX22 (4)	CRX23 (5)	CRX23 (6)	CRX25 (1)	CRX25 (2)	CRX25 (5)	CRX29 (5)	
GM	GM	GM	GM	GM	GM	GM	GM	GM	GM	GM	GM	GM	GM	GM
49.99	52.32	51.97	55.63	53.07	50.76	49.25	50.37	51.33	52.59	55.60	53.94	53.98	52.44	
2.36	1.92	2.39		1.41	2.83	2.83	2.82	2.16	1.77	0.56	1.48	1.47	1.79	
5.07	3.14	3.09	0.85	2.58	4.75	6.13	4.51	4.43	2.65		1.60	2.66	2.88	
9.25	8.11	7.63	8.51	7.95	8.52	8.60	9.99	8.47	8.07	8.36	7.47	7.51	7.63	
11.78	13.28	13.40	15.58	13.94	12.83	11.94	11.63	12.79	13.59	14.88	14.30	13.46	13.74	
20.95	20.81	20.98	19.09	20.60	19.83	20.76	20.15	20.34	20.87	20.60	20.77	20.41	21.16	
0.60	0.41	0.55	0.34	0.45	0.49	0.49	0.54	0.48	0.44		0.44	0.51	0.36	
100.00	99.99	100.01	100.00	100.00	100.01	100.00	100.01	100.00	99.98	100.00	100.00	100.00	100.00	100.00
36.78	40.51	40.91	45.72	41.98	40.27	37.68	36.67	39.77	41.04	43.29	42.79	41.62	41.35	
16.20	13.88	13.07	14.01	13.43	15.00	15.23	17.67	14.77	13.67	13.64	12.54	13.03	12.88	
47.01	45.62	46.03	40.27	44.59	44.73	47.09	45.66	45.46	45.29	43.07	44.67	45.36	45.77	

C.2 Datos análisis SEM intrusivos

- **Mediciones puntuales realizadas en los fenocristales presentes en los xenolitos: plagioclasa, feldespatos potásicos y cuarzo. Para orientación de los puntos de medición, se adjuntan imágenes a nícoles cruzados con los cristales enumerados. Número que aparece en la segunda fila de las tablas. El número entre paréntesis corresponde a la enumeración interna del SEM de los puntos de medición. Solo se encuentran los análisis de los feldespatos.**

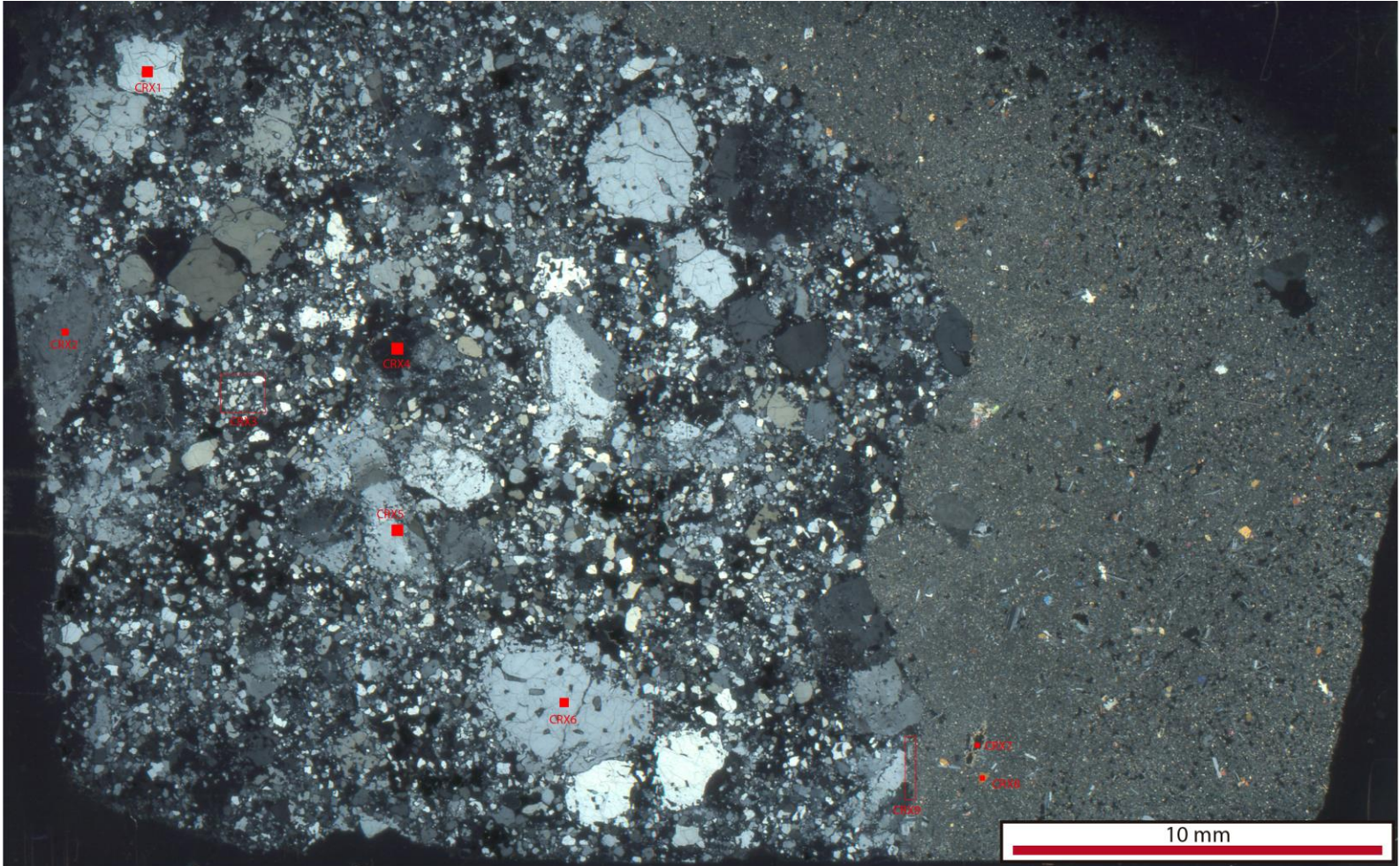


Fig. 68. Imagen a polarizadores cruzados de la muestra JV240220-2xeno.

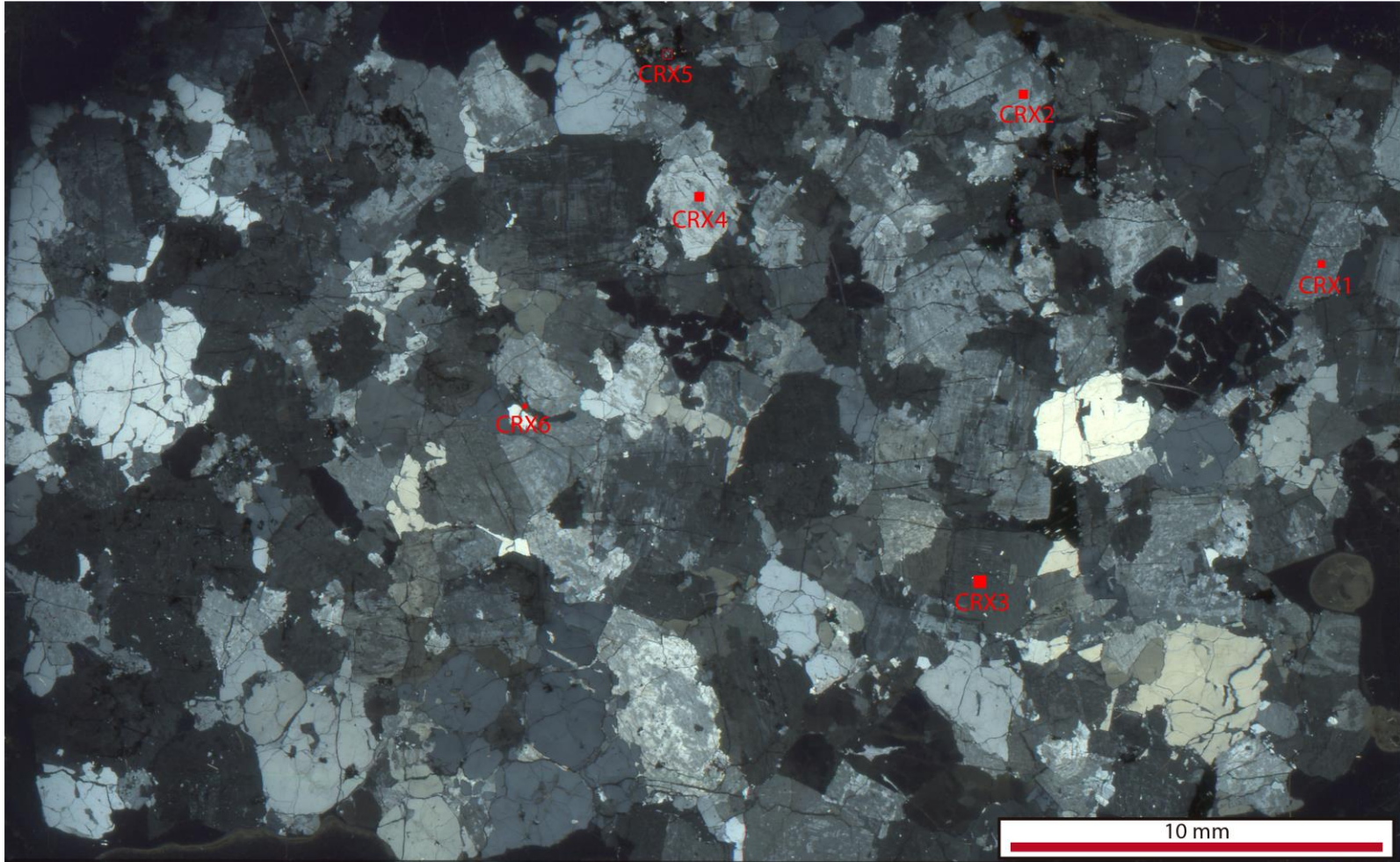


Fig. 69. Imagen a polarizadores cruzados de la muestra JV240220-3xen.

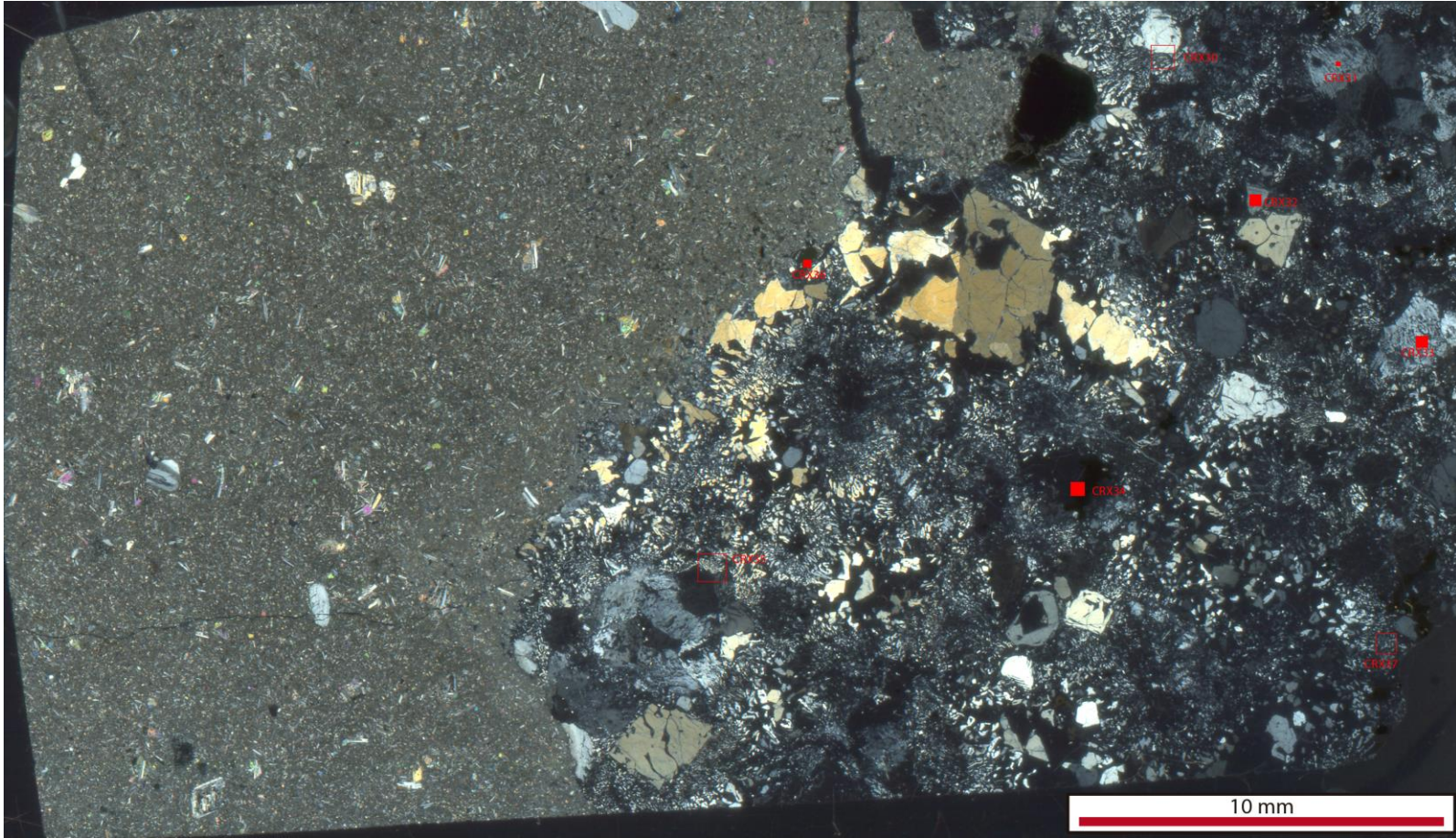


Fig. 70. Imagen a polarizadores cruzados de la muestra JV250220-6xeno.

1. Feldespato

Sample Crystal/Zone [C: Core, R: Rim] Type [PC: phenocryst, MPC: microphenocryst, GM: groundmass]	240220-2 xeno	240220-2 xeno	240220-2 xeno	240220-2 xeno	240220-2 xeno	240220-2 xeno	240220-2 xeno	240220-2 xeno
	CRX1 (2)	CRX1 (3)	CRX2 (5)	CRX3 (7)	CRX4 (9)	CRX5 (11)	CRX6 (12)	CRX6 (13)
	PC	PC	PC	PC	PC	PC	PC	PC
SiO2	70.52	67.71	68.80	71.66	68.88	69.77	67.65	71.28
Al2O3	17.22	19.45	18.37	16.59	19.08	18.06	19.44	16.36
FeO	0.79							0.45
CaO		1.42					1.54	
Na2O	6.27	7.69	7.27	6.20	7.21	6.96	7.84	5.85
K2O	5.20	3.73	5.56	5.55	4.83	5.22	3.54	6.07
Total								
An	0.00	7.18	0.00	0.00	0.00	0.00	7.72	0.00
Ab	64.70	70.36	66.52	62.93	69.41	66.96	71.14	59.43
Or	35.30	22.46	33.48	37.07	30.59	33.04	21.14	40.57

Sample Crystal/Zone [C: Core, R: Rim] Type [PC: phenocryst, MPC: microphenocryst, GM: groundmass]	240220-3 xeno	240220-3 xeno	240220-3 xeno	240220-3 xeno	240220-3 xeno	240220-3 xeno	240220-3 xeno	240220-3 xeno	240220-3 xeno	240220-3 xeno
	CRX1 (2)	CRX1 (3)	CRX2 (4)	CRX2 (5)	CRX3 (6)	CRX3 (7)	CRX3 (8)	CRX4 (9)	CRX4 (10)	CRX4 (11)
	PC	PC	PC	PC	PC	PC	PC	PC	PC	PC
SiO2	67.55	68.12	68.23	68.19	61.26	60.22	60.93	67.00	67.40	66.81
Al2O3	19.75	18.26	19.45	17.97	18.10	17.82	16.66	19.62	18.15	19.76
FeO										0.19
CaO	1.23		0.93		0.90	0.93		1.01		0.99
Na2O	11.09	4.46	10.70	3.31	11.54	11.24	3.23	11.85	3.73	11.99
K2O	0.38	9.16	0.69	10.52	0.20	0.22	8.62	0.52	9.81	0.26
Total										
An	5.65	0.00	4.40	0.00	4.09	4.32	0.00	4.38	0.00	4.30
Ab	92.26	42.53	91.70	32.35	94.83	94.46	36.28	92.94	36.62	94.35
Or	2.08	57.47	3.89	67.65	1.08	1.22	63.72	2.68	63.38	1.35

Sample	250220-6 xeno	250220-6 xeno	250220-6 xeno	250220-6 xeno	250220-6 xeno	250220-6 xeno
Crystal/Zone [C: Core, R: Rim]	CRX30 (41)	CRX31 (44)	CRX33 (47)	CRX34 (48)	CRX35 (49)	CRX37 (52)
Type [PC: phenocryst, MPC: microphenocryst, GM: groundmass]	PC	PC	PC	PC	PC	PC
SiO2	70.61	68.95	70.98	69.79	72.14	71.15
Al2O3	18.14	18.75	18.25	18.38	16.69	18.09
FeO		0.35	0.41	1.04	0.22	0.34
CaO		0.73				
Na2O	5.31	6.08	4.55	4.95	4.63	4.42
K2O	5.94	5.15	5.81	5.84	6.33	5.99
Total						
An	0.00	4.09	0.00	0.00	0.00	0.00
Ab	57.60	61.59	54.34	56.30	52.64	52.86
Or	42.40	34.33	45.66	43.70	47.36	47.14

Annex D

D.1 Termo-oxibarometría en muestra evolucionada

Los estudios de equilibrio de fases en el sistema FeO-Fe₂O₃-TiO₂ permiten determinar la temperatura y la fugacidad de oxígeno de la formación de pares coexistentes de magnetita titanífera e ilmenita en muchas rocas (Buddington y Lindsley, 1964). En este caso, fue posible aplicar el geotermómetro de magnetita-ilmenita y el barómetro de oxígeno en la muestra JV031219-4 donde coexisten ambas fases (Fig. 71).

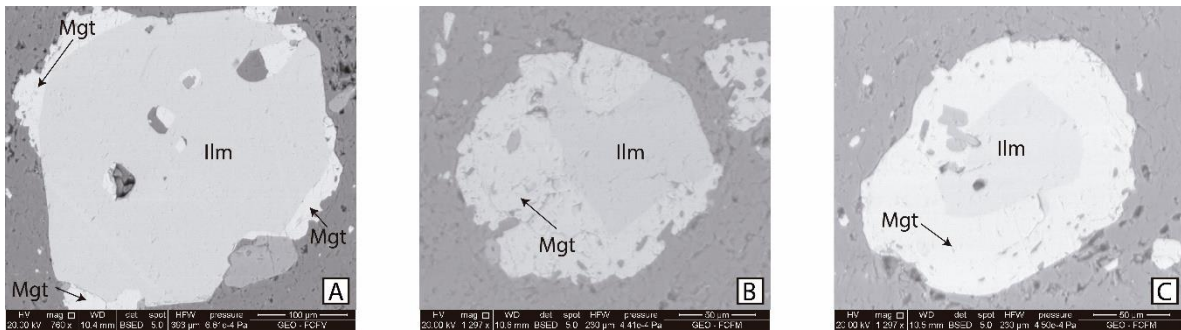


Fig. 71. Pares de magnetita-ilmenita encontrados en la muestra JV031219-4. (A) crx21, (B) crx27 y (C) crx29. Las imágenes fueron tomadas por un microscopio electrónico de barrido (SEM).

Para aplicar este método es necesario demostrar el equilibrio entre las fases. Bacon y Hirschmann (1988) propusieron la prueba de intercambio Mg/Mn. La partición de Mg y Mn entre la titanomagnetita e ilmenita ferrífera de rocas volcánicas proporciona una prueba de equilibrio entre fases coexistentes. Para ello, es necesario un gráfico de $\log(\text{Mg}/\text{Mn})_{\text{mgt}}$ vs. $\log(\text{Mg}/\text{Mn})_{\text{ilm}}$ con una regresión lineal dada por $\log(\text{Mg}/\text{Mn})_{\text{mgt}} = 0.9317 * \log(\text{Mg}/\text{Mn})_{\text{ilm}} - 0.0909$. Los pares de óxidos volcánicos que no se superponen a la línea de equilibrio o que caen significativamente fuera del error calculado probablemente no registran condiciones magmáticas de equilibrio y, por lo tanto, no deben utilizarse para geotermometría y barometría de oxígeno.

Para ello, se midió varias veces la composición de ambas fases (Ti-magnetita e ilmenita) con ayuda del SEM, y se introdujeron en el programa WinMIgob desarrollado por Yavuz (2021) para comprobar el equilibrio. Los resultados se muestran en la Fig. 72 y en la Table 8. Cuatro pares pasaron la prueba mientras que otros cuatro no.

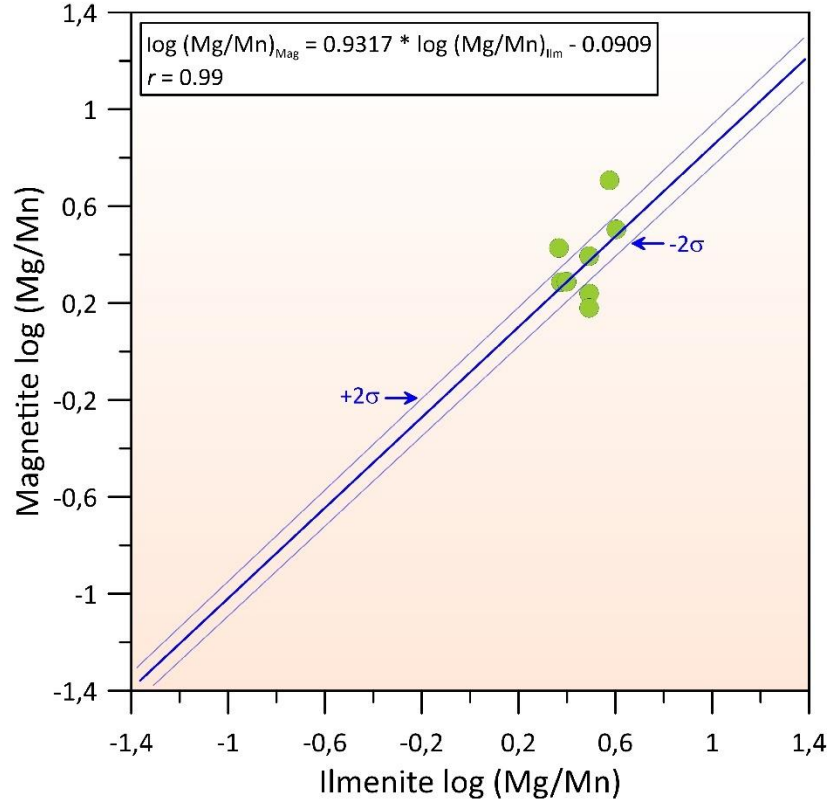


Fig. 72. Aplicación del test de intercambio Mg/Mn (Bacon y Hirschmann, 1988) para los pares seleccionados de magnetita-ilmenita para la muestra JV031219-4. Solo 4 pares pasaron el test. La línea gruesa del medio y las otras dos delgadas corresponden a la regresión lineal promedio y al error involucrado ($\pm 2\sigma$), respectivamente.

	ox crx21 (14)	ox crx21 (17)	ox crx21 (18)	ox crx21 (19)	ox crx27 (30)	ox crx27 (28)	ox crx29 (47)	ox crx29 (48)
Magnetite								
TiO2	23.05	21.97	22.7	21.2	23.32	22.45	24.43	24.19
Al2O3		2.03		1.76				
FeO	74.22	72.93	74.51	74.16	74.36	75.21	72.35	72.14
MnO	0.97	1.54	1.5	1.2	0.92	1.12	1.53	0.94
MgO	1.76	1.52	1.29	1.69	1.4	1.23	1.69	2.72
	ox crx21 (13)	ox crx21 (16)	ox crx21 (16)	ox crx21 (16)	ox crx27 (27)	ox crx27 (26)	ox crx29 (39)	ox crx29 (34)
Ilmenite								
TiO2	51.33	50.75	50.75	50.75	50.98	50.85	51.68	53.02
Al2O3								
FeO	45.19	45.44	45.44	45.44	44.68	45.02	44.69	41.42
MnO	1.06	1.38	1.38	1.38	1.87	1.76	1.5	1.77
MgO	2.42	2.43	2.43	2.43	2.47	2.37	2.13	3.79
Bacon and Hirschmann (1988) Test	Passed	Failed	Failed	Passed	Failed	Passed	Passed	Failed

Table 8. Composición química de los tres pares magnetita-ilmenita encontrados en la muestra JV031219-4. En paréntesis se muestra el número de la medición en SEM. Para el número de los cristales ver Fig. 71.

Tras aplicar el filtro de equilibrio, el geotermómetro de magnetita-ilmenita muestra que JV031219-4 tiene temperaturas de equilibrio de 758°C a 858°C, con valores de fugacidad de oxígeno logarítmica (fO_2) de -16.75 a -13.93 utilizando el geotermómetro de magnetita-

ilmenita ($^{\circ}\text{C}$) y la fugacidad de oxígeno logarítmica ($f\text{O}_2$) de Spencer y Lindsley (1981) utilizando el método de cálculo de Lindsley y Spencer (1982). Para más detalles y otros resultados utilizando diferentes geotermobarómetros, ver la Table 9.

	ox crx21 (14)M ox crx21 (13)I		ox crx21 (19)M ox crx21 (16)I		ox crx27 (28)M ox crx27 (26)I		ox crx29 (47)M ox crx29 (39)I	
	T $^{\circ}\text{C}$	log fO ₂	T $^{\circ}\text{C}$	log fO ₂	T $^{\circ}\text{C}$	log fO ₂	T $^{\circ}\text{C}$	log fO ₂
Powell and Powell (1977)								
Carmichael (1967)	873.77	-9.85	874.71	-10.17	895.39	-9.96	863.98	-9.67
Anderson (1968)	876.92	-9.99	887.19	-10.30	904.64	-10.10	865.86	-9.77
Lindsley and Spencer (1982)	881.98	-9.83	894.69	-10.07	907.21	-9.95	877.03	-9.65
Stormer (1983)	870.93	-9.94	902.02	-10.08	896.34	-10.05	859.87	-9.74
Spencer and Lindsley (1981)								
Carmichael (1967)	783.81	-15.87	815.48	-14.80	836.97	-14.42	737.82	-17.32
Anderson (1968)	804.44	-15.22	845.86	-13.95	865.86	-13.63	758.45	-16.64
Lindsley and Spencer (1982)	797.26	-15.53	845.02	-14.14	858.14	-13.93	758.21	-16.75
Stormer (1983)	788.91	-15.66	859.09	-13.80	846.62	-14.12	742.49	-17.12
Andersen and Lindsley (1985)								
Carmichael (1967)	796.81	-15.87	819.21	-14.91	837.42	-14.66	760.68	-17.17
Anderson (1968)	811.93	-15.30	841.39	-14.22	857.57	-14.01	776.85	-16.54
Lindsley and Spencer (1982)	807.87	-15.60	842.35	-14.41	853.78	-14.28	778.45	-16.70
Stormer (1983)	800.01	-15.67	852.83	-14.15	843.75	-14.40	763.81	-16.96

Table 9. Temperatura y $f\text{O}_2$ calculada para la composición de los pares coexistentes de magnetita e ilmenita usando los geotermómetros de Powell y Powell (1977), Spencer y Lindsley (1981) y Andersen y Lindsley (1985). A la izquierda se encuentran los diferentes métodos usados para calcular la fracción molar de hematita, ilmenita, magnetita y ulvoespinela (*Xhem*, *Xilm*, *Xmag* y *Xulv*). M: magnetita, I: ilmenita.

La coexistencia de óxidos Fe-Ti y sus composiciones son importantes en la estimación de la fugacidad de oxígeno y la temperatura de equilibrio durante la evolución de estas rocas magmáticas. Los óxidos Fe-Ti representados por magnetita con ilmenita están presentes como fases accesorias en la masa fundamental de la muestra JV031219-4.

En los sistemas magmáticos que evolucionan naturalmente, las composiciones de los óxidos coexistentes cambian continuamente adaptándose a las nuevas condiciones. Por lo tanto, el termo-oxibarómetro de óxido Fe-Ti registra las últimas condiciones de equilibrio que pueden ser "congeladas" en los óxidos reequilibrados. Así, las condiciones pre-eruptivas sólo pueden ser registradas en caso de un enfriamiento muy rápido como en las erupciones Plinianas, cuando hay fuertes evidencias de un rápido ascenso y desgasificación (Hou et al., 2020).

Los resultados muestran temperaturas relativamente altas ($T > \sim 800^{\circ}\text{C}$) y fugacidades de oxígeno de moderadas a bajas ($-2 < \Delta\text{NNO} < 0$, donde NNO es el buffer níquel-níquel).

Es común encontrar intercrecimientos de ilmenita en titanomagnetita mostrando enrejados, sándwich, y lamelas compuestas de ilmenita en magnetita (Haggerty, 1991) pero aquí hay

una textura coronítica donde la ilmenita está rodeada por magnetita. Esta textura implica un cambio en la condición de oxidación desde una zona más oxidante (núcleo) a una zona menos oxidante (borde). El borde tiene una composición más alta de ilmenita y más baja de hematita mientras que el núcleo tiene composiciones intermedias entre ulvöspinel y magnetita (Fig. 73)

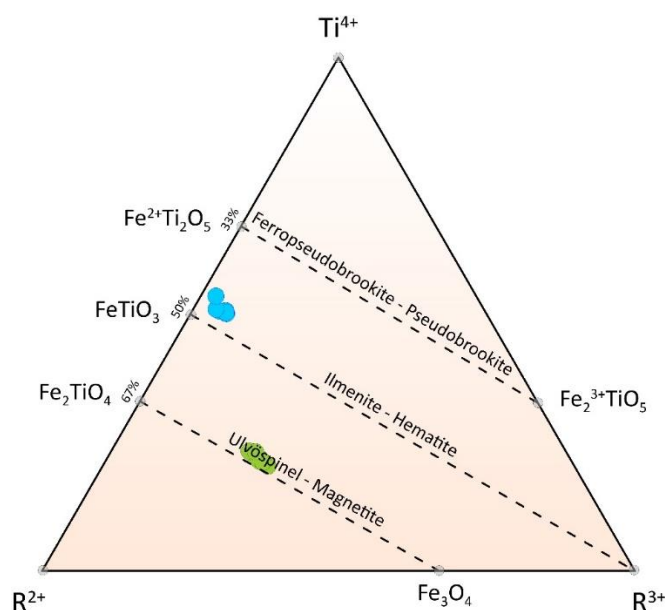


Fig. 73. Composición de los óxidos Fe-Ti en un diagrama de FeO-Fe₂O₃-TiO₂. Las líneas punteadas corresponden a las soluciones sólidas ilmenita-hematita y magnetita-ulvöspinel.

Debido a la falta de precisión en el análisis, por el uso de una herramienta semicuantitativa para la medición química, y de datos suficientes, este capítulo no se ha considerado dentro del cuerpo de la tesis y queda también fuera de los objetivos establecidos al principio. Además, la muestra traquítica tiene claras evidencias de mezcla, por lo que los valores obtenidos aquí no serían directamente aplicables a la evolución de la misma, mostrando una interpretación errónea si no se cuenta con mayores análisis.

No obstante, se trata de resultados que podrían anticipar el comportamiento del sistema y que deben ser apoyados con nuevos datos.